Quinine Copolymer Reporters for Enhanced Gene Editing and Raman Imaging

A Dissertation
SUBMITTED TO THE FACULTY OF THE
UNIVERSITY OF MINNESOTA
BY

Craig Van Bruggen

IN PARTIAL FULFILLMENT OF THE REQUIREMENTS
FOR THE DEGREE OF
DOCTOR OF PHILOSOPHY

Prof. Theresa M. Reineke, Advisor

January 2022

Acknowledgments

First, I would like to thank my advisor, Prof. Theresa Reineke. She inspired me with her dedication to her work and her unwavering leadership and mentorship proved to be fertile ground for me to grow as independent scientist. I am grateful to my close collaborators in research: Prof. Renee Frontiera, Prof. David Punihaole, Dr. Ariel Alperstein, Allison Keith, Punarbasu Roy, Nick Kreofsky, Andy Schmitz, Samantha Linn. They are Team Quinine! An amazing cohort of superhero researchers that worked hard in trenches with me to do great science. We even managed to have some fun while doing it!

I owe sincere gratitude to my oral preliminary and final defense committee members: Prof. Marc Hillmyer, Prof. Wei Shen, Prof. Mark Distefano. I also owe much appreciation to all the faculty members who taught my classes and provided advisement along the way. I would like to give a special thanks to my instructor during my TA position, Prof. Jane Wissinger, as well as the incredibly helpful staff and admininstrators I have worked with including Joseph Hexum, Nancy Thao, Nick Erickson, Prof. Aaron Massari, Chuck Tomlinson, Justin Thao, and Dr. Letitia Yao.

I relied heavily on a subset of mentors to learn biological lab techniques and to help run the cell biology lab, and I am deeply grateful for their help. These wizards include Dr. William Boyle, Dr. Yogesh Dhande, Dr. Haley Phillips, Dr. Pranav Agrawal, Prof. Ramya Kumar, Dr. Zhe Tan, Ngoc Le, Stephanie Mitchell, and collaborators/friends in the group of Dean Jakub Tolar. I also relied heavily on my colleagues in the synthesis lab and appreciate their help and support. These mad scientists include Dr. Matt Bockman, Dr. Jeff Ting, Dr. Anatolii Purchel, Dr. Leon Lillie, Dr. Nayereh Dadoo, Dr. Cristiam Santa Chalarca, Dr. Piril Ertem, Dr. Mammad Nasiri, Dr. Mitra Ganewatta, Dr. James Gallagher, Dr. Yaming Jiang, Dr. Seyoung Jung, Dr. Victoria Szlag, Dr. Rui Ding, Dr. Quanxuan Zhang, Dr. Dustin Sprouse. As my grad school career progressed, having reliable, helpful, intelligent, and fun colleagues in the Reineke Group were indispensable, and I cherish the friendships I developed there. These badasses include Dr. Hussnain Sajjad, Rishad Dalal, Ethan Gormong, Dr. Monica Ohnsorg, Dr. Derek Saxon Dr. Annie Luke, Mckenna Hanson, Christian Grimme, Soumi Das, Mayuri Kiran Porwal, Michael Leyden, Erin Maines, Emily Prebihalo, Christopher LaSalle, Kaylee Barr, Nathan Rackstraw, among other Reinek Group members, past and present.

Also, developing friendships throughout the UMN community was critical to my work and happiness here. I’m happy to enjoy my time of life here with friends including Dr. Patrick Crossland, Dr. Amy Ott, Hannah Degraaf, Mary Packard, Dr. Lindsay Johnson, Prof. Wilson Bailey, Dr. Alysha Dicke, Greg Kosinski, Katie Stanton, Amber Allemand, Dr. Michelle Pinharry, Michaela Roslawski, Dr. Lisa Fazzino, Dr. Cecilia Hall, Dr. Guilhem De Hoe, Dr. Hanna Macaranas, Dr. David Goldfeld, Dr. Beth Dewing, Dr. Kailey Soller, Ryan Soller, Dr. Sean O’Mara, Dr. Megan Weisenberger, Dr. Curtis Payne, Dr. Robin Harkins, Dr. Grant Fahnhorst, Stephen Dempsey, Jacob Prat, Dr. Ryan Daley, Dr. Benjamin Neisen, Caitlin Bouchey, Dr. Courtney Elwell, Dr. Bianca Ramirez, and Dr. Nicole Gagnon (among others in SciMentors). In addition my funding was also critical to my time here! Funding sources included the CSE Fellowship, Frieda Martha Kunze Fellowship, Limelight Bio, and the NSF (DMR-1904853).

Lastly, I would not have made it through my PhD without the unwavering support of my family and my fiancé, Charlene Chew (who I met at the UMN). Thank you for your patience and love through the years. You are appreciated more than you know.

To my friends, family, and mentors.

Abstract

After decades of development, gene therapy has finally reached the forefront of medicine and has led to new cures for genetic disorders and the development of life-saving vaccines. The field has been buoyed by the development of more precise and user-friendly targeted nucleases, such as those used for clustered regularly interspersed palindromic repeats (CRISPR)-based editing. These useful gene-editing technologies, however, are still stymied by the challenge of delivering exogenous nucleic acids and proteins into the cells of interest. The emerging gene therapy industry is investing heavily in developing more efficient and safe non-viral vehicles as alternatives to costly and immunogenic viral vectors. Cationic polymers are promising non-viral vectors due to their manufacturing scalability, their chemical stability, and their synthetic tunability. Improvements in delivery efficiency are necessary, however, for widespread adoption of polymeric vehicles for gene therapy. One challenge in improving performance, however, is the difficulty and limited methodology for elucidating the intracellular mechanics of polymeric vehicles. In this thesis, I describe my research focused on the development of a novel quinine-containing polymer, called a Quinine Copolymer Reporter (QCR), that enhanced transient transfections of cultured cells with plasmids and improved gene editing of cultured cells through the simultaneous delivery of the CRISPR-associated protein Cas9 and DNA donor template. In addition, I describe collaborative research performed with colleagues in the research group of Prof. Renee Frontiera that characterized a band in quinine's Raman spectrum that is diagnostic of its chemical environment. Using this chemical sensitivity in conjunction with Raman microscopic imaging, we help elucidated the intracellular unpackaging mechanisms of the QCR-nucleic acid complexes.

Table of Contents

List of Tables

List of Figures

List of Equations

List of Abbreviations

°	degree
°C	degree Celsius
×g	times gravity (units of centrifugal force)
Å	angstrom
α	fraction of quinine's with unprotonated quinoline rings
Đ	dispersity
ε	dielectric constant
λ	wavelength
λ_{ex}	excitation wavelength
λ_{em}	emission wavelength
σ	cross section
$\tilde{\nu}$	frequency
$\vec{\mu}$	dipole moment
μg	microgram
μL	microliter
μm	micrometer
Ω	solid angle
a	cavity radius
AAV	adeno-associated virus
aC	attocoulomb
ACS	American Chemical Society
AEMA	*N*-(2-aminoethyl) methacrylamide
AF488	Alexa Fluor 488
AIBN	azobisisobutyronitrile
Am	acrylamide
ASO	antisense oligonucleotide
AT	adenine-thymine base pair
atm	atmosphere
BSA	bovine serum albumin
c	speed of light
C	carbon
CAR-T	chimeric antigen receptor T-cell
Cas9	CRISPR associated protein 9
CDP	4-cyano-4-[(dodecylsulfanylthiocarbonyl)sulfanyl]pentanoic acid
CG	cytosine-guanine base pair
Cl	chlorine
cm	centimeter
COVID-19	coronavirus disease of 2019
CRISPR	clustered regularly interspersed palindromic repeats
Cy5	cyanine 5
d	deuterium
D	Debye or deuterium

DAEA	dimethylaminoethyl acrylate
DEAE-D	diethylaminoethyl dextran
DFT	density functional theory
d_h	hydrodynamic diameter
DI H_2O	distilled water
DLS	dynamic light scattering
DMA	5-(*N*,*N*-dimethyl)amiloride hydrochloride
DMAm	*N*,*N*-dimethylacrylamide
DMAEMA	2-dimethylaminoethyl methacrylate
DMAEAm	2-dimethylaminoethyl acrylamide
DMEM	Dulbecco's modified Eagle medium
DMF	dimethylformamide
DMSO	dimethylsulfoxide
DNA	deoxyribonucleic acid
dn/dc	specific refractive index increment
DSB	double-strand break
$\vec{E}$	electric field
EDTA	ethylenediaminetetraacetic acid
eGFP	enhanced green fluorescent protein
EMSA	electrophoretic mobility shift assay
f	monomer feed ratio
F	polymer composition ratio
FBS	fetal bovine serum
Fig.	Figure
FRET	Förster resonance energy transfer
g	gram
G	Gibb's free energy
GFP	green fluorescent protein
gr	gratings
h	hour
h	Planck's constant
H	hydrogen
HDR	homology-directed repair
HEA	2-hydroxyethyl acrylate
HEAm	*N*-hydroxyethyl acrylamide
HeLa	human cervical carcinoma cells
HEK 293T	human embryonic kidney cells
He-Ne	helium neon
HPLC	high pressure liquid chromatography
hr	hour
I	peak intensity
IMDM	Iscove's modified Dulbecco's medium
IR	infrared
ISO	International Standards Organization
k	rate constant

K	kelvin
K562	chronic myelogenous leukemia lymphoblasts
kb	kilo base pairs
kcal	kilocalorie
kDa	kilodalton
kg	kilogram
K-SFM	defined keratinocyte serum-free media
LNP	lipid nanoparticle
LPF	Lipofectamine
LS	light scattering
M	molar
M	monomer
MAG	2-deoxy-2-methacrylamido glucopyranose
MAGalNAc	methacrylamido *N*-acetyl-D-galactosamine
MAT	methacrylamido trehalose
mb	millibarn
MD	molecular dynamics
MHz	megahertz
mg	milligram
min	minutes
miRNA	microRNA
mL	milliliter
mm	millimeter
mM	millimolar
mmol	millimole
M_n	number average molar mass
mol	mole
mRNA	messenger ribonucleic acid
MRSEC	Materials Research, Science, and Engineering Center
ms	millisecond
mSv	millisievert
MV	megavolt
mW	milliwatt
M_w	weight average molar mass
n	replicated number
n	refractive index
N	nitrogen
Na	sodium
NA	numerical aperture
Nd:YAG	neodymium-doped yttrium aluminum garnet
NHEJ	non-homologous end-joining
NIPAm	*N*-isopropylacrylamide
NLS	nuclear localization signal
nm	nanometer
NMR	nuclear magnetic resonance

N/P	charged amine to DNA phosphate ratio
NPT	isothermic-isobaric ensemble
ng	nanogram
ns	nanosecond
NSF	National Science Foundation
N/TERT	immortalized keratinocytes
O	oxygen
OD	optical density
P	phosphorous
PAMAM	polyamidoamine
PBS	phosphate buffered saline
PC	principle component
PCA	principle component analysis
PCL	polycaprolactone
pDNA	plasmid
PED	Potential Energy Distribution
PEG	polyethylene glycol
PEI	polyethylenimine
PGAA	poly(glycoamidoamine)
pH	$-\log[H^+]$
PI	propidium iodide
pK_a	-log of acid dissociation constant (K_a)
PLGA	poly(lactic-*co*-glycolic acid)
PLL	poly-L-lysine
PEG	polyethylene glycol
PS	polystyrene
ps	picosecond
PTFE	polytetrafluoroethylene
Q	quinine
QCR	quinine copolymer reporter
r	reactivity ratio or radius
RAFT	reversible addition-fragmentation chain-transfer
RLUs	relative light units
RI	refractive index
RNP	ribonucleoprotein
s	seconds
S	sulfur
SARS-CoV-2	severe acute respiratory syndrome coronavirus 2
SD	standard deviation
sec	seconds
SEC	size exclusion chromatography
sgRNA	single guide RNA
SI	supporting information
siRNA	small interfering RNA
spd	small particle detector

sr	steradian
ssODN	single stranded oligo donor
TAE	buffer containing Tris, Acetic acid, and EDTA
TALEN	transcriptor activator-like endonuclease
TEM	transmission electron microscopy
TFA	trifluoroacetic acid
THF	tetrahydrofuran
UMN	University of Minnesota
USP	United States Pharmacopeia
UV	ultraviolet
V	volt
V-ATPase	vacuolar-type H^+-adenosine triphosphatase
v/v	volume/volume
wt	weight
w/	with
w/v	weight/volume

1. Introduction

Excerpts adapted with permission from:

Van Bruggen, C.; Hexum, J. K.; Tan, Z.; Dalal, R. J.; Reineke, T. M.; *Acc. Chem. Res.,* **2019**, *52*, (5), 1347-1358. Copyright 2019 American Chemical Society.

Kumar, R.; Santa Chalarca, C. F.; Bockman, M. R.; Van Bruggen, C.; Grimme, C. J.; Dalal, R. J.; Hanson, M. G.; Hexum, J. K.; Reineke, T. M.; *Chem. Rev.,* **2021**, DOI: 10.1021/acs.chemrev.0c00997. Copyright 2021 American Chemical Society.

1.1 Gene Therapy Overview

1.1.1 *Current State of Gene Therapy*

Transport of exogenous genetic material into cells in an efficient and nontoxic manner is universal and essential for life science and medical research, including gene therapy. Decades of work in the field of gene therapy, which aims to treat patients by modulating gene expression through the delivery of therapeutic genes, has finally led to breakthrough treatments for formerly intractable genetic diseases. In 2017, the Food and Drug Administration (FDA) approved a gene therapy treatment for the first time when they approved a therapeutic called Kymriah, a treatment for acute lymphoblastic leukemia.[1] Since then, the FDA has granted approval for gene therapies that treat diseases such as Leber's congenital amaurosis,[2] transthyretin-mediated amyloidosis,[3] and large B-cell lymphoma.[4] The clinical trial pipeline currently contains exciting possible gene therapy treatments for genetic disorders such as β-thalassemia[5] and Duschenne muscular dystrophy.[6] As of February 2020, over 4000 clinical trials of gene therapy treatments have been conducted or are ongoing,[7] and investment in the field has been quickly accelerating. The well-known SARS-CoV-2 vaccines developed by Pfizer, Moderna, and Johnson & Johnson, which, at the time of this writing, are currently being administered worldwide in an effort to control the COVID-19 pandemic, are themselves gene therapies and are testaments to the increasing role gene therapy is playing in medicine and public health.[8]

One of the factors contributing to the fast growth of gene therapy is the advent of more precise and efficient gene-modifying technologies such as transposons,[9] ribonucleic acid interference (RNAi) gene silencing,[10] zinc-finger nucleases (ZFNs),[11] transcriptor activator-like nucleases (TALENS),[12] clustered regularly interspersed palindromic repeats

(CRISPR),[13] and base editing.[14] While all of these technologies have been employed for gene therapy strategies, CRISPR has caused an exceptional amount of excitement for those developing gene therapeutics due to its ease of use and flexibility in targeting almost any gene with minimal modification. The mechanism underlying CRISPR-based gene editing is described below in *Section 1.1.5*.

All of these gene editing strategies rely on specialized nucleic acids, often in the form of deoxyribonucleic acid (DNA), ribonucleic acid (RNA), and/or proteins, such as the CRISPR associated protein 9 (Cas9) needed for CRISPR, in order to perform the desired genetic manipulation. These nucleic acids and/or proteins must be delivered either into the cytoplasm or nucleus of target cells in order to perform their task. If a virus is used to help deliver the required components, the manipulation is known as *transduction.* If a nonviral vehicle is used for this process, the manipulation is most commonly referred to as *transfection* (Fig. 1.1). A description of the most common reagents used for this process are described in *Section 1.1.3*. When the target cells to be transduced/transfected are located inside a living organism, as is the case for the SARS-CoV-2 vaccine, the treatment is defined as an *in vivo* gene therapy. Transduction/transfection of cells that have been removed from the body prior to being treated before re-injection, which is the case for therapies such as chimeric antigen receptor T cell (CAR-T) immunotherapy that was used for the FDA-approved therapy for large B-cell lymphoma mentioned above,[4] is defined as an *ex vivo* treatment. Whether the delivery is *in vivo* or *ex vivo*, the successful delivery of the nucleic acids and/or protein components to the target cells is often the bottleneck to successful implementation of the therapy[15-17] and can contribute to their enormous costs.[18] Approximately 70% of gene therapy clinical trials performed so far have used engineered viruses for the delivery of the therapeutic cargo,[19] and this heavy reliance on viral vectors is mainly due to their high efficiency in delivery.[20] The drawbacks of viral vectors and the push for their replacement by nonviral alternatives are discussed in the following sections.

1.1.2 *Viral Vectors*

Viral vectors are viruses that have been engineered to deliver therapeutic genetic cargo to host cells without replicating and causing a deleterious infection.[21] The most efficient and common viral vectors used in gene therapies are adenoviruses, adeno-associated viruses (AAV), retroviruses, and lentiviruses.[21] Adenoviruses (which is the viral vector used for the Johnson & Johnson's Janssen SARS-CoV-2 vaccine)[22] and AAV viruses are well-established vehicles for *in vivo* gene therapy, while retroviruses and lentiviruses are the most common vectors for *ex vivo* applications.[21] Each virus type varies in its type of genetic cargo, cargo capacity, host range, level of immunogenicity and toxicity, speed of onset, method of genetic integration, and expression level.[19] Viruses are far and away the most efficient vectors for gene delivery. There are issues, however, with the limited genetic cargo capacity, safety risks, and cost/scalability of viral vector production, which fuels the demand for non-viral alternatives.[23]

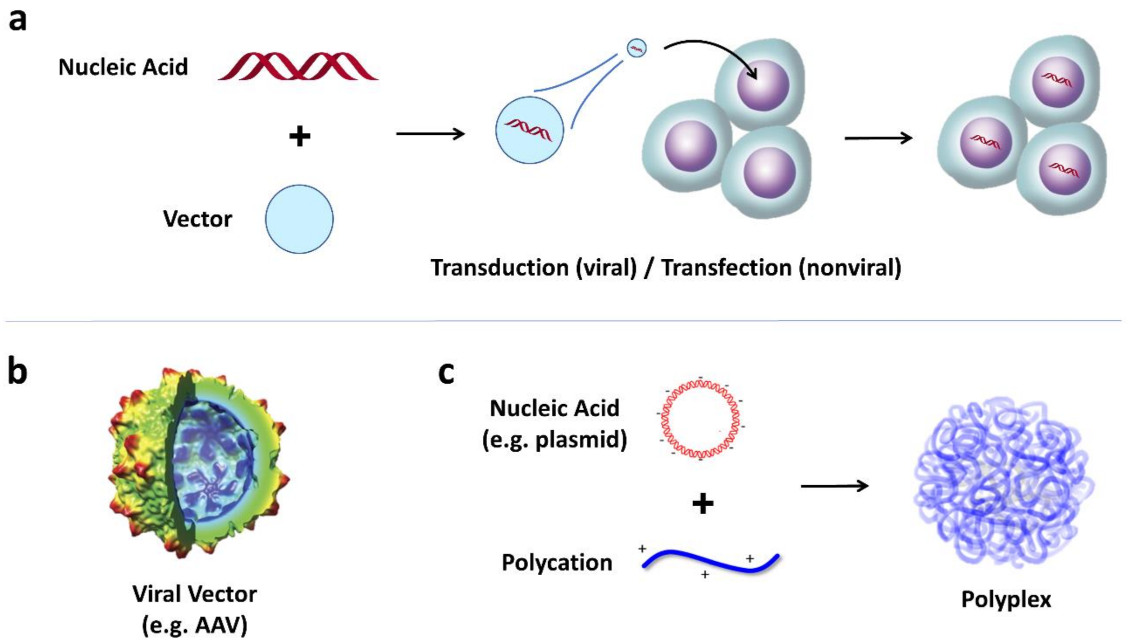

Figure 1.1. The process of gene delivery with viral and nonviral vectors. a) A therapeutic nucleic acid is packaged in a vehicle called a vector. The delivery of this vehicle and its cargo into target cells is known as transduction (for viral vectors) or transfection (for nonviral vectors). b) An example of a viral vector is an engineered adeno-associated virus (AAV), whose electron density map cross-section is shown (adapted from ref 24 with permission. Copyright 2012 American Society of Microbiology). c) An example of nonviral vector is a polycation that can electrostatically-bind nucleic acids (such as plasmids) to form complexes called polyplexes that are similar in scale to viral vectors.

1.1.3 *Nonviral Methods for Gene Delivery*

Compared to virus-based vectors, nonviral platforms boast advantages in their low cost of production, large cargo capacities, and immunocompatibility.[25] Despite these attractive features, most of these chemical systems are less efficient than viral vectors and, in some instances, can be cytotoxic.[26] Therefore, significant effort has been made to develop a nonviral delivery system that transfects with high efficiency while exhibiting minimal toxicity towards cells. Most nonviral delivery platforms can be grouped into several categories (listed below), each presenting advantages and disadvantages with their application.

Physical methods of delivery achieve translocation of hydrophilic macromolecules into the intracellular space of cells by transiently permeabilizing the cellular membrane via mechanical means.[27] These processes include microinjection, particle bombardment, electroporation, magnetofection, sonoporation, photoporation, mechanical deformation, and hydroporation.[27] Most of these physical methods are most effective for the transfection of cells in culture or of localized tissue, and they often require specialized equipment.[27]

Alternatively, gene delivery can be achieved using *chemical carriers* that typically bind the nucleic acid cargo non-covalently and facilitate its intracellular uptake and delivery. Although the chemical diversity of these systems is vast, chemical carriers can generally be categorized as inorganic, peptide, lipid, or polymer-based systems.[28] Examples of materials used for *inorganic* gene delivery particles include calcium phosphate, silica, gold, magnetic metals, carbon nanotubes, and quantum dots, among others. These inorganic nanoparticles can vary greatly in size, shape, and surface chemistry, and they are often functionalized with polymeric or bioactive compounds to tune their biological properties.[29]

Nucleic acids can also be conjugated or electrostatically bound to biologically-derived compounds, such as *peptides*, to their uptake. Peptides for gene delivery can be broadly categorized as either cell-penetrating, targeting, endosome-disrupting, or nuclear localization signal (NLS) peptides. While providing effective methods to overcome certain biological barriers, these peptides often suffer from short circulation half-lives, poor stability, and low DNA-binding affinity.[30]

The most widely utilized non-viral gene delivery vehicle are *lipid nanoparticles* (LPNs). Lipids, which consist of a hydrophilic head and hydrophobic tail, can form bilayer vesicles called liposomes. If lipids with cationic heads are present in the lipid mixture, nucleic acids can electrostatically bind and become encapsulated in a lipid bubble, called a liposome, to form a lipoplex or LPN. These LPNs are often mixtures of charged lipids, uncharged lipids, and cholesterol that can promote fusing and lipid exchange with endogenous cellular membranes. Lipoplexes can also be functionalized with PEG-based coatings or bioactive compounds to improve transfection efficiency, stability, or promote tissue-specific targeting.[31] Each of the non-viral methods listed above has been developed over the last several decades in parallel to *polymer-based* gene delivery, which is discussed in detail in *Section 1.2*, and each method has its own advantages and disadvantages for any given gene-delivery application.

1.1.4 *Nucleic Acid Cargo for Nonviral Delivery, with a Focus on Plasmids*

Polymeric vehicles can be assembled with various nucleic acid modalities varying widely in their structure and therapeutic application. These nucleic acid types include plasmids (or pDNA), messenger RNA (mRNA), antisense oligonucleotides (ASOs), small interfering RNA (siRNA), and microRNA (miRNA), among others. An overview of each of these nucleic acids in relation to gene therapy is given in a review by our group.[32] The most predominant nucleic acid featured in the gene delivery literature (and in this Thesis) is plasmid DNA, and will, therefore, be described in more detail.

Plasmids are circular double-stranded DNA molecules that are replicated inside bacteria separate from chromosomal DNA. Along with their utility in cloning DNA fragments and producing large quantities of proteins in culture, plasmids have been widely used as vectors in gene therapy.[33] The two primary portions of plasmids are (1) the bacterial backbone, which contains an antibiotic resistance gene and origin of replication for production in bacteria, and (2) the expression cassette, which is the transcriptional fragment containing the gene of interest and regulatory sequences.[34] The expression cassette can encode therapeutic RNAs or proteins, and if successfully delivered to the nucleus of a target cell, endogenous cellular machinery can produce the therapeutic construct in large quantities.[33] Unlike some other nucleic acid payloads, plasmids requires nuclear entry to be effective, placing additional constraints while designing gene delivery vehicles. Once they reach the nucleus, plasmids do not integrate into the genome, so an expression of the transgene is transient and will diminish over time, especially as the cell divides.[35] Plasmids are still widely used for transient gene delivery applications due to the ability to accommodate large gene payloads, their ease of construction, low production cost, and relative resistance to degradation.[35]

1.1.5 *Genome Editing with CRISPR*

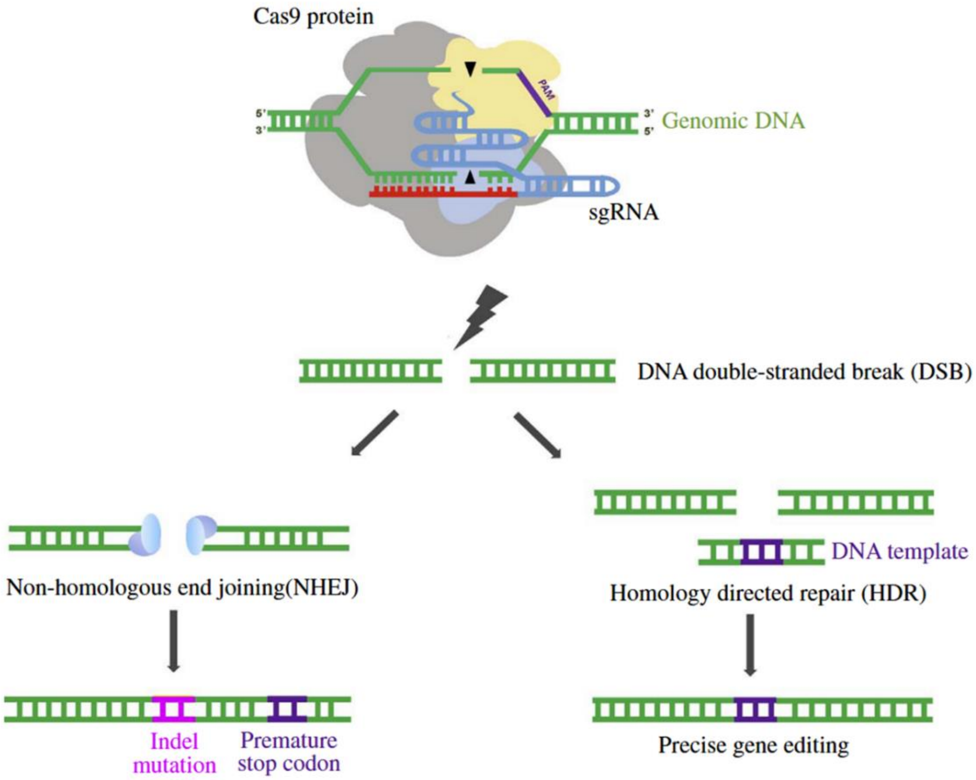

Figure 1.2. CRISPR/Cas9-based mechanisms for editing of genomic DNA. A double strand break (DSB) by Cas9/sgRNA complex initiates one of two DNA repair pathways that can be used for either a gene knock-out (NHEJ) or a gene knock-in (HDR). Figure was adapted from ref. 36 with permission.

As mentioned above, delivery of plasmids to mammalian cells leads to transient gene expression, so continued modulation of gene expression with plasmids require multiple administrations. Many gene therapies, however, rely on permanently altering the genome of target cells in a process known as gene editing. Precise genome editing can be achieved with targeted nucleases such as TALENs, meganucleases, and the CRISPR/Cas9 system. These systems induce a double-strand break (DSB) in a precise location of the genome, which stimulates endogenous cellular repair machinery.[37] Repair of the DSB can occur through non-homologous end-joining (NHEJ) or homology-directed repair (HDR) as depicted in Figure 1.2. The NHEJ pathway ligates the broken ends of the DNA and often introduces insertions and/or deletions (indels) that can disrupt genes at the site of the break, leading to a gene knock-out. In contrast, the HDR pathway can repair the break by using a DNA template containing a homologous sequence, and by doing so, inserting an exogenous gene of choice, which is called a gene repair or gene knock-in.[38]

CRISPR-based editing requires the delivery of nucleic acid components to the cell. In the case of standard HDR-based gene insertion with CRISPR/Cas9, a ribonucleoprotein complex, consisting of a complexed single guide RNA (sgRNA) and Cas9 protein, must be delivered to the nucleus to induce a DSB concurrently with the delivery of a template DNA. The template DNA can be delivered with a plasmid or single-stranded oligo donor (ssODN), while the components of a ribonucleoprotein can be delivered directly or expressed from a plasmid or mRNA.[39] Delivery requirements for these multi-component gene editing systems are demanding, and there is an urgent need for efficient gene delivery strategies in order to achieve the desired outcomes.[39] Polymer-based delivery platforms, as discussed below, are well-suited for the concurrent delivery of these large constructs.

1.2 Overview of Polymer-based Gene Delivery Systems

1.2.1 *Introduction to Polymeric Vectors*

One of the most promising nonviral gene delivery platforms being developed in research groups across the world are polymer-based vectors. Polymer-based systems are attractive since they can be produced cheaply in large quantities, are shelf-stable, and provide extensive synthetic and structural flexibility to overcome a range of extra- and intracellular barriers to transfection.[40] These polymer systems typically contain amine groups with pK_a values above or near physiological pH, which give the polymer a positive charge and the ability to electrostatically bind polyanions, such as DNA, to form complexes termed *polyplexes* that are on the order of 100 nm in hydrodynamic diameter (Fig. 1.1d).[41] Once bound to the polymer, the DNA is compacted and protected from degradation by nucleases.[42] If an excess of positive charges is present, the positively-charged polyplex binds electrostatically to the negatively-charge proteoglycans coating the cell's surface, allowing for uptake.[43] Polymer vectors can accommodate the integration of degradable components, targeting moieties, and stimuli-responsive functional groups to help overcome the biological barriers to delivery (see *Section 1.3* for more discussion on intracellular biological barriers).[44] The efficacy of the polymer can also be affected by placement of these components within several levels of its overall architecture (Fig. 1.1a–c). *Section 1.4* will discuss some of the synthetic strategies employed to overcome biological barriers to polycationic delivery with an emphasis on the use of carbohydrate moieties by the Reineke group.

1.2.2 ***First-Generation Polymeric Vectors***

One of the first polymers recognized for its potential in gene delivery was diethylaminoethyl-dextran (DEAE-D) by Vaheri and Pagano in 1965 when they discovered that DEAE-D stabilized and increased expression of poliovirus RNA.[45] In 1975, U. K. Laemmli found that another polycation, poly-L-lysine (PLL), collapsed DNA exceptionally well.[46] In 1988, Wu and Wu demonstrated *in vitro* and *in vivo* gene delivery to rat hepatocytes using PLL.[47] These seminal works demonstrated the potential of using protonatable amine-containing polymers for gene delivery, and the hunt was on for better-performing polycations. In 1993, Haensler and Szoka found that hyperbranched polycations, called polyamidoamine (PAMAM) dendrimers, containing tertiary and primary amines were efficient delivery vehicles of plasmids,[48] and in 1995, Boussif et al. showed that improved transfection efficacy could be achieved with the commercially-available polyethylenimine (PEI). Ever since this discovery, both branched and linear PEI have become gold standards in polymeric gene delivery (Fig. 1.3). Since then, a myriad of sophisticated polycation structures for improved gene delivery have been developed. I will point the reader to extensive reviews on the topic written by our group[32] and others[25, 49] for an overview of the large breadth of polycations developed for this application.

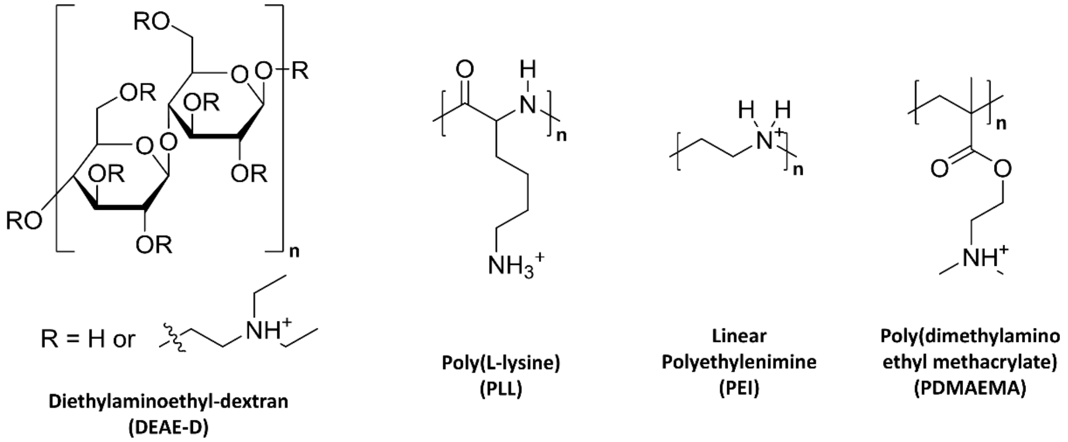

Figure 1.3. Chemical structures of some first-generation linear polycations used for gene delivery.

1.3 Biological Barriers to Polymeric Delivery

1.3.1 Overview

For *in vivo* gene therapy, polymeric vehicles must overcome a series of extracellular barriers prior to even reaching the target cell. These extracellular barriers include serum-induced aggregation, enzymatic degradation, immune activation, and organ targeting. Since this Thesis focuses on materials designed for *ex vivo* gene therapy, extracellular barriers will not be discussed in detail. Both *in vivo* and *ex vivo* gene therapeutics, however, must overcome intracellular barriers that all significantly impede delivery. These obstacles include (1) cellular binding, (2) endocytosis, (3) endosomal escape, (4) intracellular transport, (5) unpackaging, (6) nuclear uptake, and (7) cytotoxicity.[32] While viruses have benefited from billions of years of evolution to overcome these hurdles, polymer scientists must be creative in engineering polymers with the chemical functionality to overcome these barriers in successive fashion. Even for vehicles that manage to overcome these barriers, however, there is still insufficient mechanistic insight into how these vehicles overcome these challenges. Even after over 25 years of study, there is still controversy over how PEI overcomes endosomal entrapment, which one of the most well-studied polymer-specific capabilities in the field.[50] For the sake of brevity, I turn the reader to my discussion of each one of these barriers in our group's recent review.[32] For the purposes of this Thesis, two of these intracellular barriers, endosomal escape and unpackaging of the nucleic acid from the polyplex, will be summarized here.

1.3.2 *Endosomal Escape*

With few exceptions, the endocytosis of a given polyplex leads to entrapment of the polyplex in the degradative endolysosomal pathway and its exclusion from the cytoplasm. Endosomes that are not recycled back to the surface arrive at late endosomes (pH 6.0−4.8), which are acidified by vacuolar-type H^+-adenosine triphosphatase (V-ATPase) proton pumps. Late endosomes eventually merge with lysosomes, whose acidic lumen (pH ≈ 4.5) and high hydrolase content facilitate the degradation of the cargo.[51] Endosomal entrapment is a severe bottleneck in gene delivery,[50, 52] and considerable energy has been devoted to developing and modifying polymer-based systems to overcome this barrier.[25, 53] It was proposed that PEI manages to avoid endosomal degradation by acting as a “proton sponge” (Fig. 1.4a),[54, 55] where the amino groups of PEI, which have a broad buffering capacity in the pH range of endosomes (pH 4−7),[56] act as potent “proton sponges” during the V-ATPase-driven acidification of endosomes. According to this theory, buffering against this acidification causes a passive influx of chloride ions that causes an osmotic swelling of the endosome leading to its rupture and subsequent release of the polyplex.[54] This proton sponge theory has been thought to apply to other polymers that exhibit broad buffering capacities such as PAMAM[48] and poly(2-(dimethylamino)ethyl methacrylate) (pDMAEMA).[57] The addition of chloroquine, an antimalarial that accumulates in endosomes and causes endosome destabilization, improves transfection efficiency when added in conjunction with some polymeric vectors.[52, 58, 59] It is often thought that chloroquine improves transfection by enhancing endosomal escape through endosomal buffering.[52]

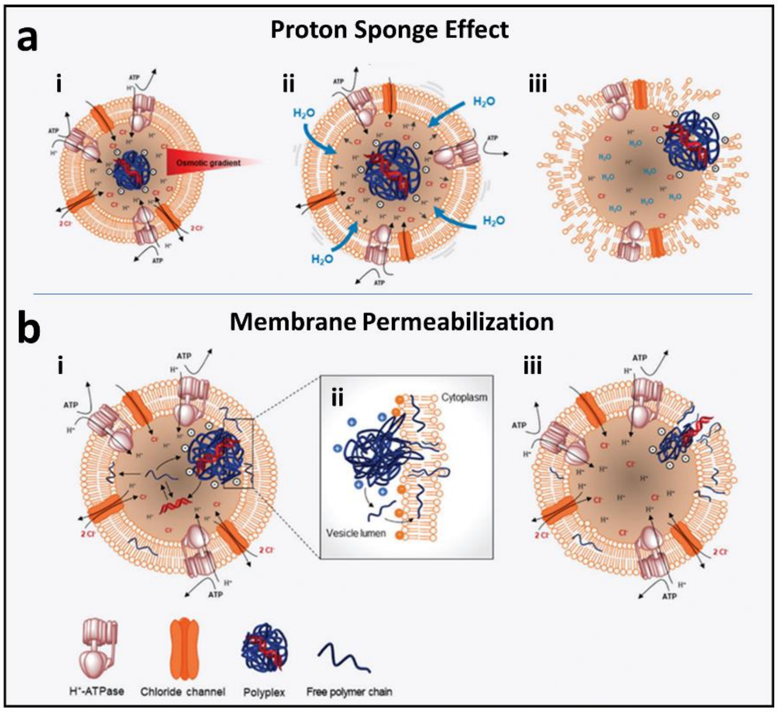

Figure 1.4. Possible mechanisms for the endosomal escape of PEI-based polyplexes. (A) The proton sponge hypothesis suggests the following steps: (i) Polyplexes buffer the endosome during its V-ATPase-driven acidification process. (ii) This causes an influx of protons and chloride ions, which increases osmotic pressure and (iii) leads to a rupture of the endosome, allowing the polyplex to escape. (B) An alternative theory of endosomal escape, the membrane permeabilization theory, suggests a slightly different mechanistic hypothesis: (i) Free PEI chains are present alongside the polyplex that (ii) penetrate the endosomal membrane. (iii) Membrane defects and/or nano-holes are formed that allow for the escape of the polyplex without a full rupture of the endosome. Figure was adapted from ref 50 with permission. Copyright 2018 Royal Society of Chemistry.

While the proton sponge theory is widely posited as explaining the gene delivery efficacy of PEI and other polycationic agents, there is mounting evidence that alternative mechanisms are at work, including direct membrane penetration (Fig. 1.4b).[60-62] It has been suggested that the proton sponge effect and membrane permeabilization may be functioning together in a synergistic fashion.[61, 63, 64] In addition, Sullivan et al. and Reineke et al. showed that caveolin-dependent endocytosis could bypass endosomal degradation by a retrograde transport,[65, 66] offering another compelling alternative to both the proton sponge and the direct membrane permeabilization hypotheses. We point the reader to a review by Bus et al.[50] and ourselves[32] for in-depth commentary on the on-going debate.

1.3.3 Unpackaging

Another biological barrier relevant to the work in this Thesis is the intracellular unpackaging (or unpacking) of the nucleic acid cargo from the polymer. It is not clear as to the preferred location/time of polyplex unpackaging within the cell, but it likely depends on the type of polymer, cell, endocytotic pathway, and nucleic acid type used. It is generally agreed, however, that unpackaging must occur at some point to allow for the nucleic acid to perform its ultimate function. A fine balance must be achieved so that the polymer properly protects the nucleic acid from degradation in the extracellular and intracellular space while releasing it at the optimal time and place.[67] Premature release in the degradative endolysosomal system[68] or intracellular space can lead to degradation of the cargo due to nuclease activity. Naked plasmid DNA has a half-life of ∼50−90 min in the cytoplasm of HeLa and COS cells.[69] For this reason, it is suggested that polyplexes should be programmed to release DNA near the nucleus or inside the nucleus.[70] Simple parameters of the polycation can be tuned to achieve the right balance of protection and release including the polymer length,[71, 72] charge density,[73, 74] and structural rigidity.[75, 76] The release performance can also be improved with the incorporation of chemical moieties that allow for intracellular degradation of the polymer.[67, 77, 78]

While great progress has been made in “smart” stimuli-responsive polymeric gene delivery agents,[79] many of these materials are derivatives of canonical polycations like PLL and PEI. Therefore, it is still valuable to understand how and to what degree canonical polycations like PLL or PEI manage to release their cargo. Schaffer et al. found that PLL-based polyplexes could reach the nucleus intact but were unable to unpackage their cargo to allow for gene expression.[71] Others have also attributed poor transfection efficiency of PLL to its inability to unpackage nucleic acid cargo.[80-83] Chloroquine, a lysosomotropic

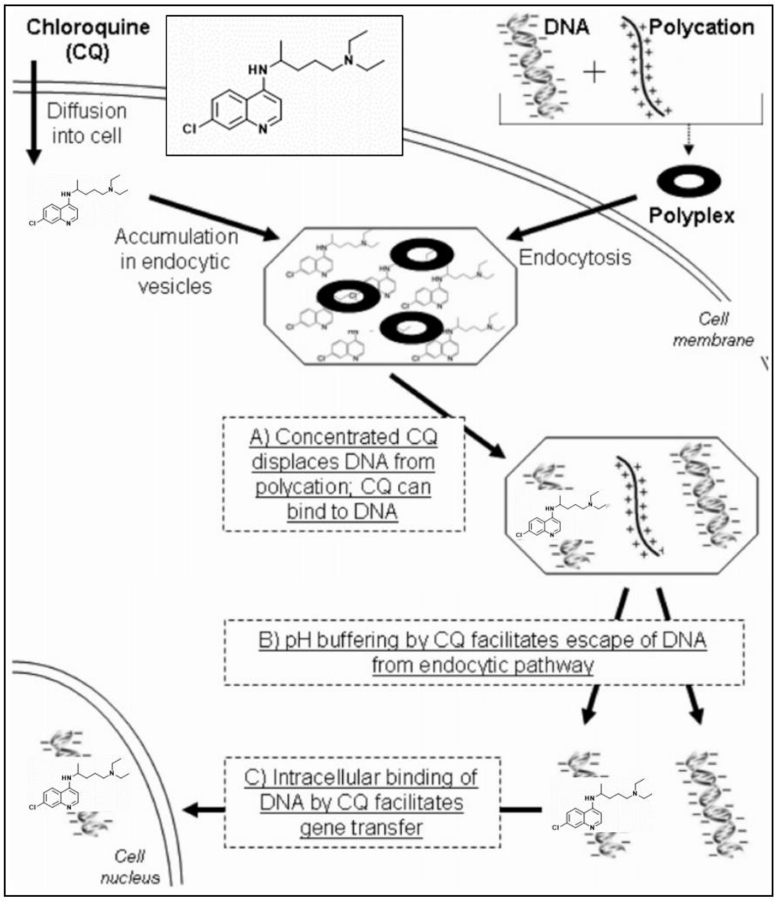

Figure 1.5. Proposed mechanism of how the antimalarial chloroquine enhances transfection of polycationic vehicles. Study by Cheng et al. suggests that the intracellular accumulation of chloroquine in endosomes allows for both improved endosomal escape as well as decomplexation of the cargo from the polycation.[84] Figure adapted from reference 84 with permission. Copyright 2006 American Chemical Society.

antimalarial has been used in conjunction with PLL to improve its transfection properties.[85-87] While chloroquine's mode of action is usually attributed to its ability to promote endosomal escape (as discussed in *Section 1.3.2*), several studies suggest that chloroquine actually improves the transfection efficiencies of strong-binding polycations (such as PLL) by competitively binding and promoting release of the nucleic acid cargo (Fig. 1.5).[84, 86]

In contrast to PLL, PEI unpackages much more efficiently[80] and does not require chloroquine for efficient transfection.[88] Studies have shown that PEI polyplexes can be induced to relinquish DNA cargo in the presence of biological polyanions such as glycosaminoglycans,[82, 83] RNA,[89] and cytosolic proteins.[90] It is unclear, however, whether competitive binding with native biomolecules is responsible for unpackaging in the cells and, if so, which macromolecule is ultimately responsible.[50, 64] The intracellular location of polyplex unpackaging is also unclear. Chen at al. used Förster resonance energy transfer (FRET) to quantify PEI unpacking kinetics in the endolysosome, cytoplasmic, and nuclear compartments and found that the unpackaging of PEI begins in the endo/lysosome and continues at a similar rate in the cytosol.[91] While others have also observed PEI unpackaging in the cytosol,[92] several others have observed intact polyplexes in the nuclei of cells and witnessed unpackaging occurring after nuclear uptake.[80] It is not entirely clear whether unpackaging prior or post nuclear uptake is optimal for transcription and to what degree the polyplex must be unpackaged. Pack and coworkers have reported a 58-fold increase in delivery efficiency, merely by weakening PEI-DNA interactions through an acetylation of primary amines within PEI. Despite significant losses in buffering capacity caused by acetylating up to 57% of primary amines, they observed improved polyplex unpackaging within HEK 293 cells via FRET.[93] This work shows that polymeric vehicles must be engineered to achieve a balance between sufficient DNA-polymer compaction prior to uptake and the ability to release the cargo once inside the cell.[94-97]

1.4 Polymeric Vehicles Developed by the Reineke Group

1.4.1 Overview

After the first generation polymeric gene delivery vehicles, such DEAE-D, PLL, PAMAM, and PEI (see *Section 1.2.2*), established polycations as a promising new nonviral gene delivery platform, research groups across the world joined in the effort to improve upon the performance and biocompatibility of these polymers. As mentioned in *Section 1.2.2*, the structural diversity of improved polymeric reagents is vast, therefore, this section will limit its focus on some of the innovations brought to field by the Reineke group. Study of the work by the group of Prof. Theresa M. Reineke in this field reveals a great overview of the various synthetic strategies that can be employed to create improved vehicles for a range of *in vivo* and *ex vivo* applications.

1.4.2 Carbohydrates

As ubiquitous components of biological systems, carbohydrates are a rich class of compounds that can be harnessed to improve the biocompatibility of non-native polymers, such as linear polyamines used for promoting transfection. Through the years, the Reineke group has developed several classes of *glycopolymers* that generally incorporate saccharide moieties as uncharged hydrophilic moieties to not only improve biocompatibility of the polycation, but impart other advantageous properties such as degradation, tissue-specific targeting, and colloidal stability.[98] An in-depth account of the work by the Reineke group in the field of glycopolymers can be found in the review by Van Bruggen et al.[98]

Among the carbohydrates synthetically modified for incorporation into polycation structures, the Reineke group incorporated ring-opened sugars D-glucarate, *meso*-galactarate, D-mannarate, and L-tartarate into polycationic structures by step-growth polymerization with linear ethyleneamines to form poly(glycoamidoamine)s (PGAAs).[99, 100] These glycopolymers were shown to serve as both efficient and biocompatible transfection reagents. Systematic modifications of the structural components of the PGAA system revealed structure–activity relationships important to its function, including its ability to degrade *in situ*.[101] Following this development, ring-closed sugars were made into vinylic monomers that allowed for more varied polymer architecture, including multiblock and statistical polymers (as discussed in *Section 1.4.3*). For example, monosaccharide-based cationic polymers were made through the copolymerization of 2-deoxy-2-methacrylamido glucopyranose (MAG) with vinylic amine-containing monomers such as *N*-(2-aminoethyl) methacrylamide (AEMA) through a reversible addition-fragmentation chain-transfer (RAFT)-controlled chain-growth polymerization technique. Incorporation of glucose-containing blocks enhanced the colloidal stability of polyplexes and reduced the toxicity of plasmid delivery with a variety of cell types.[96, 97, 102, 103] Similarly, a series of diblock glycopolymers were made with methacrylamido *N*-acetyl-D-galactosamine (MAGalNAc), which not only helped with colloidal stability and toxicity but allowed for the targeting of hepatocytes via asialoglycoprotein receptors.[104, 105] Lastly, the disaccharide trehalose was incorporated into polycationic structures using both step-growth and RAFT polymerization techniques (Fig. 1.6). The trehalose in these copolymers imparted the polycation with increased colloidal stability and yielded polyplexes (formed with plasmid or siRNA) that resisted aggregation upon lyophilization and reconstitution in water.[106-108] The sequence of the sugar-containing monomers in relation to the cationic comonomers was also important to the properties of the polyplex, as discussed in the following section.

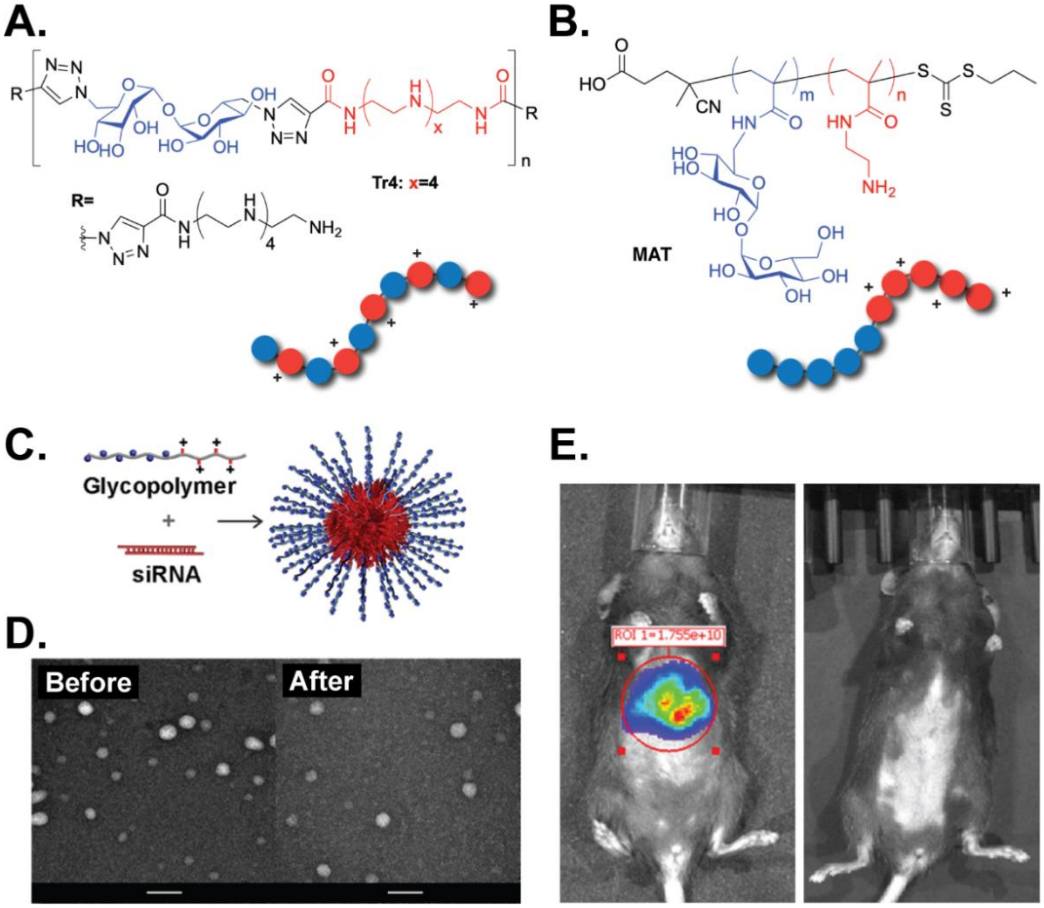

Figure 1.6. Trehalose-based glycopolymers for siRNA delivery. Structure of (A) trehalose click-copolymers and (B) methacrylamido trehalose (MAT)-AEMA diblock copolymers. (C) MAT-diblock copolymers form core–shell structures with siRNA. (D) After lyophilization and resuspension in water, MAT-diblock polyplexes retained colloidal stability as shown by transmission electron microscopy (TEM) (scale bar = 100 nm). (E) Luminescence images of a hydrodynamically injected mouse with p(MAT-*b*-AEMA) and luciferase plasmid (left) show significant increase in luminescence as compared to control injected with 5% dextrose in water (right). Reprinted with permission from ref 98. Copyright 2019 American Chemical Society.

1.4.3 Architecture

The glycopolymers developed by the Reineke group exemplify the vast range of architectures that can be achieved with standard polymerization techniques. Along with the chemical composition, the architecture (how the monomers are arranged in space) can impart valuable properties to the vehicle. Most of the polymers described above are linear polymers. The cationic and non-charged comonomers can be interspersed/statistically-distributed amongst each other[96, 99, 100, 106] or arranged in blocks.[96, 97; 102, 104, 107, 108] In general, the diblock copolymers, with charged and hydrophilic/non-charged blocks, form core-shell polyplexes that are more colloidally-stable than polyplexes without a block structure. The Reineke group has also explored how these blocks can be arranged in branched structures such as star polymers.[109, 110]

More recently, the group has developed diblock and triblock linear polymers that self-assemble into higher-ordered structures called micelles. These micelles have a hydrophobic core that holds the chains together and a cationic core that allows for binding to negatively charged cargo, such as DNA, to form *micelleplexes*.[111, 112] These micelles were can be made with a polyethylene glycol (PEG) outer layer that improves their colloidal stability and reduces adherence of serum proteins. These micelles were found to be superior transfection reagents in the delivery of plasmid compared to the linear analogues lacking the hydrophobic block/core[112] and have become a promising transfection platform in the Reineke Group.

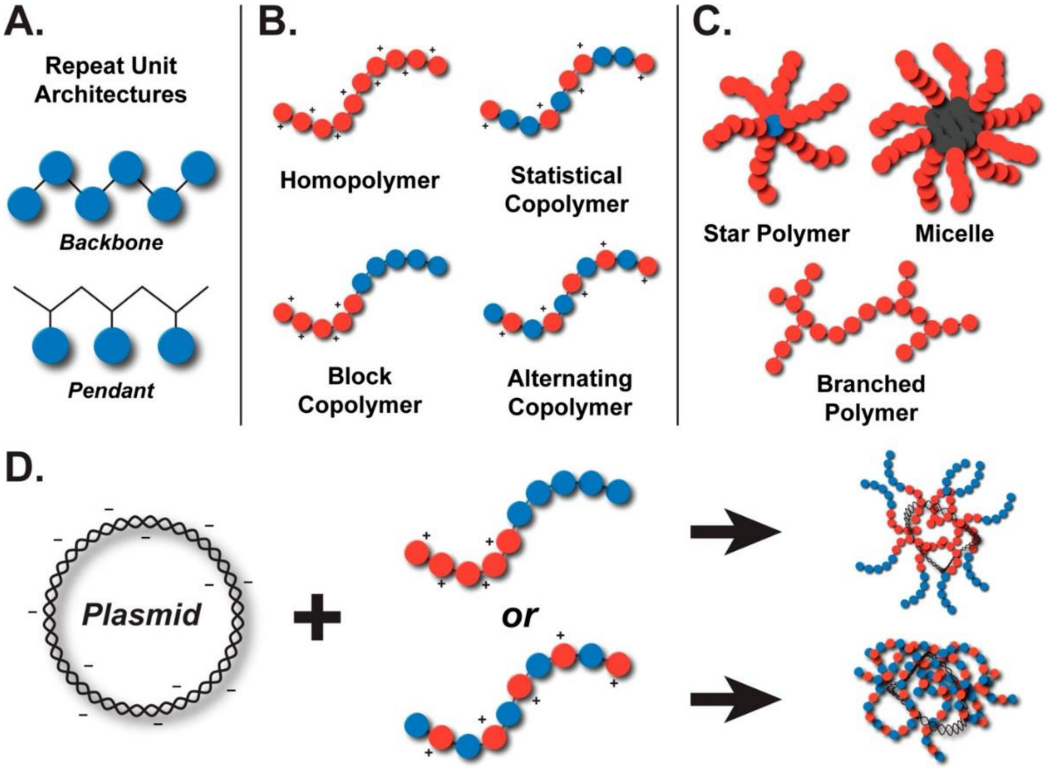

Figure 1.7. Graphical illustration of polymer vehicle architecture variations. Architecture can vary on the level of (A) repeat unit, (B) copolymer composition types, and (C) higher-order assembly of polymer chains. (D) Architectural characteristics, such as the composition of the copolymer, can yield interpolyelectrolyte complexes (polyplexes) with varying morphologies and transfection properties. Reprinted with permission from ref 98. Copyright 2019 American Chemical Society.

1.4.4 Ribonucleoprotein delivery

The Reineke Group has explored a vast array of polymeric structures for the delivery of nucleic acids such as plasmids and siRNA. The group is now in the process of expanding the breadth of cargoes that its polymeric vehicles can deliver. For example, the micelles mentioned above were not only found to efficiently deliver plasmid, but were also found to efficiently deliver RNP for CRISPR-based editing.[113] Delivery of RNPs (which contain a targeting sgRNA sequence) is a common strategy for achieving CRISPR-based gene editing (as described in *Section 1.1.5*).[41] While Tan et al. showed that a micelle-based system composed of linear block polymers worked well for the delivery RNP, Kumar et al. found that statistical linear polymers (with hydrophilic and cationic comonomers statistically incorporated throughout the chain), also could be used for RNP delivery.[114] After characterizing the transfection capabilities of a statistical copolymer library made with commercially available comonomers, Kumar et al. used machine learning to ascertain the physical traits of polymers that led to efficient delivery of RNPs. These screening tools, established with the work of Tan et al.[113] and Kumar et al.,[114] serve as a foundation for future CRISPR gene editing studies (see *Chapter 4*) that will allow for the creation of improved polymeric vehicles for delivering CRISPR components.

1.4.5 *Hydrophobic Cationic Moieties in Polymer-based Vehicles*

While the Reineke group and others have made great strides in improving polymeric vehicles with novel uncharged moieties, more attention is needed in developing the next generation of cationic moieties. A majority of polycationic gene delivery vehicles formed with chain-growth polymerization techniques rely on only a handful of amine-containing cationic monomers. The most common of these monomers include the methacrylate, methacrylamide, and acrylamide analogues of AEMA and DMAEMA.[25, 57, 96, 98] One of the common methods of tuning these cationic monomers is to change the number[97] and length of the alkyl substituents on the pendant amine group.[114] In the high-throughput screening of copolymers performed by Kumar et al. (described in *Section 1.4.4*), the best performing polymer contained the most hydrophobic cationic monomer from the set: 2-

(diisopropylamino)ethyl methacrylate (DIPAEMA),[114] a pH-sensitive hydrophobic monomer used in stimuli-responsive micelles.[115, 116] Increasing the alkylation and hydrophobicity of cationic moieties in polycationic vectors has been widely employed to increase the transfection efficiency of polymeric vehicles.[117, 118] In order to address this need to integrate more sophisticated hydrophobic cations in polymer-based vehicles, we turn our attention to quinine, which is described in detail in the following section.

1.5 Quinine in Chemistry and Medicine

1.5.1 *Overview*

A naturally-occurring alkaloid called quinine (Fig. 1.8a), isolated from the bark of several cinchona and Remijia tree species (Fig. 1.8b), is most well-known as the bitter additive in tonic water.[119, 120] While its role as a bittering agent in beverages may be considered a humble societal contribution, one should not mistake quinine as being anything but remarkable. It can be argued that quinine is "the drug to have relieved more human suffering than any other in history"[121] (see *Section 1.5.2*), and it has played an outsized role in the history of organic synthesis (see *Section 1.5.3*). This section explains the well-established properties of quinine, along with its exceptional history in both chemistry and medicine, that has made it an intriguing target for biomaterial applications.[122, 123] *Section 1.7.3* will explain how we leverage quinine's properties for advancing polymeric gene delivery.

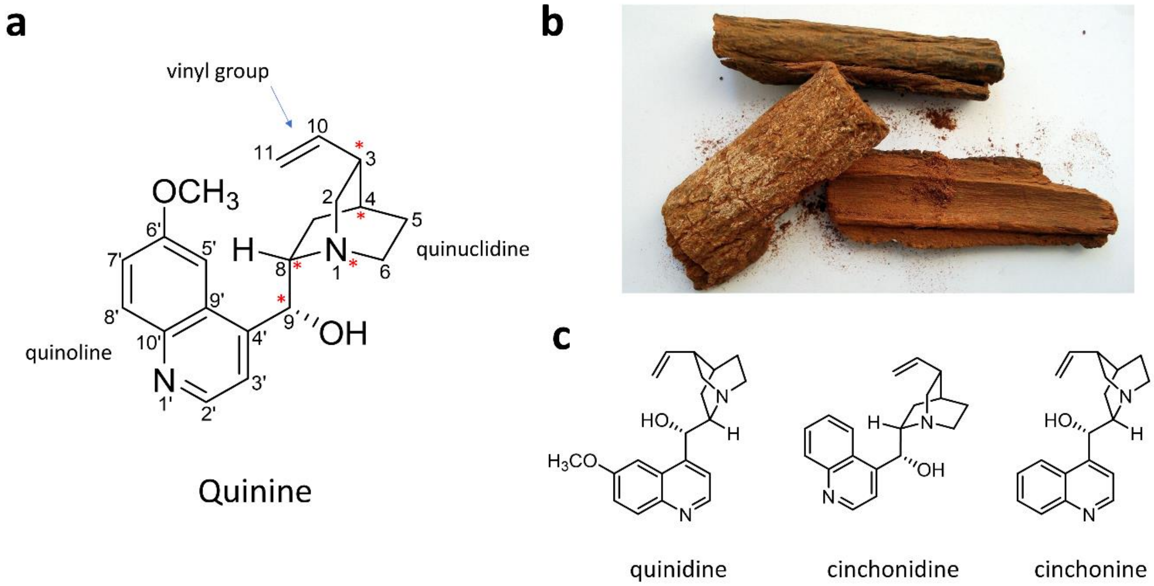

Figure 1.8. Overview of cinchona alkaloids. a) The most potent antimalarial of the cinchona alkaloids is quinine. The stereogenic centers of quinine are highlighted with a red * symbol. b) The cinchona alkaloids are found in the bark of cinchona and Remijia trees originally found on the eastern slopes of the Andes mountains in South America. Natives called the bark "quina-quina" (translated as "bark of barks").[119] c) The cinchona alkaloids are referred to as "pseudoenantiomers" since they are enantiomeric at 2 of their 5 stereogenic centers (C8 and C9 carbons). Quinine and quinidine differ from cinchonine and cinchonidine by the methoxy groups at the C6' position of the quinoline ring.

1.5.2 *Antimalarial*

For over 300 years, quinine was the only known effective treatment of malaria, a mosquito-borne infectious disease that affects approximately 40 percent of the world's population and infects 400 million people annually.[119] Although alternative medications are more widely used today in treating the disease, quinine is still an important second-line treatment in many areas of the world for chloroquine-resistant malaria when artesunate is not available.[124, 125] The emergence of drug-resistant malarial strains has reinvigorated interest in the compound since it has surprisingly retained at least some broad-spectrum efficacy against all four *Plasmodium spp.* parasites responsible for malaria.[126] Despite its long history and continued importance as an antimalarial, quinine's principal mechanism of action remains unclear.[127] The compound exerts multiple toxic effects on both parasitic and mammalian host cells, which complicates the elucidation of the principal mode of action.[128-130] Three main hypotheses have been proposed for quinine's antimalarial activity. The first hypothesis is that quinine works through its lysosomotropic properties,[59, 131] which causes alkalinization of the acidic food vacuoles of malarial parasites, disrupting hemoglobin metabolism. Another hypothesis proposes that quinine binds hematin and disrupts hemozoin biocrystallization,[132, 133] effectively killing the parasites with their own metabolic waste. A third hypothesis is that quinine disrupts transcription and replication by intercalating into DNA of the malarial parasites.[134] These potential mechanisms of quinine's antimalarial activity, especially those involving its interactions with acidic vesicles and DNA, underly some of quinine's properties that can be utilized for gene delivery (see *Section 1.7.2*).

1.5.3 *Synthetic Target*

During its time as the world's only known antimalarial, securing sources of cinchona bark, from which quinine is isolated, was critically important for colonial empires jockeying for expansion in tropical locations where malaria was endemic.[119] A 70-year endeavor to isolate the active antimalarial from cinchona bark culminated in the triumphant isolation of quinine and cinchonine by Pierre Joseph Pelletier and Joseph Bienaimé Caventou in 1820.[119] Following its isolation, quinine became the holy grail target in the nascent field of synthetic organic chemistry for over a century. As a synthetic target, the quest for quinine fueled landmark discoveries including the invention of the first synthetic dye by William H. Perkin in 1856, which gave birth to the industry of fine-chemical production.[119, 135] The elucidation of quinine's structure was a difficult task for early organic chemists who mainly relied on degradation studies. Determining quinine's structure required decades of work by many prominent chemists in the later half of the 19th century, and was finally successfully proposed by Paul Rabe in 1908.[119] Then, in April 1944, Robert Burns Woodward and

William von Eggers Doering shocked the world when they successfully produced quinine synthetically for the first time, ending the near century-long quest.[136] This landmark accomplishment opened a new age of total natural product synthesis, and quinine continued to serve as a preeminent target for improved stereoselective synthetic strategies into the 21st century.[119, 137-141]

1.5.4 *Asymmetric Catalyst*

In addition to being known as a coveted synthetic target, quinine has a rich history in organic chemistry as an invaluable tool in asymmetric transformations.[142] Each cinchona alkaloid, including quinine and its naturally-occurring pseudoenantiomers (Fig. 1c), contain five stereogenic centers and are among the earliest and most well-known class of chiral auxiliaries in asymmetric catalysis, racemic mixture separation, and chiral transition metal chemistry.[142] The tertiary quinuclidine nitrogen of the cinchona alkaloids can either act directly as a reactive site for organocatalysis or allow the alkaloids to bind to metals as ligands and impart enantioselectivity in metal-catalyzed processes.[119] Quinine and other cinchona alkaloids have been used in "an astonishing variety of important enantioselective reactions"[143] ranging from asymmetric dihydroxylation reactions, enantioselective Diels Alder reactions, Michael additions, dehydrohalogenations, and hydrogenations, among many others.[119, 120, 142]

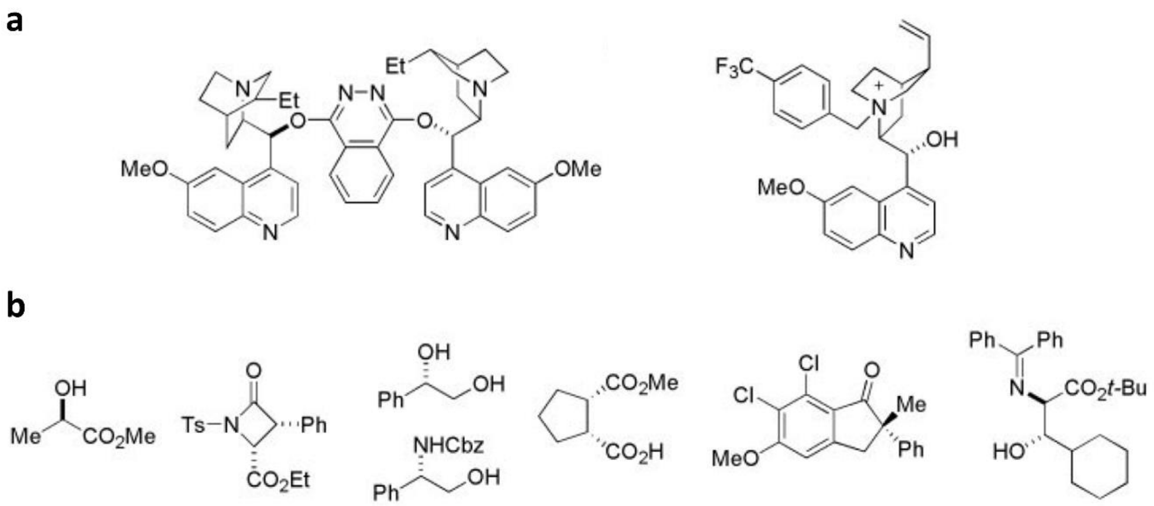

Figure 1.9. Asymmetric catalysts made from cinchona alkaloids. a) Examples of dimeric and quaternized chiral catalysts synthesized from quinuclidine. b) Examples of chiral products made with cinchona alkaloid-based chiral catalysts. Figured adapted from ref 143 with permission. Copyright 2003 American Association for the Advancement of Science.

1.5.5 *Quinine-Containing Polymers*

Due to its utility as a chiral auxiliary for asymmetric transformations, several groups have incorporated quinine into a polymer in order improve the recoverability of the chiral catalyst.[144-149] For example, Sharpless and coworkers' developed an enantioselective dihydroxylation of alkenes with OsO_4 using a quinine-based catalyst,[150] work which eventually contributed to Sharpless winning the Nobel Prize in Chemistry in 2001.[120] They were able to improve the recoverability of their cinchona catalysts by attaching quinine to a polymeric scaffold to form a heterogenous catalyst that retained its efficiency in inducing asymmetry.[147] Other researchers have also explored attaching cinchona alkaloids to polymeric scaffolds, and this has been achieved either through conjugation of alkaloid's secondary hydroxyl,[145, 148, 151] tertiary amine,[146, 149, 152] or vinyl group.[123, 144, 147, 153, 154]

According to Kobayashi and Iwai, the alcohol amino part of quinine, N(1)-C(8)-C(9)-OH, plays an important role in asymmetric induction, and that modifying either the alcohol or the quinuclidine tertiary amine should be avoided in forming an asymmetric catalyst.[144] In order to leave these groups unmodified, Kobayashi and Iwai (in 1978) targeted the vinyl group as a handle to attach quinine to the polymer scaffold.[144] They formed their quinine-containing polymeric catalyst in one step by performing a free-radical polymerization, which is one of the most widespread methods used by industry for the large-scale production of polymers.[155] The researchers copolymerized quinine with acrylonitrile using thermally-initiated free radicals and used the resulting copolymer to induce high enantiomeric excess in the asymmetric Michael reaction.[144]

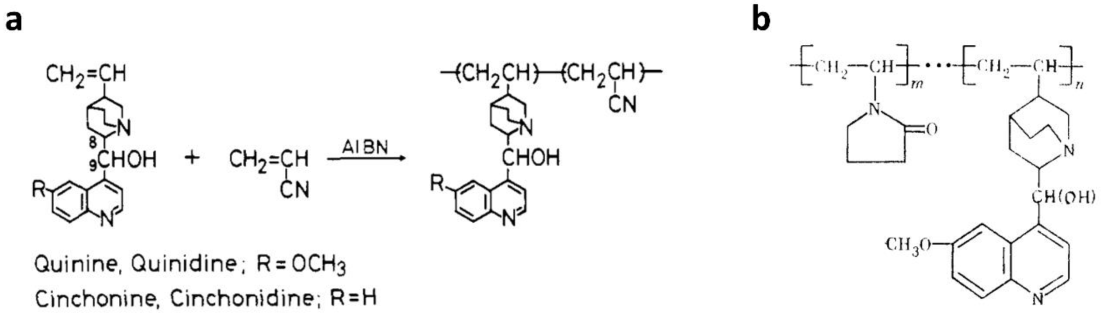

Figure 1.10. Literature precedent of quinine undergoing free radical copolymerization with vinyl-containing comonomers. a) Kobayashi and Iwai were the first to form copolymers of quinine, and other cinchona alkaloids, by free radical polymerization techniques. Their copolymers of quinine and acrylonitrile worked as efficient heterogenous chiral catalysts in a variety of asymmetric transformations. Figure reprinted from ref 144 with permission. Copyright 1978 American Chemical Society. b) Borchan et al. formed a copolymer containing quinine and N-vinyl pyrrolidone that was a water-soluble polyelectrolyte. Figure reprinted from ref 154 with permission. Copyright 1988 Pergamon Journals Ltd.

Kobayashi and Iwai note that their attempts at homopolymerization of quinine were unsuccessful.[144] This observation is consistent with the fact that other α-olefins and 1,1-dialkyl olefins, which includes industrially useful monomers such as propylene and isobutylene, due not readily homopolymerize under free-radical polymerization conditions.[156] The free-radical homopolymerization of these monomers typically give low-molecular weight amorphous polymers and can only be synthesized by free-radical polymerization at extremely high temperatures and pressures.[156] This result is attributed to facile chain transfer to the monomer in a process called "degradative chain transfer," where the allylic proton is abstracted by the radical of the propagating chain to yield a stabilized allylic radical that resists further propagation.[157]

As an α-olefin-containing compound that resists homopolymerization, it is somewhat surprising that quinine can undergo a *co*-polymerization with more reactive comonomers such as acrylonitrile, as shown by Kobayashi and Iwai.[144] Similar behavior, however, has been shown for other monomers like maleic anhydride and stilbene.[157] Propene and isobutylene can also readily copolymerize under free radical conditions when paired with the proper comonomer.[157] A report by Borchan et al. in 1987 expands the comonomer scope of the free-radical copolymerization of quinine by reacting it with *N*-vinylpyrrolidone.[154] In this work, they quantified the reactivity ratios of this comonomer pair using the Mayo-Lewis copolymerization model (see *Section 3.3.1*, eqns. 3.1-3.3) among others. They found that that reactivity ratios were $r_1 = 2.60$ and $r_2 = 0.38$ for N-vinylpyrrolidone and quinine, respectively. Here, the product $r_1 \cdot r_2 = 0.988$ is close to 1, which means the copolymerization is close to being "ideal." In other words, the propagating radical will maintain the same preference for adding each comonomer no matter which monomer is at the chain end.[157] Based upon the reactivity ratios, we can conclude this copolymer system is composed of long *N*-vinylpyrrolidone segments interspersed with short stretches of quinine. Borchan et al. identified this copolymer as a weak polyelectrolyte and speculated that it may have biological applications. Our work aims to expand the comonomer scope of these studies, provide physical characterization unavailable to researchers of this time, and advance Borchan et al.'s supposition of quinine-based polyelectrolytes being useful for biological applications.

1.5.6 *Fluorescence*

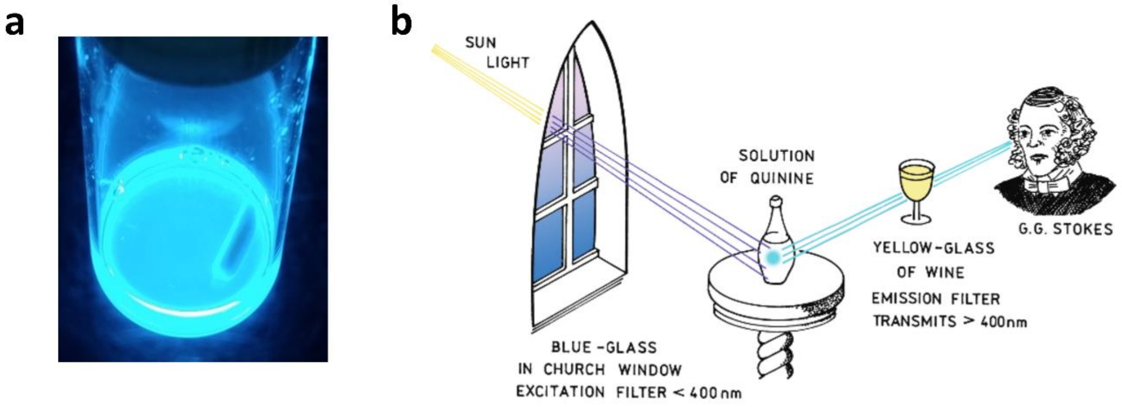

Figure 1.11. Fluorescence of quinine. a) A solution of quinine in neutral or acidic aqueous conditions emits blue light (emission max λ = 450 nm) when illuminated with UV light (excitation max λ = 250 and 350 nm). b) In 1852, Sir George Gabriel Stokes illuminated a solution of quinine with filtered sunlight and analyzed the blue light emitted by the solution and coined the term “fluorescence.” Panel (b) reprinted with permission from ref 158. Copyright 2006 Springer.

In 1845, Sir John Fredrich William Herschel found that an acidic solution of quinine exhibited a “beautiful celestial blue color” (Fig. 1.11a) when held under the proper incidence of sunlight. Herschel’s studies of quinine’s fluorescence under the sun’s ultraviolet light made quinine the first known fluorophore.[158, 159] Sir George Gabriel Stokes continued the study of quinine’s fluorescence and discovered that the energy of the absorbed light is less than that of the emitted light (Fig. 1.11b) .[158, 160] The source of quinine’s fluorescence is its aromatic quinoline ring, and its fluorescence spectra is contains two excitation maxima of 250 and 350 nm and an emission max wavelength of 450 nm.[161] Quinine sulfate dissolved in dilute sulfuric acid has been the most popular standard for calibrating fluorescence spectrophotomers and measuring quantum yields for the last 60 years since it is photostable, resists oxygen quenching, reabsorbs little of its own fluoresced light, and has a high quantum fluorescence efficiency.[162, 163] Interestingly, the first fluorescence spectrophotometers were developed during World War II to help quantify quinine and other antimalarials in the blood.[158, 164] Surprisingly, it was not until 2012 that the inherent fluorescence of quinine was used for the microscopic analysis of quinine's antimalarial activity in *Plasmodium falciparum* parasites.[165] In this 2012 study, Bohórquez et al. found quinine localized in the food vacuole of the parasites where haemozoin is located, supporting a haemozoin-associated mechanism of action.[165] As exemplified by this study, the fluorescent properties of quinine provide an additional method to monitor quinine in the biological milieu as it performs its therapeutic task. Thus, therapeutic materials containing quinine can potentially be "theranostic" (*thera-* = therapeutic, *-nostic* = diagnostic) [166] in nature since the fluorescence imparted by the quinine helps illuminate the material's mode of action.

1.6 Raman Spectroscopy for Biological Imaging

1.6.1 *Overview*

While quinine has strong and well-established fluorescent properties, quinine also has some exceptional Raman spectroscopic properties that were only recently discovered by collaborators at the University of Minnesota (UMN). While working as a post-doctoral associate in the lab of Prof. Renee Frontiera, Dr. Dave Punihaole (now an assistant professor at the University of Vermont) found that the shift of a particularly strong Raman peak in quinine's Raman spectrum gave insight into quinine's chemical environment (see *Chapter 2* for details). This discovery and further collaboration with the Frontiera group led to Raman imaging being an important component of this Thesis and introduced a powerful new method to the field of polymer-based gene delivery. Therefore, some basic concepts and literature related to Raman-based biological imaging is introduced in more detail here.

1.6.2 *Introduction to Raman Imaging*

Raman-based spectroscopic imaging has become an increasingly popular imaging technique in cellular biology in the last several decades.[167] Raman scattering is the inelastic scattering of photons by a molecule. The energy difference between the incident light, which is typically a narrow-band source, and the scattered light corresponds to the energy of a molecular vibration and is known as the Raman shift.[167] The Raman scattering bands of a particular molecule act as the molecule's chemical fingerprint and can be sensitive to the local chemical environment, giving rich spectroscopic information about the target.[167] Raman scattering bands are 10-100 times narrower compared to fluorescence emission bands[168] and does not undergo the photobleaching that is typical for fluorophores.[169] The signatures of multiple species can be gathered with the same laser,[170] identifying biological compounds in complex mixtures including proteins, lipids, and nucleic acids.[171] Infrared (IR) absorption spectroscopy is another spectroscopic technique that relays rich chemical information on molecular vibrations. IR, however, is sensitive to water, which complicates the analysis of hydrated biological samples. Raman's insensitivity to water makes it ideal for examining label-free biological samples in their native-state.[170]

Inelastic scattering of photons, however, is a rare occurrence (1 in 10^6 – 10^{10} photons), which makes Raman signals far weaker than fluorescence.[168] The cross section for most Raman scattering is approximately 10^{-26} to 10^{-30} cm^{-2}, while for the typical fluorescent probes (with a molar absorptivity, ε, of ~10^4 $\mathrm{M}^{-1}\,\mathrm{cm}^{-1}$), the cross section can be approximately 10^{-16} cm^{-1}. This ten orders-of-magnitude difference in scattering intensity necessitates that Raman microscopes have sensitive detectors and perform long scan times to achieve high signal-to-noise ratios.[167] To overcome the low sensitivity of imaging with spontaneous Raman spectroscopy, a variety of nonlinear Raman techniques have been developed that can dramatically increase Raman signal. These techniques include stimulated Raman spectroscopy (SRS), coherent anti-stokes Raman spectroscopy (CARS), and surface enhanced Raman spectroscopy (SERS). These techniques can achieve high sensitivity and rapid image acquisition, but also require either absorption onto metal surfaces or high-powered pulsed lasers that can damage biological components and have limitations in molecular concentration profiling in cells.[172] Each technique has its benefits and drawbacks, and the most appropriate technique for a particular imaging applications depends on many factors including the composition of the compound of interest, the target specimen, and the chemical information needed.

1.6.3 *Raman Spectroscopic Imaging of Nanoparticles in Biological Systems*

The full array of linear and nonlinear Raman spectroscopic techniques have been utilized for the imaging of nanoparticles in biological systems. These systems can utilize near-infrared lasers that have little light attenuation and autofluorescence in tissues[170] and have even been used for monitoring of nanoparticle distribution in live small-animal subjects.[173] SERS is especially well-adapted for metal-nanoparticle-containing therapeutics[170] and has also been employed for carbon nanomaterials such as carbon nanotubes and nanodiamonds as well.[174]

Researchers have employed Raman spectroscopy for the imaging of organic nanoparticles, including liposomes[175, 176] and polymers, which are commonly encountered in the field of gene delivery. Polymers monitored with Raman imaging include polystyrene,[169, 177] quaternary ammonium palmitoyl glycol chitosan,[178] poly(lactic-*co*-glycolic acid) (PLGA),[179] and poly(caprolactone) (PCL).[176, 179] The Raman scattering signal from these polymeric materials is generally low, so in order to increase signal strength, the research group of Wei Min has attached Raman specific probes to cationic polystyrene beads that include nitriles, alkynes, C-D groups.[177] Recently, they further improved signal intensity by impregnating the polystyrene beads with oligo-alkyne probes.[180] Similarly, strong signals could be achieved with polydiacetylene.[181] These Raman probes are conceptually similar to fluorescent dyes in that they act as spectroscopic markers that need to be attached to the biological material of interest. Therefore, use of these probes discounts this type of Raman-based imaging as a label-free technique. Work of Max Diem's group, however, showed PLGA and PCL nanoparticle degradation inside HeLa cells, without the aid of external labels, by careful monitoring of the polymer's spectroscopic signature over time.[176, 179] This work shows the power of Raman spectroscopy to directly analyze the molecules and bonds of a chemical target instead of indirect analysis through an intermediary dye or probe.

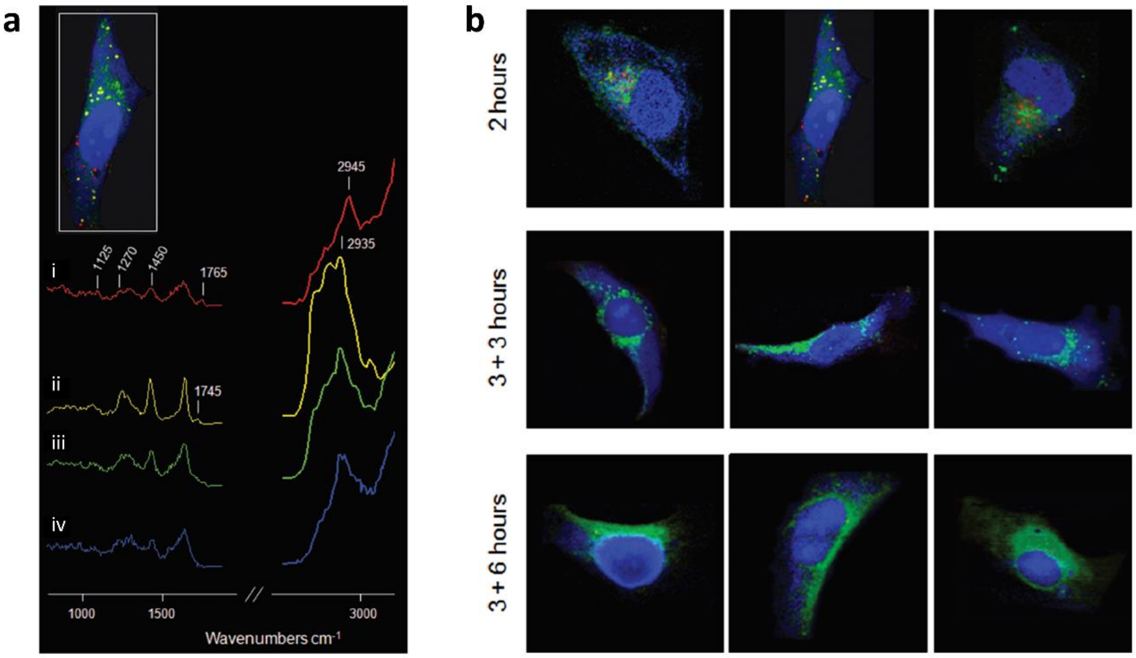

Figure 1.12. Raman imaging of HeLa cells exposed to PLGA-nanoparticles. a) Pseudo-color image of a cell created with spectral analysis of Raman spectra broken down into components corresponding to different chemical features. (i) Red regions and its corresponding trace denote PLGA aggregates; (ii) yellow regions show lipid/phospholipid inclusions; (iii) green regions are membrane-rich organelles such as the endoplasmic reticulum, Golgi, and mitochondria; and (iv) blue regions correspond to protein. b) Raman spectral images of HeLa cells with PLGA nanoparticles showing nanoparticle degradation over time. Figures adapted from ref 179 with permission. Copyright 2009 American Chemical Society.

In addition, Raman spectroscopy can image the biological components of the cell directly. For example, in the studies of PGLA and PCL nanoparticles by Diem's group, they were able to identify the intracellular location of the polymeric nanoparticles (Fig. 1.12).[176, 179] Organelles have their own spectral finger print that allows for their identification without labels.[172] Raman spectroscopy has been used to monitor the association of nanoparticles with membrane-rich organelles such as the Golgi apparatus,[179] nucleus,[175] and mitochondria.[175] Raman spectroscopy has also been used to discern many other biological processes (i.e. cell cycle analysis and drug-cell interactions), as well as discriminate between cell types (i.e. normal vs malignant cells), or even differentiate prokaryotic cell types.[182] With the ability to directly image the nanoparticles and native biological structures directly, this technique is well suited to help answer mechanistic questions in the field of polymeric gene delivery.

1.7 Thesis Overview

1.7.1 *Summary of Current Status in Polymeric Gene Delivery*

As discussed in *Section 1.1*, new gene editing technologies, such as CRISPR, are allowing for the rapid expansion of gene therapeutics that are tackling formerly intractable genetic disorders and public health crises. *Section 1.2* explains the basic principles of gene delivery with polymer-based vehicles and how they are promising nonviral vectors to help expand the accessibility of gene therapeutics. Polymeric vehicles, however, are still inefficient compared to viral vectors, partially due to the barriers explained in *Section 1.*3, and there is still a need for improved polymer-based systems that have increased transfection efficiency with limited toxic side effects. *Section 1.4* summarizes some of the innovations brought to the field of polymer-based gene delivery by the Reineke group including new carbohydrate-based monomers and tailored polymeric architectures for RNP delivery. *Section 1.4* also describes how hydrophobic cationic monomers can improve transfection performance and how there is a need to explore more sophisticated hydrophobic cationic moieties for next-generation polycationic vehicles.

1.7.2 Quinine as Cationic Monomer in Polymer-based Vehicles

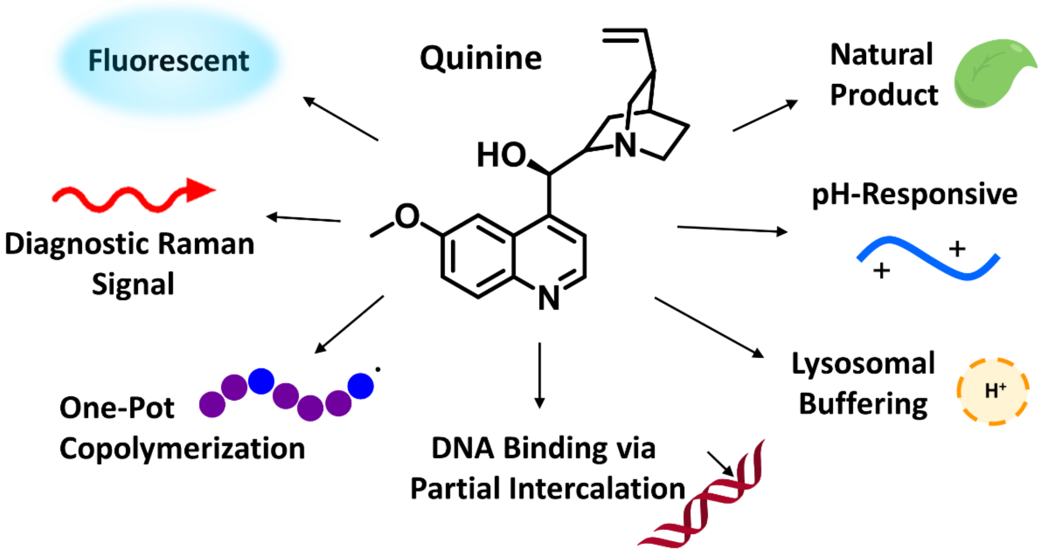

Figure 1.13. Summary of quinine's traits that make the alkaloid an attractive target as a cationic moiety for a polymeric gene delivery vehicle.

Quinine has several remarkable properties (Fig. 1.13) that have made it an exciting target for incorporation into biomaterials (as discussed in *Section 1.5*). In order to expand the breadth and functionality of hydrophobic cationic monomers in polycationic vectors, I hypothesized that the incorporation of quinine as the cationic moiety in a polymeric vector would impart a number of advantageous properties to the vehicle. Some of these advantages are explained below.

1) **pH-Sensitive Hydrophobicity:** As a hydrophobic alkaloid with multiple tertiary amines (pK_as of 8.5 and 4.1), quinine can serve as a cationic moiety, to allow for binding of nucleic acids, while providing pH-sensitive hydrophobicity, similar to DIPAEMA used by Kumar et al. (see *Section 1.4.5*), which has been shown to improve transfection performance of linear polycations.

2) **Endosome Disruption:** Chloroquine is a lysosomotropic anti-malarial used as an additive to improve endosomal escape (see *Section 1.3.2*) and promote unpackaging in polymeric gene delivery (see *Section 1.3.3*). Similarly, quinine is a lysosomotropic antimalarial (see *Section 1.4.2*) that may also disrupt endosomes and improve endosomal escape of polyplexes in a similar fashion.

3) **Intercalation:** Quinine can bind DNA via partial intercalation (see *Chapter 2*) through its aromatic quinoline ring, providing an extra mode to bind DNA.[183, 184] This enhanced binding minimizes the overall charge density of the polymer necessary to compact DNA, which can reduce the toxicity profile of the polycation.[25] In addition, minimizing the percentage of the cationic comonomer in the copolymers allows for increasing the percent incorporation of an uncharged comonomer that can serve a complimentary function, such as promoting unpackaging (see *Chapter 3*).

4) **One-Step Synthesis:** Quinine has a vinyl group that has been shown to be amenable to free-radical copolymerization with several vinylic comonomers (see *Section 1.5.5*), providing a facile, one-step route to incorporating quinine into a polymeric scaffold.

5) **Fluorescence:** As a fluorescent compound (see *Section 1.5.6*), the incorporation of quinine into a polymeric delivery vehicle allows the polyplex to be easily tracked via fluorescence microscopy while being trafficked in the intracellular space.

6) **Raman:** In addition, collaborative work with the Frontiera Group shows that quinine's Raman spectrum contains a peak whose shift gives insight into quinine's immediate chemical environment (see *Chapter 2*). By examining quinine's Raman spectrum while performing Raman biological imaging of transfected cells (see *Section 1.6*),

direct molecular insight into the functional behavior of the polymer's cationic moiety can be ascertained.

7) **Natural Product:** As a research group, we are focused on using naturally-derived components for the creation of sustainable high-performance polymers. Quinine is an attractive polymer building block because it is natural product (see *Section 1.4.1*) produced on the scale of hundreds of tons annually,[119] making the production of a quinine-containing polymeric vehicle cheap, accessible, and sustainably-sourced.

For the reasons listed above, quinine is an intriguing new cationic monomer to be incorporated into a polymeric gene delivery vehicle. A quinine-containing copolymer shows the promise of being an efficient nonviral gene delivery vehicle as well as serving as a spectroscopic reporter to give diagnostic information, making the system theranostic in nature. In the following chapters, I recount the collaborative work between myself in the Reineke Group and members of the Frontiera Group in the development of quinine copolymer reporters (QCRs).

1.7.3 Overview of Chapters

In summary, I describe in *Chapter 2* a collaboration with the Frontiera Group that showed quinine's Raman spectrum sensitivity to its immediate chemical environment, and that quinine's Raman band at 1370 cm^{-1} can be used to quantify quinine's intercalation with DNA. In *Chapter 3*, I describe how QCRs were synthesized and how they efficiently bind plasmid DNA. I show how a QCR containing quinine and 2-hydroxyethyl acrylate (HEA) efficiently transfects a variety of cell types, and how its fluorescence can be used to fine-tune transfection parameters. In addition, I describe how we used Raman imaging to visualize how QCR-based polyplexes unpackage in the cell in the presence of protein. In *Chapter 4,* I characterize how the HEA-containing QCR can also bind RNP simultaneously with plasmid and can be used to achieve efficient CRISPR gene editing compared to commercial controls in a model cell type.

2. Quinine as Raman Reporter for DNA Binding

Reproduced in part with permission from:

Punihaole, D.; Workman, R. J.; Upadhyay, S.; Van Bruggen, C.; Schmitz, A.J.; Reineke, T. M.; Frontiera, R. R. *J. Phys. Chem. B,* **2018**, *122*, 9840-9851. Copyright 2018 American Chemical Society.

2.1 Overview

Among the potential mechanisms for quinine's antimalarial activity (discussed in *Section 1.5.2*) is that quinine inhibits transcription and translation important to the *Plasmodium* parasite. Although this mechanism has not been verified, its examination in the past century has shown that quinine does indeed bind with DNA. Ultraviolet (UV) absorption and fluorescence-based studies used to study this phenomenon, however, have lacked the chemical specificity to develop an unambiguous molecular-level picture of the binding interaction. Greater insight into the interaction between quinine and DNA will not only help elucidate quinine's anti-malarial mechanisms but allow for analyzing quinine's ability to bind nucleic acids in polyplex formulations. As a member of a team lead by Dr. Dave Punihaole, a member in the research group of Prof. Renee Frontiera, we explored quinine's interaction with DNA by Raman spectroscopy and molecular dynamics (MD). We demonstrated that quinine's strongest Raman band in the fingerprint region, which derives from a symmetric stretching mode of the quinoline ring, is highly sensitive to the local chemical environment and pH. The frequency shifts observed for this mode in solvents of varying polarity can be explained in terms of the Stark effect using a simple Onsager solvation model, indicating that the vibration reports on the local electrostatic environment. We used this vibration as a spectroscopic probe to investigate the binding interaction between quinine and DNA. We found that, when the quinoline ring is protonated, quinine weakly intercalates into DNA by forming π-stacking interactions with the base pairs. The Raman spectra indicated that quinine can intercalate into DNA with a ratio reaching up to roughly one molecule per 25 base pairs. Our results were confirmed by MD simulations, which also show that the quinoline ring adopts a t-shaped π-stacking geometry with the

DNA base pairs, whereas the quinuclidine head group weakly interacts with the phosphate backbone in the minor groove. This work verified that quinine could serve as an exceptional binder of nucleic acids if incorporated into a polymeric structure. In addition, this work provides the experimental and theoretical foundation for using quinine as Raman reporter of DNA-binding in polyplex formulations used in *Chapters 3* and *4*.

2.2 Introduction

The interaction of quinine and its derivatives with DNA has been studied since the late 1940s in order to elucidate the compound's antimalarial behavior and has recently seen a renewal of interest for anticancer drug development.[185, 186] Early studies relied on UV absorption and viscometric measurements to show that antimalarials such as quinine, chloroquine, and mefloquine bind DNA weakly, at high concentrations.[134, 186-192] Using crude CPK space-filling models, these studies suggest quinine and chloroquine can partially intercalate into the DNA duplex to enable π-stacking interactions with the base pairs.[192] Later, fluorescence spectroscopy was used to show that hydrophobic forces were important in quinine−DNA interactions, and that the binding is spontaneous due to the complex dependence of quinine's fluorescence intensity to self-quenching, chloride ions, and DNA.[193] These studies, however, failed to provide a molecular-level picture of the quinine−DNA binding geometry.

Vibrational spectroscopy, such as Raman, is an especially powerful tool for investigating the local structure and chemical environment of biologically-relevant molecules (as discussed in *Section 1.6*). Previous studies by Wesełucha-Birczyńska and Nakamoto[194, 195] attempted to use Raman spectroscopy to investigate the binding of the quinine derivative, cinchonine, to DNA, but were unable to develop a molecular-level picture of the binding interaction. The degree to which the quinoline ring modes of cinchonine were environmentally sensitive was not yet known, so they were unable to capitalize on the sensitivity of quinine as a Raman probe. The frequency shifts seen for vibration probes in different chemical environments are due to either bond polarization changes or changes in the local electric field, which perturb the vibrational energy transitions.[196] Frequency shifts arising from changes in the bond force constants are due to more polar environments stabilizing resonance structures with weaker bonds. This effect changes the relative displacement of the ground-state energy potential along the vibrational normal coordinate relative to the first excited state potential, as well as alters its anharmonicity.[196] In contrast, frequency sensitivity to local electric field changes is due to the vibrational Stark effect. This phenomena is derived from local environment exerting an electric field onto a chromophore, altering its vibrational transition energy in a manner that depends on the difference in the dipole moments of the ground and first excited vibrational states. Recent work by the Boxer group[197-201] and others[202-206] show that the frequency variation of some vibrational probes, such as carbonyls[200, 201, 204] are well described by the vibrational Stark effect.

Punihaole investigated the vibrational solvatochromism of quinine in different aprotic and non-aromatic solvents of varying polarity to discern whether any of its modes are sensitive to their local electrostatic environment. Punihaole found that the solvatochromic shifts of the quinoline ring symmetric stretching mode are well described by the vibrational Stark effect, indicating that this vibration reports on the local electrostatic environment. He also showed that solvents capable of forming hydrogen bonding and π-stacking interactions with quinine shift the frequency of this mode in a manner that is difficult to understand in terms of a simple, linear Stark effect, but perturb the frequency in characteristic manners. I assisted Punihaole in capitalizing on the discovery of this vibrational mode's environmental sensitivity to probe the binding interaction between quinine and DNA. Work by collaborators Dr. Riley Workman and Shiv Upadhyay complemented our Raman measurements with MD simulations. In addition, I lead work on fluorescence spectroscopic measurements as a complimentary form of analysis to verify the DNA-based interactions observed with quinine. In combination, these results were used to develop a molecular-level picture of the binding interaction between DNA and quinine. For the purposes of this Thesis, discussion of certain analyses, such as MD calculations, are abbreviated, while work that I was directly involved, such as the fluorescence studies, are elaborated in more detail.

2.3 Results and Discussion

2.3.1 Raman Spectrum of Quinine

The Raman spectrum of quinine in methanol solution, whose acquisition was led by Punihaole, is shown in Figure 2.1a. Previous studies have suggested band assignments for quinine[207, 208] and its derivatives[194, 195, 208, 209] on the basis of density functional theory (DFT) calculations. We used these previous studies and the Raman spectrum of quinoline (Fig 2.1b) to guide our band assignments quinine, including those at 770, 820, 1370, 1580, 1630, and 1640 cm^{-1} (see Supporting Information (SI) of manuscript by Punihaole et al. for complete set of bands and assignments).[210]

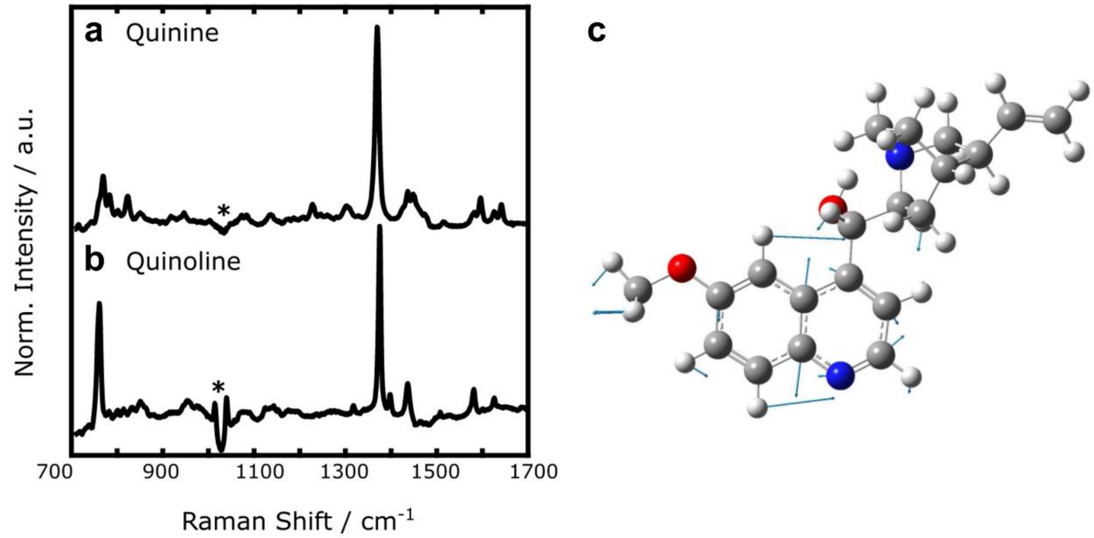

Figure 2.1. Raman spectra of quinine and quinoline. The Raman spectra of (a) quinine and (b) quinoline in methanol excited at 785 nm and (c) the atomic displacements of the quinine vibrational mode for the 1370 cm^{-1} Raman band. The spectra were baseline-corrected to remove the broad fluorescence background, and the spectral contributions of methanol were subtracted. The spectra are normalized with respect to their maximum peak intensities. The * symbol shows an artifact of subtracting the spectral contribution of methanol.

To more definitively assign the spectrum, collaborators performed DFT frequency calculations using M06-2X/aug-cc-pVDZ level of theory[211, 212] and explicitly calculated the potential energy distribution (PED) of quinine's normal modes. Overall, the assignments are in good agreement with previous reports that discuss the topic in greater detail.[195, 207, 208] The most intense Raman bands of quinine and quinoline are located at ca. 1370 and 1375 cm^{-1}, respectively. According to the normal mode analysis, the main contributions to the PED of this vibration are stretching motions of the atoms located in the quinoline ring (Fig 2.1c). We, therefore, assigned the 1370 cm^{-1} band of quinine to a quinoline ring symmetric stretching mode. This mode, as noted by Frosch et al.,[207] exhibits a significant frequency shift going from aqueous solution to solid state. They consequently proposed that this band serves as a spectroscopic marker to monitor the local chemical environment of the quinoline ring moiety of quinine. Building upon this hypothesis of Frosch et al.,[207] the team set out to further investigate the environmental sensitivity of the quinoline ring vibrations of quinine. We discuss the physical origins of the environmental sensitivity of the quinoline ring symmetric stretching mode below.

2.3.2 Environmental Sensitivity of Quinine's Quinoline Ring Symmetric Stretching Mode

Because many vibrational transitions depend significantly on local changes in the electric field, one method to examine the environmental sensitivity of a probe is through Stark spectroscopy. A vibrational probe exhibiting a Stark effect experiences a change in its local electrostatic environment that leads to a frequency shift ($\Delta\tilde{\nu}$) that is linearly proportional to the difference in the electric field ($\Delta\vec{E}$) [199]

$$\Delta\tilde{\nu}\ (\mathrm{cm}^{-1}) = -\frac{\Delta\vec{\mu}_{probe}}{hc}\cdot\Delta\vec{E} \qquad \mathbf{(2.1)}$$

where h is Planck's constant, c is the speed of light, and $\Delta\vec{\mu}_{probe}$ is the difference dipole moment between the ground and excited vibrational states. The magnitude of $\Delta\vec{\mu}_{probe}$ is known as the Stark tuning rate.[213]

Equation 2.1 specifies that the change in the vibrational frequency can be related to the difference in the electric field between two electrostatic environments. If eq 2.1 is referenced to vacuum, it can be rearranged to give

$$\tilde{\nu}_i\ (\mathrm{cm}^{-1}) = -\frac{\Delta\vec{\mu}_{probe}}{hc}\cdot\Delta\vec{E}_i + \tilde{\nu}_{vacuum} \qquad \mathbf{(2.2)}$$

where $\vec{E}_i$ is the electric field felt by the probe in the ith solvent environment and $\tilde{\nu}_{vacuum}$ is the frequency of the probe in the gas phase. The electric field in vacuum is taken to be 0 MV cm^{-1}.

A simpler method than Stark spectroscopy to investigate the environmental sensitivity of a vibrational probe is to measure its frequency shifts in different solvents that vary in properties such as their polarity, donor number, or acceptor number. The frequency shifts observed in the vibrational probe in different solvents can be correlated to their dielectric constants and other polarity scales. In addition, solvating molecules exert an electric field, called a reaction field, on the solute that depends on the solvent polarity. Therefore, a useful correlation is to relate the reaction fields to the frequency shifts observed for a vibrational probe in different solvents of varying polarities. The solvatochromic shifts should correlate linearly with the solvent reaction fields, as described by equation 2.1, if electrostatics primarily influence the frequency of the vibrational probe. This technique, known as Stark shift spectroscopy, has been popularized in recent years by Boxer and co-workers,[199, 201] who have shown that the solvatochromic shifts of many vibrational probes can surprisingly be described in terms of a simple linear Stark effect.

Inspired by the Boxer group, Punihaole measured the Raman spectra of quinine in different solvents of varying polarities and examined the frequency changes that occur in the quinoline ring modes. He estimated the average electric fields that these solvents exert on quinine using the Onsager model,[214] which assumes the solute of interest occupies a spherical cavity that is embedded in a continuum dielectric that represents the solvent. The magnitude of the solvent's reaction field is calculated using the following equation[199]

$$\left|\vec{E}_{Onsager}\right| = \frac{|\vec{\mu}_0|}{a^3}\left[\frac{(2\varepsilon-1)(n^2+2)}{3(2\varepsilon+n^2)}\right] \tag{2.3}$$

The term, ε, is the solvent's dielectric constant, whereas n, a, $\vec{\mu}_0$ are the solute's refractive index, cavity radius, and electronic ground-state gas-phase dipole moment, respectively. For all calculations using eqn. 2.3, a reference value was used for the refractive index of quinine (n = 1.625).[215] The term, a^3 (106 Å^3 molecule^{-1}), was calculated by first finding the cavity volume and then multiplying this value by a factor of 3/4π. [200] The cavity volume was found by dividing quinine's molar mass (324.42 g mol^{-1}) by its density (1.21 g mol^{-3}). The gas-phase dipole moment, $\vec{\mu}_0$, was obtained from DFT energy calculations, the magnitude of which was determined to be 3.1679 D. To calculate the solvent reaction fields, the following conversion factors were used:[198] 1 D = 0.03336 aC Å and 1 Å^3 of polarizability volume = 0.01113 aC Å^2 V^{-1}.

Punihaole examined the solvatochromic frequency responses of the quinine modes (see SI of manuscript by Punihaole et al. for all response curves)[210] for several aprotic, nonaromatic solvents (dimethyl sulfoxide, acetonitrile, acetone, dichloromethane, tetrahydrofuran, and chloroform). Compared with the other modes, the quinoline ring symmetric stretching vibration displays the largest solvatochromic response and the strongest linear correlation with an r^2 coefficient of 0.99. Least-square fitting of the data corresponding to the quinoline ring symmetric stretching mode (Figure 2.2a,b) to eqn. 2.2 yields the following

$$\tilde{\nu}\,(\mathrm{cm}^{-1}) = -0.88(\mathrm{cm}^{-1}/\mathrm{MV\,cm}^{-1})\vec{E}_{Onsager}(\mathrm{MV\,cm}^{-1}) + 1376\,(\mathrm{cm}^{-1}) \tag{2.4}$$

The slope in eqn. 2.4 corresponds to the apparent Stark tuning rate.[201] The strong correlation with aprotic, nonaromatic solvents observed in Figure 2.2b suggests that the solvatochromic shifts of the quinoline ring symmetric stretching mode can be parsimoniously described by the Stark effect using a simple Onsager solvation model.

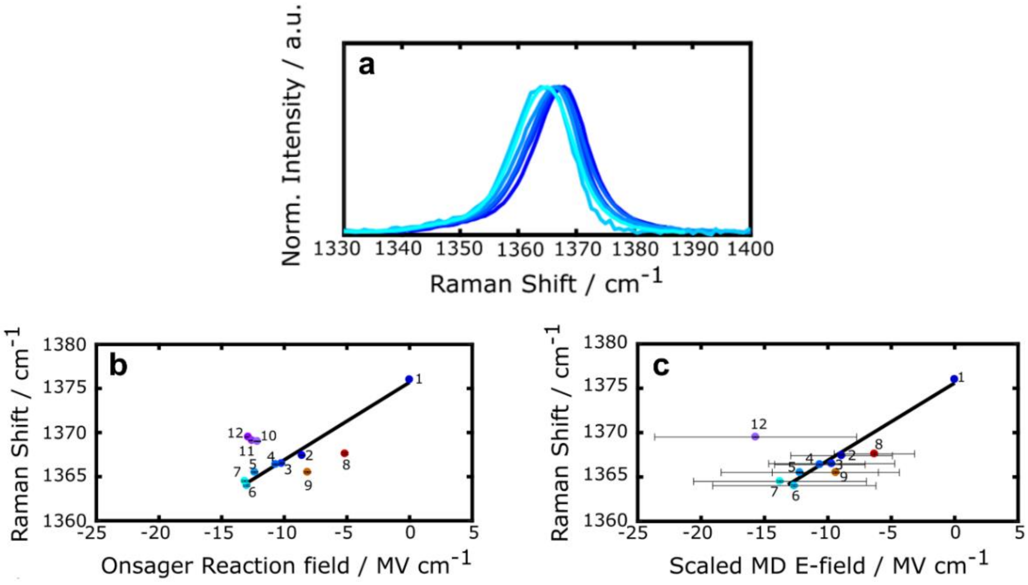

Figure 2.2. Solvatochromic data for quinine's ca. 1370 cm^{-1} quinoline ring stretching mode. (a) Raman spectra of quinine's 1370 cm^{-1} mode in six different aprotic solvents (from left to right: acetonitrile, dimethyl sulfoxide, acetone, dichloromethane, tetrahydrofuran, and chloroform). The spectra are normalized with respect to their peak maxima. (b) Plot of the 1370 cm^{-1} quinoline ring stretching mode frequency as a function of the Onsager reaction field for different aprotic (blue), protic (purple), and aromatic solvents (orange). Standard error bars for the frequencies are shown for each point and are $\leq$0.1 cm^{-1}. (c) Plot of ca. 1370 cm^{-1} mode frequency as a function of the average MD-calculated electric fields projected onto the vibration. The MD-calculated electric fields (CHARMM36) were scaled by a factor of 1.91 to enable a direct comparison with the Onsager reaction fields shown in (b). The error bars for the electric fields were obtained by computing the standard deviation of the local electric field calculated from the MD simulations. The numbered points in (b) and (c) denote the following solvents: (1) gas phase, (2) chloroform, (3) tetrahydrofuran, (4) dichloromethane, (5) acetone, (6) acetonitrile, (7) dimethyl sulfoxide, (8) toluene, (9) anisole, (10) isopropanol, (11) ethanol, and (12) methanol. The gas-phase frequency of the ca. 1370 cm^{-1} mode was obtained from Sen et al.[216]

Our collaborators, Workman and Upadhyay, further tested the validity of the Onsager model to describe the vibrational solvatochromic shifts observed in the quinoline ring symmetric stretching mode by calculating the solvent reaction fields using atomistic MD simulations.[210] Figure 2.2c shows the observed Raman frequencies of the quinoline ring symmetric stretching mode with respect to the scaled CHARMM36 calculated electric fields. The data recapitulate the trend observed in Figure 2.2b with remarkable quantitative agreement. The resultant regression line of the data shown in Figure 2.2c exhibits a slope (0.87 MV cm^{-1}) that essentially matches the one in Figure 2.2b. The excellent agreement between the data shown in Figure 2.2b,c suggests that the solvatochromic shifts observed for quinine's quinoline ring symmetric stretching mode in aprotic and nonaromatic solvents is sufficiently described by the Onsager model.

2.3.3 Effects of Hydrogen Bonding and π-Stacking on the 1370 cm^{-1} Mode

Punihaole initially avoided using protic and aromatic solvents because they can hydrogen bond and π-stack with quinine, which can lead to electrostatic interactions not captured by the Onsager model.[199] In addition, these interactions can perturb the frequencies of vibrations in a manner not described by the Stark effect. To assess the impact of these interactions, Punihaole did examine the frequency shifts of the quinoline ring symmetric stretching mode in toluene, anisole, methanol, ethanol, and isopropanol. As shown in Figure 2.2b, the frequency shifts of the quinoline ring mode in these solvents deviate significantly from the linear trendline described by eqn. 2.4. For anisole and toluene, the quinoline ring mode is downshifted relative to the trendline prediction, whereas for the alcohols, the vibration is upshifted. The MD simulations (Fig. 2.2c) recapitulate the systematic deviations observed in aromatic and protic solvents. These deviations suggest that the Onsager model cannot be used to predict the solvent reaction fields of quinine in aromatic and protic solvent molecules. More importantly, however, these simulations reinforce is that the frequency variation of the quinoline ring symmetric stretching mode cannot be described purely in terms of a simple, linear Stark effect.

2.3.4 pH Dependence of 1370 cm^{-1} Mode

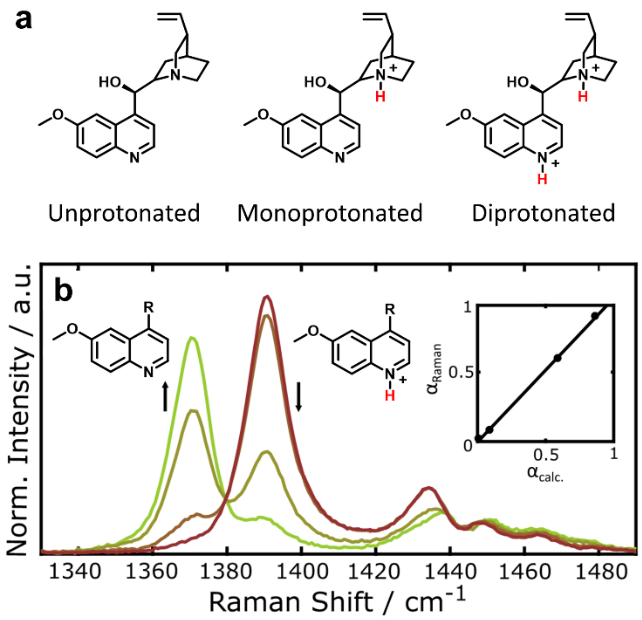

Figure 2.3. Sensitivity of the quinoline ring stretching mode to pH for dilute quinine in aqueous solution. (a) Chemical structures of unprotonated, monoprotonated, and diprotonated quinine. (b) Raman spectra were measured at pH 2.3, 3.3, 4.4, and 5.1. The arrows point toward increasing pH. Inset: Correlation between α calculated using the pK_a of quinine's quinoline ring amine group (α_{calcd}) and Raman measurements (α_{Raman}). The spectra were normalized with respect to the intensity of the ca. 918 cm^{-1} band of acetonitrile, which we used as an internal intensity standard.

Roman et al.[208] noted that protonation of the quinoline and quinuclidine moieties results in dramatic changes to quinine's Raman spectrum. As shown in Figure 2.3, the most dramatic spectral change occurs to the quinoline ring stretching mode, which splits into two bands located at ca. 1370 and 1390 cm^{-1}. The relative intensities of these bands are pH-dependent: as the pH increases from 2.3 to 5.1, the 1390 cm^{-1} band decreases in intensity, while the 1370 cm^{-1} band increases (Fig. 2.3b). Because of these bands' apparent sensitivity to pH, Roman et al.[208] have suggested that the 1370 and 1390 cm^{-1} bands are diagnostic of the protonation state of the quinoline ring of quinine.

To better understand the origins of this band splitting, the team performed DFT calculations and analyzed the normal mode composition of the quinoline ring symmetric stretching mode for unprotonated, monoprotonated, and diprotonated quinine (Fig. 2.3a) (see SI of manuscript by Punihaole et al. for more details).[210] The DFT calculations confirm that the ca. 1370 and 1390 cm^{-1} bands spectroscopically report on the protonation state of quinine's quinoline ring. Thus, the intensities of these bands can be used to determine the relative concentrations of quinine molecules with protonated and unprotonated quinoline rings. The fraction of quinine with unprotonated quinoline rings, α, can be calculated (see inset of Fig. 2.3b) using the following equation

$$\alpha = \frac{\sigma'_{1370\ \mathrm{cm}^{-1}} I_{1370\ \mathrm{cm}^{-1}}}{\sigma'_{1370\ \mathrm{cm}^{-1}} I_{1370\ \mathrm{cm}^{-1}} + \sigma'_{1390\ \mathrm{cm}^{-1}} I_{1390\ \mathrm{cm}^{-1}}} \qquad \mathbf{(2.5)}$$

where $I_{1370\ \mathrm{cm}^{-1}}$ and $I_{1390\ \mathrm{cm}^{-1}}$ are the relative peak intensities of the 1370 and 1390 cm^{-1} bands, respectively. The terms $\sigma'_{1370\ \mathrm{cm}^{-1}}$ and $\sigma'_{1390\ \mathrm{cm}^{-1}}$ denote the differential Raman cross sections for the 1370 and 1390 cm^{-1} modes, respectively. The spectra shown in Figure 2.3 were measured in solutions containing 1% (v/v) acetonitrile as an internal standard. To estimate the differential scattering cross sections of the quinine Raman 1390 cm^{-1} band, we used the following equation

$$\sigma_{\mathrm{i}}' = \frac{\mathrm{d}\sigma_{\mathrm{i}}}{\mathrm{d}\Omega} = \frac{I_{\mathrm{i}}C_{\mathrm{r}}}{I_{\mathrm{r}}C_{\mathrm{i}}}\left(\frac{\mathrm{d}\sigma_{\mathrm{r}}}{\mathrm{d}\Omega}\right) \tag{2.6}$$

where $\mathrm{d}\sigma_{\mathrm{i}}/\mathrm{d}\Omega$ is the differential cross section of the 1390 cm^{-1} quinine Raman mode and $\mathrm{d}\sigma_{\mathrm{r}}/\mathrm{d}\Omega$ is the differential cross section of the 918 cm^{-1} C–C stretching mode of acetonitrile. C_{r} and C_{i} are the concentrations of acetonitrile and quinine, respectively. The differential cross section of the 918 cm^{-1} reference band, with 785 nm excitation, was estimated to be ca. 2.2×10^{-4} mb $\mathrm{molecule}^{-1}$ sr^{-1} by extrapolating the cross-sectional measurements of Dudik et al.[217] We used the Raman spectrum at pH 2.3, where essentially all quinine molecules are diprotonated, to estimate the differential cross section of the 1390 cm^{-1} mode. We estimated the cross section to be ca. 3.7×10^{-3} mb $\mathrm{molecule}^{-1}$ sr^{-1}. The $\mathrm{pK_a}$ values for the quinoline ring and quinuclidine head of quinine are ca. 4.3 and 8.4, respectively. To estimate the differential Raman cross section of the 1370 cm^{-1} mode, we correlated the apparent normalized peak intensities at each solution pH to α. We estimate the differential cross section of the 1370 cm^{-1} mode to be ca. 3.5×10^{-3} mb $\mathrm{molecule}^{-1}$ sr^{-1} by extrapolating to $\alpha=1$.

2.3.5 MD Simulation of Quinine-DNA Binding

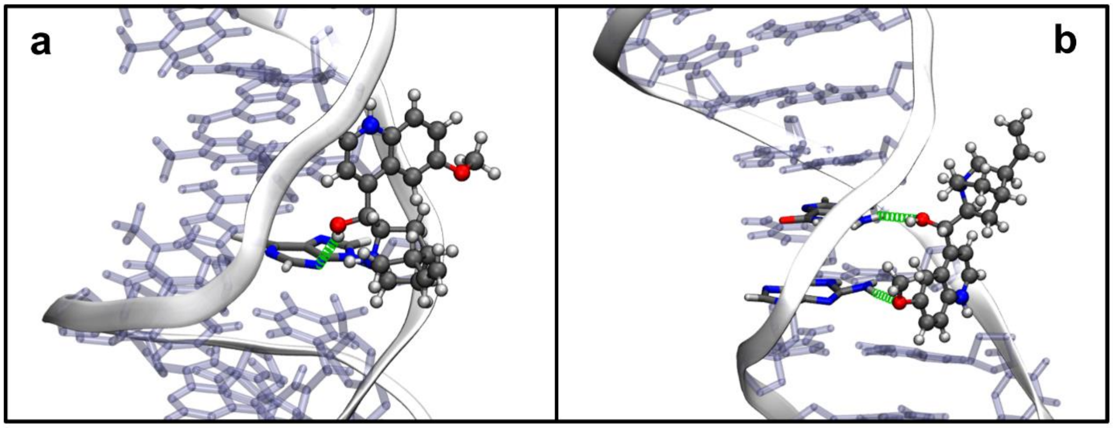

Figure 2.4. Representative snapshots from the MD trajectories of quinine binding to (a) $(AT)_{11}$ and (b) $(GC)_{11}$ DNA helices.

Previous UV absorption studies suggest that quinine and its derivatives weakly bind DNA, yet a detailed molecular-level understanding of their binding remains unclear.[134, 186-192] To develop a clearer molecular-level picture, Workman and Upadhyay performed MD simulations to investigate the binding of quinine to DNA (see manuscript by Punihaole et al. for more details of MD parameters).[206] Two different DNA helices were used in these systems, one with 11 adenine−thymine base pairs, $(AT)_{11}$, and one with 11 cytosine−guanine base pairs, $(CG)_{11}$. Both of these DNA double helices were simulated to monitor any potential preference or selectivity of quinine in binding to DNA base pairs.

Their analysis of the quinine−DNA simulation trajectories revealed that diprotonated quinine favorably binds to the minor groove of the DNA double helices for both systems. For the bound structures, they observed persistent hydrogen bonding and π-stacking interactions that are conserved throughout the relevant portions of the MD trajectories. These persistent interactions stabilize the binding of quinine to DNA. We show a representative MD snapshot of the quinine−$(AT)_{11}$ DNA complex in Figure 2.4a. In this complex, the aromatic quinoline moiety of quinine fits in the cavity between the two phosphate backbones of the DNA and A−T bases. The quinoline ring is stabilized by plane-edge ring π-stacking interactions with two bases, as well as from a persistent hydrogen bond between quinine's alcohol functional group to the N(3) unprotonated aromatic nitrogen of the adjacent adenine. In the $(CG)_{11}$ system, they also observed quinine interacting with the minor groove of DNA via a related but slightly different interaction. Similar to the bound structure observed for the $(AT)_{11}$ duplex, the quinoline ring of quinine inserts into the minor groove between the DNA backbone and sits against the two bases, forming plane-edge ring π-stacking interactions. In this complex, quinine forms two hydrogen bonds with DNA: both the alcohol and methoxy oxygens of quinine accept hydrogen bonds from the primary amines of two guanine bases. We show a representative structure of this complex in Figure 2.4b.

Interestingly, we also observed transient electrostatic interactions between the protonated amine group of the quinuclidine head of quinine and the negatively charged phosphate oxygens of DNA in both the $(CG)_{11}$ and $(AT)_{11}$ systems (see SI of manuscript by Punihaole et al. for more details).[210] These interactions appear to stabilize the DNA-bound quinine geometry by anchoring the otherwise freely rotating quinuclidine head group. When the quinuclidine head electrostatically binds to the phosphate backbone in the minor groove, we hypothesize that quinine retains conformational flexibility to dynamically search for more rigid and stable DNA-bound structures.

The calculated local electric field felt by quinine in the minor groove bound structures of $(AT)_{11}$ and $(CG)_{11}$ and free-energy calculations (see manuscript by Punihaole et al. for more details)[210] confirm that diprotonated quinine intercalates favorably to the minor groove of DNA through the formation of t-shaped, plane-edge ring stacking interactions, as well as preferential hydrogen bonds to adenine and guanine.

2.3.6 Raman Spectra of Quinine-DNA Complexes

I then worked with Punihaole to utilize the quinoline ring symmetric stretching mode as a probe to experimentally interrogate the binding and possible intercalation of quinine to DNA. We measured the spectra under acidic conditions (pH 4.3), in sodium acetate buffer, to maintain the solubility of quinine. Upon mixing the quinine and DNA solutions, an increase in viscosity was observed, which was verified by rheological analysis performed by Andy Schmitz with consultation from David Giles (see SI of manuscript by Punihaole et al. for more details).[210] This increase in viscosity is in congruence with Estensen et al.[218] and Jones et al.'s[191] observations, who report increases in viscosity upon mixing quinine and chloroquinine solutions with DNA. This change in the viscoelastic profile of the DNA solution upon introduction of quinine suggests an interaction between quinine and DNA.

Figure 2.5 shows the Raman spectrum of quinine in the presence of calf-thymus DNA (Fig. 2.5a), as well the spectra of unbound quinine (Fig. 2.5b) and DNA only (Fig. 2.5c). The spectra of quinine and quinine−DNA are dominated by the ca. 1370 and 1390 cm^{-1} bands of the quinoline ring stretching modes. In contrast, the spectrum of DNA shows only a weak, asymmetric band at ca. 1375 cm^{-1}, which derives from the ring stretching modes of the thymine, guanine, and adenine bases.[219] The main spectral change that occurs in DNA-bound quinine is an apparent increase in the 1390 cm^{-1} band relative to the 1370 cm^{-1} band. To better highlight the changes, we subtracted the spectra shown in Figure

2.5b,c from the quinine−DNA spectrum depicted in Figure 2.5a. The resulting difference spectrum (Fig. 2.5d) shows a negative feature at 1370 cm^{-1} and a positive feature at ca. 1380 cm^{-1}. The presence of these features demonstrate that the quinine−DNA spectrum (Fig. 2.5a) cannot be modeled simply as a linear combination of the monomeric quinine and DNA spectra (Fig. 2.5b,c).

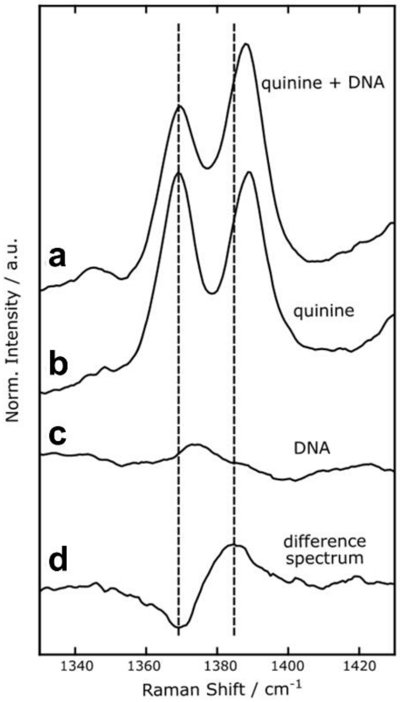

Figure 2.5. Raman spectra of (a) quinine and DNA mixed together in solution, as well as free (b) quinine and (c) DNA. The difference spectrum shown in (d) was calculated by subtracting the spectra in (b) and (c) from the spectrum shown in (a). All samples were prepared in sodium acetate buffer at pH 4.3. The spectra were all normalized to the ca. 900 cm^{-1} C−C stretching mode of acetate. The spectra shown here were conservatively smoothed for clarity using a Savitzky−Golay filter[220] with a fourth-order polynomial over an 11-point range.

The difference spectrum indicates that, in the presence of DNA, there is a decrease in the concentration of monoprotonated quinine and an increase in the concentration of diprotonated quinine. On the basis of the intensity changes, we estimated that the concentration of quinine with protonated quinoline rings increases roughly by 11%. Interestingly, the positive feature in the difference spectrum is downshifted ca. 10 cm^{-1} from the characteristic 1390 cm^{-1} mode of monomeric diprotonated quinine, which signals π-stacking interactions. Therefore, we interpret the Raman difference spectrum as follows: quinine binds to DNA and the quinoline ring amine group becomes concomitantly protonated. The protonated quinoline ring forms π-stacking interactions with the DNA base pairs. On the basis of the magnitude of the intensity changes in the difference spectrum, we roughly estimate that one quinine molecule intercalates per every 25 base pairs. This binding density corresponds to an apparent association constant (K_a) of 5.2×10^5 M^{-1}.

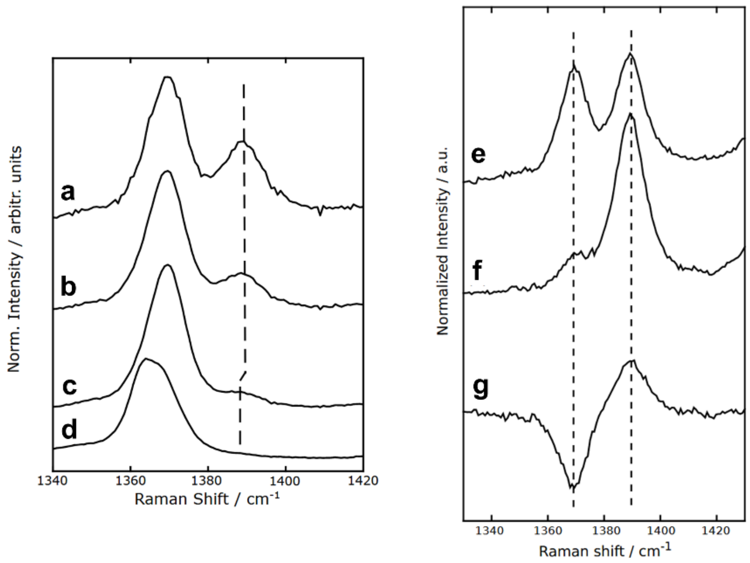

Figure 2.6. Changes in Raman spectra of quinine due to changes in concentration and Na_2HPO_4 concentration. (a-d) Concentration-dependent changes in the Raman spectra of quinine in 0.1 M sodium acetate buffer. Quinine solutions in (a – c) were prepared at (a) 6.15 mg mL^{-1}, (b) 12.3 mg mL^{-1}, and (c) 19.4 mg mL^{-1}. Solution (b) was close to the saturation point, while solution (c) was super-saturated. The spectrum shown in (d) is of high molecular weight quinine aggregates. Raman spectra of quinine (e) without Na_2HPO_4 and (f) with 1 M Na_2HPO_4 in 0.1 M sodium acetate buffer (pH 4). The difference spectrum (g) shows changes in peak intensity between the two conditions (e,f).

A competing interpretation of the downshifted ca. 1380 cm^{-1} feature in Figure 2.5d is that it derives from stable populations of π-stacking quinine molecules that occur in the presence of DNA. Such a situation can occur, for example, if two neighboring quinine molecules electrostatically bind the phosphate backbone of DNA via their protonated quinuclidine head groups and form π-stacking interactions between their quinoline rings. To test this hypothesis, we sought to determine the spectral signatures of quinine molecules forming complexes with each other through π-stacking interactions. We examined these signatures by measuring the Raman spectra of quinine at different concentrations ranging above, below, and at its saturation point (Fig. 2.6a-d). At low concentrations (6.15 mg mL^{-1}), we expect quinine to be monomeric, whereas saturated and supersaturated solutions (12.3 and 19.4 mg mL^{-1}, respectively) are expected to contain stable populations of interacting quinine molecules. We find that the Raman spectrum of a saturated solution of quinine (Fig. 2.6b) is essentially identical to that of monomeric quinine (Fig. 2.6a). The only difference is that the spectrum of the saturated solution shows an increase in the 1370 cm^{-1} band relative to the 1390 cm^{-1} band, which is due to self-buffering of the quinine. In supersaturated solutions, the 1390 cm^{-1} band downshifts by ca. 3 cm^{-1} (Fig. 2.6c) due to quinine molecules forming π-stacking interactions. In contrast, a dispersion of quinine composed of high-molecular-weight aggregates exhibits a Raman spectrum (Fig. 2.6d) that shows no 1390 cm^{-1} mode and a 1370 cm^{-1} mode that is downshifted by ca. 5 cm^{-1} due to π-stacking interactions that occur between monoprotonated quinine molecules. The magnitudes of the 3−5 cm^{-1} downshifts observed for mono-and diprotonated quinine molecules in Figure 2.6c,d are too small to assign the ca. 1380 cm^{-1} feature observed in Figure 2.6d to inter-quinoline ring π-stacking interactions. On the basis of these observations, we can rule out formation of stable quinine−quinine π-stacking due to the presence of DNA.

We also ruled out the possibility that the 1380 cm^{-1} feature in Figure 2.6d derives from electrostatic interactions between the cationic quinoline ring of diprotonated quinine molecules with the phosphate backbone of DNA. To investigate this possibility, we measured the Raman spectrum of quinine in a high-ionic-strength (1 M) solution of NaH_2PO_4 (Figure 2.6e-g). In this solution, the concentration of NaH_2PO_4 is ca. 1000× higher than that of quinine. However, the 1370 and 1390 cm^{-1} modes of quinine surprisingly do not exhibit any significant frequency shifts, indicating that the quinoline ring moieties of mono- and diprotonated quinine do not form stable salt bridge interactions with phosphate ions. The only significant spectral change is that the relative intensity of the 1390 cm^{-1} band increases compared with the 1370 cm^{-1} band due to the change in the solution pH upon addition of NaH_2PO_4.

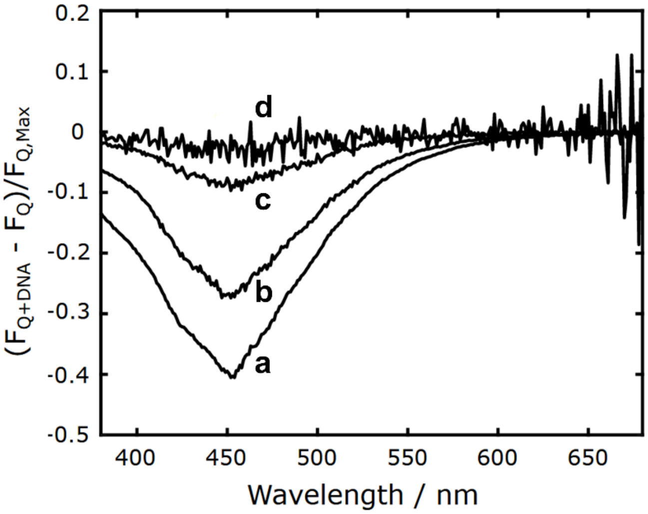

Figure 2.7. Normalized fluorescence difference spectra of quinine-DNA mixed together in solution. The solution corresponding to the difference spectrum in (a) was prepared at a concentration of 4 mg mL^{-1} DNA and 1.5 mg mL^{-1} quinine. The solutions corresponding to the difference spectra shown in (b), (c), and (d) were of 1:10, 1:100, 1:1000 dilutions, respectively, of the solution prepared in (a).

I further attempted to validate our interpretation of the Raman difference spectrum by monitoring quinine−DNA binding using fluorescence spectroscopy (Fig. 2.7). The fluorescence of quinine is expected to quench in the presence of DNA due to its intercalation into the base pairs.[193] At low concentrations (1.5×10^{-3} to 1.5×10^{-2} mg mL^{-1}) of quinine and DNA (Fig. 2.7c,d), I saw a fluorescence reduction by ca. 5−8%, qualitatively consistent with the Raman data. However, at higher concentrations (0.15−1.5 mg mL^{-1}), I observed a significantly larger decrease in the fluorescence signal (Fig. 2.7a,b). In particular, I observed a ca. 40% apparent decrease in the fluorescence at the same concentrations of DNA−quinine used in the Raman measurements.

One compelling reason for the apparent discrepancy between the Raman and fluorescence measurements could stem from dynamic self-quenching that occurs between transiently interacting quinine molecules at high concentrations. Such self-quenching phenomena has been reported by Krimer et al.[221] for quinine solutions prepared at concentrations similar to that used in our Raman and fluorescence measurements. In addition, Edward et al.[151] observed self-quenching for small quinine-functionalized polycarbonate polymers, where π-stacking interactions between the quinoline rings of neighboring covalently linked quinine molecules can occur. We envision that dynamic self-quenching occurs if the local concentration of cationic mono- and diprotonated quinine molecules increases in the vicinity of DNA. This can occur if quinine molecules electrostatically bind the negatively charged phosphate backbone of DNA. On the basis of our Raman data (Fig. 2.5-6), these electrostatic interactions do not occur between the DNA phosphate backbone and quinine’s quinoline ring. A more likely scenario is that the quinuclidine head group of quinine weakly binds the phosphate backbone through transient electrostatic interactions, as observed in our MD simulations.

Wesełucha-Birczyńska and Nakamoto[194, 195] propose that electrostatic interactions between the quinuclidine headgroup and DNA occurs for the quinine derivative, cinchonine. Their supporting evidence, however, is indirect since they only observe a small Raman frequency shift in the symmetric stretching mode of the DNA phosphate backbone and not in any cinchonine bands. For quinine, we also see no clear spectroscopic evidence supporting this hypothesis, although we do not have a good vibrational probe to specifically monitor the local environment around the quinuclidine moiety. On the basis of the lack of clear spectroscopic evidence, the electrostatic interactions between the quinuclidine headgroup and DNA must be very weak and transient if they indeed occur.

Estensen et al.[218] used UV absorption and viscometric measurements to investigate quinine−DNA binding. Their data indicates that quinine binds DNA in two different regimes. One binding regime occurs at low (sub-millimolar) quinine concentrations, whereas the other occurs at high concentrations (millimolar). At low concentrations, they observe that one molecule of quinine binds per 40 base pairs. They hypothesize that this binding mode corresponds to quinine intercalating into DNA through π-stacking interactions. This binding density is similar to but slightly lower than that estimated from our Raman measurements. The discrepancy between the two values could stem from the fact that our measurements are performed under acidic conditions, whereas Estensen et al.'s[218] measurements are performed at pH 7.4. The second binding mode that Estensen et al.[218] observe occurs at millimolar concentrations, where one quinine molecule binds approximately every 8−9 base pairs. Estensen et al.[218] speculate that this second binding regime corresponds to quinine molecules electrostatically interacting with the DNA phosphate backbone via their quinuclidine moieties, presumably in the minor groove. They argue that this binding mode can account for the observed viscosity change at millimolar concentrations that occurs when quinine and DNA are mixed together in solution.

Overall, it seems reasonable that cationic quinine molecules form transient and weak interactions with the phosphate backbone of DNA, which would give rise to dynamic self-quenching of the fluorescence. However, it is ultimately difficult to definitively conclude on what causes the 40% reduction in fluorescence at high concentrations of quinine and DNA. This is because electronic spectroscopies such as UV absorption and fluorescence lack the chemical specificity of vibrationally resolved methods such as Raman spectroscopy. This makes it difficult to clearly discern the molecular-level origins of the observed absorption and fluorescence intensity changes without extensive a priori knowledge. This is especially the case for quinine, whose fluorescence intensity changes are confounded by several factors, including concentration-dependent self-quenching, pH, chloride ions, DNA, and other environmental factors. In contrast, the Raman measurements are not confounded by these competing factors and clearly indicate that quinine molecules intercalate into the DNA by forming π-stacking interactions between its protonated quinoline ring and the DNA base pairs.

2.4 Concluding Remarks

Our team showed that quinine's prominent quinoline ring symmetric stretching mode is an excellent spectroscopic probe for monitoring quinine's local chemical environment. In solvents that do not interact strongly with quinine, the solvatochromic shifts of this mode can be quantitatively understood in terms of the Stark effect through the use of the Onsager model, which simplistically treats the solvent environment as a continuum dielectric. However, the Onsager model and Stark effect fail to adequately describe the frequency shifts observed in the quinoline ring symmetric stretching mode for solvating molecules that can interact with quinine through hydrogen bonding and π-stacking interactions. With this knowledge, the solvatochromic shift measurements establish a benchmark for interpreting spectroscopic data to assess the interaction of quinine's quinoline ring moiety with its environment through electrostatics, hydrogen bonding, or π-stacking.

Using the environmental sensitivity of this vibrational probe, we investigated the binding of quinine to calf-thymus DNA. The Raman data indicates that the intercalation of quinine into the DNA base pairs is accompanied by protonation of the tertiary amine of the quinoline ring. The predominant binding mode of quinine to DNA is through π-stacking interactions between the quinoline ring and the base pairs, rather than electrostatic interactions with the phosphate backbone. On the basis of the Raman spectral changes, we estimate that, under acidic conditions, roughly one quinine molecule intercalates per 25 base pairs of DNA. The conclusions that we draw from our Raman measurements are reinforced by MD simulations.

The chemical specificity of vibrationally resolved methods such as Raman spectroscopy offers tremendous advantages over traditional fluorescence and absorption-based methods in probing the molecular interactions of quinine with its environment. The quinoline ring symmetric stretching mode can serve as a spectroscopic probe to interrogate quinine's antimalarial activity. For the purposes of this project, however, this spectroscopic probe was used for analyzing quinine's binding state with DNA within polyplexes containing quinine as a cationic moiety. The principles of the vibrational probe established in this chapter will be used in the following chapters to provide unprecedented insight into the DNA-binding and unpackaging mechanisms underlying transfections with quinine-containing polymeric reagent.

2.5 Experimental

2.5.1 *Materials*

Acetonitrile (99.8% purity), dichloromethane (≥99.5%), chloroform (99.5%), anisole (99%), methanol (99.8%), quinoline (98%), water (HPLC-grade), hydrochloric acid (ACS-grade), and calf-thymus DNA (Premium-grade) were purchased from Sigma-Aldrich. Acetone (99.9%), toluene (99.9%), isopropanol (99.9%), and tetrahydrofuran (certified-grade) were purchased from Fisher Chemical. Ethanol (ACS/USP-grade) was purchased from Pharmco-Aaper, and quinine (99% total base, up to 5% dihydroquinine) was purchased from Alfa Aesar. Sodium acetate trihydrate (EMSURE, ACS, ISO, Reag. Ph. Eur.-grade) was obtained from Merck, and glacial acetic acid (ACS-grade) purchased from VWR.

2.5.2 *Sample Preparation*

Solutions of quinine in organic solvents for the solvatochromic shift experiments were prepared at concentrations ranging from ca. 5 to 25 mg mL^{-1}, depending on the solubility. For the pH-dependent experiments, quinine solutions were prepared in water at 10 mg mL^{-1}. HCl was used to adjust the acidity of the solutions to pH values ranging from 2.3 to 5.1. The solutions were also prepared with 1% (v/v) acetonitrile, which was used as an internal intensity standard for the Raman spectroscopic measurements. Stock solutions of quinine and calf-thymus DNA were prepared at 6 and 8 mg mL^{-1}, respectively, in 0.1 M sodium acetate buffer (pH 4.3). These stocks were sonicated and used to prepare solutions of quinine (1.5 mg mL^{-1}), DNA (4 mg mL^{-1}), and quinine (1.5 mg mL^{-1}) mixed with DNA (4 mg mL^{-1}) in sodium acetate buffer.

2.5.3 *Raman Spectroscopy*

Raman spectra were measured using a 785 nm diode laser purchased from Innovative Photonic Solutions. The beam was directed through a 30/70 beamsplitter (CVI Laser) and focused onto the sample with an infinity-corrected Olympus Ach 10×/ 0.25 NA objective. Typical laser powers used ranged from 35 to 40 mW at the sample. The scattered light was collected using a 180° backscattering geometry and redirected through the beam-splitter into the spectrometer (Acton SpectraPro 2500i). The light was dispersed in the spectrometer using a 600 gr/mm grating and imaged using a PIXIS CCD camera (Princeton Instruments). The acquisition times and frames collected varied depending on the sample and the concentrations used, but typically ranged between 10 ms and 300 s.

2.5.4 *Computational Work*

A detailed description of the computational methods is presented in the Supporting Information of the manuscript by Punihaole et al.[210] Briefly, MD simulations were performed using NAMD[222] version 2.12 and forcefield parameters from CHARMM36[223]/CGenFF[224] or Amberff99SB[225]/GAFF.[226] All simulations were conducted under the NPT ensemble at 300 K and 1 atm. Systems of one quinine molecule were solvated in $40 \times 40 \times 40$ Å^3 periodic boxes of tetrahydrofuran, dimethyl sulfoxide, acetone, acetonitrile, anisole, chloroform, dichloromethane, methanol, toluene, and TIP3P[227] water. Each of these systems were simulated for 100 ps of equilibration and 2 ns of data production MD. Quinine−DNA systems composed of diprotonated quinine molecules and 11-base pair adenine−thymine (AT) or cytosine−guanine (CG) DNA duplexes were solvated in 68 × 68 × 82 $Å^3$ periodic boxes of TIP3P[227] water. These systems were equilibrated for 400 ps, and data was collected during 40 ns production simulations. The trajectories from the quinine−DNA production simulations were analyzed with VMD,[228] and structures of quinine bound in the minor groove of both the $(AT)_{11}$ and $(CG)_{11}$ DNA systems were identified by searching for persistent hydrogen bonding and π-stacking interactions between the molecules. To do this, we defined a hydrogen bond as having a heavy atom donor−acceptor distance of ≤ 3.5Å and bond angles of 180 ± 35°. We defined plane-edge π-stacking interactions using a distance metric of ≤5 Å between the edge of the nucleobases to the plane of the quinoline ring of quinine, similar to that in the analysis of histidine-adenine stacking by Rutledge et al.[229] Only the quinine−DNA-bound structures that fit these criteria were extracted from the simulation and analyzed further to quantify the local electric field due to binding. Details regarding the methods used to calculate the local electric fields and binding free energies are discussed in the SI of the manuscript by Punihaole et al.[210]

2.5.5 Fluorescence Measurements and Sample Preparation

Stock solutions of DNA and quinine were prepared in sodium acetate buffer (pH 4, 0.1 M) at the same concentrations and in the same manner as described for the Raman measurements in the main text (vide supra). Due to quinine's sensitivity to quenching by chloride ions, great care was made to ensure any residual chloride ion impurities from the calf thymus DNA was present in equal concentrations in all samples. To control for this, we dialyzed a 5 mL aliquot of the DNA stock solution using a Centrifugal Filter Unit (10 kDa MWCO), which was centrifuged at 3220×g for 172 min. We collected 3.5 mL of the supernatant, which contained any potential residual chloride ions, to prepare the DNA (4 mg mL^{-1}), quinine (1.5 mg mL^{-1}) and quinine-DNA (1.5 mg mL^{-1}) quinine, (4 mg mL^{-1}) sample solutions. From these solutions, we also prepared additional samples by serial diluting 0.1, 0.01, and 0.001×. Aliquots of each solution (100 μL) were placed on black Greiner Cellstar 96 well plates with flat bottoms. The fluorescence spectra of these solutions were measured using a Synergy H1 Hybrid Reader (BioTek, Winooski, VT). The excitation wavelength was 350 nm and peak emission was monitored at 450 nm.

2.6 Acknowledgements

We thank Professor Nicholas Levinson (University of Minnesota, UMN) for useful discussions. Funding for this work was provided by the National Institutes of Health, 5R35-GM119441 (DP, RRF), and the UMN (CVB, TMR). D.P. gratefully acknowledges postdoctoral funding from the Ford Foundation. C.V.B. acknowledges graduate student funding under the Frieda Martha Kunze and College of Science and Engineering Graduate Fellowships (UMN). MD simulation and DFT calculation computer time was supported by XSEDEMCB060069, and the computer equipment was purchased from funds provided by the National Science Foundation (NSF), CHE-1126465 and P116Z080180 (RJW and SU). Part of this work was carried out in the College of Science and Engineering Polymer Characterization Facility, University of Minnesota, which has received capital equipment funding from the NSF through the UMN MRSEC program under Award Number DMR-1420013.

3. Quinine Copolymer Reporters Promote Efficient Intracellular DNA Delivery and Illuminate a Protein-Induced Unpackaging Mechanism

Reproduced in part with permission from:

Van Bruggen, C.; Punihaole, D.; Keith, A. R.; Schmitz, A.J.; Tolar, J.; Frontiera, R. R., Reineke, T. M.; *Proc. Natl. Acad. Sci. U. S. A.*, **2020**, *117*, 32919-32928. Copyright 2020 National Academy of Sciences.

3.1 Overview

As discussed in *Sections 1.1-1.2*, polymeric vehicles that efficiently package and controllably release nucleic acids enable the development of safer and more efficacious strategies in genetic and polynucleotide therapies. Developing delivery platforms that endogenously monitor the molecular interactions, which facilitate binding and release of nucleic acids in cells, would aid in the rational design of more effective vectors for clinical applications. This chapter discusses the facile synthesis of a copolymer containing quinine and HEA that effectively compacts plasmid DNA (pDNA) through electrostatic binding and intercalation. This polymer system, poly(quinine-*co*-HEA), packages pDNA and shows exceptional cellular internalization, transgene expression, and low cytotoxicity compared to commercial controls for several human cell lines, including HeLa, HEK 293T, K562, and keratinocytes (N/TERTs). Using quinine as an endogenous reporter for pDNA intercalation (as discussed *Chapter 2*), Raman imaging revealed that proteins inside cells facilitate the unpackaging of polymer–DNA complexes (polyplexes) and the release of their cargo. Our work showcases the ability of this quinine copolymer reporter to not only facilitate effective gene delivery but also enable diagnostic monitoring of polymer–pDNA binding interactions on the molecular scale via Raman imaging. The use of Raman chemical imaging in the field of gene delivery yields unprecedented insight into the unpackaging behavior of polyplexes in cells and provides a methodology to assess and design more efficient delivery vehicles for gene-based therapies.

3.2 Introduction

Transport of exogenous genetic material into cells in an efficient and nontoxic manner is universal and essential for life science and medical research (see *Section 1.1.1*). Developing effective delivery vehicles is a major limiting factor for the clinical translation of nucleic acid-based gene therapies (e.g., DNA, RNA, and CRISPR/Cas9).[15-17] The most commonly used delivery vectors in clinical trials are recombinantly engineered viruses that often suffer from translational limitations, such as long manufacturing times, high cost, small cargo capacity, immunogenicity, and limited shelf-life (see *Section 1.1.2*).[23, 230] As such, progress in the field of gene and cell therapy has been limited despite recent breakthroughs with costly Food and Drug Administration–approved treatments.[231, 232] Chemically synthesized vehicles such as polymer- and lipid-based systems serve as attractive alternatives due to their high-throughput and inexpensive production, ability to be chemically tuned, capacity to encapsulate a large breadth of cargo sizes (oligonucleotides to large plasmids), and accommodation of multiple dosing regimens (see *Section 1.2*).[25, 35, 233] Despite these attractive features, however, the delivery efficiency of most polymeric vehicles is lower than viruses, and they can exhibit cytotoxicity.[26]

Polymer delivery vehicles package their nucleic acid cargo into nanoparticle complexes called polyplexes (see *Section 1.2.1*). Polyplexes perform many dynamic functions during their biological transport pathway, including cargo stabilization en route to the tissue of interest, cell surface contact, endocytosis and intracellular transport, as well as localization and unpackaging at the site of action within the cytoplasm or nucleus (see *Section 1.3*).[50] The successful delivery and expression of a plasmid after this process is known as transfection. One contributing factor for the lower transfection efficiencies of polymer delivery systems lies in the fact that polyplexes must be stable outside of the cell (to prevent premature unpackaging) yet enable destabilization once inside the cell to release their nucleic acid cargo (see *Section 1.3.3*). However, for most polymer-based delivery systems, there is relatively little understanding of the factors and mechanisms that govern the release of nucleic acids from polyplexes within the cell—a necessary step in efficient transgene delivery. It has long been speculated that polyplex unpackaging in cells is facilitated by the interaction of cytosolic proteins and nucleic acids with polymers.[64, 90, 234] However, direct structural evidence for protein-induced unpackaging inside cells is lacking, and it is unclear how or where in the cell they interact with polymers to facilitate cargo release.[50, 64] Understanding these and other factors that dictate intracellular unpackaging is necessary to control the fine balance between polyplex stability from extracellular transport, unwanted tissue interactions that can lead to toxicity, and intracellular cargo release to promote gene regulatory efficacy.

Alongside several synthetic methods,[183, 184, 235, 236] the administration of the antimalarial drug chloroquine during transfection has been commonly employed to promote intracellular plasmid DNA (pDNA) unpackaging.[59] In addition to promoting endosomal escape,[86, 237, 238] chloroquine has been shown to facilitate unpackaging of pDNA by competitive binding (see *Sections 1.3.2-3*).[84, 239] Like chloroquine, the structurally similar Cinchona alkaloid, quinine, can bind DNA through both electrostatic interactions with the phosphate back-bone and intercalation through π-stacking interactions with nucleobases.[188, 210] Therefore, incorporating quinine into a polymer would enable robust DNA binding and polyplex stabilization via multiple binding mechanisms, which minimizes the overall charge density of the polymer necessary to compact DNA. Reducing the polymer's charge density reduces its toxicity profile[25] while allowing for increased incorporation of an uncharged comonomer, like HEA, that serves a complementary function such as promoting unpackaging. In addition, quinine has well-characterized spectroscopic properties and is a natural product produced in large scale. Thus, facile methods to incorporate quinine into a polymer could yield an inexpensive and effective gene delivery agent with endogenous spectroscopic properties for diagnostic polyplex imaging (see *Section 1.7*). Currently, there is no precedent for incorporating quinine into polymeric delivery vehicles to enhance transfection.

Efforts to rationally design polymers that can more efficiently release nucleic acids at their site of action have been hindered by the difficulty of quantitatively tracking the intracellular transport and cargo unpackaging of polyplexes in cells. Most experimental methods to study polyplex unpackaging involve fluorescently labeling nucleic acids and/or their polymeric carriers with large organic probes and monitoring the colocalization of their respective signals.[240, 241] The major drawback to this method, however, is that the carrier and cargo must separately diffuse roughly 200 nm, beyond the resolving power of the microscope, in order to detect the dissociation of polyplexes. This distance is two orders of magnitude larger than the spatial scales relevant to polymer binding to nucleic acids, which means that most physiologically relevant unpackaging dynamics in polyplexes are missed using conventional microscopy methods. Although FRET has aided in understanding polyplex unpackaging,[91] accurate quantification of dissociation using fluorescence-based techniques is complicated by spectral cross-talk, photobleaching, phototoxicity, and inconsistent labeling efficiency. In addition, the necessity of using bulky organic fluorophores or quantum dots may perturb the biological mechanisms and unpackaging dynamics of polyplexes.[85, 238]

Raman imaging is a powerful tool for characterizing intra-cellular polyplex unpackaging without the need for utilizing bulky labels. In recent years, Raman microscopy has been increasingly used in biological applications, including monitoring cell changes during drug delivery[242] as well as the distribution of lipids[243, 244] and metabolites[245] that cannot be easily monitored with fluorescence-based techniques (see *Section 1.6*). A major advantage of Raman spectroscopy is that it monitors vibrations that are intrinsically sensitive to the structure and interactions of molecules.[246-251] We recently showed, for example, that the Raman bands of quinine show characteristic frequency shifts that report on its electrostatic, hydrogen bonding, and π-stacking interactions, which can be used to monitor its intercalation with DNA (see *Chapter 2*).[210] Despite this, the rich chemical information encoded in Raman spectra has surprisingly not been exploited in imaging applications to probe how macromolecules dynamically interact with their local physiochemical environment in situ.

We hypothesized that direct incorporation of quinine into polymeric delivery vehicles could 1) improve the transfection efficiencies of polyplexes via enhanced binding and release mechanisms and 2) enable direct monitoring of cargo unpackaging in cells by exploiting its unique fluorescence and Raman-active spectroscopic properties (see *Section 1.7.2*) To accomplish this, I copolymerized quinine with HEA in a one-step free-radical polymerization reaction. In collaboration with Allison Keith in the group of Dean Jakub Tolar, we demonstrated that this copolymer was exceptionally efficient at delivering plasmids to several human cell types, including keratinocytes, for which suitable transfection methods are limited. I found that poly(quinine-*co*-HEA) exhibits strong binding to pDNA in polyplexes due to quinine's ability to intercalate between nucleotides. Working with Punihaole, we exploited quinine's spectral sensitivity to perform Raman imaging that directly revealed that proteins facilitate the deintercalation of quinine from pDNA and the unpackaging of polyplexes inside cells (Fig. 3.1). This collaborative works highlights the tremendous potential of quinine copolymer reporters (QCRs) as an efficient, trackable delivery platform and showcases the unique ability of Raman microscopy to quantitatively probe the molecular interactions in situ that facilitate polyplex internalization, cellular transport, and unpackaging.

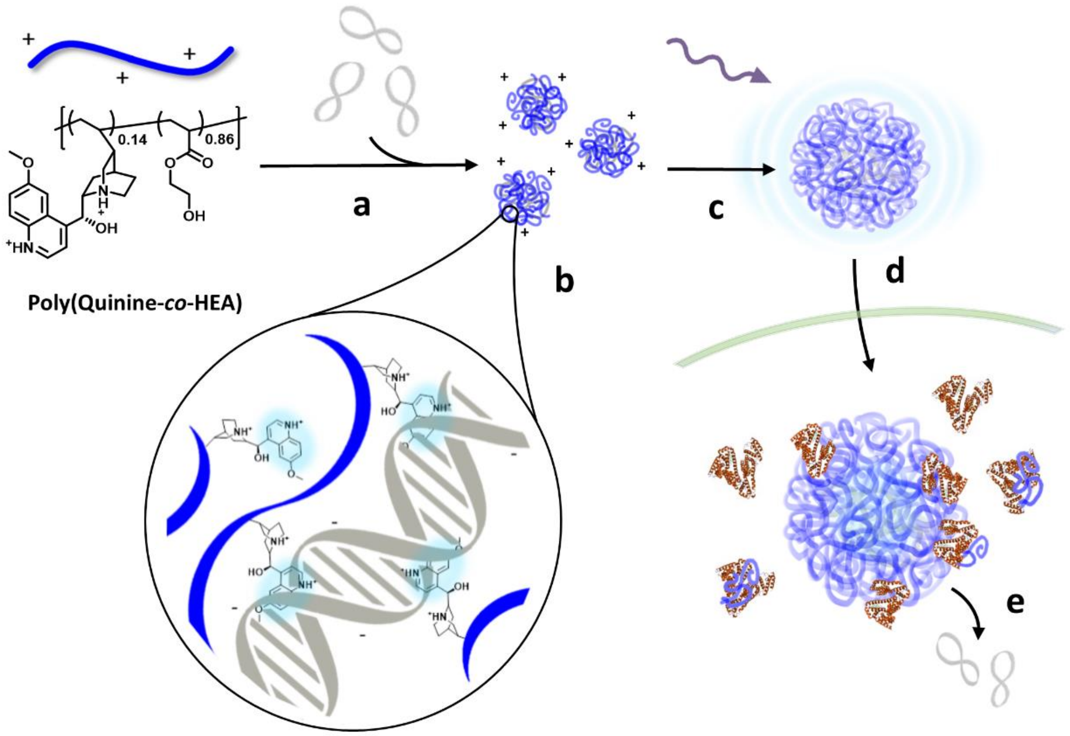

Figure 3.1. Mechanisms underlying unique plasmid binding and release mechanisms of QCRs. (a) Poly(quinine-*co*-HEA) self-assembles with pDNA at low pH (3–4) to form polyplexes and compacts the plasmid (b) via electrostatic forces as well as binding via π-stacking interactions. (c) Dilution in cell media causes aggregation of the polyplexes, which promotes sedimentation of plasmid to the cell surface. The fluorescent particles (λ_{ex} = 350 nm, λ_{em} = 450 nm) are uptaken (d), in part, by macropinocytosis. (e) Raman imaging is used to quantify release of pDNA by exposure to intracellular proteins.

3.3 Results and Discussion

3.3.1 *QCR and Control Polymer Synthesis*

I sought a facile, one-pot reaction to incorporate quinine into a polymer using inexpensive, commercially available starting materials. Quinine contains several functional handles that enable it to be incorporated into a polymeric scaffold, including its secondary hydroxyl,[145, 148, 151] tertiary amine,[146, 149, 152] and α-olefin groups (Fig. 3.2a).[123, 144, 147, 153, 154] I first pursued development of reaction conditions that would promote the direct incorporation of quinine into a polymeric backbone via radical propagation of its α-olefin group (see *Section 1.5.5*). While degradative chain transfer and steric hindrance of the bulky quinuclidine ring were necessary challenges to overcome,[154, 156, 157] the advantage to a direct approach is threefold: 1) Quinine can be used directly in a copolymerization reaction to enable a rapid, inexpensive, and scalable production method; 2) the quinuclidine amine can be protonated, aiding electrostatic interactions with DNA; and 3) the quinoline ring is distal from the backbone, which allows these polymer pendant groups to effectively intercalate into DNA without steric hindrance and allows reporting of binding and release via microscopic and spectroscopic methods.

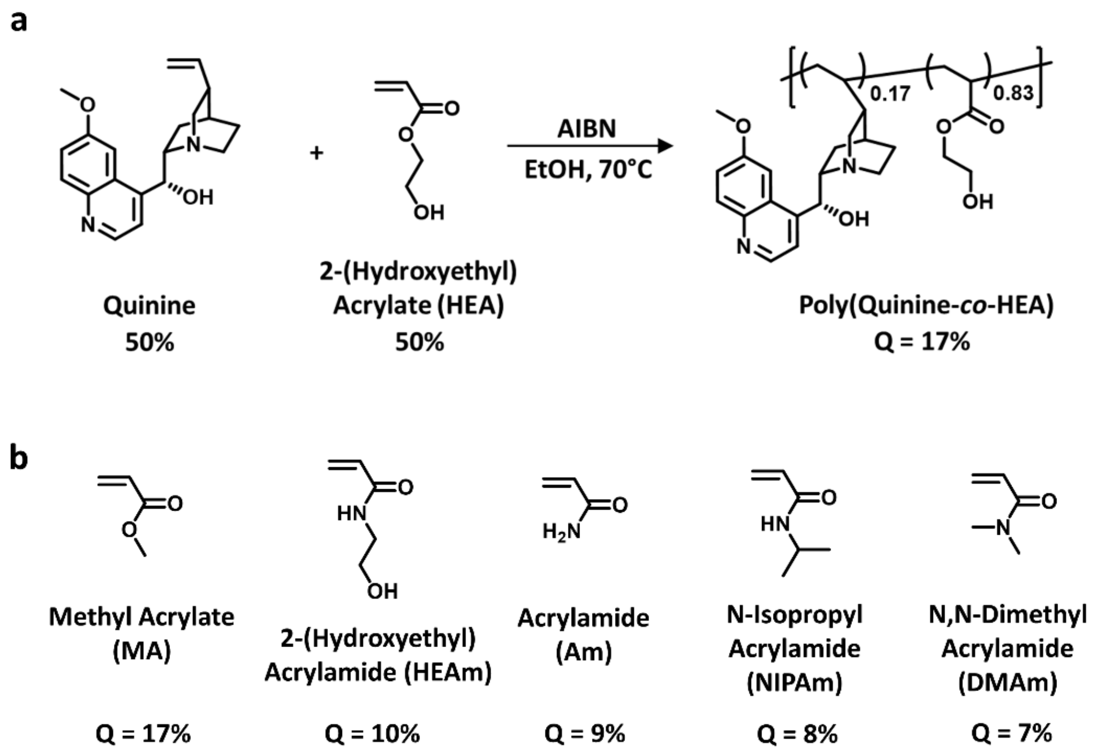

Figure 3.2. Compatibility of comonomers in copolymerization with quinine. (a) The reaction scheme shows the conditions used for the free radical copolymerization of HEA and quinine with a 50/50 monomer feed ratio. (b) Other acrylate-and acrylamide-based monomers were copolymerized with quinine at 50/50 feed ratios and showed a range of quinine (Q) incorporation (%) in the final isolated polymer as determined by ^{1}H NMR.

While quinine cannot be directly homopolymerized,[144] I found that quinine was active to free radical copolymerization with more reactive comonomers. I copolymerized quinine with several hydrophilic acrylate- and acrylamide-based comonomers that have not been copolymerized with quinine previously including HEA, 2-hydroxyethyl acrylamide (HEAm), acrylamide (Am), *N*,*N*-dimethyl acrylamide (DMAm), and *N*-isopropylacrylamide (NIPAm) (Figs. 3.2-3.3). The quinine copolymers contained up to 17% quinine by molarity, as determined by ^{1}H NMR (Fig. 3.4, Figs. 3.33-3.36). The copolymers ranged between 9 and 22 kDa in molar mass as determined by size exclusion chromatography (SEC) (Fig. 3.3b, Fig. 3.5, and Table 3.1).

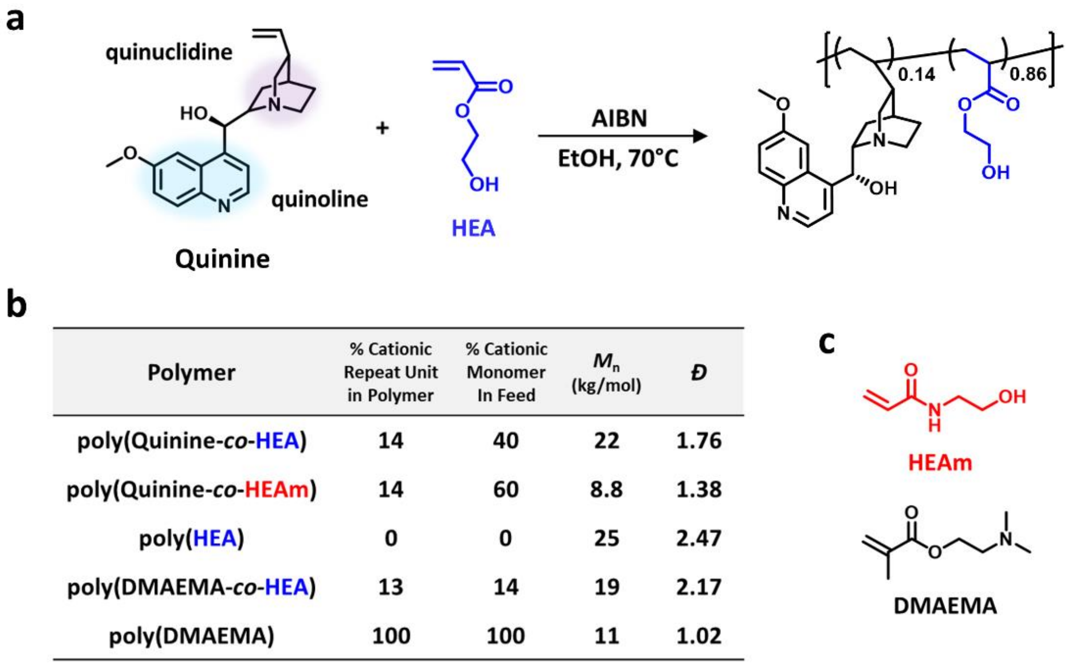

Polymer	% Cationic Repeat Unit in Polymer	% Cationic Monomer In Feed	M_n (kg/mol)	*Đ*
poly(Quinine-*co*-HEA)	14	40	22	1.76
poly(Quinine-*co*-HEAm)	14	60	8.8	1.38
poly(HEA)	0	0	25	2.47
poly(DMAEMA-*co*-HEA)	13	14	19	2.17
poly(DMAEMA)	100	100	11	1.02

Figure 3.3. Synthesis and characterization of QCRs and controls. (a) Free-radical copolymerization scheme used in this study to incorporate quinine, consisting of a bicyclic quinuclidine head group and fluorescent quinoline ring (λ_{ex} = 350 nm, λ_{em} = 450 nm), into copolymers with comonomers such as HEA (blue). (b) Structural properties of polymers used in biological studies as determined by ^{1}H NMR and SEC. (c) Quinine was copolymerized with various acrylamides including HEAm, and HEA was copolymerized with canonical cationic comonomers such as DMAEMA.

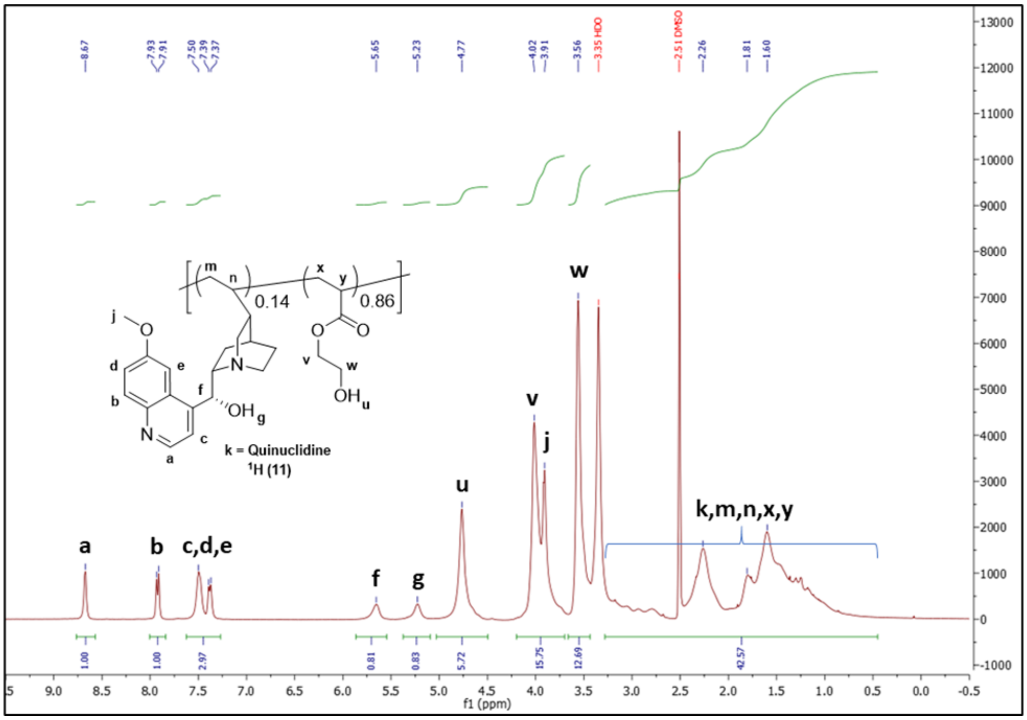

Figure 3.4. ^{1}H NMR spectra and peak assignments of poly(quinine-*co*-HEA). The copolymer was dissolved in DMSO-d$_6$, and the comonomer ratio in the copolymer was obtained using the integrations from peaks corresponding to each comonomer. Ratio of HEA/quinine = ((v,j)-3.00)/2 = 6.38

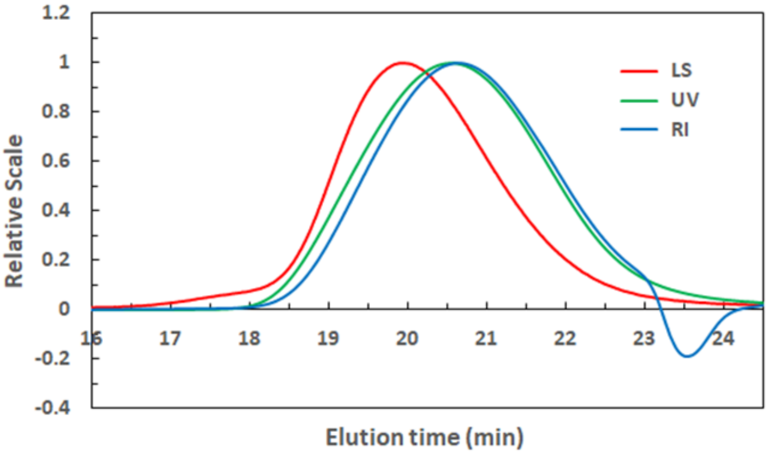

Figure 3.5. Aqueous size exclusion chromatography (SEC) trace of poly(quinine-*co*-HEA). Light scattering (LS) trace (red) and refractive index (RI) trace (blue) were used to determine M_n, M_w, and $Đ$ for quinine copolymers. The UV absorption peak (green) was obtained at λ = 280 nm.

Table 3.1. Structural properties of polymers used in biological studies

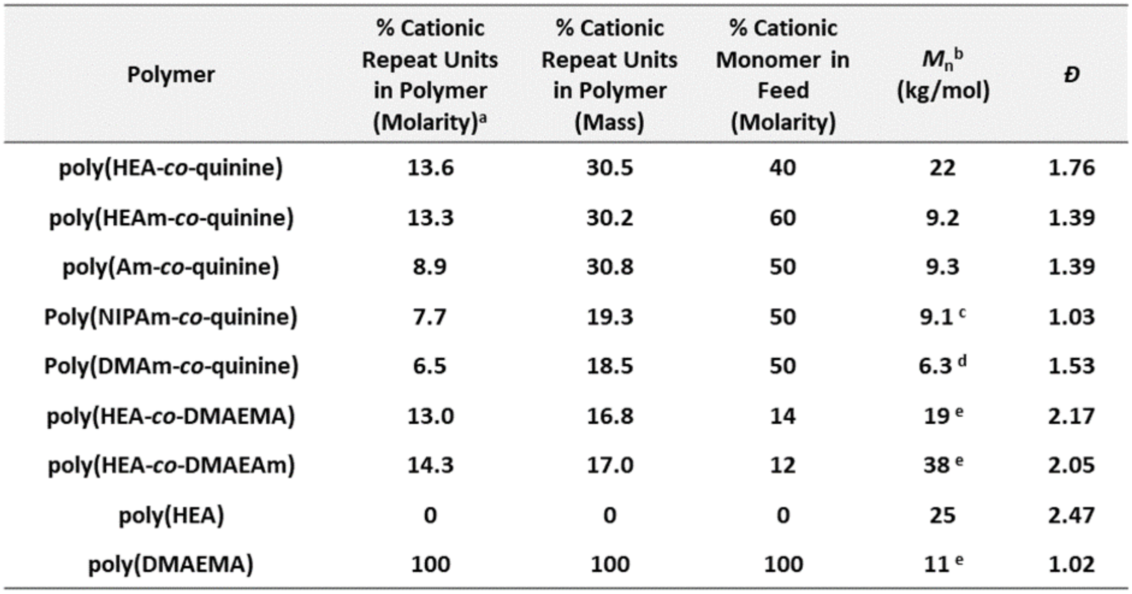

Polymer	% Cationic Repeat Units in Polymer (Molarity)[a]	% Cationic Repeat Units in Polymer (Mass)	% Cationic Monomer in Feed (Molarity)	M_n[b] (kg/mol)	*Đ*
poly(HEA-*co*-quinine)	13.6	30.5	40	22	1.76
poly(HEAm-*co*-quinine)	13.3	30.2	60	9.2	1.39
poly(Am-*co*-quinine)	8.9	30.8	50	9.3	1.39
Poly(NIPAm-*co*-quinine)	7.7	19.3	50	9.1 [c]	1.03
Poly(DMAm-*co*-quinine)	6.5	18.5	50	6.3 [d]	1.53
poly(HEA-*co*-DMAEMA)	13.0	16.8	14	19 [e]	2.17
poly(HEA-*co*-DMAEAm)	14.3	17.0	12	38 [e]	2.05
poly(HEA)	0	0	0	25	2.47
poly(DMAEMA)	100	100	100	11 [e]	1.02

[a] Determined via ^{1}H NMR as shown in Fig. 3.F4 and Figs. 3.M.1-4.

[b] Unless otherwise noted, M_n and *Đ* was determined via aqueous SEC. The *dn/dc* of the copolymers was calculated using eqn 3.4 with measured *dn/dc* values of quinine (0.266) and corresponding homopolymers; pHEA (0.128), pHEAm (0.186), and pAm (0.169). The values are p(quinine-*co*-HEA) *dn/dc* = 0.170, p(quinine-*co*-HEAm) *dn/dc* = 0.186, p(quinine-*co*-Am) *dn/dc* = 0.199.

[c] The *dn/dc* value for the homopolymer p(NIPAm) in aqueous buffer (0.167) was determined from literature[252] and used to calculate *dn/dc* of copolymer (0.1861) using eqn 3.4.

[d] M_n and *Đ* determined via THF SEC with an estimated *dn/dc* = 0.180 (polystyrene)

[e] The *dn/dc* value for the homopolymer pDMAEMA (0.174) was measured in the aqueous SEC buffer. This value was used to calculate the *dn/dc* of poly(DMAEMA-*co*-HEA) (0.135) using eqn 3.4, which was used as the *dn/dc* for DMAEAm copolymer.

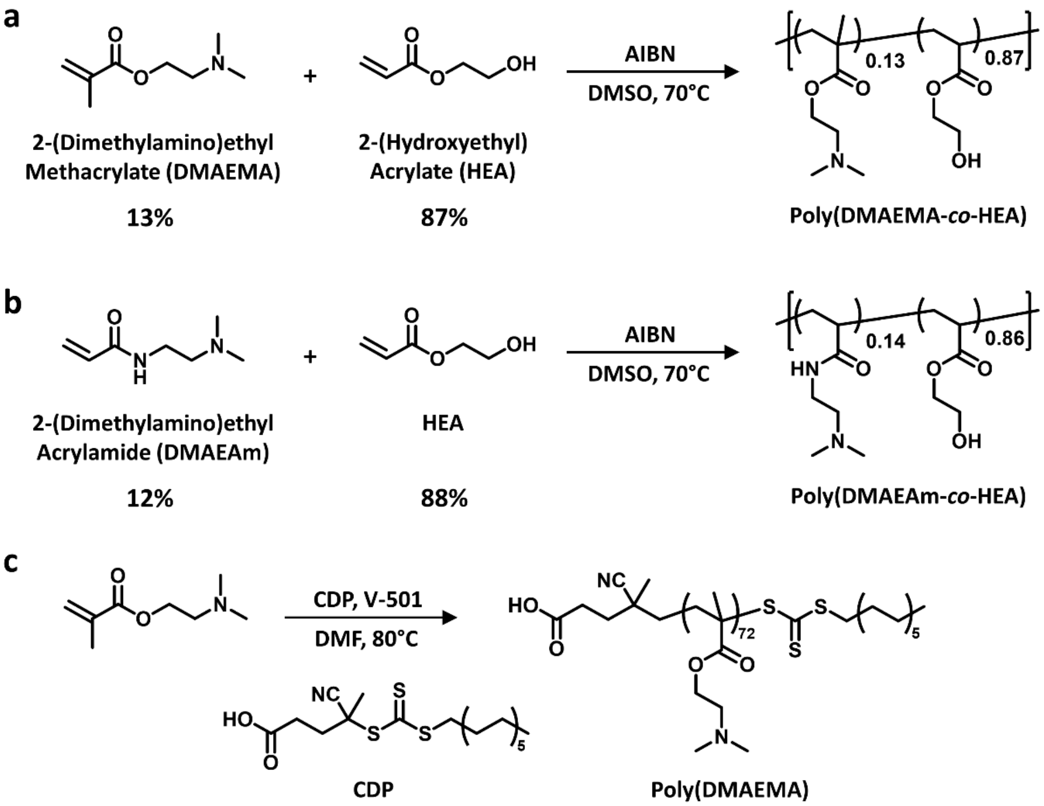

Figure 3.6. Synthesis of DMAEMA and DMAEAm control polymers. Free radical copolymerization of HEA was performed with (a) DMAEMA and (b) DMAEAm. (c) Homopolymerization of DMAEMA was performed via RAFT. The methacrylate (DMAEMA) and acrylamide (DMAEAm) tertiary amine-containing monomers were used instead of the acrylate-based analogue, dimethylaminoethyl acrylate, since the acrylate analogue shows significant degradation due to self-catalyzed hydrolysis of the ester by back-biting of the amine.[253]

Along with determining molar mass and dispersity, the SEC allowed me to rule out that the quinine is a simply a small molecule contaminant in the polymer product. The SEC trace (Figure 3.5) showed a UV absorption peak overlapping with the LS and RI peaks, which indicated that quinine is present as a macromolecule. The presence of only one peak in the trace also verified that quinine did not polymerize separately as a homopolymer and that quinine and the comonomer (HEA) are indeed copolymerized together.

In addition, I fully characterized the reactivity ratios of quinine with several comonomers to give insight into the microarchitecture of the copolymer chains. The reactivity ratios of quinine with comonomers HEA, HEAm, and Am were monitored via ^{1}H NMR (Fig. 3.7). In these three copolymerizations, HEA, HEAm, and Am are defined as M_1 and quinine is defined as M_2. The reactivity ratios for each comonomer/quinine pair, r_1 and r_2, are defined as a ratio of rate constants for each comonomer, where

$$r_1 = k_{11}/k_{12} \tag{3.1}$$

$$r_2 = k_{22}/k_{21} \tag{3.2}$$

and k_{11} is the rate constant for the addition of M_1 to a propagating chain ending with M_1 (homo-propagation) and k_{12} is the rate constant for the addition of M_2 to the same chain end (hetero-propagation). In summary, the reactivity ratio r_1 is the ratio of the homo- and hetero-propagation rate constants for propagating chains ends consisting of M_1. The reactivity ratios for each comonomer pair can be determined by plotting f_1 against $F_1$and fitting the points with the Mayo-Lewis equation:

$$F_1 = \frac{r_1{f_1}^2 + f_1f_2}{r_1{f_1}^2 + 2f_1f_2 + r_2{f_2}^2} \tag{3.3}$$

where the value $F_1$is the mole fraction of M_1 in copolymer. The value f_1 is the mole fraction of M_1 in the comonomer feed while f_2 corresponds to mole fraction of M_2 in the comonomer feed. The reactivity ratios, $r_1$and r_2, for all three comonomers were greater than 10 and less than 0.12 (Fig. 3.7b), respectively, which indicated that the propagating radical chain-ends, consisting of either M_1 or M_2, prefer addition of the activated comonomer M_1 (acrylate or acrylamide) over M_2 (quinine) at all points in the polymerization. This tendency means that quinine is incorporated as isolated units statistically throughout the polymer chain (Figure 3.7c) and is unlikely to form quinine-rich blocks, even upon consumption of the activated monomer M_1. Stretches of hydrophilic repeat units act as spacers between hydrophobic/cationic quinine repeat units, which reduces the charge density of the polymer. Introducing hydrophilic spacers (such as

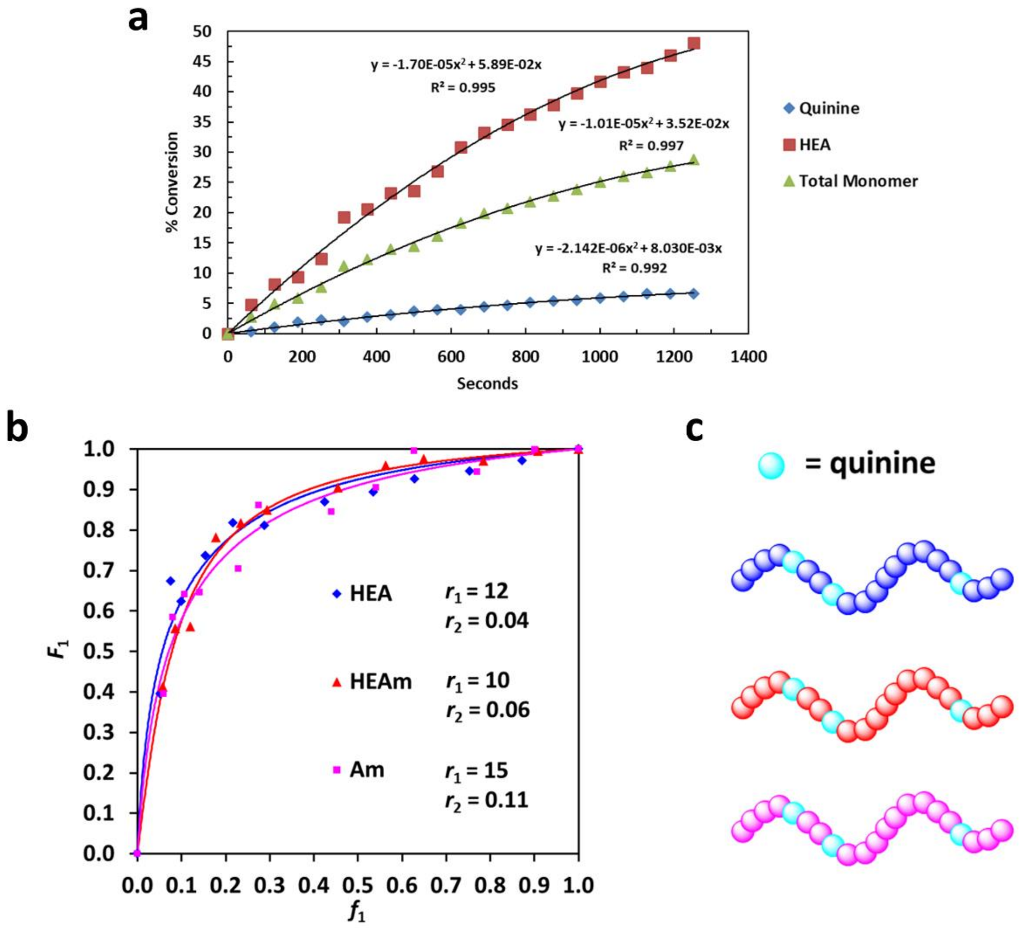

Figure 3.7. Determination of reactivity ratios in the free radical copolymerization of quinine with acrylate HEA and acrylamides HEAm and Am. (a) Variable-temp ^{1}H NMR was used to monitor alkene peak integrations, which correlates to comonomer conversion, during radical polymerization. The conversion of comonomers was plotted over time. (b) Copolymerizations were run at eleven different comonomer feed ratios (f_1). The resulting comonomer ratio in the copolymer (F_1) was measured via ^{1}H NMR and plotted above. The points for each comonomer were fitted with the Mayo-Lewis equation (eqn. 3.3) to give the reactivity ratios for each comonomer with quinine. (c) Representation of the resulting copolymers of quinine with HEA, Am, and HEAm.

Carbohydrates) to polycations (such as PEI), has been commonly employed to reduce charge density and toxicity of polycations (see *Section 1.4.2*).[25, 96, 99, 254] Overall, the molar masses, dispersities, and architectures of the synthesized copolymers are comparable to other effective polymeric delivery agents.[106, 255, 256] This direct approach to successfully propagate quinine via free radical copolymerization is a simple, inexpensive, reproducible, and readily scalable method that is amenable for numerous fundamental and translational research endeavors.

3.3.2 *Quinine Facilitates Enhanced Binding to DNA in Polyplexes*

Our previous work (see *Chapter 2*) shows that monomeric quinine interacts with DNA electrostatically via the quinuclidine moiety, as well as through intercalation via the quinoline ring.[210] I hypothesized that the quinine copolymers would efficiently bind and compact pDNA and form self-assembled polyplexes in solution via both binding modes, allowing for protection against degradation and efficient cellular delivery. Electrophoretic mobility shift assays (EMSAs) demonstrated that all of the quinine copolymer variants were able to bind pDNA (Fig. 3.8) at a range of formulation N/P ratios as low as N/P = 0.5, which is defined as the molar ratio of quinuclidine amines (N) to DNA phosphate groups (P). Dynamic light scattering (DLS) showed that quinine copolymers self-assemble with plasmids in solution to form positively charged polyplexes (Fig. 3.10) between roughly 80 and 200 nm in hydrodynamic diameter (d_h) (Fig. 3.9). Like many transfection reagents, we found that poly(quinine-*co*-HEA) polyplexes aggregated upon dilution in serum-free cell media due to deprotonation at neutral pH (Fig. 3.9-11).[256, 257] Interestingly, we discovered that the aggregation of poly(quinine-*co*-HEA) polyplexes upon addition of serum-free Dulbecco's modified Eagle's medium (DMEM) could be controlled as the mean polyplex

polyplex size (d_h) and quinine-copolymers fluoresce blue (see Fig. 3.18) and are shown migrating towards the anode.

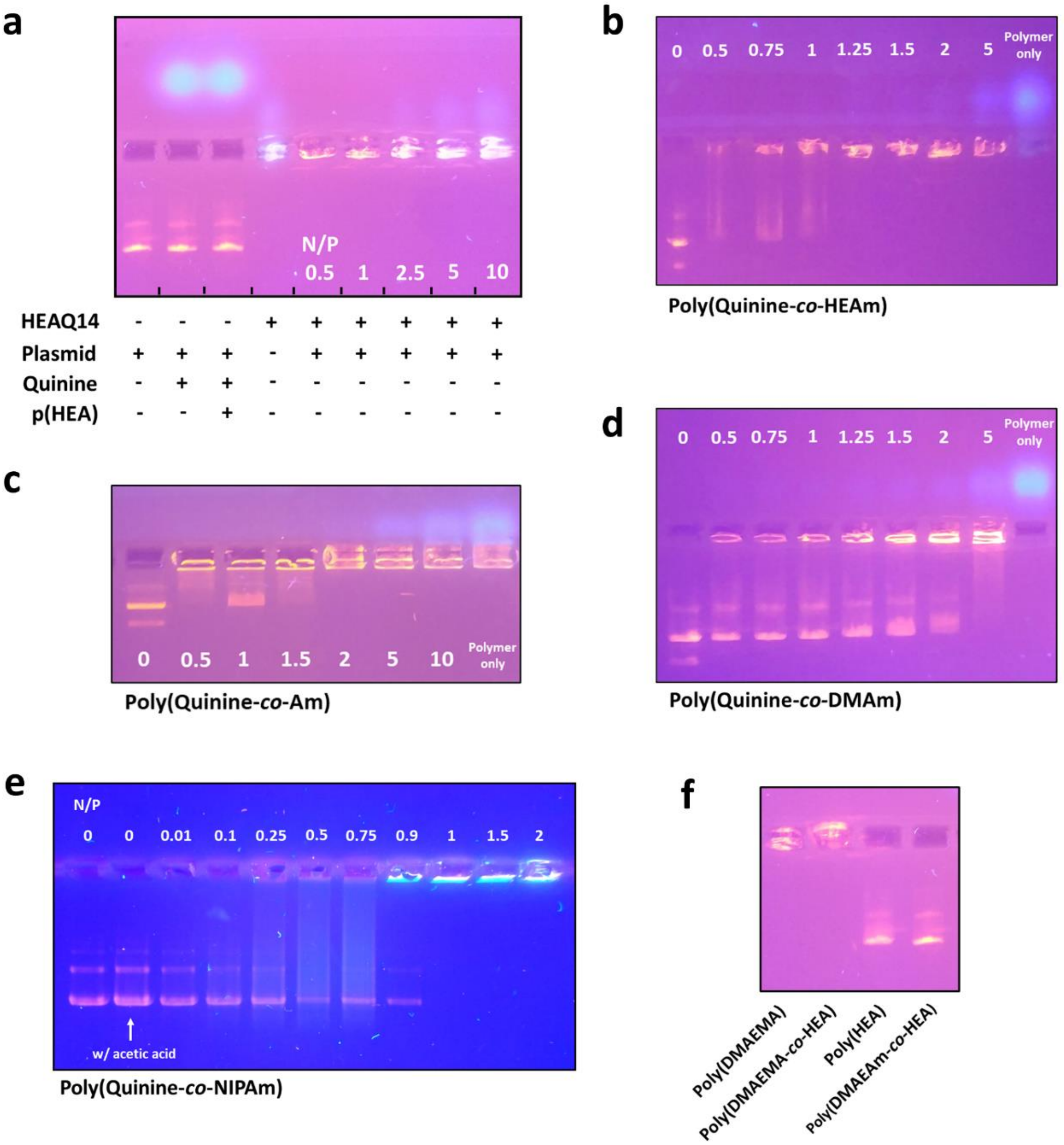

Figure 3.8. Electrophoretic mobility shift assay (EMSA) of quinine copolymers with ZsGreen-encoding plasmid (4.7 kb, 0.5 µg) with increasing N/P ratios of (a) poly(quinine-*co*-HEA), (b) poly(quinine-*co*-HEAm), (c) poly(quinine-*co*-Am), and (d) poly(quinine-*co*-DMAm) as shown in Table 3.1. In (e), poly(quinine-*co*-NIPAm) contained 21% quinine by molar incorporation (derived via precipitation as discussed in *Section 3.5.3.5*). For the controls in (a) and (f), the N/P ratio = 10 or contained the molar equivalence of subunits to poly(quinine-co-HEA) at N/P = 10. The plasmid was visualized with ethidium bromide (orange) excited at medium-wavelength UV (λ_{ex} = 312 nm). Under UV excitation, quinine and quinine-copolymers fluoresce blue (see Fig. 3.18) and are shown migrating towards anode.

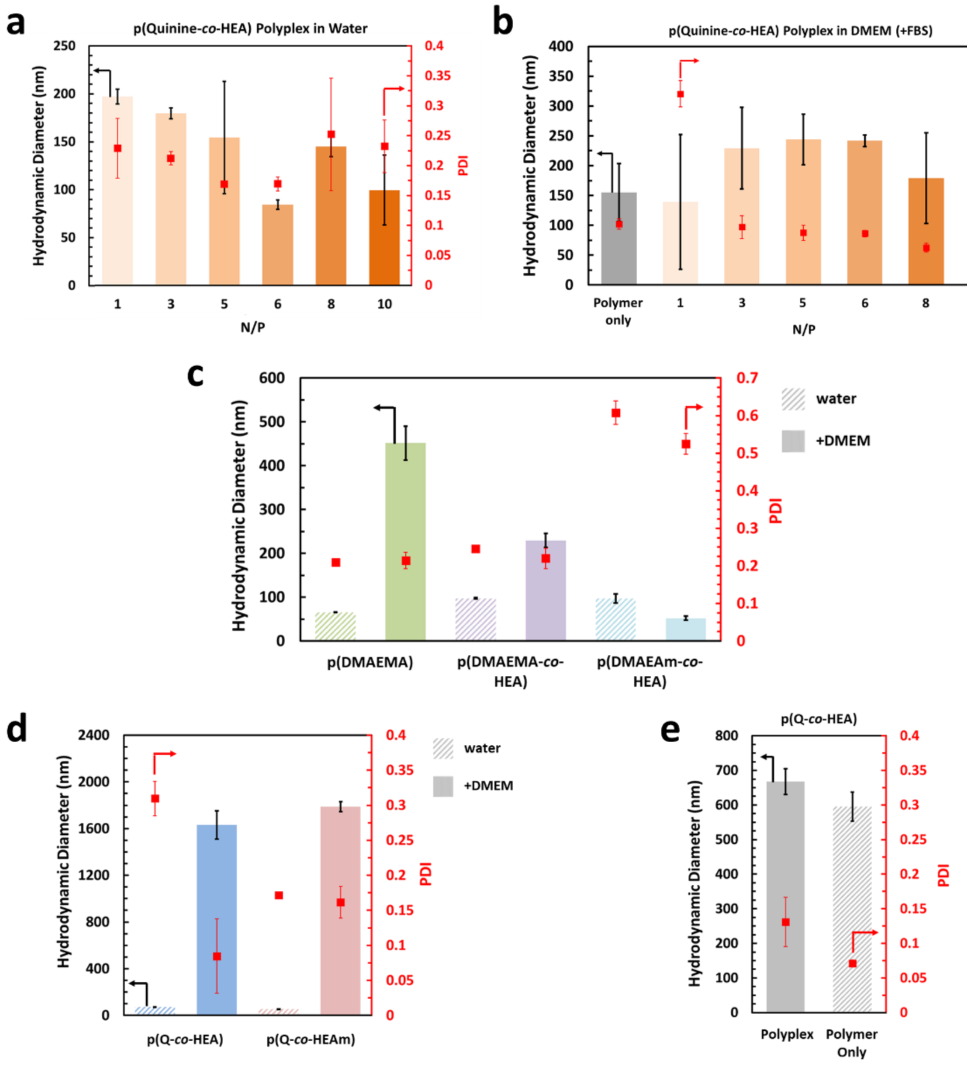

Figure 3.9. Dynamic light scattering (DLS) of polyplexes. (a) Polyplexes were formed from mixing poly(quinine-*co*-HEA) with plasmid under aqueous conditions with increasing N/P ratios. Sufficient signal was not observed for plasmid only, polymer only (N/P = 6), quinine only (N/P = 6), poly(HEA) + plasmid (mass equiv. to N/P = 6), and poly(HEA) + quinine + plasmid (mass equiv. to N/P = 6). (b) Poly(quinine-*co*-HEA) polyplexes were diluted (3×) in DMEM (+FBS, 10% v/v) with increasing N/P ratios. (c) Control polymers were mixed with plasmid (N/P = 6) in water and diluted (3×) in serum-free DMEM. (d) Comparison of poly(quinine-*co*-HEA) vs poly(quinine-*co*-HEAm) polyplexes in water and after dilution (3×) in serum-free DMEM (after ~60 min of incubation). (e) Poly(quinine-*co*-HEA) polyplexes and polymer-only after incubation in buffer containing $NaHCO_3$ buffer (44 mM) and dextrose (25 mM) as used in zeta potential measurements (Fig. 3.10, see *Section 3.5.9*). Data represented as the mean ± SD (n = 3).

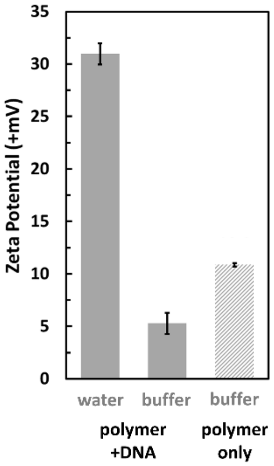

Figure 3.10. Zeta potential of poly(quinine-*co*-HEA) polyplexes in water and bicarbonate buffer (see *Section 3.5.9*). The zeta potential of the polyplexes are compared to aggregates formed from polymer only. Data represented as the mean ± SD (n ≥3).

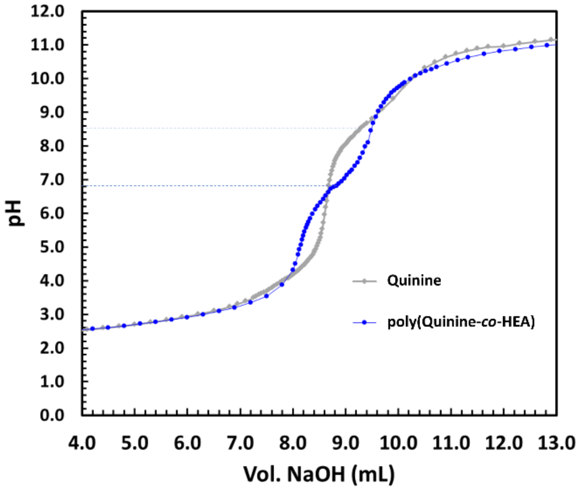

Figure 3.11. Potentiometric titration of poly(quinine-*co*-HEA) and monomeric quinine. Quinine contains a basic amine on the quinuclidine head (pK_a = 8.5) as well as on the quinoline ring (pK_a = 4.1).[258] In this potentiometric titration, the pK_a for the quinuclidine amine is easily observed for both the monomer (pK_a = 8.5) and copolymer (pK_a= 6.8), which is the only relevant protonatable amine at physiological pH. This decrease in the pK_a of the cationic moiety upon incorporation polymerization is commonly observed for polycations.[96] Although it is not easily measured via standard aqueous titration,[259] the pK_a quinoline amine, which is likely suppressed further (< 4.1), may aid in buffering of lysosomes to promote escape into the cytoplasm.[260]

increases monotonically to ~1 μm within 60 min (Fig. 3.12e). Indeed, polyplex aggregation has been shown to promote transfection by increasing sedimentation of DNA, which concentrates the polyplexes at the cell surface and increases the amount DNA that is internalized.[112, 261-263] This control in particle size can be used to directly tune and improve biological efficacy (see *Section 3.3.3*).

Analogous copolymer controls were created that replaced quinine with canonical amines, such as DMAEMA[96, 112] (Fig. 3.3, Fig. 3.6, and Table 3.1) to remove the intercalation ability for comparison. Using a dye-exclusion assay, I found that when quinine was replaced with DMAEMA in a HEA copolymer, the ability of the copolymer to compact pDNA was completely inhibited (Fig. 3.12a, Fig. 3.13d). The QCRs maintained more pDNA compaction upon dilution in serum-free media compared to polyplexes formed with the DMAEMA homopolymer (Fig. 3.12b, Fig. 3.13a-c). This result shows that quinine has exceptional DNA binding and compaction properties compared to canonical amine-containing monomers such as DMAEMA, which is likely due to the dual binding mechanism of electrostatics and intercalation.

The mechanism underlying the exceptional compaction of pDNA by quinine in poly(quinine-*co*-HEA) was further investigated using Raman spectroscopy in collaboration with Punihaole. We previously proved that the quinoline ring symmetric stretching mode (referred to as the quinoline ring mode henceforth) quantitatively reports on the local interactions of quinine with its chemical environment (see *Chapter 2*).[210] In the case of monomeric quinine, the quinoline ring mode characteristically upshifts in frequency upon deintercalation from DNA due to the loss of π-stacking interactions with nucleobases (Table 3.2).

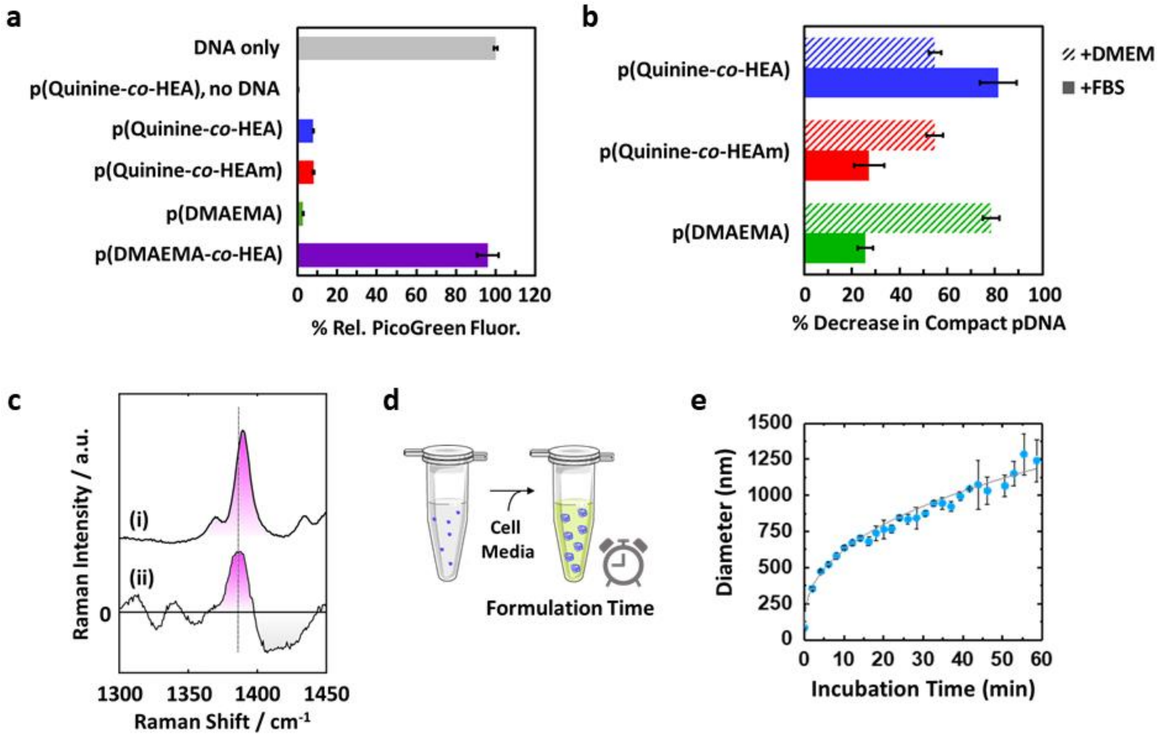

Figure 3.12. Characterization of QCR–DNA binding. (a) Dye-exclusion assay monitors pDNA compaction in polyplexes (N/P = 6) formed in acidic aqueous media (pH 3 to 4). The fluorescence of PicoGreen intercalation in polyplexes is normalized to the fluorescence from free pDNA. (b) The polyplex solution in “a” is diluted first in cell media (DMEM) followed by addition of FBS (10% v/v). The change in relative PicoGreen fluorescence upon sequential addition of solutions is used to calculate the percent decrease in compact pDNA between steps (as shown in Fig. 3.14). (c) (i) Raman spectrum of unbound poly(quinine-co-HEA) polymer under acidic solution conditions and (ii) difference spectrum highlighting the spectral shift that occurs in the quinoline ring mode of poly(quinine-*co*-HEA) due to DNA intercalation. The difference in the quinoline ring mode frequency (3 cm^{-1}) between intercalated and deintercalated quinine can be used to monitor poly(quinine-*co*-HEA) polyplex unpackaging. (d) Schematic of polyplex aggregation in serum-free DMEM prior to exposure to cells (defined as *formulation time*). (e) Plot showing the hydrodynamic diameter of poly(quinine-*co*-HEA) polyplexes (N/P = 8) over time after addition of serum-free DMEM. Data for (a), (b), and (e) are represented as the mean ± SD (n = 3).

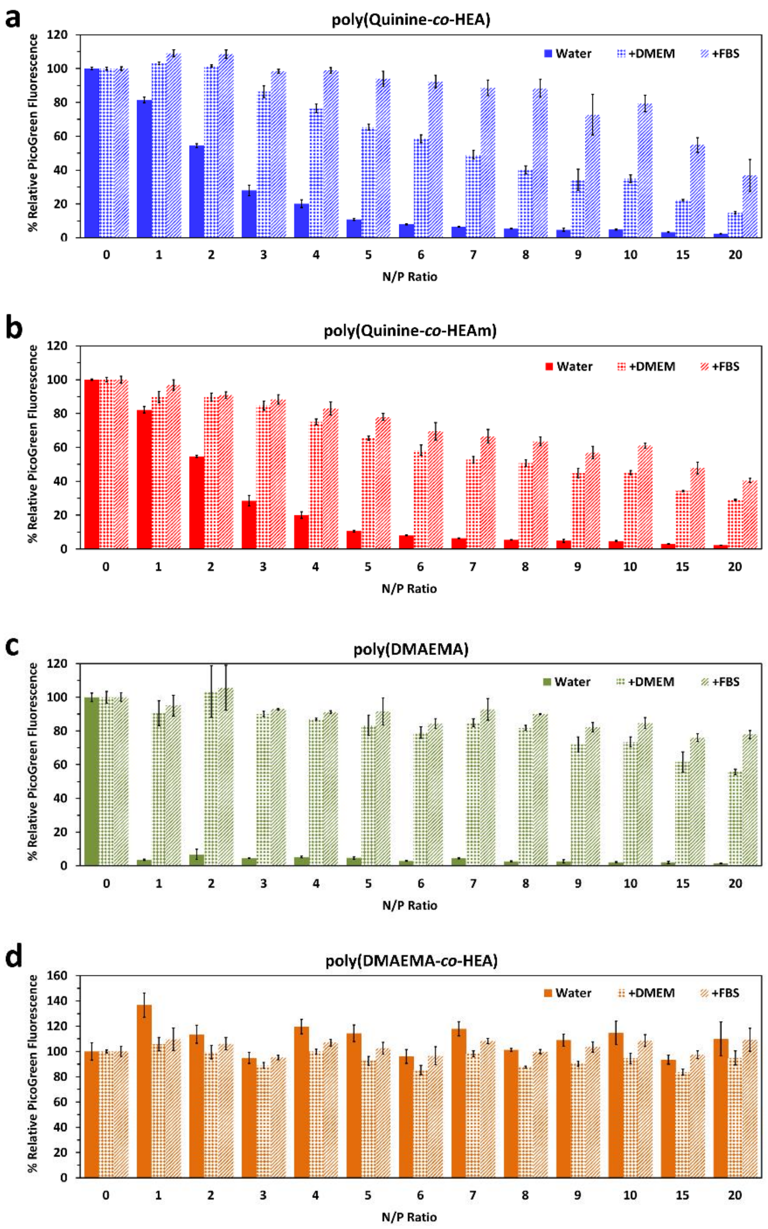

Figure 3.13. Monitoring plasmid binding by quinine copolymers and controls at various N/P ratios via PicoGreen Dye Exclusion Assay. The exclusion of PicoGreen from intercalating into the plasmid is due binding of the polymer to DNA and is compaction in the polyplex. Increases in relative PicoGreen fluorescence (λ_{ex}= 480 nm, λ_{em}= 520 nm) correlate to decreased polymer-induced plasmid compaction. Serum-free cell media (DMEM) was added to polyplexes in water at concentrations identical to those performed in transfection. Fetal bovine serum (FBS, 10% v/v) was then added to the diluted polyplexes and the relative change in fluorescence was monitored. Polyplexes were at N/P = 0-10, 15, and 20 for polymers (a) poly(quinine-*co*-HEA), (b) poly(quinine-*co*-HEAm), (c) p(DMAEMA), and(d) poly(DMAEMA-*co*-HEA). Data represented as the mean ± SD (n = 3).

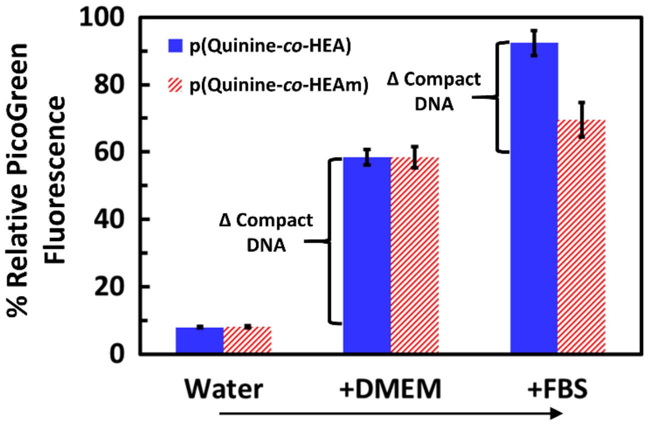

Figure 3.14. Comparison of poly(quinine-*co*-HEA) and poly(quinine-*co*-HEAm) at an N/P = 6, which shows the change in plasmid decompaction through sequential dilution with DMEM and addition FBS (+10%). Data represented as the mean ± SD (n = 3).

To examine the binding of quinine to DNA in the copolymers, we measured the Raman spectra of poly(quinine-*co*-HEA) polyplexes under similar pH conditions as the DLS and dye-exclusion assays. Figure 3.15a shows the Raman spectrum of the poly(quinine-*co*-HEA) polyplexes. The spectrum is complex, showing spectral features that derive from both DNA and polymer vibrational modes. The most intense spectral feature is located at 1388 cm^{-1} and can be assigned to the protonated quinoline ring symmetric stretching mode of quinine in poly(quinine-co-HEA) polymers. Most of the other spectral features are significantly weaker than the quinoline ring mode and can be mainly assigned to vibrational modes localized to the nucleobases of DNA. To understand the spectral changes that occur due to poly(quinine-*co*-HEA) binding to DNA, the polyplex spectrum was compared to the spectra of DNA and aggregated poly(quinine-co-HEA) polymers. In order to highlight the polymer spectral changes due to DNA binding, we calculated a difference spectrum by subtracting the spectral contributions of aggregated poly(quinine-co-HEA) polymer and DNA. The resulting difference spectrum (Fig. 3.12c and Fig. 3.15d) showed Raman bands that derive from the DNA in the form of two broad negative features at 1241 cm^{-1} (assigned to deoxythymine, deoxyadenosine, and deoxycytidine modes) and 1415 cm^{-1} (assigned to a deoxyadenosine mode), as well as a positive feature at 1486 cm^{-1} (assigned to deoxyadenosine and deoxyguanosine modes). In addition, the difference spectrum showed a prominent positive feature at 1,386 cm^{-1} that derives from the quinoline ring mode and is downshifted 3 cm^{-1} from the same band in the unbound polymer solution (Fig. 3.12c and Table 3.2). This frequency shift, therefore, quantitates the intercalation of quinine into pDNA and can be used as a spectroscopic marker to monitor the degree of polyplex packaging and unpackaging.

Taken together, the dye exclusion and Raman spectroscopic results indicated that quinine binds to DNA through both electrostatic interactions with the phosphate backbone and π-stacking with the nucleobases, which contributes to the overall stability of the polyplex formulations. Collectively, the confluence of these characteristics confers copolymers containing quinine with considerable compaction capabilities compared to canonical cationic amine-containing constituents.

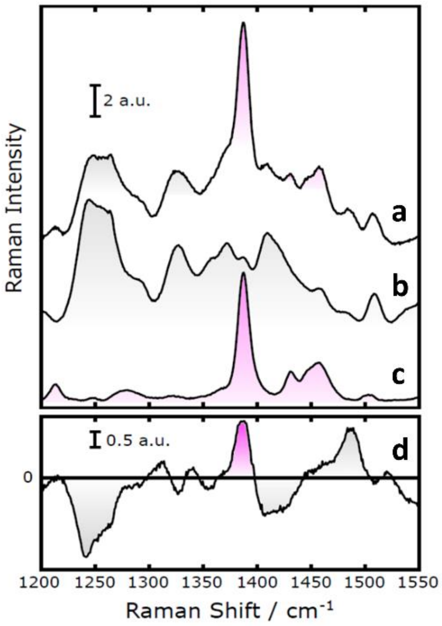

Figure 3.15. Raman spectra of poly(quinine-*co*-HEA) and DNA in solution. The traces include Raman spectra of (a) poly(quinine-*co*-HEA) polyplexes, (b) DNA, and (c) poly(quinine-*co*-HEA) polymer aggregates. The difference spectrum shown in (d) was calculated by subtracting the spectra shown in (b) and (c) from that shown in (a).

Table 3.2. Comparison of quinoline ring mode frequencies and their interpretation for monomeric quinine and poly(quinine-*co*-HEA) polymer in various states.

Quinine Type	**State**	$\tilde{\nu}$ (cm^{-1})[a]	$\Delta\tilde{\nu}$ (cm^{-1})[b]	**Interpretation**
Monomeric Quinine	Dissolved	1390	-1	Quinoline ring-water interactions in monomeric quinine
poly(Quinine-*co*-HEA)	Dissolved	1389	-	Quinoline ring-water interactions in poly(quinine-*co*-HEA)
poly(Quinine-*co*-HEA)	Aggregated	1388	1	Possibly either weak π-stacking interactions between quinoline ring moieties in poly(quinine-*co*-HEA) or quinoline ring-water interactions
poly(Quinine-*co*-HEA)	Aggregated	1386	3	π-stacking interactions between quinoline rings of poly(quinine-*co*-HEA) and DNA nucleobases

[a] frequency of the protonated quinoline ring symmetric stretching mode

[b] frequency difference with respect to poly(quinine-*co*-HEA) polymer in solution

3.3.3 *Optimization of Delivery Performance*

I first screened the library of QCRs for their ability to deliver plasmids encoding for either luciferase or ZsGreen (a green fluorescent protein) to HeLa cells. I determined transfection efficiency by either measuring the total output of protein by a culture (luciferase) or by measuring the percentage of cells positive for ZsGreen. Interestingly, when quinine was copolymerized with an acrylamide, such as HEAm, Am, NIPAm, or DMAm, the resulting polyplexes were unable to achieve transgene expression (Fig. 3.16).

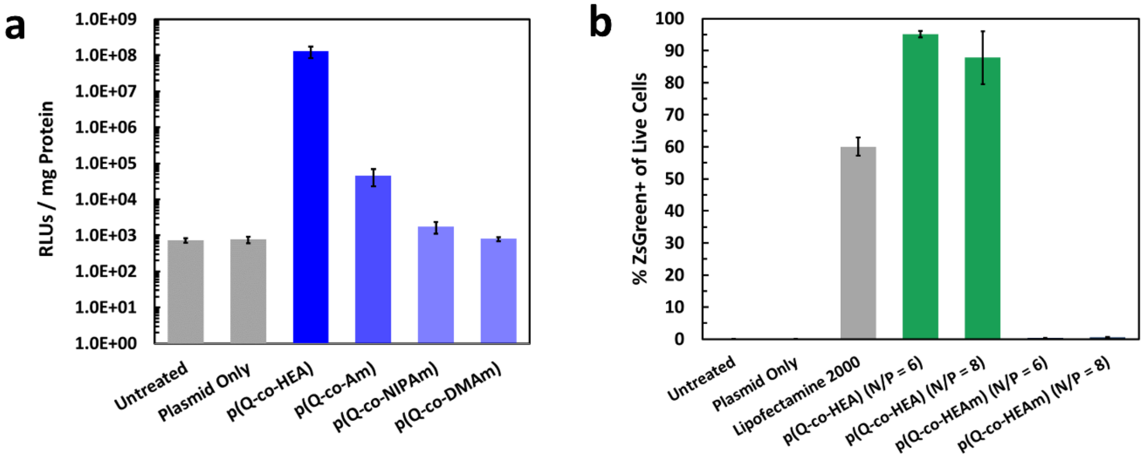

Figure 3.16. Transfection screens in HeLa cells comparing transfection efficiency of quinine copolymers with various hydrophilic comonomers. (a) Luciferase transfection assays showing ineffective transfection with poly(quinine-*co*-NIPAm), poly(quinine-*co*-DMAm), and poly(quinine-*co*-Am) (see Table 3.1 for polymer characteristics). (b) ZsGreen transfection assay comparing poly(quinine-*co*-HEA) and poly(quinine-*co*-HEAm) shows clear superiority of the acrylate copolymer in promoting transfection. Data represented as the mean ± SD (n = 3).

Poly(quinine-*co*-HEA), however, showed exemplary transfection efficiencies with both reporter plasmids and provided a 58% increase in ZsGreen expression efficiency as compared to the gold-standard commercial reagent Lipofectamine 2000 (Fig. 3.16). Upon finding a hit comonomer type, we determined the optimal molar ratio of quinine needed for transfection using a luciferase-based transfection screen with a small library of poly(quinine-*co*-HEA) copolymers containing between 3 and 17% quinine by molarity (Fig. 3.17). I found that the variant containing 14% quinine by molarity yielded at least threefold higher gene expression compared to the other variants (Figure. 3.16).

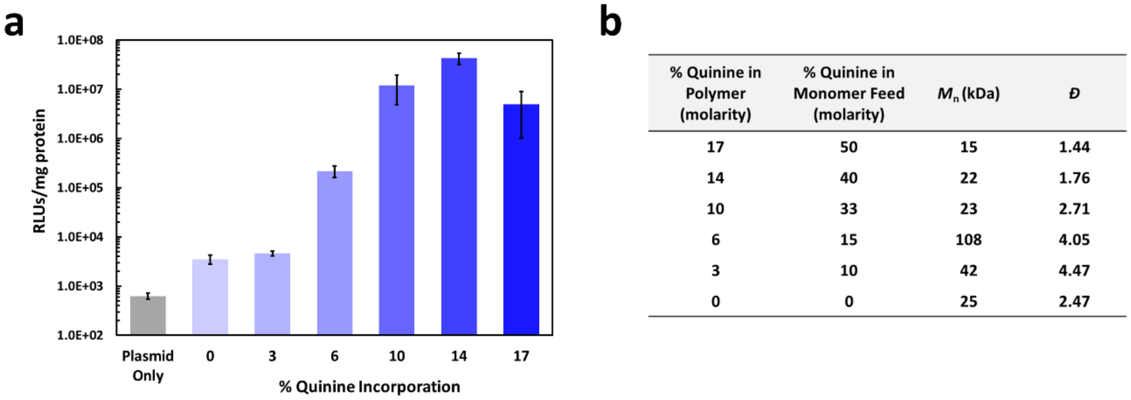

% Quinine in Polymer (molarity)	% Quinine in Monomer Feed (molarity)	M_n (kDa)	$Đ$
17	50	15	1.44
14	40	22	1.76
10	33	23	2.71
6	15	108	4.05
3	10	42	4.47
0	0	25	2.47

Figure 3.17. Effect of varying quinine incorporation in poly(quinine-*co*-HEA) on transfection efficiency. (a) Luciferase reporter transfection assay in HeLa cells with poly(quinine-*co*-HEA) with varying levels of quinine incorporation. Polyplexes were formed at N/P = 10. Data represented as the mean ± SD (n = 3). (b) Physical properties of poly(quinine-*co*-HEA) copolymers with varying degrees of quinine incorporation used in accompanying luciferase transfection assay (a). The percent quinine incorporation was determined via ^{1}H NMR as shown in Fig. 3.4. The M_n and $Đ$ was determined via aqueous SEC. The *dn/dc* of copolymers was calculated using eqn 3.4. with measured *dn/dc* values of quinine (0.266) and corresponding homopolymer pHEA (0.128).

Focusing on optimizing biological performance with the variant of poly(quinine-*co*-HEA) containing 14% quinine, I looked to the previous discovery of polyplex size control (Fig. 3.12d,e). By adding the polyplex solution to cells at specific periods along the aggregation time course, we could control the average diameter of polyplexes that the cells were exposed to during the transfection experiments and correlate its efficiency in transfection to particle size. Using quinine's endogenous fluorescence (Fig. 3.18), I used fluorescence microscopy to measure and track particles of various sizes in the intracellular space (Fig. 3.19-22).

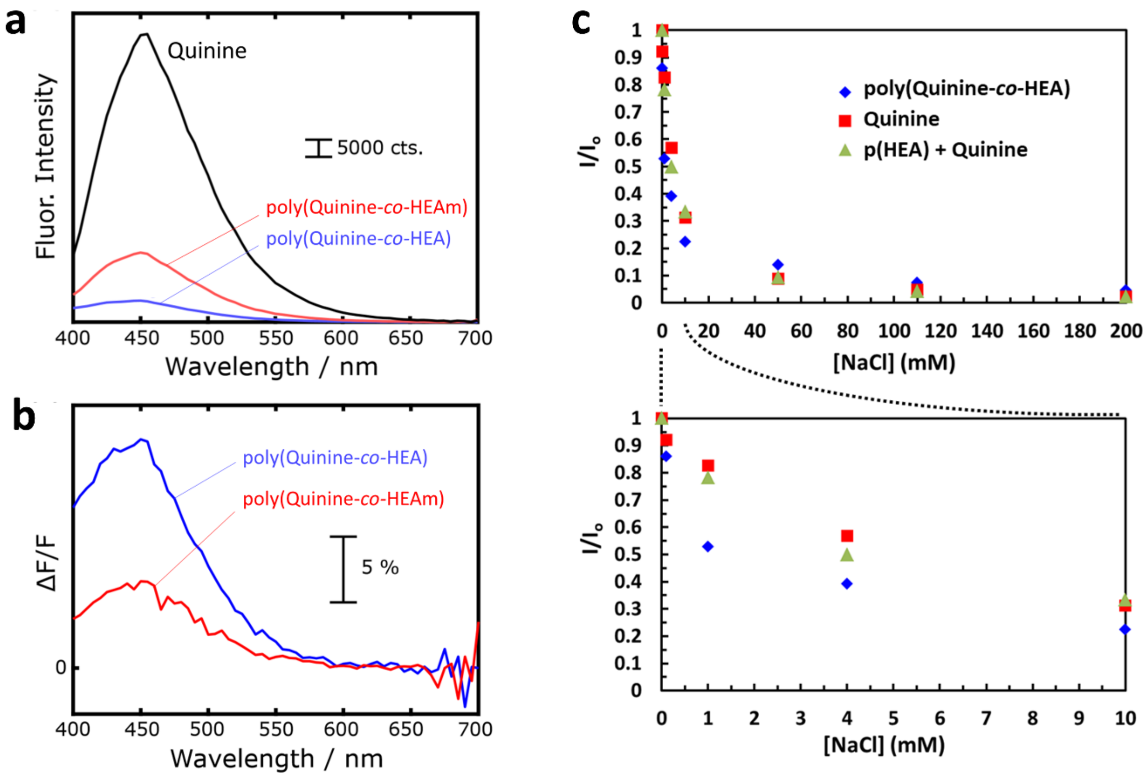

Figure 3.18. Fluorescence of quinine copolymers and its quenching by chloride. (a) The fluorescence spectra (λ_{ex} = 350 nm) of quinine was compared to those obtained with poly(quinine-*co*-HEA) and poly(quinine-*co*-HEAm) at equimolar concentrations of quinine (equivalent to the concentration of quinine moieties used in transfection). This reduction in fluorescence intensity of the copolymers is likely due to self-quenching by quinine repeat units.[151] (b) A difference spectrum of the compounds before vs after addition of plasmid (N/P = 6) shows a significant decrease in the fluorescence intensity upon introduction of DNA. This reduction in fluorescence is indicative of intercalation of quinine into DNA.[210] (c) Quenching of quinine fluorescence by chloride ions, under physiologically relevant concentrations, is dose-dependent for both quinine monomer and copolymers.[161] The dramatic decrease in fluorescence intensity of polyplexes outside the cell vs inside the cell can be explained, in part, by the concentration gradient that exists between the extracellular environment (cell media [Cl$^-$] = 110 mM) vs the intracellular space ([Cl$^-$] ~4 mM).

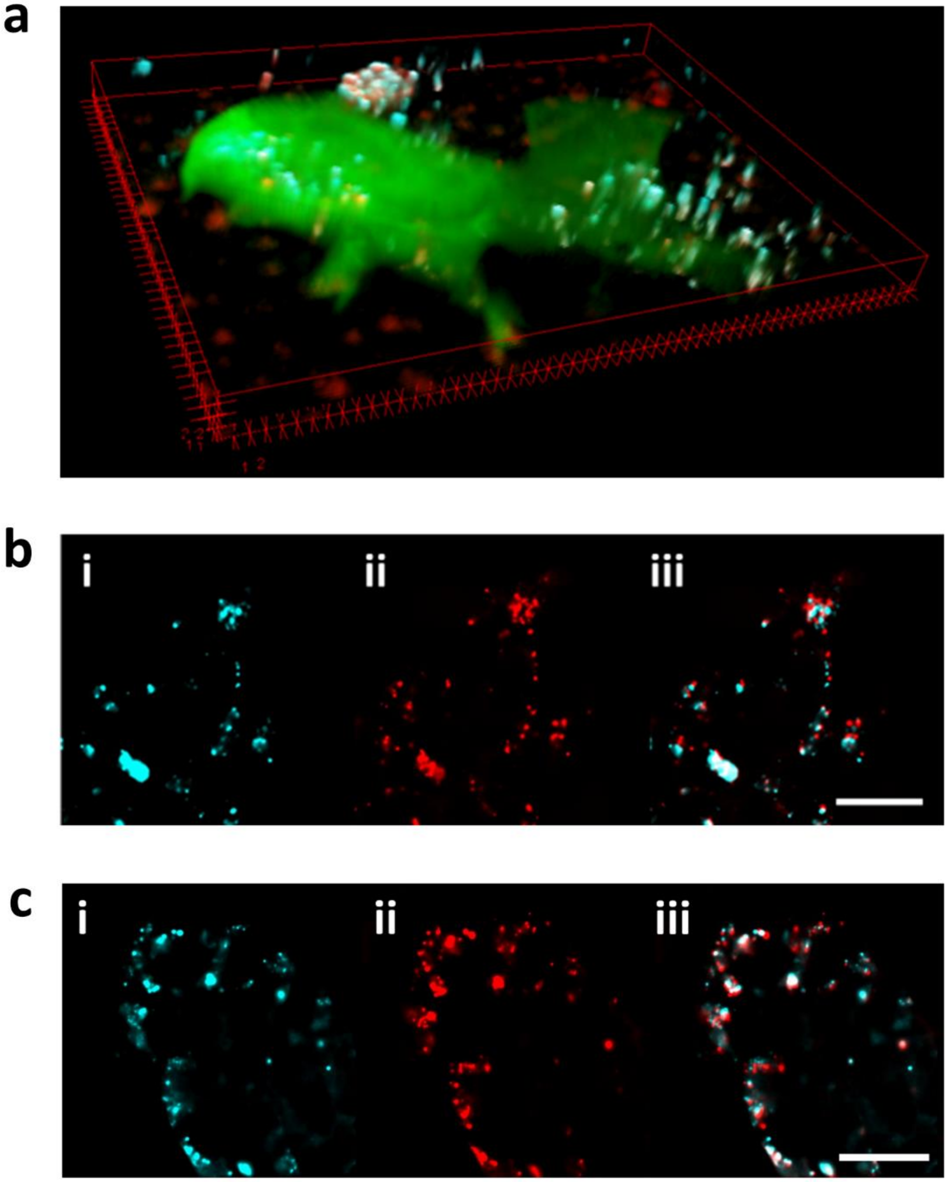

Figure 3.19. Internalization of cyanine 5 (Cy5)-labeled DNA and its colocalization with poly(quinine-*co*-HEA). (a) Three-dimensional image of live HEK 293T cells (100× magnification) 24 hrs post-transfection with poly(quinine-*co*-HEA) (blue) and Cy5-labelled plasmid (red) exhibiting ZsGreen expression (green). Dimensions: 81.92 μm × 81.92 μm × 3.84 μm. (b,c) Slices of z-stacked images produced with widefield fluorescence microscopy with deconvolution of live HEK 293T cells transfected at (a) 4 hrs and (b) 24 hrs prior to analysis. Component images include (i) poly(quinine-*co*-HEA), (ii) Cy5-labeled plasmid, and (iii) overlay image. Scale bar = 25 μm.

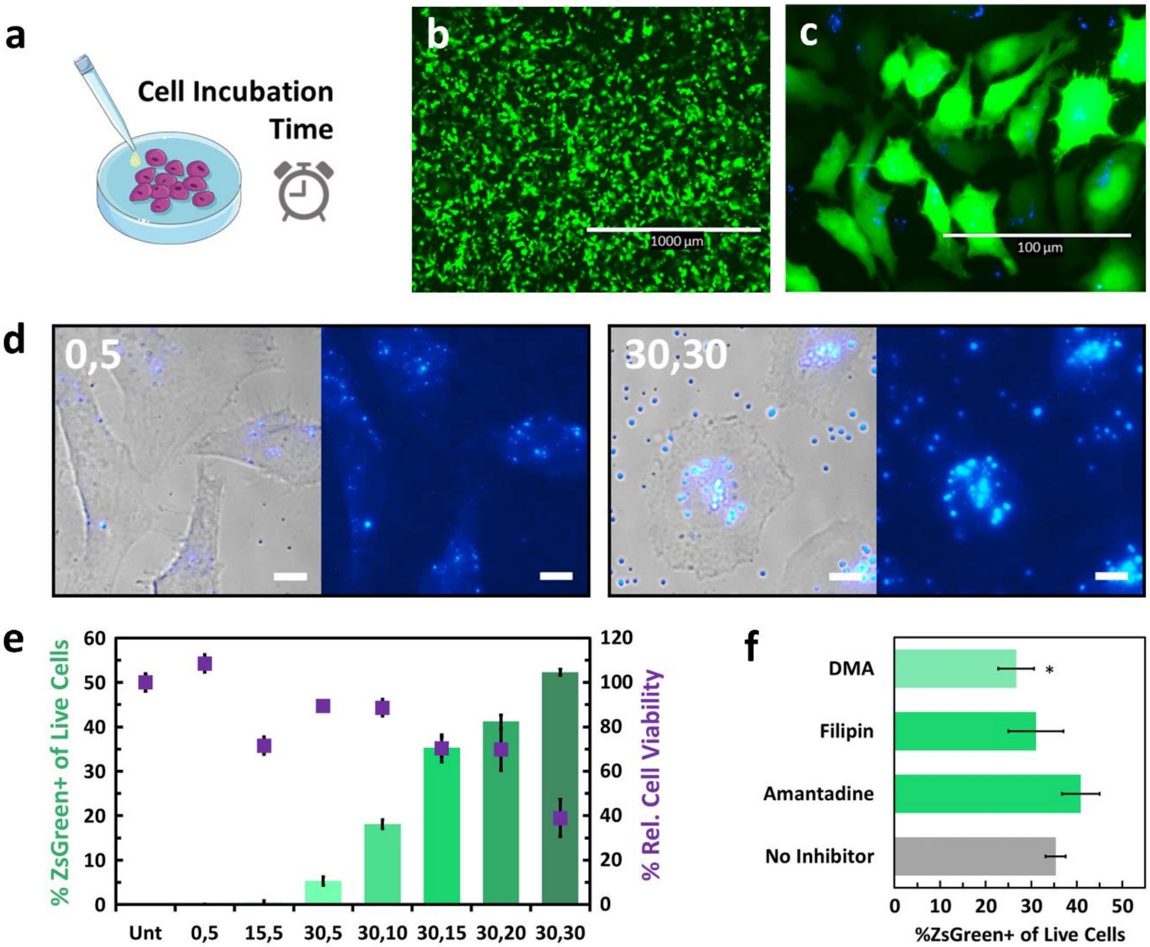

Figure 3.20. Fluorescence of intracellular polyplexes containing quinine and size-dependent activity. (a) After the *formulation time* (Fig. 312d) to achieve the desired mean particle diameter, the poly(quinine-*co*-HEA) polyplexes were incubated with HeLa cells for a defined time (defined as *cell incubation time*). (b, c) Images of fixed HeLa cells 48 h post-transfection with pZsGreen and poly(quinine-*co*-HEA) (N/P = 8) at (b) 4× magnification with poly(quinine-*co*-HEA) (blue) and (c) 40× magnification. (d) Images of HeLa cells fixed 6 h post-transfection with poly(quinine-*co*-HEA) at various formulation and cell incubation times. The sample names [*x*, *y*] are derived from *x* = formulation time (Fig. 3.12d) and *y* = cell incubation time (Fig. 3.F18a). The left image in each pair is an overlay of transmission and polymer (blue), and the right image is of polymer only. (Scale bars = 10 µm.) (e) Bar graph showing the percent transfection efficiency of live HeLa cells (as determined by flow cytometry) and relative cell viability (as determined by CCK-8 cell counting kit) 48 h post transfection. (f) HeLa cells transfected with the conditions shown for sample [30,15] in (e) were incubated with endocytosis inhibitors. Incubation with DMA (macropinocytosis inhibitor) gives a statistically significant reduction in transfection compared to no inhibitor indicating macropinocytosis contributes to successful transfection of aggregated polyplexes. Data for (e) and (f) are represented as the mean ± SD (n = 3); *$P < 0.05$.

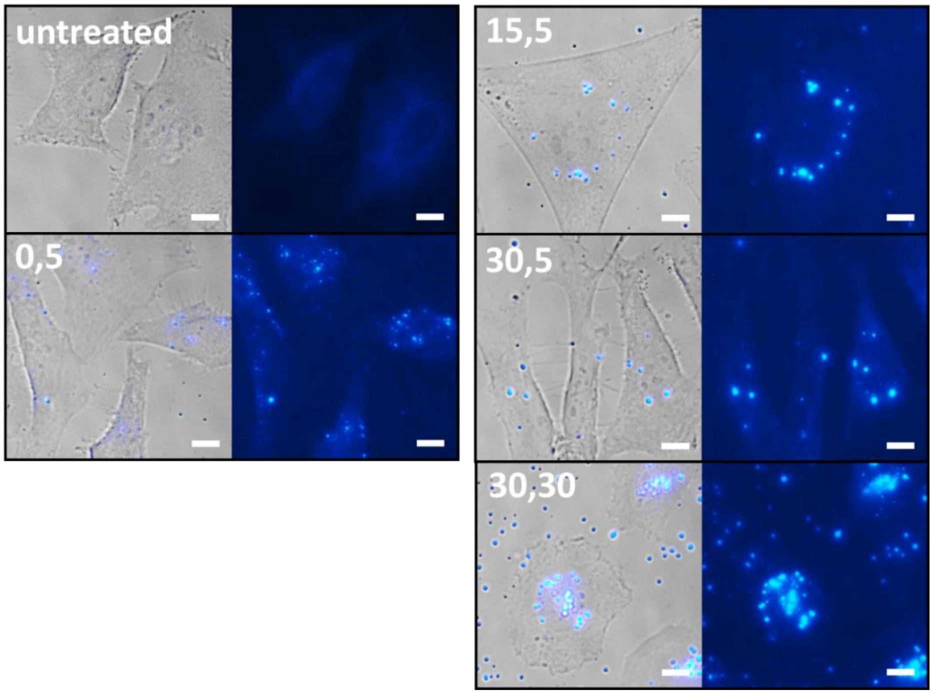

Figure 3.21. Widefield fluorescent images of HeLa transfected with poly(quinine-*co*-HEA) with various incubation parameters. The HeLa cells were fixed 6 hrs post-transfection with poly(quinine-*co*-HEA) at various formulation and cell incubation times. The sample names [*x*, *y*] are derived from *x* = formulation time (Fig. 3.12d) and *y* = cell incubation time (Fig. 3.18a). Left image in each pair is an overlay of transmission and polymer (blue), while the right image is of polymer only. Scale bar = 10 um.

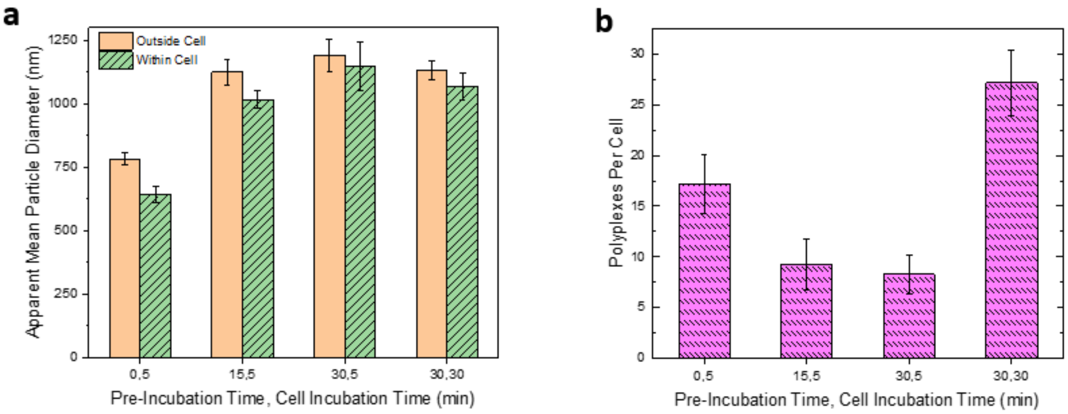

Figure 3.22. Imaging analysis of poly(quinine-*co*-HEA) polyplexes. (a) Mean particle diameter of poly(quinine-*co*-HEA) polyplexes both in and outside of cells at various incubation periods. (b) Dependence of incubation period on polyplex particle count determined via optical microscopy. Data represented as the mean ± SD (n = 3).

In collaboration with undergraduate student Andy Schmitz, we determined the calculated mean diameters of the internalized particles in the wide-field images were similar to the hydrodynamic diameters measured via DLS for the corresponding formulation time (Fig. 3.22a). In addition, microscopy verified that increased cell incubation times led to an increase in internalized particles (Fig. 3.22b). I measured the transfection efficiency with ZsGreen for each timeframe and observed that both particle size and number of internalized particles positively correlated to ZsGreen expression efficiency as well as cytotoxicity (Fig. 3.20e). Indeed, a fine balance between transfection performance and cytotoxicity in this system existed and can be tailored by controlling the incubation periods that affect both polyplex size and number of particles internalized by cells. This tight control allowed for differential transgene delivery to target cell populations without introducing variability into cargo load.

To understand why large particles enabled higher transfection efficiencies, I investigated which internalization mechanism was the greatest contributor to transgene expression of large particles by inhibiting different modes of endocytosis with small-molecule inhibitors. I probed clathrin-mediated endocytosis, caveolae-dependent endocytosis, and macropinocytosis with the inhibitors amantadine, fillipin III, and 5-(N,N-dimethyl)amiloride hydrochloride (DMA), respectively (Fig. 3.20f). A decrease in transfection efficiency for DMA-treated cells suggested that macropinocytosis contributed as an internalization route of poly(quinine-*co*-HEA) polyplexes that led to gene expression. It is possible that aggregation of the polyplexes allowed the polyplexes to bypass unproductive endocytic routes limited to smaller size capacities.[264, 265]

3.3.4 *Efficient Transfection in Multiple Cell Types*

Efficient transgene delivery is a challenge in many cell-focused investigations, particularly in experiments involving primary or transfection-resistant cell types important for research and cell therapy development. To explore the utility of the QCR poly(quinine-*co*-HEA) variant containing 14% quinine in overcoming this barrier in other cell types, I identified the N/P ratios that balanced efficient delivery of a ZsGreen fluorescent reporter plasmid with minimal cytotoxic effects. Excellent delivery performance with poly(quinine-*co*-HEA) was achieved with transfection-amenable adherent cell types such as HEK 293T (Fig. 3.23a and Fig. 3.24a) and HeLa (Figs. 3.20 and Fig. 3.23a). In HEK 293T cells, I observed high transfection efficiency (≥92% ZsGreen+) at N/P ≥ 6 (Fig. 3.23a and Fig. 3.24a), which is the minimum N/P ratio needed for full compaction of DNA (Fig. 3.9 and Fig. 3.13). In comparison, Lipofectamine 2000 demonstrated a lower transfection efficiency (48%) but higher relative cell viability (93%; Fig. 3.23c and Fig. 3.24b). Next, I assessed its application in a suspension cell type (lymphoblast line K562) by increasing complex dose to account for decreased surface area in suspension cells. We found that the transfection efficiencies achieved with QCR poly(quinine-*co*-HEA) at an N/P = 6 and 8 (5.1 and 5.8%, respectively) in K562 cells exhibited a threefold improvement over Lipofectamine 2000 (1.8%) (Fig. 3.23b and Fig. 3.F25). Indeed, these results support previous work that sedimentation of polyplexes onto the cell surface (Fig. 3.20) aids optimal transgene delivery.

Next, Keith and I tested the efficacy of poly(quinine-*co*-HEA)–mediated gene delivery in keratinocytes, a transfection-resistant cell type that is a vital component in the upper layer of the skin and important to the modeling and treatment of genetic skin disorders such as epidermolysis bullosa. Gene editing of keratinocytes, performed for autologous transplants to repair diseased and damaged skin, have primarily relied on viral vectors due to their high transfection efficiency.[266-268] Viral vectors, however, are severely restricted in cargo capacity (i.e., adeno-associated viruses are limited to ~4.7 kb of cargo), which limits their ability to deliver large therapeutic proteins or gene editing machinery (see *Section 1.1.2*). In addition, common nonviral alternatives have proven to be inefficient in transfecting keratinocytes.

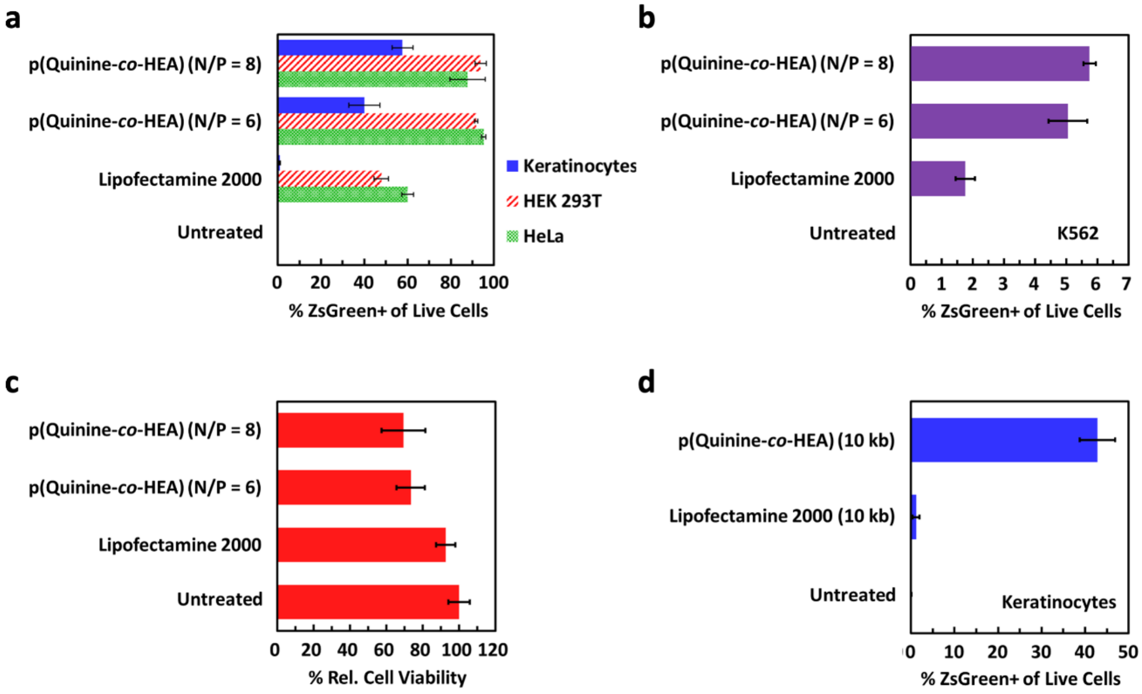

Figure 3.23. QCR variant of poly(quinine-co-HEA) containing 14% quinine efficiently transfects a variety of cell types. (a,b) The transfection efficiency in the delivery of pZsGreen (4.7-kb plasmid) to adherent cell lines (HeLa and HEK 293T), keratinocytes, and suspension cell line K562 was improved significantly by using poly(quinine-*co*-HEA) compared to Lipofectamine 2000 as determined by flow cytometry 48 h post-transfection. (c) The cell viability of HEK 293T cells was determined 48 h post-transfection via CCK-8 assay. (d) Efficient transfection of keratinocytes using a large plasmid (10 kb, pZsGreen) was maintained using poly(quinine-*co*-HEA). Data in (a-d) are represented as the mean ± SD (n = 3).

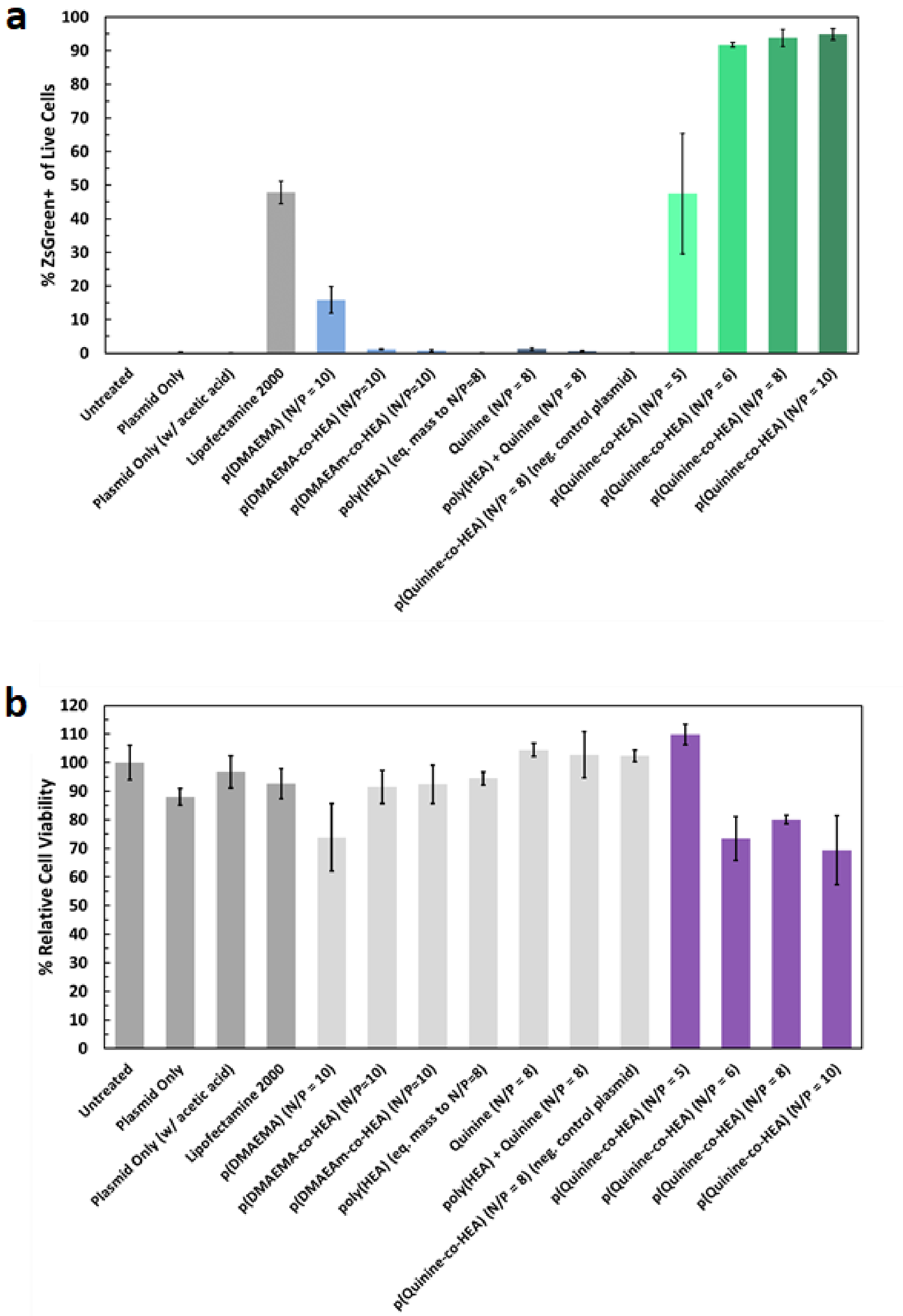

Figure 3.24. ZsGreen reporter transfection screen in HEK 293T with all controls. (a) Transgene expression assay, including all controls, measured with flow cytometry 48 hours post-transfection (same assay as shown in Fig. 3.23a). (b) Cell viability assay, including all controls, measured with CCK-8 after 48 hours post-transfection (same assay as shown in Fig. 3.23c). Data represented as the mean ± SD (n = 3).

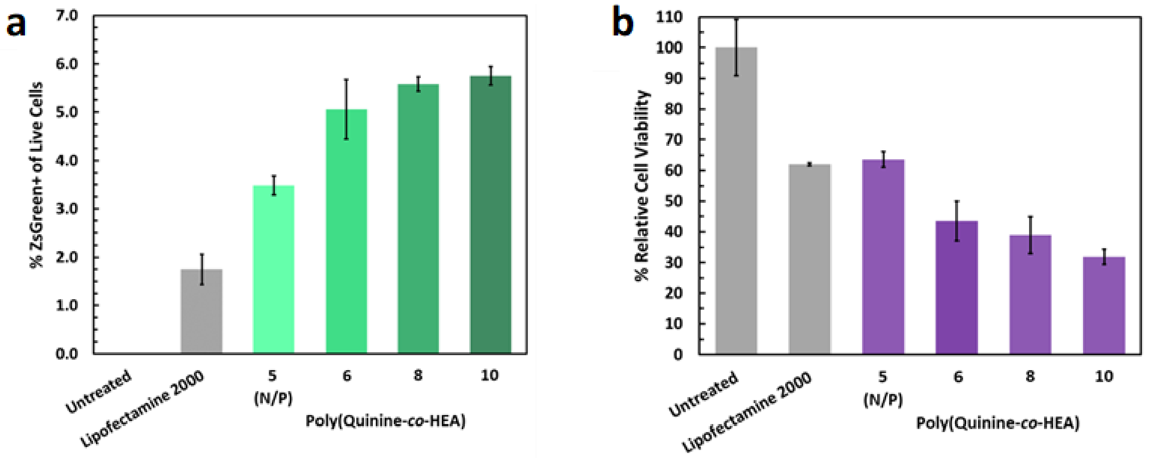

Figure 3.25. ZsGreen reporter transfection screen in K562 with all controls. (a) Transgene expression assay, including all controls, measured with flow cytometry 48 hours post-transfection (same assay as shown in Fig. 3.23b). (b) Cell viability assay, including all controls, measured with CCK-8 after 48 hours post-transfection. Data represented as the mean ± SD (n = 3).

We performed a ZsGreen transfection in this cell type (Fig. 3.23a) with Lipofectamine 2000 and found poor transfection efficiencies (<1% ZsGreen+) that corroborated the results seen in literature (0 to 4% transfection efficiency).[269-271] Efficient transfection could be achieved, however, with the poly(quinine-*co*-HEA) (58% ZsGreen+ for N/P = 8). Interestingly, we also performed a transfection with a plasmid double in size (10 kb; Fig. 3.23d), which yielded 43% ZsGreen+ cells after transfection with poly(quinine-*co*-HEA) as compared to only 1.2% for Lipofectamine 2000. These results demonstrated the versatility of this vehicle for diverse and transfection-resistant cell types as well as large gene payload sizes relevant to numerous challenging diseases (i.e., dystrophin for muscular dystrophy treatment and collagen for genetic skin diseases).

3.3.5 *HEA Facilitates Decompaction of DNA in the Presence of Protein*

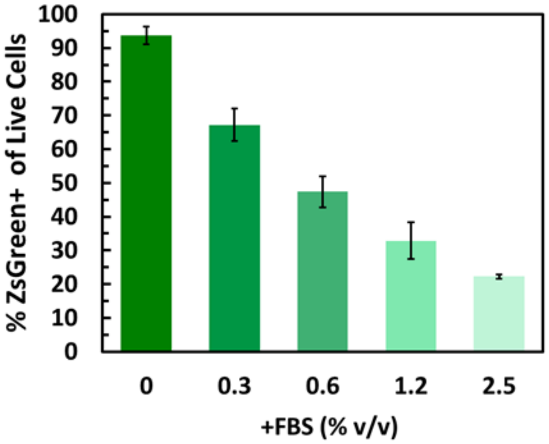

Figure 3.26. Effect of protein on transfection efficacy. HEK 293T cells were transfected with pZsGreen and poly(quinine-*co*-HEA) (N/P = 8). After diluting the polyplexes with serum-free DMEM, FBS was added to the mixture prior to its incubation with cells. Increasing concentrations of FBS in the transfection media led to reductions in transfection efficiency in a dose-dependent manner. Data represented as the mean ± SD (n = 3).

I hypothesized that the interplay between polymer binding to DNA and release of the cargo plays an important role in the excellent performance of the QCR poly(quinine-*co*-HEA). It has been shown known that, for in vivo applications, protein binding can cause premature unpackaging of polyplexes.[257] Consistent with this, I observed that titrating increasing amounts of fetal bovine serum (FBS) into poly(quinine-*co*-HEA) polyplex solutions prior to transfection leads to a dose-dependent decrease in transgene expression (Fig. 3.26). I recognized, however, that for important ex vivo cell therapy applications, serum-free media can be used during transfection. Thus, exposure to protein can be limited to the intracellular space (after endocytosis), which could be an important factor to stimulate the unpackaging of polyplexes. To examine the influence of protein binding, I added FBS to polyplex solutions diluted in cell media and monitored their unpackaging using a dye-exclusion assay (Fig. 3.12b). Upon addition of FBS, the pDNA bound by poly(quinine-*co*-HEA) decomplexed by over threefold more than poly(DMAEMA). When the acrylate in the copolymer (HEA) was replaced with an acrylamide analog (HEAm), this dramatic decomplexation by FBS was eliminated. This result indicated that the acrylate in poly(quinine-*co*-HEA) facilitates polymer binding to protein, which also leads to pDNA unpackaging. This finding is supported by DLS (Fig. 3.9b) and by work from Zhao et al., who observed higher levels of serum binding to the HEA polymer brushes compared to the acrylamide analog due to decreased surface hydration.[272-274] This investigation supported the hypothesis that while quinine is needed for efficient binding of pDNA outside the cell, the HEA comonomer facilitates pDNA release from polyplexes upon exposure to intracellular protein.

3.3.6 *Raman Imaging Verifies Protein-Induced Unpackaging Within Cells*

The utility of the inherent reporting properties of poly(quinine-*co*-HEA) was highlighted by confocal Raman microscopy tracking experiments that quantify quinine deintercalation and further support the hypothesis that proteins facilitate polyplex unpackaging inside cells. Punihaole and I performed confocal Raman imaging to monitor the quinine–pDNA binding within poly(quinine-*co*-HEA) polyplexes, and we were able to correlate the presence of protein within the polyplexes to pDNA unpackaging during the transfection process. To do this, I treated HeLa cells with poly(quinine-*co*-HEA) polyplexes and fixed them for Raman hyperspectral imaging 4, 24, and 48 h after transfection. Each pixel in these hyperspectral images contained a Raman spectrum that roughly spanned a region from 900 to 1,800 cm^{-1} (Fig. 3.27). Punihaole analyzed these hyperspectral images using

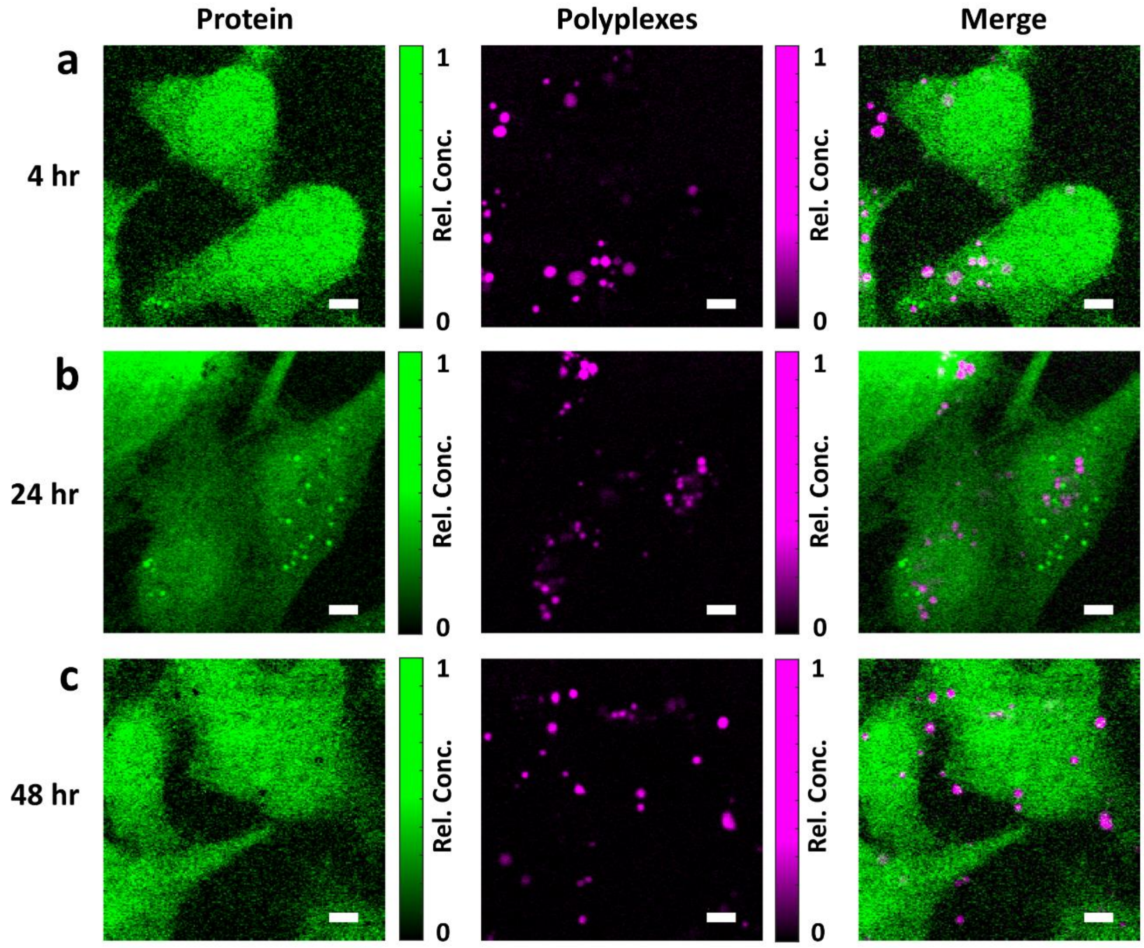

Figure 3.27. Representative Raman images of HeLa cells and QCR polyplex particles after (a) 4 hr, (b) 24 hr, and (c) 48 hr post-transfection. Cells (green) were visualized using the integrated intensity of the protein Amide I band (1,660 cm^{-1}), while polyplex particles (magenta) were visualized by the quinoline ring mode of quinine (1,369 cm^{-1}). The overlay of these images shows the presence of both intracellular and extracellular particles at all timepoints. (Scale bars = 5 μm.)

principal component analysis (PCA) in order to identify spectroscopic signatures of polyplex dissociation (Figs. 3.28 and 3.29). Figure 3.28 shows representative loading vectors and score maps obtained from our analysis of the Raman hyperspectral images. In the analysis, Punihaole considered the first ten PCs for each hyperspectral image and generally found that the first three or four PCs exhibited loading vectors that contained physically meaningful Raman spectral features. For example, the first four PCs showed spectral features that were readily assigned to distinct chemical species, such as CH_2 deformation modes from glycerol (PC 1 and 2; 1465 cm^{-1}) and lipids (PC 4; 1447 cm^{-1}). The loading vectors corresponding to PCs 1 and 3 contained spectral features that were assigned to packaged and unpackaged poly(quinine-*co*-HEA) polyplexes, respectively. In the case of PC 1, the quinoline ring mode appeared at 1369 cm^{-1} and was assigned to intercalated quinine moieties in poly(quinine-*co*-HEA) polyplexes that are engaged in π-stacking interactions with DNA nucleobases. In PC 3, the quinoline ring mode was upshifted 3 cm^{-1} to 1372 cm^{-1}, which matches the frequency shift that occurs due to the deintercalation of quinine from DNA (c.f. Table 3.2).

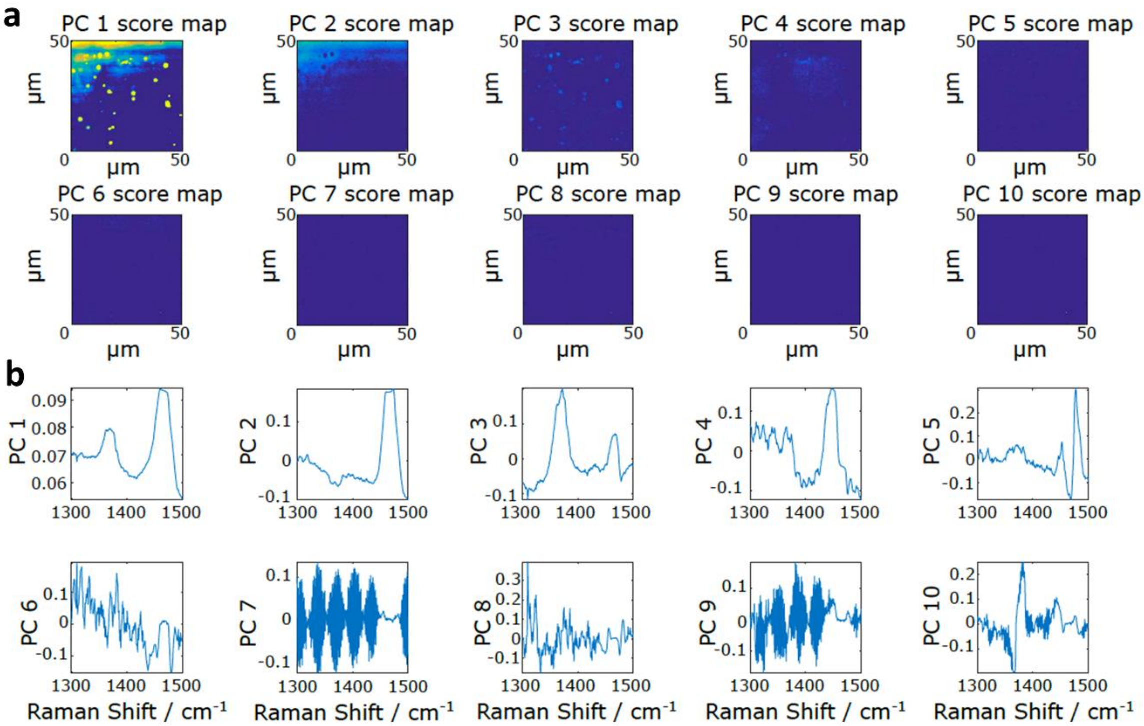

Figure 3.28. Representative results from PCA of Raman hyperspectral images. (a) The score maps and (b) corresponding loading vectors for the first ten PCs are shown for HeLa cells that were imaged after fixation 48 h post-transfection.

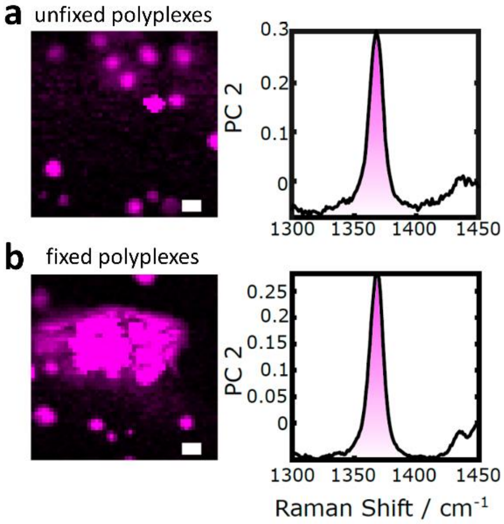

Figure 3.29. Raman images and PC loading vectors of fixed poly(quinine-*co*-HEA) polyplexes. Polyplexes were (a) unfixed and (b) fixed by treatment with 4% (v/v) formaldehyde. The PC loading vectors for both samples show that the frequency of the quinoline ring mode is 1369 cm^{-1} for both samples, indicating that formaldehyde fixation does not perturb the structure of polyplexes. Scale bars = 2 μm.

Additionally, we performed PCA on the Raman hyperspectral images of polyplex samples (no HeLa cells present) to rule out the possibility that formaldehyde fixation gave rise to the spectral features observed in the PC 3 loading vectors (Fig. 3.29).

All of the images that were analyzed contained at least one principal component (PC) whose loading vector showed the quinoline ring mode at 1,369 cm^{-1} (Fig. 3.30a,b), which was indicative of the quinine moieties in poly(quinine-*co*-HEA) intercalating into DNA. However, in the 48-h post-transfection images shown in Fig. 3.27c, we identified PCs whose loading vectors showed quinoline ring modes that were upshifted to 1,372 cm^{-1} (Fig. 3.30a,b), which signaled the deintercalation of quinine from pDNA. The PC score maps in Fig. 3.30a,c were used to determine the percent deintercalation of quinine moieties (Fig. 3.37), which allowed for the degree of polyplex unpackaging to be quantified (Fig.

3.30f). On average, we observed that roughly 10 to 30% of quinine moieties were deintercalated from DNA in the polyplexes shown in Fig. 3.27c. However, our analysis allowed us to observe unpackaging heterogeneities not only between but also within the particles themselves. For example, while many particles exhibited a fairly uniform unpackaging landscape, some particles showed most of their unpackaging on the exterior, giving rise to ring-shaped patterns (Fig. 3.30f, Inset). The presence of these ring-shaped patterns suggests that the unpackaging of the DNA suffuses from the outside in, akin to surface erosion.

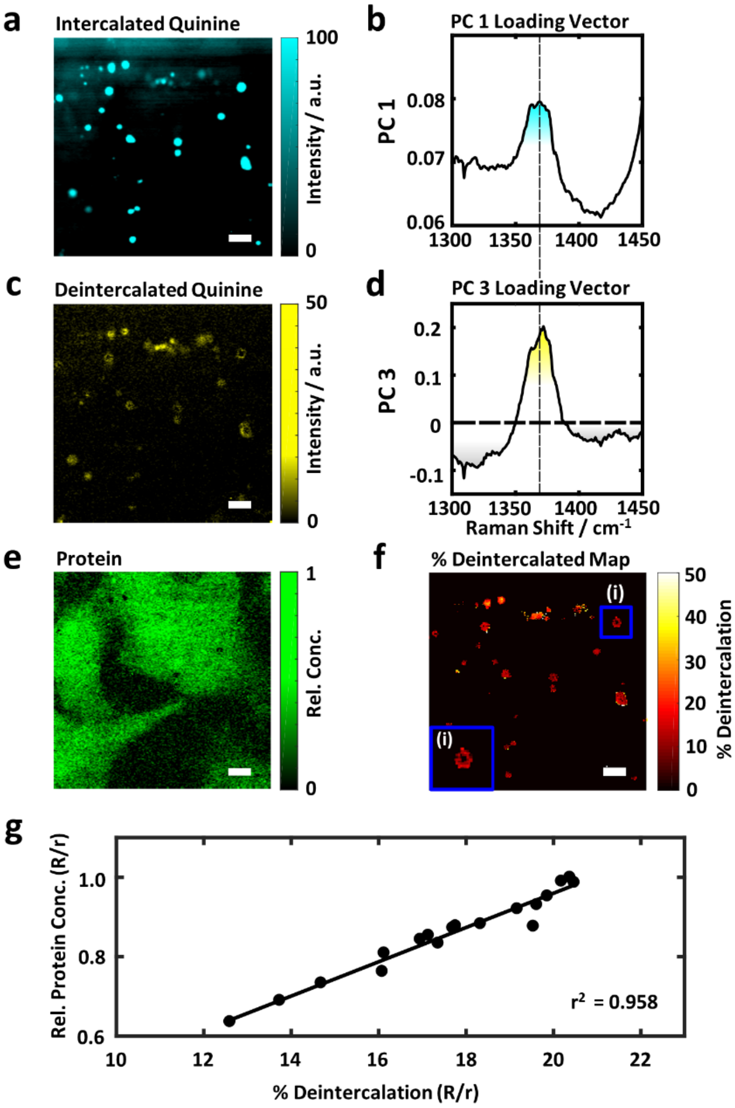

Figure 3.30. Results from PCA of Raman hyperspectral images for HeLa cells 48 h post-transfection. (a) PC 1 score map showing the relative concentration of quinine moieties in poly(quinine-*co*-HEA) polyplexes that are DNA-intercalated. (b) PC 1 loading vector showing the 1,369-cm^{-1} quinoline ring stretching mode spectral signature indicative of quinine–DNA intercalation. (c) PC 3 score map showing the relative concentration of quinine moieties in polyplexes that are deintercalated from pDNA. (d) PC 3 loading vector showing the 1,372-cm^{-1} quinoline ring stretching mode indicative of quinine deintercalation. (e) Raman image showing the relative concentration of protein distributed in the cells. The PC score maps shown in (a) and (c) were used to determine (f) the percent deintercalation for every pixel of the polyplex particles. (f, inset) A magnified region containing a polyplex with a ring-shaped unpackaging behavior. (g) Correlates the percent deintercalation with respect to the relative concentration of protein as a function of the normalized distance (R/r) from the centroids of polyplex particles inside cells (see Fig. 3.31). Scale bars = 5 µm.

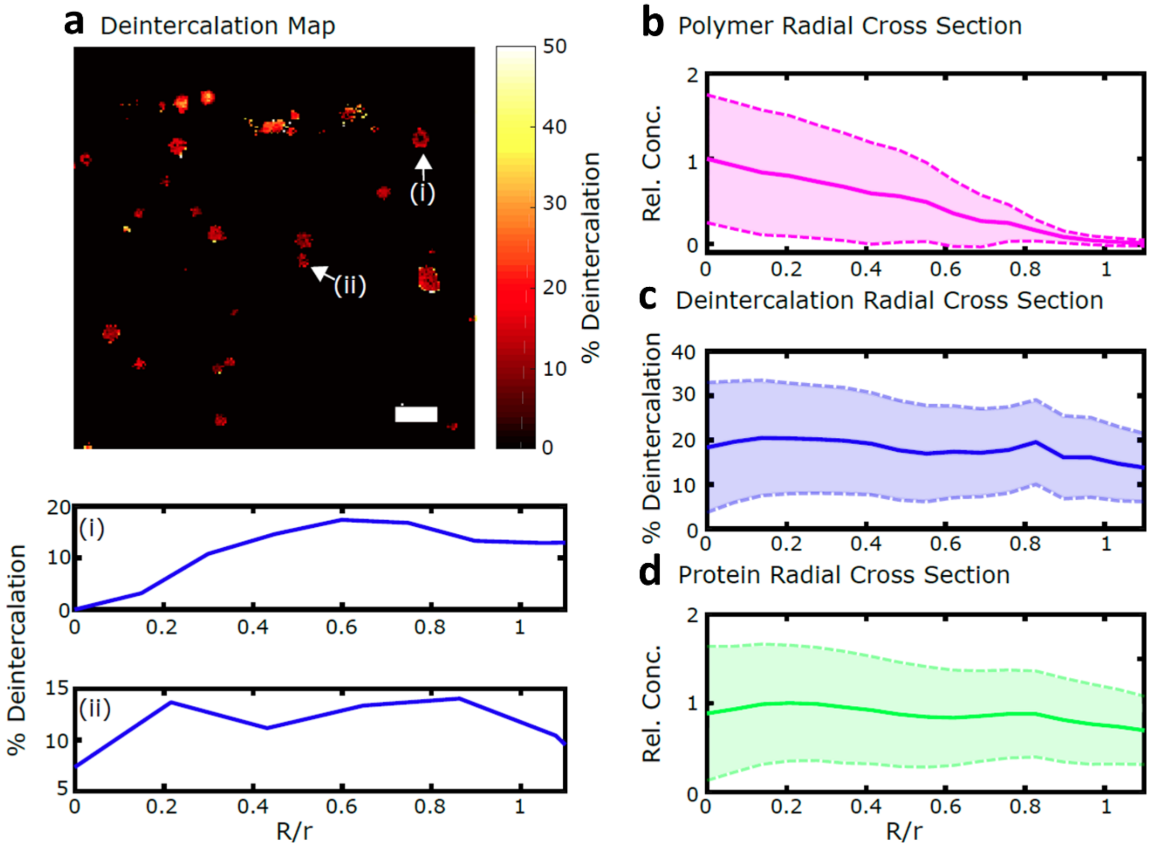

Figure 3.31. Radially-averaged cross sections quantifying the distribution of polymer, percent deintercalated quinine moieties, and protein for polyplex particles in HeLa cells after 48 hrs post-transfection. (a) Deintercalation map show the percent deintercalated quinine moieties of poly(quinine-*co*-HEA) polymers for polyplex particles. Panels (i) and (ii) show the radially-averaged cross sections of two different polyplexes with respect to the percent deintercalation. The radially-averaged cross sections quantify the relative concentration of (b) polymer, (c) deintercalated quinine moieties, and (d) protein for all polyplex particles colocalized with cells. Scale bars = 5 μm.

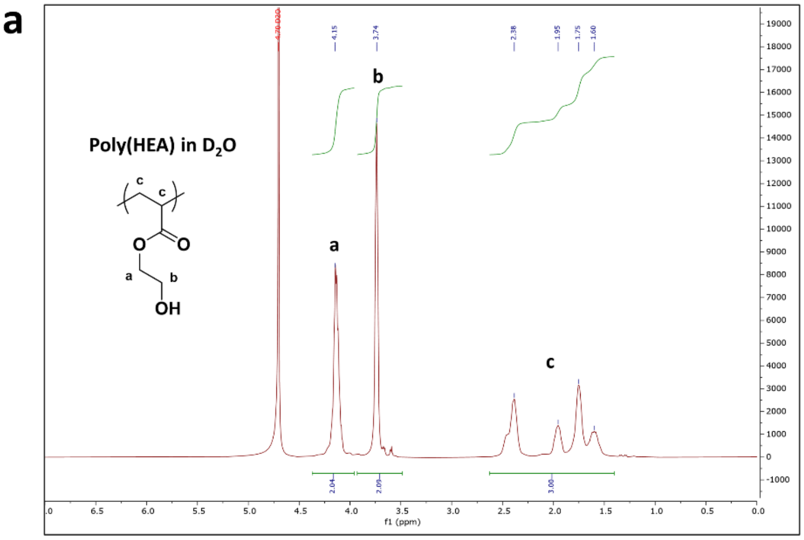

b

Solvent	pH	% Hydrolysis after 1 hr	% Hydrolysis after 72 hrs
NaOH in D_2O	13.5	78	97
PBS in D_2O	7.0	0	0
D_2O	5.3	0	0
TFA in D_2O	2.3	0	5

Figure 3.32. The dependence of poly(HEA) hydrolysis in terms of pH as determined with ^{1}H NMR. (a) A representative ^{1}H NMR spectra of poly(HEA) in D_2O is shown. The integration of methylene protons closest to the ester group was monitored in relation to the protons on the hydrolysis-resistant backbone of the polymer. b) The percent of hydroxyethyl pendant group hydrolysis was quantified at variety of pH values soon prior and post incubation at 37 °C. As expected, our positive control in basic conditions showed rapid hydrolysis within minutes, but no other solution showed significant levels of hydrolysis (> 5%) after 72 hrs. These results showed that the acid-catalyzed hydrolysis of the pendant groups would be negligible in the mildly acidic conditions encountered in the cell.

In order for the particles to undergo unpackaging from the surface inward there is likely some component in the intracellular milieu that is facilitating unpackaging. It is unlikely that the unpackaging of the polyplexes is facilitated by hydrolysis of the HEA pendant groups since HEA is stable within the intracellular pH range encountered by polyplexes (Figure. 3.32). Instead, our dye-exclusion results (Fig. 3.12b) indicated that intracellular proteins are likely causing polyplex unpackaging. If this were the case, we would expect to observe a correlation between the concentration of protein and pDNA deintercalation in the polyplex particles. To investigate this, we calculated the radially averaged cross-sections of all of the individual particles to quantify the distribution of poly(quinine-*co*-HEA), pDNA unpackaging, and proteins as a function of distance inside the polyplexes (Fig. 3.31). The radial cross-section of the relative polymer concentration decreased monotonically from the centroid of the particles. In contrast, the radial cross-sections corresponding to the deintercalation of poly(quinine-*co*-HEA) from pDNA and the relative protein concentration do not follow this monotonic behavior but instead mirrored each other. In fact, as indicated in Fig. 3.30g, the relative concentration of protein colocalized with polyplex particles is strongly correlated ($r^2 = 0.958$) with the percentage of poly(quinine-*co*-HEA) quinine moieties that are deintercalated from the DNA cargo. This remarkable linear correlation indicates that proteins dominate the unpackaging of the poly(quinine-*co*-HEA) polyplexes inside the cells. Despite the heterogeneity observed between the different particles, the radial cross-sections (Fig. 3.31) show that, on average, proteins are distributed throughout the polyplexes and are strongly colocalized with deintercalated quinine moieties of poly(quinine-*co*-HEA) polymer chains. Our unique combination of chemical vector design and Raman chemical imaging reveals that polyplexes are porous inside cells. Indeed, this quality enables proteins to percolate into the polyplexes, there by unwrapping pDNA (Fig. 3.1e) for highly efficient transcription.

3.4 Concluding Remarks

In summary, I developed a polymeric gene delivery platform that capitalizes on the natural abundance and unique chemical and spectroscopic properties of quinine. The synthetic approach to create QCRs uses a facile free-radical polymerization reaction that is inexpensive and scalable, making it ideal for industrial manufacture and applications. The QCR poly(quinine-*co*-HEA) performed as a robust delivery vehicle of pDNA in vitro and achieves efficient transgene expression across a variety of human cell types, including keratinocytes. In comparison to more conventional cationic polymers, the excellent transfection performance of this QCR can be partially attributed to two key properties. The first is that the QCR packages DNA cargo through both electrostatic interactions and intercalation, which robustly stabilizes polyplex formulations during the transfection process. The second key property is that the interaction of proteins with the QCR facilitated the release of pDNA cargo inside cells. These two critical attributes gave the QCR the proper balance between polyplex stability and cargo release to allow for increased transgene expression efficiency for clinical gene therapy applications. The well-characterized sensitivity of quinine's vibrational modes to its local chemical environment enabled our team to exploit the chemical sensitivity encoded in Raman spectra to quantify the degree of polyplex unpackaging. In comparison to fluorescence-based methods, Raman imaging was particularly well-suited to quantify intracellular protein concentrations without the need for labeling. Punihaole and I employed this method to elucidate the contribution that proteins play in promoting unpackaging of a quinine-based polycationic transfection system. Our findings support the long-standing speculation that intracellular proteins can contribute to the release of DNA from polyplexes.[64] The Raman chemical imaging approach applied in this work can be applied broadly to other functional materials containing quinine and also serves as a foundation for chemical imaging of nonquinine-containing materials in situ. Many functional biomaterials contain large numbers of endogenous Raman-active probes such as carbonyl, amide, nitrile, and other functional groups that, like quinine, are sensitive to their local chemical environment and can be probed by this technique. This work highlighted both the potential of using QCRs as a trackable therapeutic platform and the promise of Raman-based chemical imaging methods to yield unprecedented insights into monitoring interactions of biomaterials in situ.

3.5 Experimental

3.5.1 *Materials*

3.5.1.1 Synthesis

The monomers 2-hydroxyethyl acrylate (HEA), N-hydroxyethyl acrylamide (HEAm), N,N-dimethylacrylamide (DMAm), N-isopropylacrylamide (NIPAm), and 2-(dimethylaminoethyl) methacrylate (DMAEMA); the chain transfer agent 4-cyano-4-[(dodecylsulfanylthiocarbonyl)sulfanyl]pentanoic acid (CDP); the initiatorsazobisisobutyronitrile (AIBN) and 4,4'-azobis(cyanovaleric acid) (V-501); and the endocytosis inhibitors amantadine hydrochloride, filipin III from *Streptomyces filipinensis*, and 5-(N,N-dimethyl)amiloride hydrochloride (DMA) were purchased from Sigma-Aldrich (St. Louis, MO). Quinine (anhydrous, 99% total base with ≤ 5% dihydroquinine) was purchased from Alfa Aesar (Tewksbury, MA). All chemicals were used as received unless mentioned otherwise. All solvents were ACS grade. Dialysis tubing (M_w cut-off = 1 kDa) was purchased from Spectra/Por, treated with 0.1 wt % ethylenediaminetetraacetic acid (EDTA) solution, stored in ~0.05 wt % sodium azide solution, and triple rinsed with distilled water before use.

3.5.1.2 Polyplex/Transfection Reagents

The pZsGreen (4.7 and 10 kb), gWiz-luc, and pCMV-lacZ plasmids were purchased from Aldevron (Fargo, ND). CCK-8 cell counting kit was purchased from Dojindo Molecular Technologies (Rockville, MD). Lipofectamine 2000, propidium iodide (PI, 1.0 mg/mL solution in water), PicoGreen (Quant-iT PicoGreen, dsDNA reagent), UltraPure ethidium bromide (10 mg/mL), methanol-free formaldehyde (16% w/v), and Pierce BCA Protein Assay Kit was purchased from ThermoFisher Scientific (Waltham, MA). Cy-5 labeled pZsGreen plasmid was used as prepared in a previous study by Tan et al.[105] Luciferase Assay System with lysis buffer was purchased from Promega (Madison, WI).

3.5.1.3 Cell Culture Reagents

Dulbecco's Modified Eagle Medium (DMEM; high glucose, pyruvate, and Glutamax supplemented), Fluorobrite DMEM (phenol red-free media), Iscove's Modified Dulbecco's Medium (IMDM), Reduced Serum Medium (Opti-MEM), Defined Keratinocyte Serum-Free Media (K-SFM) with Growth Supplement, Trypsin-EDTA (0.05%) with and without phenol red, phosphate buffered saline (PBS) pH = 7.4, UltraPure DNAse/RNAse-Free distilled water (DI H_2O) Antibiotic-Antimycotic (100×), Gentamicin/Amphotericin (500×), and heat-inactivated fetal bovine serum (HI FBS) were purchased from Life Technologies-ThermoFisher Scientific (Carlsbad, CA).

3.5.1.3 Cell Lines

Human cervical carcinoma cells (HeLa, ATCC CCL-2) were purchased from ATCC (Manassas, VA). Human embryonic kidney cells (HEK 293T) were received as a gift from the laboratory of Mark Osborne at the University of Minnesota. Chronic myelogenous leukemia lymphoblasts (K562) were received as a gift from the laboratory of Jennifer Adair at the Fred Hutchinson Cancer Research Center. Immortalized keratinocytes (N/TERT) were received as a gift from Ellen van den Bogaard at the Dermatology Department at Radboudumc, Netherlands.

3.5.2 *Instrument Details*

3.5.2.1 Synthesis

^{1}H NMR spectra used to characterize polymers were obtained on a Bruker (Billerica, MA) Avance III AX-400 MHz NMR Spectrometer with a BBO SmartProbe with 64 scans per 5 spectra and a relaxation delay of 10 seconds. ^{1}H NMR spectra gathered to monitor polymerization kinetics were obtained on a temperature-controlled Bruker Avance III AV-500 MHz NMR spectrometer with a TBO triple resonance PFG probe with 4 scans per spectra and a relaxation delay of 1 second. Molar mass (M_n and M_w) and dispersity ($Đ$) of polymers were characterized by aqueous size exclusion chromatography (SEC) with an Agilent Technologies (Santa Clara, CA) 1260 Infinity system with an aqueous mobile phase containing 0.10 M Na_2SO_4 and 1.0 wt % acetic acid and a flow rate of 0.4 mL/min, Eprogen (Downers Grove, IL) columns [CATSEC1000 (7 µm, 50 × 4.6), CATSEC100 (5 µm, 250 × 4.6), CATSEC300 (5 µm, 250 × 4.6), and CATSEC1000 (7 µm, 250 × 4.6)], and variable wavelength UV-detector. A Wyatt HELEOS II light scattering detector (λ = 662 nm) and Optilab rEX refractometer (λ = 658 nm; Wyatt technologies; Santa Barbara, CA) were used as in-line light scattering and differential refractive index detectors for SEC analysis. Astra VII software (Wyatt Technologies; Santa Barbara, CA) was used for the determination of M_n, M_w, $Đ$, and *dn/dc* of polymers. The following equation was used for determining the *dn/dc* of quinine copolymers: [275]

$$(dn/dc)_{\mathrm{ab}} = x_{\mathrm{a}}\,(dn/dc)_{a} + (1 - x_{a})(dn/dc)_{b} \tag{3.4}$$

where the *dn/dc* of the copolymer $(dn/dc)_{\mathrm{ab}}$ is calculated using the *dn/dc*'s of quinine (*a*) and the homopolymer (*b*) and the weight fraction of quinine (x_{a}).

3.5.2.2 Polyplex/Biological

Zeta potential and dynamic light scattering (DLS) measurements (not contributing to kinetic plot) were made with a Zetasizer Nano ZS (Malvern; Worcestershire, UK) with a 4.0 mW He-Ne laser (λ = 633 nm). DLS measurements contributing to the kinetic plot were made with a DynoPro Plate Reader (Wyatt Technologies; Santa Barbara, CA). Gels in the electrophoretic mobility shift assay (EMSA) were illuminated using a Bi-O-Vision UV transilluminator (λ_{ex}= 366 nm) (Spectrolin; Westbury, NY) and photographed with a 16 megapixel digital camera with 28 mm lens (LG G4; Seoul, South Korea). Cell suspensions were counted with a Countess II automated cell counter (ThermoFisher Scientific; Waltham, MA) with dead cell discrimination by dilution (1:1) with trypan blue (0.4%). Percent ZsGreen expression of transfected cells were measured with a BD FACSVerse flow cytometer (BD Biosciences; San Jose, CA) with dual lasers (λ = 488 nm and 640 nm), seven detectors, and analyzed using FlowJo software (Ashland, OR). Widefield fluorescence microscopy was carried out using an EVOS Digital Microscope (AMG Life Technologies; Grand Island, NY). Widefield fluorescence microscopy with deconvolution was carried out using a Zeiss TIRF Scope (Oberkochen, Germany). Fluorescence and absorbance measurements were acquired using a Synergy H1 multimode plate reader (BioTek; Winooski, VT). pH measurements were made with AB15 digital pH meter (Accumet Basic, Fisher Scientific, Pittsburgh, PA).

3.5.3 *Polymer Synthesis*

*3.5.3.1 Poly(Quinine-*co*-HEA)*

Prior to reacting, HEA was passed through activated basic alumin aprior to reacting it to remove stabilizer and then passed through a PTFE filter (0.22 μm). Quinine (1.56 g, 4.80 mmol), HEA (0.836 g, 7.20 mmol), and 2,2'-azobis(2-methylpropionitrile) (AIBN) (19.7 mg, 0.120 mmol) were dissolved in 200 proof ethanol (5 mL) and mixed with a magnetic stir bar in a sealed vial. The reaction mixture was sparged with N_2 for 30 min, heated to 70 °C, and left to stir for 24 hours. The reaction mixture was dialyzed in 75/25 (v/v) methanol/THF (solvent replaced 4× over 48 hours) and then dialyzed in deionized water (solvent replaced 4× over 48 hours). The resulting off-white precipitate and suspension were lyophilized yielding an off-white powder 6 (0.978 g, 56% yield, 13.6% quinine incorporation). (Note: yield based on molar incorporation of comonomers in copolymer). The product was characterized using ^{1}H NMR (Fig. 3.4, Table 3.1) and aqueous SEC (Fig. 3.5, Table 1).

*3.5.3.2 Poly(Quinine-*co*-HEAm)*

Prior to reacting, (HEAm) was passed through activated basic alumina to remove stabilizer, dissolved in ethanol (1 mL), and then passed through a PTFE filter (0.22 μm). Quinine (0.973 g, 3.00 mmol), HEAm (0.230 g, 2.00 mmol), and AIBN (8.2 mg, 0.050 mmol) were dissolved in 200 proof ethanol (5 mL) and mixed with a magnetic stir bar in a sealed vial. The reaction mixture was sparged with N_2 for 30 min, heated to 70 °C, and left to stir for 24 hours. The reaction mixture was precipitated into acetone (3×), filtered, and dried under vacuum. The resulting off-white flakes (0.226 g, 32% yield, 13.3% quinine incorporation)

(Note: yield based on molar incorporation of comonomers in copolymer). Product was characterized using ^{1}H NMR (Fig. 3.33, Table 1) and aqueous SEC (Table 3.1).

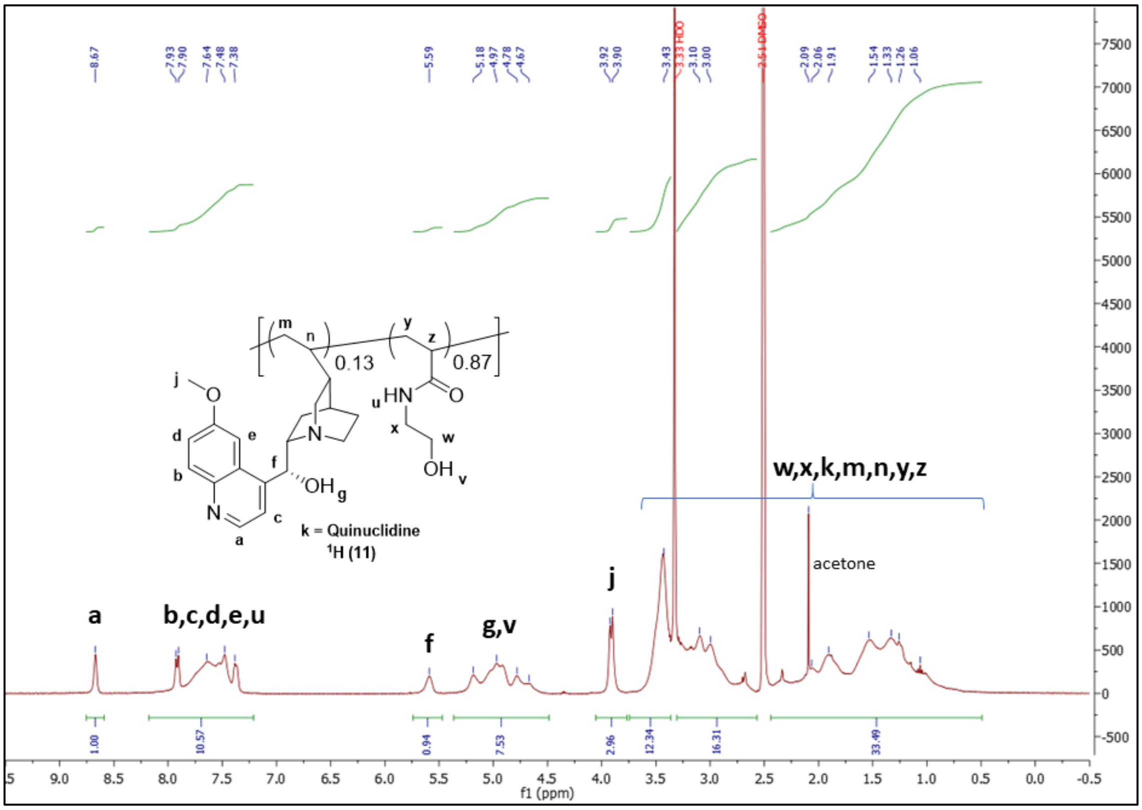

Figure 3.33. ^{1}H NMR spectra and peak assignments of poly(quinine-*co*-HEAm). The copolymer was dissolved in DMSO-d_6, and the comonomer ratio in the copolymer was obtained using the integrations from peaks corresponding to each comonomer. Ratio of HEAm/quinine = (b,c,d,e)-4.00= 6.57

*3.5.3.3 Poly(Quinine-*co*-Am)*

Quinine (0.973 g, 3.00 mmol), acrylamide (0.213 g, 3.00 mmol), and AIBN (9.9 mg, 0.06 mmol) were dissolved in 200 proof ethanol (5 mL) and mixed with a magnetic stir bar in a sealed vial. The reaction mixture was sparged with N_2 for 30 min, heated to 70 °C, and left to stir for 24 hours. The off-white suspension formed during the course of the reaction was centrifuged and washed with ethanol (3×) and then dried under vacuum. The resulting off-white flakes (0.214 g, 38% yield, 8.9% quinine incorporation) (Note: yield based on molar incorporation of comonomers in copolymer). The product was characterized using ^{1}H NMR (Fig. 3.34, Table 3.1) and aqueous SEC (Table 3.1).

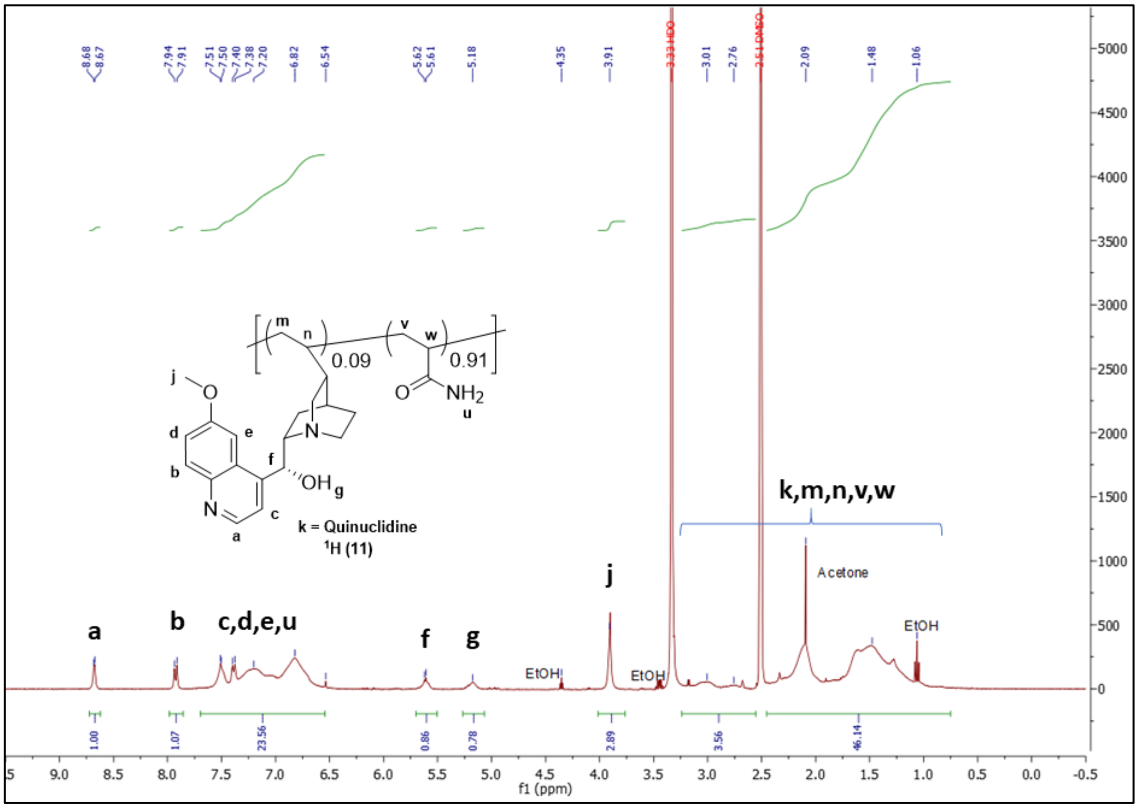

Figure 3.34. ^{1}H NMR spectra and peak assignments of poly(quinine-*co*-Am). The copolymer was dissolved in DMSO-d_6, and the comonomer ratio in the copolymer was obtained using the integrations from peaks corresponding to each comonomer. Ratio of Am/quinine =((c,d,e)-3.00)/2 = 10.28

3.5.3.4 *Poly(Quinine-*co*-DMAm)*

Prior to reacting, DMAm was passed through activated basic alumina to remove stabilizer. Quinine (1.95 g, 6.00 mmol), DMAm (0.595 g, 6.00 mmol), and AIBN (197 mg) were dissolved in 200 proof ethanol (10 mL) and mixed with a magnetic stir bar in a sealed vial. The reaction mixture was sparged with N_2 for 30 min, heated to 70 °C, and left to stir for

24 hours. After dialyzing the reaction mixture in ethanol, the dialysis solvent was gradually transitioned to ethanol/deionized water mixtures with increasing water content until all ethanol was removed. The purified product was lyophilized yielding an off-white solid (0.438 g, 32% yield, 6.5% quinine incorporation). (Note: yield based on molar incorporation of comonomers in copolymer). The product was characterized using ^{1}H NMR (Fig. 3.35, Table 3.1) and aqueous SEC (Table 3.1).

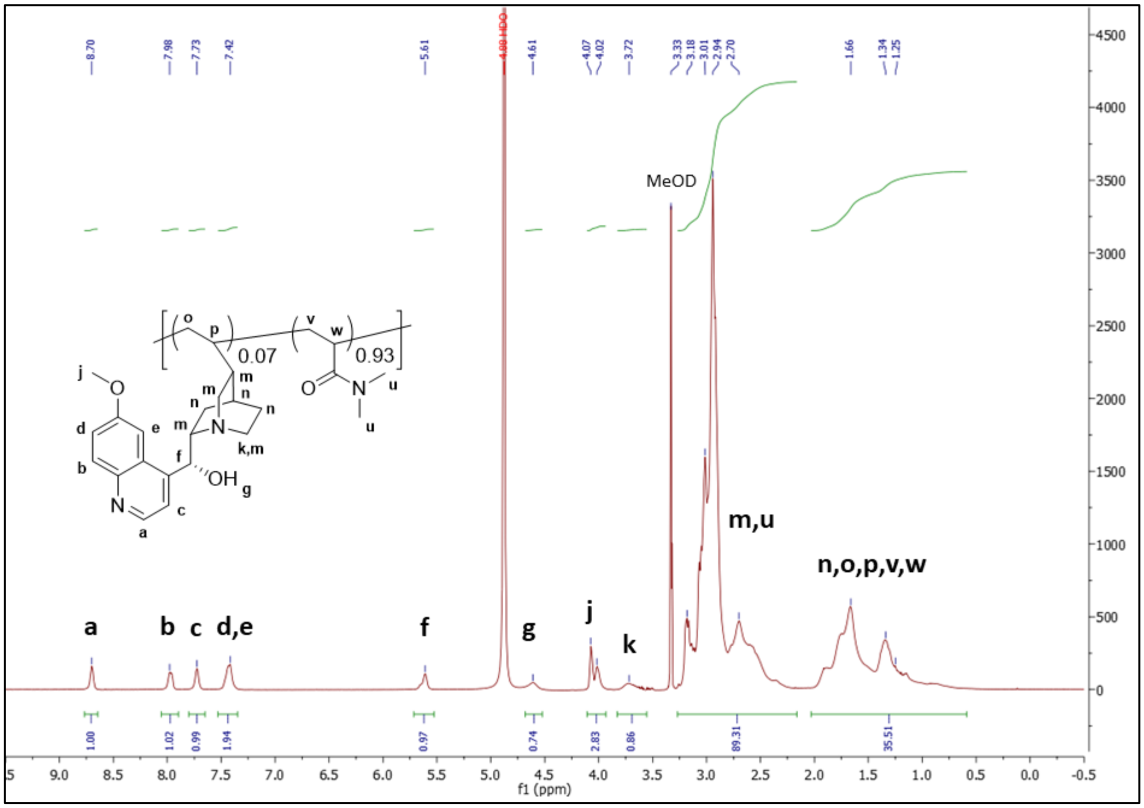

Figure 3.35. ^{1}H NMR spectra and peak assignments of poly(quinine-*co*-DMAm). The copolymer was dissolved in MeOD, and the comonomer ratio in the copolymer was obtained using the integrations from peaks corresponding to each comonomer. Ratio of DMAm/quinine = ((m,u)-5.00)/6 = 14.05

3.5.3.5 *Poly(Quinine-*co*-NIPAm)*

Quinine (0.487 g, 1.50 mmol), NIPAm (0.170 g, 1.50 mmol), and AIBN (49.7 mg, 0.300 mmol) was dissolved in DMF (6 mL) and mixed with a magnetic stir bar in a sealed vial. The reaction mixture was sparged with N_2 for 30 min, heated to 70 °C, and left to stir for 24 hours. One method of work-up involved dialyzing the reaction mixture in methanol and then transitioning the dialysis solvent to methanol/deionized water (1:1 v/v), and then to pure deionized water. Lyophilization of the purified product yielded a white powder (38 mg, 10% yield, 7.7% quinine incorporation). Alternatively, the reaction mixture was worked up by precipitation in 3:1 (v/v) ether/hexanes (3×) to yield an off-white solid (50

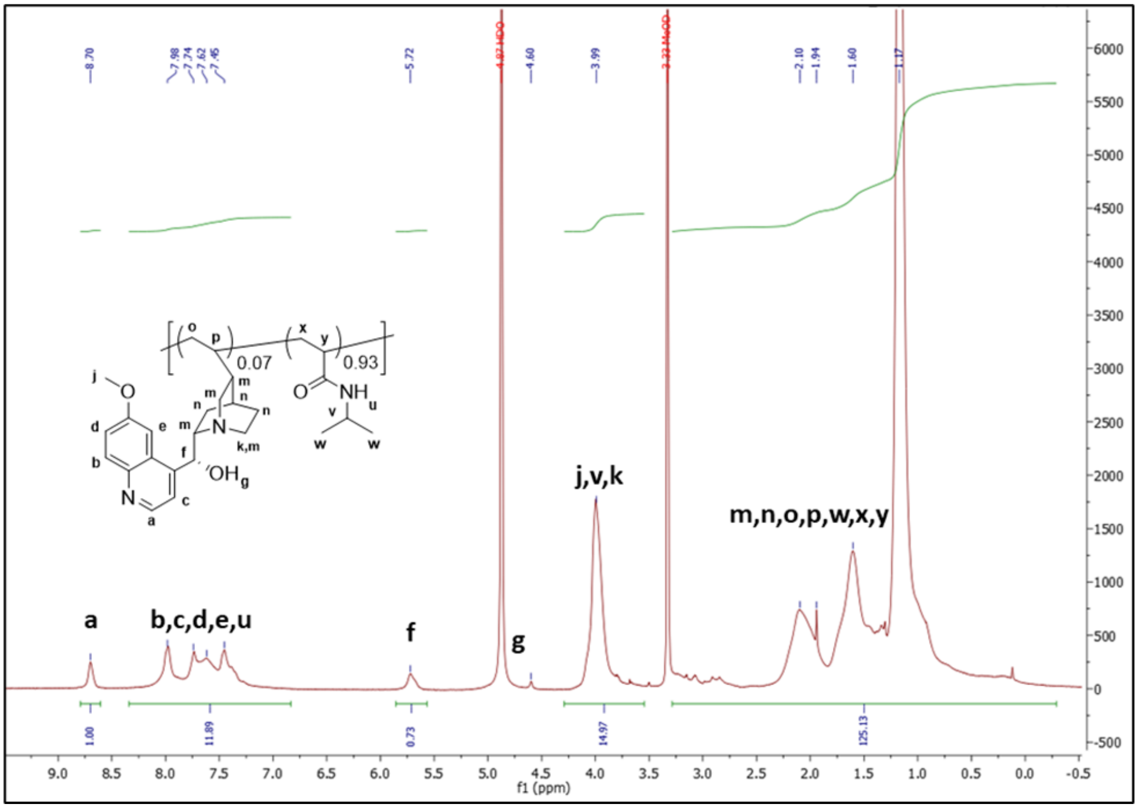

Figure 3.36. ^{1}H NMR spectra and peak assignments of poly(quinine-*co*-NIPAm). The copolymer was dissolved in MeOD, and the comonomer ratio in the copolymer was obtained using the integrations from peaks corresponding to each comonomer. Ratio of NIPAm/quinine = (j,v,k)-4.00 = 11.97

mg, 11% yield, 21% quinine incorporation). Products were characterized by ^{1}H NMR (Figure 3.36, Table 3.1) and aqueous SEC (Table 3.1).

3.5.3.6 Poly(DMAEMA-co-*HEA)*

Prior to reacting, DMAEMA was passed through activated basic alumina to remove stabilizer. DMAEMA (0.110 g, 0.700 mM), HEA (0.499 g, 4.30 mM), and AIBN (8.2 mg, 0.050 mmol) were dissolved in DMSO (4.4 mL) and mixed with a magnetic stir bar in a sealed vial. The reaction mixture was dialyzed in deionized water (solvent replaced 6× over 3 days) and lyophilized to yield an amorphous solid (0.447 g, 73.6% yield, 13.0% DMAEMA incorporation). The product was characterized by ^{1}H NMR (Table 3.1) and aqueous SEC (Table 3.1).

3.5.3.7 Poly(HEA)

Prior to reacting, HEA) was passed through activated basic alumina to remove stabilizer and then passed through a PTFE filter (0.22 μm). HEA (1.39 g, 12.0 mmol), and 2,2'-azobis(2-methylpropionitrile) (AIBN) (19.7 mg, 0.120 mmol) were dissolved in 200 proof ethanol (5 mL) and mixed with a magnetic stir bar in a sealed vial. The reaction mixture was sparged with N_2 for 30 min, heated to 70 °C, and left to stir for 24 hours. The reaction mixture was dialyzed in 75/25 (v/v) methanol/THF (solvent replaced 4× over 48 hours) and then dialyzed in deionized water (solvent replaced 4× over 48 hours). Lyophilization of the purified product yielded a clear amorphous solid (1.24 g, 89% yield). The product was characterized by ^{1}H NMR (Table 3.1) and aqueous SEC (Table 3.1).

3.5.3.8 Poly(DMAEMA)

The RAFT polymerization of DMAEMA was performed according to the protocol described in a previous study.[112] Prior to reacting, DMAEMA was passed through activated neutral alumina to remove stabilizer. DMAEMA (5.00 g, 31.8 mmol), CDP (0.183 g, 0.454 mmol), and V-501 (12.7 mg, 0.0454 mmol) were dissolved in dimethylformamide (DMF) with a final monomer concentration of ~30 wt %. The reaction mixture was degassed via freeze-pump-thaw cycles, pressured with argon, and polymerized at 80 ºC overnight. The polymerization was quenched by cooling the reaction mixture in an ice bath. The polymer was purified by precipitation in cold hexane (3×), dissolved in benzene, and freeze dried, yielding a light-yellow powder (4.50 g, 90% yield). The product was characterized by ^{1}H NMR (Table 3.1) and aqueous SEC (Table 3.1).

3.5.4 *Reactivity Ratios*

The reactivity ratios between quinine and several acrylate/acrylamide comonomers (including HEA, HEAm, and Am) were measured by running free radical copolymerizations (1 M total comonomer concentration) with AIBN (0.01 M) in an NMR tube (0.5 mL total volume), which was sealed by a rubber septa degassed with N_2. The reaction was run at 70 °C in DMSO-d_6 while monitoring via ^{1}H NMR (1 min between each measurement). The conversion of each comonomer was calculated by integrating the corresponding alkene peak and normalizing to an internal standard (aromatic proton of quinine). Copolymerizations were run at eleven different comonomer feed molar ratios (f_1) per comonomer (ranging between 0.95-0.10). The conversion of each comonomer was determined at the time of 5% total monomer conversion (Fig. 3.7a). It was assumed that the ratio of the comonomers consumed at 5% total monomer conversion was equivalent to the ratio of comonomers incorporated into the copolymer (F_1) at that time. For each comonomer, F_1 was plotted against f_1 and fitted (Fig, 3.7b) with the Mayo-Lewis equation (eqn. 3.3) to give the reactivity ratios (r_1 and r_2) with quinine.

3.5.5 *Potentiometric Titration*

Poly(quinine-*co*-HEA) (7.50 mg) and quinine (2.30 mg) were dissolved separately in aqueous HCl (7.5 mL, 13.3 mM HCl) to afford solutions containing equal molar concentrations of quinine (0.947 mM) at pH = 2.0. While measuring the pH of the solution while stirring with a pH-probe at 23 °C, known increments of NaOH (0.01 M) were added to the solution. The pK_as of the polymer and monomer were calculated from the derivative values of the titration curve, which corresponds to the inflection point.

3.5.6 *Polyplex Formation*

All solutions were prepared by diluting components in DNAse/RNAse-free water, unless otherwise specified. Plasmid DNA solution in water (1.0 mg/mL) was diluted to achieve a concentration of 0.02 μg/μL. A polymer stock solution (11.0 mg/mL) was obtained by dissolving dried polymer powder into aqueous acetic acid (0.507 M). This polymer stock solution is diluted to the appropriate concentration necessary so that upon mixing with the diluted plasmid solution at equal volumes, the appropriate N/P ratio is achieved. In the case of poly(quinine-co-HEA), 0.291 μL of the polymer stock is necessary for every 1 μg of plasmid at an N/P = 1. For example, to make a polyplex sample containing 3.3 μg of plasmid at N/P = 6 for a transfection, 6.34 μL of polymer stock was diluted in 175.16 μL of water to yield an excess (1.1×) of dilute polymer solution. The dilute polymer solution

(165 µL) was added slowly to the dilute plasmid solution (165 µL) and left to incubate for 30 min at room temperature prior to use.

3.5.7 *Electrophoretic Mobility Shift Assay*

Polyplexes with N/P ratios ranging between 0-10 were formed with pZsGreen in water. In order to formulate the polyplexes prior to gel loading, a pZsGreen stock (50 ng/µL) was aliquoted in batches of 10 µL. Polymer solutions (>10 µL) were formulated in accordance with the protocol outlined above. Equal volume aliquots of the polymer solutions were added to the DNA solutions to form polyplex solutions (total volume = 20 µL each), which were then incubated at room temperature for 30 min. Each polyplex solution was then spiked with 2 µL of 30% glycerol solution in water prior to loading 10 µL of solution onto an agarose gel (0.6% agarose in TAE buffer) containing ethidium bromide (0.3 µg/mL) and run at 80 V for 45 minutes. The plasmid and quinine-containing polymer within gel was imaged upon illumination by a UV transilluminator with UV-blocking cover.

3.5.8 *Dynamic Light Scattering*

The hydrodynamic diameter (d_h) of polyplexes in water and DMEM was determined via DLS using a Malvern Zetasizer Nano ZS (λ = 633 nm) with a scattering angle of 173º at a temperature of 25 ºC. Polyplexes were formed with pZsGreen in accordance with the protocol outlined above for a range of N/P ratios. The concentration of plasmid in the DLS samples, for both polyplexes in water and polyplexes diluted in DMEM (serum-free), was equivalent to those used in the PicoGreen dye exclusion studies and transfection studies. The interval of time between addition of media and sample measurement was kept constant for all samples. The mean d_h was the mean Z-average diameter (calculated by the instrument) for three independent replicates. The kinetic plot showing the change in d_h of poly(quinine-co-HEA) polyplexes upon dilution in DMEM (serum-free) (Fig. 3.12e) was obtained using a Wyatt DynaPro Plate Reader at 25ºC. The d_h of poly(quinine-co-HEA) polyplexes (N/P = 8) at time = 0 min corresponds to the mean d_h of the polyplexes prior to diluting in DMEM. Upon diluting the polyplex solution in DMEM, the dh was measured repeatedly over the course of 1 hour. The measurement at each timepoint was determined by 10 acquisitions (5 sec each) with a 1 min waiting period between measurements leading to approximately 120 second intervals between measurements. The mean d_h at each timepoint was determined by averaging three independent replicates.

3.5.9 *Zeta Potential*

Zeta potential measurements of polyplexes were obtained with a Malvern Zetasizer Nano ZS at 25 °C in folded capillary cell cuvettes. Polyplexes were formed with pZsGreen in water in accordance with the protocol outlined above at equivalent concentrations. After measuring the zeta potential of the polyplexes in water, the polyplex solution was diluted (3×) in a $NaHCO_3$ buffer (44 mM) containing dextrose (25 mM) that was pre-incubated overnight in a 5% CO_2 environment. This NaCl-free buffer was chosen to mimic DMEM as closely as possible while maintaining the conductivity of the solution < 5 mSv/cm. The reported zeta potential was the mean of independent replicates ($n \geq 3$).

3.5.10 *PicoGreen Dye Exclusion Assay*

The dye exclusion assay protocol was adapted from a previous study by McLendon et al.[276] All solutions were prepared by diluting components in DNAse/RNAse-free water, unless otherwise specified. Aqueous PicoGreen solution was formed by diluting the PicoGreen stock in water (1:200). Two plasmid stocks (0.02 μg/μL) were made by diluting pZsGreen with either the aqueous PicoGreen solution or water alone. Polyplexes were formed as described above for N/P ratios of 0, 1-10, 15, and 20 with both the plasmid stock containing PicoGreen well as with the plasmid stock containing no dye (to serve as a blank) and left to incubate for 30 min at room temperature. The polyplex solutions (50 μL) were dispensed into a black flat-bottom 96-well microplate using a multichannel pipette or in triplicate, and the fluorescence endpoint was measured using a microplate reader equipped with fluorescence filter cube (λ_{ex} = 485/20 nm, λ_{em} = 528/20 nm). The relative fluorescence of each sample was calculated by subtracting the blank (dye-free sample of the corresponding N/P ratio) and then normalizing to the polymer-free sample (N/P = 0). The polyplex solutions in the plate were then diluted 3× with phenol red-free DMEM (serum-free), and the fluorescence endpoints were taken at 5, 15, and 30 min after dilution. Subsequently, a 10% (v/v) addition of FBS (15 μL) was added to the polyplex solutions diluted with DMEM, and fluorescence endpoints were taken at 5, 15, and 30 min after dilution.

3.5.11 *Cell Culture*

The HeLa and HEK 293T cells were cultured in DMEM containing FBS (10%) and Antibiotic/Antimycotic (1×). N/TERT cells were cultured in supplemented K-SFM with Gentamicin/Amphotericin (1×). Cell media was supplemented with and cells were cultured in 75 cm^2 flasks at 37 °C under 5% CO_2 atmosphere. The cell cultures were monitored for confluency (maintained below 70%) and passaged every 2-3 days. The K562 cells were cultured in IMDM containing FBS (10%) and Antibiotic/Antimycotic (1×). Cells were cultured in 75 cm^2 flasks at 37 °C under 5% CO_2 atmosphere. The cell culture was kept below (1×10^6 cells/mL) and passaged every 2-3 days.

3.5.12 *Transfection Assay with ZsGreen Reporter Plasmid*

3.5.12.1 Transfection protocol for adherent cells

Twenty-four hours prior to transfection, cells were seeded in 24-well microplates with 1 mL/well of cell suspension (5.0×10^4 cells/mL) in FBS-supplemented DMEM (HEK 293T and HeLa) or supplemented K-SFN (N/TERT). Just prior to the transfection, polyplexes were prepared in the manner described above. For each sample in triplicate (3 wells total), 330 μL of polyplex solution (containing 3.3 μg of plasmid at a concentration of 0.01 μg/μL) was prepared, which was left to incubate at room temperature for 30 minutes. Just prior to the addition of the polyplexes to the cells, strongly adherent cells (HeLa and N/TERTs) were washed with PBS to remove residual protein-containing media. For HEK 293T cells (which can more easily be removed via washing), the cell media was gently aspirated (without washing) prior to addition of polyplexes. After removal of the cell media/washing, the polyplex solution was diluted 3× with serum-free DMEM (all adherent cell types). Unless noted otherwise, the polyplex solution was added immediately to the freshly washed cells (300 μL/well for a total dose of 1 μg of plasmid/well) after dilution with DMEM. Lipofectamine 2000 was administered at 0.5 μg/well in accordance with the commercial protocol. The cells were placed in the incubator and left to incubate with the polyplexes for 4 hours, after which 1 mL of DMEM (with 10% FBS) was added directly to the polyplex solution.

3.5.12.2 Modification for control of polyplex size and number

HeLa cells were subjected to variations in the transfection protocol in order optimize the transfection by controlling particle size. After the dilution of the polyplex solutions in DMEM, the polyplexes were incubated at room temperature for a range of times (15-30 min), defined as the formulation time. Upon addition of the polyplexes to the cells, the cells were incubated with polyplex solutions for a range of times (5-30 min), defined as the cell incubation time. After the cell incubation period, the polyplex solution was gently aspirated, replaced with DMEM (with 10% FBS), and the cells were placed back into the incubator. Lipofectamine 2000 was administered at 0.5 μg/well in accordance with the commercial protocol. 24 hours post-transfection, the media was replaced with fresh media (1 ml, DMEM with 10% FBS) and the cells were placed back into the incubator. 48 hours post-transfection, adherent cells were washed with PBS, lifted from the well surface with phenol red-free trypsin (200 μL), and diluted in 300 μL of Fluorobrite DMEM (with 10% FBS). The cell suspension was homogenized (no visible cell clumps) and 50 μL of each suspension was added to a clear flat-bottom 96-well microplate for cell viability analysis (vide infra). The remaining cell suspension was placed in Falcon tubes in order to prepare them for flow cytometry analysis (vide infra).

3.5.12.3 Transfection protocol for suspension cells

Just prior to transfection, cells were seeded in 24-well microplates with 100 μL/well of cell suspension (4.0×10^6 cells/mL) in PBS. Polyplexes were prepared in the manner described above except that the dose and volume was scaled up (4×) while maintaining constant concentration. For each sample in triplicate (3 wells total), 1.320 mL of polyplex solution (containing 13.2 μg of plasmid at a concentration of 0.01 μg/μL) was prepared, which was left to incubate at room temperature for 30 min. The polyplex solution was diluted 3× with IMDM (serum-free) and then added directly to the cells (1.200 mL/well for a total dose of 4 μg of plasmid/well). The dose delivered with Lipofectamine 2000 was also scaled by 4 × (2 μg plasmid total) and administered according to the commercial protocol. The cells were placed in the incubator and left to incubate with the polyplexes for 4 hours. Following this incubation, 800 μL of the polyplex solution was carefully aspirated from the top of the solution so as to not disturb the cells at the bottom of the wells. After this, 1 mL of IMDM (with 10% FBS) was gently added to the well and the cells were placed back into the incubator. After 48 hours following transfection, the cells were transferred into Falcon tubes for cell viability analysis. These cells were pelleted via centrifuge and the remaining supernatant was aspirated. The cells were resuspended in PBS, pelleted via centrifuge, and resuspended in 500 μL of Fluorobrite DMEM (with 10% FBS). A homogeneous portion of this cell suspension (50 μL) was added to a clear flat-bottom 96-well microplate for cell viability analysis (*vide infra*). The cell suspension remaining in the Falcon tubes was carried forward in processing for flow cytometry analysis.

3.5.12.4 Flow cytometry analysis

The cells were pelleted via centrifuge (set to 4 ºC) and the remaining supernatant was aspirated. The cells were resuspended in ice-cold PBS, pelleted via centrifuge (4 ºC), and resuspended in ice-cold PBS containing 1% FBS and PI (10 μg/mL). The samples were analyzed via flow cytometry by collecting 10,000 events per replicate. The gates for ZsGreen+ live cells (PI negative, ZsGreen positive) were set with the untreated control.

3.5.13 Transfection Assay with Luciferase Reporter Plasmid

The polyplex formulation with the gWiz-luc plasmid and the transfection procedure with adherent cells are identical to the protocol described above with the ZsGreen reporter plasmid. After 48 hours following the transfection, the cells were washed with PBS followed by addition of lysis buffer (100 μL) to each well. After incubating at room temperature for 10 min, an aliquot of cell lysate (5 μL) was pipetted both into an opaque white flat-bottom 96-well microplate for luciferase quantitation. The plate was placed in a plate reader equipped with an automatic injection system that added luciferase substrate (100 μL) to the lysate and measured the chemiluminescence for each well. The protein concentration for each sample was quantitated by following the manufacturer's protocol using a Pierce BCA Protein Assay Kit and standard curve made with bovine serum albumin (BSA). The mean relative light units (RLUs) for each sample, determined from the luciferase assay, was normalized to the mean mass of protein (mg) measured for each sample.

3.5.14 *Widefield Fluorescence Microscopy, Colocalization*

Widefield epifluorescence microscopy of HEK 293T cells, transfected with poly(quinine-co-HEA) and Cy5-labelled ZsGreen plasmid, was performed using a Zeiss TIRF scope. Three separate fluorescence channels were collected on each sample, corresponding to three fluorophores present: Cy5 (λ_{ex} = 640/30 nm, λ_{em} = 690/50 nm), ZsGreen (λ_{ex} = 470/40 nm, λ_{em} = 525/50 nm), and poly(quinine-co-HEA) (λ_{ex} = 365 nm, λ_{em} = 445/50 nm). Images were taken with dimensions of 81.92 μm × 81.92 μm with z-slices of 240 nm, with an objective of 100×. Slice number in samples ranged from a minimum of 16 to a maximum of 202. Slices and image dimensions were refined when processed to exclusively reflect cellular volume. Raw images were collected using ZEN Black 2.3 sp1 (Zeiss, Stockholm, Sweden) at the University Imaging Center at the University of Minnesota. One limitation in the area of widefield microscopy is convolution from out-of-focus z-stacks.[277] Widefield images contain residual noise from other image stacks, whereby the degree and location of the out of focus convolution is proportional to its point spread function. Deconvolution has been an iterative mathematical tool shown to alleviate this problem, and allow for point based image analysis.[278; 279] Huygens deconvolution software version:17.10.0p5 (Scientific Volume Imaging, The Netherlands) was used to perform batch deconvolution on all widefield images using the CMLE algorithm with SNR:40, Q threshold of 0.01, with a maximum iterations of 50. The Minnesota Supercomputing Institute was used to execute the necessary calculations. Colocalization of Cy5 and poly(quinine-co-HEA) was computed using an ImageJ colocalization plugin JACoP with normalized threshold values for like channels.[280; 281]

3.5.15 *CCK-8 Viability Assay*

After procuring all cell suspensions (50 μL each) in a clear flat-bottom 96-well microplate as described in the Transfection Method (see above), the samples were subjected toa CCK-8 viability assay protocol adapted from the manufacturer's instructions. Each well was spiked with 50 μL of a 5× dilution of CCK-8 reagent in phenol red-free DMEM (with 10% FBS). The samples were placed in an incubator and left to incubate for 1-3 hours depending on cell type and density. Due to settling and potential clumping of the cells, the cell suspension was homogenized by gentle pipetting (with care taken not to introduce any bubbles) prior to analysis in the plate reader. The absorption of the cell suspensions and a blank (containing all components minus cells) was taken at 450 and 650 nm. The absorption values correlating to the blank and the OD at 650 nm (the contribution to the absorption due to the light scattered by cells) was subtracted from the samples' absorption at 450 nm. This value was then normalized to the untreated sample and multiplied by 100 to give a relative % cell viability at the 48 hours time point after transfection.

3.5.16 *Endocytosis Inhibition Assay*

The transfection of HeLa cells in the presence of endocytosis inhibitors was adapted from the protocol above. The concentrations and cell incubation times needed for amantadine (clathrin), filipin III (caveolae), and DMA (macropinocytosis) was optimized in previous studies.[74, 112, 282-284] The cells were transfected with poly(quinine-*co*-HEA) (N/P = 8) and pZsGreen with pre-incubation and cell incubation times (as defined in section 3.5.12.2) of 30 min and 15 min, respectively. Prior to adding the polyplexes to the cells, the cells were incubated in DMEM (with 10% FBS) containing either amantadine (1 mM), filipin III (1 μg/mL), and DMA (100 μM) for 1 hour, 1 hour, and 5 min, respectively. In addition, the polyplexes were diluted (2×) in serum-free DMEM containing the respective endocytosis inhibitor at concentrations equivalent to those above. After the cell incubation period, the polyplex-containing media was aspirated, the cells were washed with PBS, and 1 mL of fresh DMEM (with 10% FBS) was added to the cells. The toxicity and transgene expression of the cells were quantified 48 hours later as described above.

3.5.17 *Examination of Hydrolytic Stability of the Hydroxyethyl Pendant Groups*

Poly(HEA) was dissolved (10 mg/mL) in several D_2O solutions with a range of pH values. These include ~0.1% v/v TFA (pH 2.3), unbuffered D_2O (pH 5.3), and PBS-buffered D_2O (pH 7.4). D_2O with NaOH (~1% w/v) (pH 13.5) served as a positive control for hydrolysis. These solutions were analyzed via ^{1}H NMR immediately after dissolving (1 hr) and 72hrs later after incubation at 37 ºC. By monitoring the integration reduction of the methylene peak closest to the ester (4.1 ppm, 2H) in relation to the backbone protons (1.4-2.6 ppm, 3H), we could quantify the percent of pendant group hydrolysis.

3.5.18 *Raman Spectroscopy DNA Binding Studies*

To determine the binding mechanism of poly(quinine-co-HEA) polymers with DNA, the Raman spectrum of poly(quinine-co-HEA) was measured in the presence of calf-thymus DNA at N/P ratio of 5 (Fig. 3.15a). Concentrated stock solutions of DNA and poly(quinine-co-HEA) were prepared in water under acidic conditions (1.2 % v/v HCl) to keep the polymer soluble and to mimic the conditions under which the polyplexes were performed for dye exclusion, DLS, and transfection experiments. The stock solutions were prepared with 2% (v/v) acetonitrile, which was used as an internal standard. To prepare polyplexes, the stock solutions were mixed together in a 1:1 ratio (v/v). Upon mixing, a noticeable increase in the viscosity and the formation of aggregates was observed. The viscosity change was similar to what we previously observed with monomeric quinine and indicates that the poly(quinine-co-HEA) polymer chains are binding DNA to form polyplex aggregates.[210]

The Raman spectra of the polymer, DNA, and polyplex samples were measured using a home-built setup that used a 785 nm diode laser purchased from Innovative Photonic Solutions. The beam was directed through a 30/70 beamsplitter and focused onto the sample with an infinity-corrected Olympus Ach 10×/ 0.25 NA objective. An excitation power of 40 mW was used at the sample. The Raman scattered light was collected using a 180° backscattering geometry and redirected through the beam-splitter into an Acton SpectraPro2500i spectrometer. The light was dispersed in the spectrometer using a 600 gr/mm grating and imaged using a PIXIS CCD camera purchased from Princeton Instruments. The spectra shown here were measured by averaging 30 spectra collected with 60 s acquisition times.

3.5.19 *Raman Imaging Studies on Transfected Cells*

HeLa cells were grown on glass coverslips in 6-well plates and subsequently transfected with poly(quinine-*co*-HEA) polyplexes. After this, the media was removed, and the cells were rinsed with PBS. The cells were then fixed by incubating them in a 4% (v/v) solution of formaldehyde in PBS at room temperature for 15 minutes. The formaldehyde solution was subsequently removed, and the cells were then rinsed twice with PBS. After removing residual PBS, 10 μL of mounting solution containing glycerol was applied to the fixed cells to maintain their morphologies.

Raman images of the transfected cells were measured along with control samples that contained polyplexes treated with the 4% (v/v) formaldehyde solution to assess the potential influence of fixation on the Raman spectrum of poly(quinine-*co*-HEA) polymers (vide infra). The images were measured using a commercial confocal microscope system (alpha 300R) purchased from WITec (Ulm, Germany) equipped with a UTS300 spectrometer, a DV401 CCD detector, and a piezo-driven feedback-controlled scanning stage. Samples were excited at 532 nm using a frequency doubled Nd:YAG laser. The laser light was focused onto the sample using a 100× Nikon air objective with a numeric aperture of 0.90. We typically used 10 mW of laser light power at the sample and an accumulation time of 1 s/pixel. The back-scattered Raman light was directed to the spectrometer via a fiber optic connection. The light was dispersed in the spectrometer using an 1800 gr/mm grating. The images of the cells were collected in the form of a hyperspectral data cube over a 50 μm × 50 μm area in spatial increments of 250 nm.

Each pixel in the Raman images contains a Raman spectrum that roughly spans the region from 900-1800 cm^{-1}. Prior to visualizing and further analyzing the images, the spectra were pre-processed using custom-written MATLAB scripts and functions that automatically removed cosmic ray spikes and baselined each spectrum. Most of the prominent Raman bands in the spectra derive from glycerol (1050, 1110, and 1465 cm^{-1}), which was used in the cell mounting solution. However, as discussed in Section 3.3.6, HeLa cells could be visualized by integrating the intensity of the protein-derived Amide I band (1660 cm^{-1}), while polyplexes could be visualized by integrating the intensity of the unprotonated quinoline ring symmetric stretching mode of quinine (1369 cm^{-1}).

3.5.20 *Principal Component Analysis (PCA) of Hyperspectral Raman Images*

To perform PCA, we used the *pca* function in MATLAB. Figure 3.28 shows representative loading vectors and score maps obtained from our analysis of the Raman hyperspectral images. In the case of Figure 3.28, the PC loading vectors and score maps to HeLa cells that were fixed 48 h after transfection (Fig. 3.27c). In our analysis, we initially considered the first ten PCs for each hyperspectral image and generally found that the first three or four PCs exhibited loading vectors that contained physically meaningful Raman spectral features (as described in Section 3.3.6).

3.5.21 *Calculating the Deintercalation Image Map*

The PC 1 and 3 score maps in Figure 3.28 were used to determine the deintercalation map shown in Fig. 3.30f. The workflow for processing the PC score maps and calculating the deintercalation map is shown in Figure 3.37. To calculate the deintercalation map, the uneven backgrounds present in the PC score maps were first corrected by using a “rolling ball” algorithm (Fig. 3.27b).

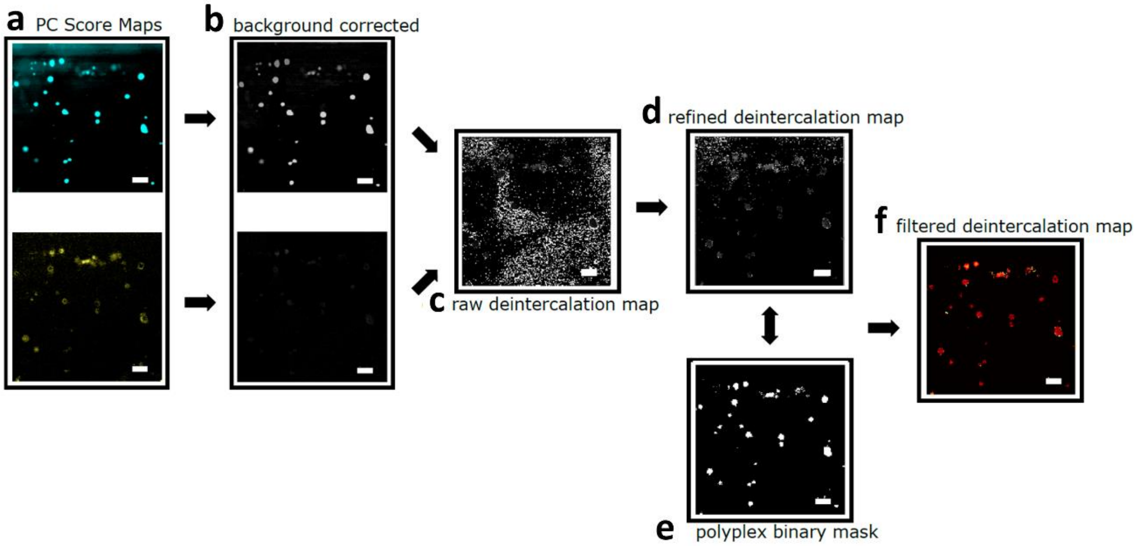

Figure 3.37. Workflow for determining the percent deintercalation map of polyplexes in HeLa cells 48 hrs post-transfection. The PC score maps shown in (a) were first converted into grayscale images and (b) background corrected using a rolling ball algorithm. (c) A raw deintercalation map was determined from the background corrected PC score maps by calculating the percent deintercalation for every pixel using eq. 3.5. The raw deintercalation map contains noise that obscures the polyplex particles. As a result, a (d) refined deintercalation map was calculated by selecting polyplexes using a uniform intensity threshold. The refined map still contains residual noise and was subsequently filtered by applying a (e) binary mask to the image. The filtered deintercalation map is shown in panel (f). Scale bars = 5 μm.

A raw deintercalation map (Fig. 3.37c) was calculated by determining the percent deintercalation for every pixel using the following equation:

$$P_i = \frac{S_{PC3,i}}{S_{PC1,i}+S_{PC3,i}} \times 100\% \qquad \textbf{(3.5)}$$

where P_i, $S_{PC1,i}$, and $S_{PC3,i}$, are the percent deintercalation, PC 1 score map intensity, and PC 3 score map intensity at the i^{th} pixel, respectively. Due to the imperfect background correction in the PC score maps, the resulting raw deintercalation map (Fig. 3.37c) contains noise features that obscures the polyplex particles. To better highlight the polyplexes, a more refined deintercalation map (Fig. 3.37d) was obtained by using an intensity threshold to select all particles and to reject as much of the noise background as possible. The intensities shown in Figure 3.37c represent deintercalation percentages that are scaled from 0 to 100%. We found that all of the particles could be selected and most of the noise could be rejected by uniformly setting the intensity thresholds between 1 and 99%. As a result of this thresholding method, the polyplex particles are clearly visible in the refined deintercalation map (Fig. 3.37d), although some residual noise features can still be observed in the upper half of the image. To remove this residual noise, we therefore applied a binary mask to filter the refined deintercalation map and produce the image shown in Figure 3.37f.

3.5.22 *Correlation Between Protein Concentration and Polyplex Unpackaging*

As described in the Section 3.3.6, the deintercalation map shown in Figure. 3.37f (as well as Fig. 3.30f) was further analyzed to understand the structural role that intracellular proteins play in polyplex unpackaging. To do this, radially-averaged cross sections of individual particles located inside the cells were calculated to quantify the distribution of polymer, protein, and deintercalated quinine moieties in the polyplexes as a function of distance (in microns), *R* (Fig. 3.31). The relative concentration of polymer and protein was determined by normalizing the intensities of the quinoline ring mode and the Amide I mode, respectively, to their corresponding maximum Raman band intensities. In order to compare the different polyplexes, the cross sections were normalized with respect to the apparent radius, *r*, of each individual particle (assuming a sphere). Figure 3.31 shows the median and standard deviation of all the radially-averaged polymer, percent deintercalation, and protein cross sections for the polyplex particles analyzed.

3.6 Acknowledgements

We thank Dr. Jeffrey Ting and Dr. Zhe Tan for their contributions in polymer synthesis and Dr. William Boyle and Dr. Yogesh Dhande for their cell culture expertise. We also thank Dr. Guillermo Marqués, Dr. Thomas Pengo, and the University Imaging Center for acquisition and processing expertise of deconvolved widefield images and Samantha Linn for help with polymer characterization. Funding for this work was provided by the NIH (R35-GM9119441, D.P. and R.R.F.) and the NSF (DMR-1904853, C.V.B., D.P., A.J.S., T.M.R., and R.R.F.). D.P. gratefully acknowledges postdoctoral funding from the Ford Foundation. C.V.B. acknowledges graduate funding under the Frieda Martha Kunze and College of Science and Engineering Graduate Fellowships (University of Minnesota). The Raman microscopy experiments were carried out in the University of Minnesota's Characterization Facility, which receives partial support from the NSF through the University of Minnesota Materials Research Science and Engineering Centers program under Award DMR-2011401.

4. Simultaneous Delivery of RNP and Donor DNA with Quinine Copolymer Reporter for Efficient CRISPR/Cas9 Editing

4.1 Overview

Advances in gene editing technology, such as the development of CRISPR/Cas9, have opened the doors to treating formerly intractable congenital disorders by permanently restoring deleterious genetic mutations. Often, correction of a genetic mutation with CRISPR requires insertion of an exogenous genetic sequence into the genome of a targeted cell. Ribonucleoproteins, which is the annealed Cas9 and sgRNA complex, can allow for gene insertion by inducing a double-strand break (DSB) in a prescribed location of the genome and allowing the cell to insert a specified genetic sequence by homology-directed repair (HDR). It is difficult, however, to simultaneously deliver the RNP complex and DNA donor template with non-viral delivery vehicles. To allow those developing gene therapies to gain the advantages of using RNPs directly and move away from viral vectors, strides must be made in improving the efficiency of chemical-based systems to simultaneously bind RNP and donor templates and deliver them into cells. Here we report how a new polymeric transfection reagent containing the antimalarial quinine, called a Quinine Copolymer Reporter (QCR), can efficiently and simultaneously bind both RNP and a DNA donor template and deliver them to cells in culture. We assess the ability of the QCR to promote both gene editing by both non-homologous end-joining (NHEJ) and HDR with a model cell line and find that it can enhance both NHEJ knockouts and double the HDR-based editing achieved by Lipofectamine CRISPRMAX without increasing cytotoxicity. The quinine in the QCR also allows for diagnostic assessment of the RNP binding properties through both its fluorescence and Raman spectroscopic properties, making the QCR a promising theranostic platform for non-viral genome editing with CRISPR.

4.2 Introduction

As described in *Chapter 3*, we developed a new polymeric agent containing the antimalarial quinine (called a Quinine Copolymer Reporter or QCR) that could efficiently deliver plasmids to hard-to-transfect cell lines. In a collaborative effort with Dr. Dave Punihaole in the Frontiera Group, we then used the sensitive 1370 cm^{-1} Raman band of quinine (established in *Chapter 2*) as a spectroscopic probe for monitoring DNA binding *in situ* and elucidated a protein-based unpackaging mechanism of the QCR-plasmid complexes. After establishing the therapeutic and diagnostic properties of this quinine-based system, we aimed to use the system for targeted and permanent alterations to the genome of a cell line. While transient transfections, similar to those achieved in *Chapter 3*, have broad therapeutic applicability,[8, 285, 286] many therapies targeting hereditary disorders require targeted genomic alterations.[7] CRISPR/Cas9 has stood out as a precise and efficient method for genome editing (see *Section 1.1.5*), and this chapter documents our work in adapting the QCR system for the delivery CRISPR/Cas9 components for more efficient non-viral genome editing.

Genomic editing of cells with CRISPR/Cas9 is quickly becoming a standard tool in biological research,[287] and it is currently being used in a variety of experimental treatments for diseases ranging from lung cancer,[288] sickle cell disease,[289] and Leber congenital amaurosis,[290] among others.[291] These treatments mainly rely on viral vectors and physical methods (see *Sections 1.1.2-3*) in order to deliver the nucleic acid components necessary to achieve gene editing. Physical methods, however, have toxicity concerns and viral vectors can promote off-target effects.[291] These drawbacks, among others, make non-viral vectors an attractive alternative to these delivery methods.

The delivery requirements needed to achieve efficient CRISPR/Cas9 editing, however, are demanding, especially for nonviral vectors which significantly trail viral vectors in delivery efficiency. To achieve targeted DSBs (see *Section 1.1.5*), an RNP must be delivered either through direct delivery or by expression through plasmid or mRNA.[39] Delivering RNPs directly, instead of through expression of a plasmid, can maintain editing efficacy while reducing off-target effects and increasing onset of action.[292] Due to this preference in delivery RNPs directly, the Reineke Group has moved towards adapting and optimizing our polycationic delivery vehicles to deliver RNPs (see *Section 1.4.4*). Tan et al.[113] and Kumar et al.[114] developed micelles and statistical copolymers, respectively, for the delivery of RNP complexes to induce mutational NHEJ edits. These efforts, among others,[293] rely on polymer interactions with sgRNA for RNP binding since binding to the Cas9 protein directly is inefficient. Modifications to the Cas9 protein, either through supercharging[294] or addition of cationic terminal segments,[295] have been made to improve polymer binding to the protein. In order for a polymer to bind directly to a native positively-charged Cas9 protein, specialized subunits in the polymeric delivery agent, such as boronic acid moieties, have been added as well.[296] Methods to improve RNP binding through simple protein-polymer interactions are of interest for those wanting to deliver RNP with polymeric carriers.

In addition, many important therapeutic applications rely on HDR-based gene insertions at DSBs, which requires co-delivery of a donor DNA template along with the RNP.[291] HDR-based editing is naturally infrequent in human cells, so significant effort has been aimed at increasing HDR-based editing events.[297] There is also the added difficulty of delivering the additional genetic components needed for HDR. Developing vehicles capable of efficiently delivering all three components (Cas9, sgRNA, and donor DNA) is a significant hurdle for HDR-based applications. In the case of RNPs, few vehicles have been designed to simultaneously deliver both RNPs and donor DNA. A gold nanoparticle-based system achieved simultaneous delivery of RNPs and oligonucleotide DNA donor for HDR editing through a multi-step complexation method of donor DNA attachment to gold nanoparticles followed by sequential attachments of the RNP and the polycationic reagent.[298] Other methods require complexation methods such as tethering of the donor to the RNP complex.[299] Efficient codelivery of RNP with donor DNA in a single complexation step with one polymeric carrier would greatly simplify the complex protocol for achieving HDR editing with a nonviral vector.

In order to bind both RNP and donor DNA efficiently in one mixing step, a polymeric carrier must carry chemical functionalities that facilitate simultaneous binding of RNP and donor DNA. Our previous work (see *Chapter 3*) showed that quinine in the QCRs allowed for strong binding of plasmid DNA through both electrostatic and π-stacking interactions. For the case of the QCR containing HEA and quinine, called poly(quinine-*co*-HEA), we showed that the comonomer HEA facilitated interaction with BSA protein and subsequent efficient release of the plasmid. This evidence, along with literature precedent for HEA promoting protein binding,[272-274] suggests that a copolymer containing HEA could allow for efficient binding of a protein, such as Cas9-based RNP. Based upon this evidence, we hypothesized a HEA-quinine copolymer could allow for simultaneous binding of both donor DNA and RNP to form a single-carrier multi-component complex for CRISPR/Cas9 editing (Fig. 1). In this chapter, we 1) characterize multi-component complexes formed with the HEA-quinine QCR , 2) assess the ability of the multi-component complexes to achieve more efficient NHEJ and HDR genome editing with CRISPR/Cas9 in a model cell line,

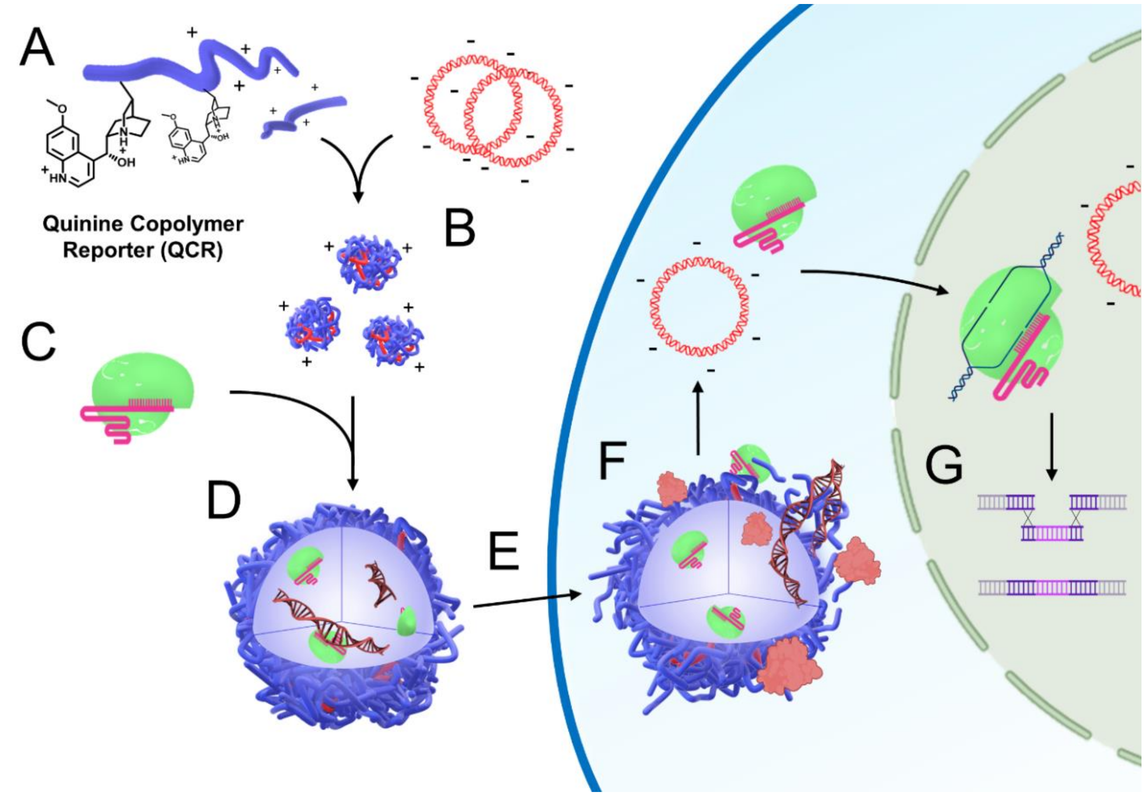

Figure 4.1. Steps towards complexation, delivery, and release of both donor plasmid and CRISPR ribonucleoprotein (RNP) with quinine copolymer reporter (QCR). (A) We solubilized the QCR in aqueous acetic acid solution. (B) Upon mixing with donor plasmid in water, the QCR and plasmid self-assemble to form polyplexes approximately 60 nm in hydrodynamic diameter through both electrostatic and π-stacking interactions. (C) The best editing performance was achieved by diluting the RNP in buffered cell media and adding it to the polyplexes after they had been formed. (D) Dilution of the QCR polyplexes with the RNP/media mixture causes formation of aggregates (approximately 1 µm in diameter) containing both plasmid and RNP. (E) Aggregation promotes sedimentation of these fluorescent particles ($\lambda_{ex} = 350$ nm, $\lambda_{em} = 450$ nm) onto HEK-293T cells, which allows for their uptake. (F) Unpackaging of the complexes by intracellular proteins was monitored directly by Raman spectral imaging. (G) A Traffic Light Reporter system (TLR) was used to monitor both repair by nonhomologous end-joining (NHEJ) and homology-directed repair.

4.3 Results and Discussion

4.3.1 *RNP is Bound in a Single-Carrier Multi-Component Complex*

In *Chapter 3,* we showed that the HEA-based QCR efficiently bound plasmid DNA. For this chapter, we assessed the ability of this polymer to simultaneously bind a plasmid along with RNP (Cas9 + sgRNA). The EMSA assay used in *Chapter 3* was modified with increased agarose and ethidium bromide concentration to assess binding of the QCR with Cas9, sgRNA, and plasmid simultaneously on the same gel. Overall, the gels in Figure 4.2 and 4.3A show that the QCR can bind both sgRNA and plasmid, separately and simultaneously. Figure 4.3A also suggests that the RNP can be bound by the QCR at N/Ps as low as N/P = 0.5. The ability of the QCR to bind RNP, however, is confounded by the gels in Figure 4.2, which shows that Cas9 migration can be impeded by both plasmid (Fig. 4.2A) and acetic acid (Fig. 4.2B). This is migration inhibition is likely due to aggregation of the Cas9 protein in the presence of plasmid and low pH conditions. To unequivocally determine if binding of the QCR to the RNP is occurring, complementary techniques are needed.

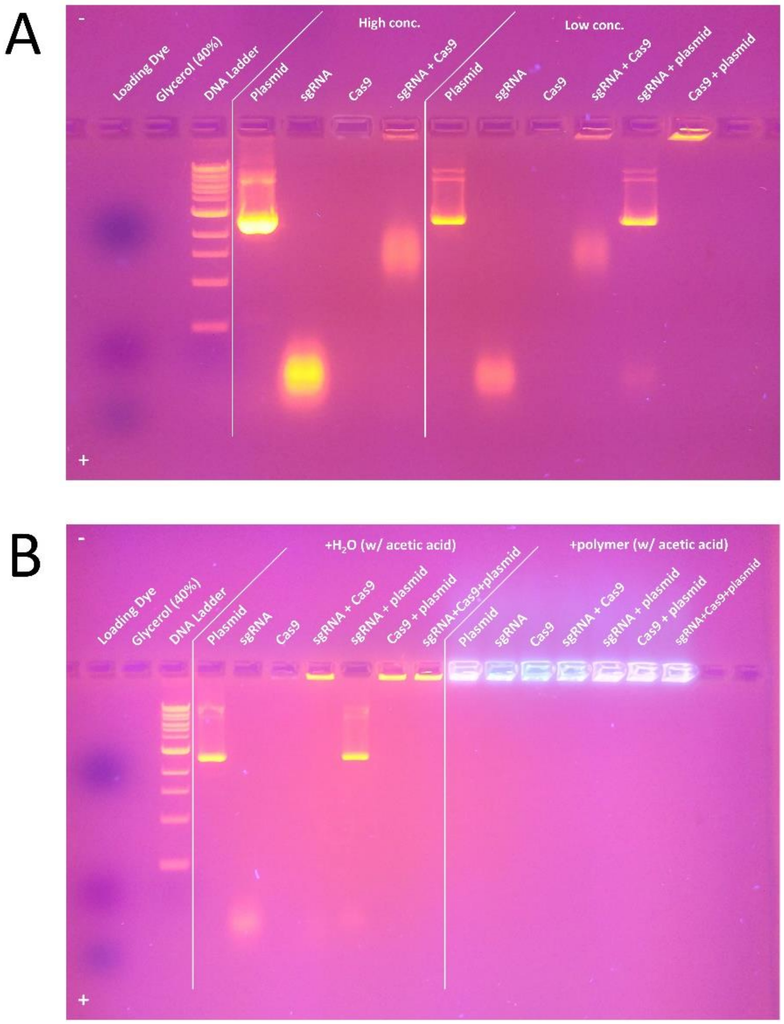

Figure 4.2. EMSA of QCR binding with Cas9, sgRNA, and plasmid. (A) Using increased agarose (1.2%) and ethidium bromide (1.67 µg/mL) concentrations, sgRNA (100 bases), and plasmid (4.7 kb) could be run and visualized simultaneously on one gel. “High conc.” denotes undiluted stock solutions (see *Section 4.5.4*) while “Low conc.” denotes dilution 1:1 with water. (B) The Cas9/nucleic acid samples were mixed with QCR at an N/P = 5 relative to total phosphate concentration (from both sgRNA and plasmid). For the left-hand samples, the Cas9/nucleic stock was mixed 1:1 (v/v) with diluted acetic acid (0.34% glacial acetic acid), while for the right-hand samples, the Cas9/nucleic acid solutions were mixed 1:1 (v/v) with acidic QCR solution.

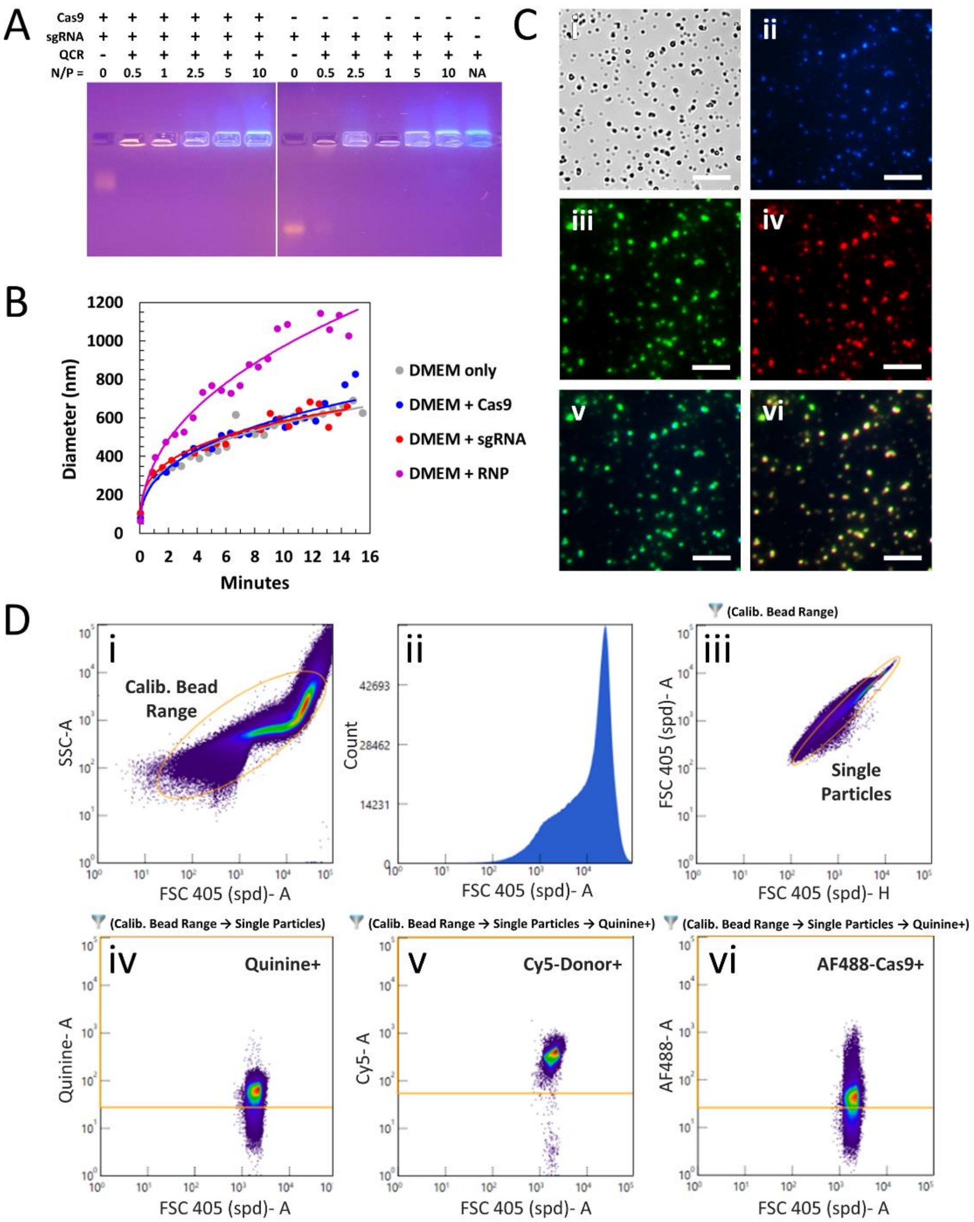

Figure 4.3. Both donor plasmid and RNP bind to QCR to form multi-component complexes. (A) We used an electrophoretic mobility shift assay (EMSA) to show that the migration of sgRNA and RNP are inhibited by the QCR. (B) We used dynamic light scattering (DLS) to examine kinetics of multi-component complex aggregation. The aggregation rate was fastest when the RNP was diluted in the cell media prior to its addition to the polyplexes. (C) The aggregates settled onto glass, which allowed us to use fluorescence microscopy to show the retention of both labeled donor plasmid and RNP in the QCR complex. Panels show (i) transmission, (ii) QCR, (iii) AlexaFluor 488 (AF488)-labeled RNP, (iv) Cy-5-labeled donor plasmid, (v) overlays of QCR and RNP, and (vi) overlay of QCR, RNP, and plasmid. Scale bar = 100 µm. (D) We used flow cytometry to quantify the number of QCR-containing complexes that contained AF488-labeled Cas9

(with and without sgRNA) and Cy5-labeled donor. Although pre-complexation of sgRNA improved the binding of the QCR to Cas9, the QCR could bind Cas9 without the presence of sgRNA, indicating that protein-polymer interactions contribute to QCR-RNP complexation. In addition, this analysis showed that RNP complexation with polyplexes was most efficient when the RNP was diluted in the cell media prior to complexation. Panels show gating for (i) particles between approximately 200-900 nm in size, (ii) histogram showing distribution of particle size range, (iii) gating for single particles, (iv) particles positive for QCR, (v) QCR particles containing Cy5-labeled donor plasmid, and (vi) QCR particles containing AF488-labeled RNP.

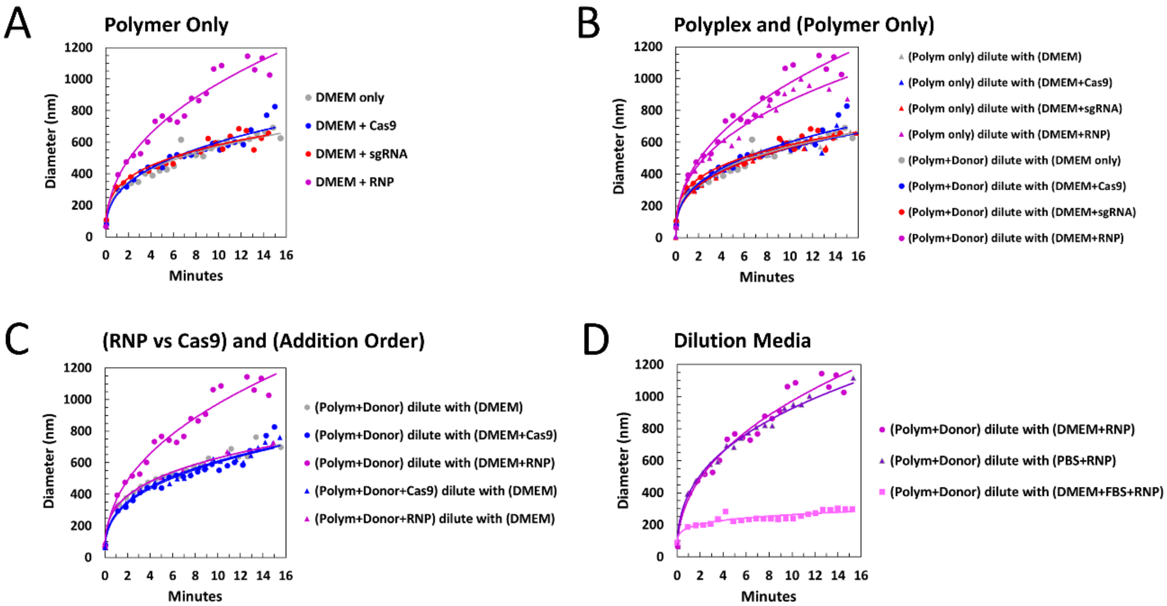

Figure 4.4. Kinetics of QCR aggregation in the presence of Cas9, sgRNA, and plasmid donor monitored by DLS. The components were mixed in accordance with the mixing protocol for transfection (see *Section 4.5.9*) where the polymer is mixed with donor in aqueous conditions prior to dilution with DMEM containing RNP (1 : 1.25 : 1 donor/Cas9/sgRNA ratio with QCR and donor at N/P = 5). The graphs compare the effect of QCR aggregation in DMEM (A) when both sgRNA and Cas9 are present together, (B) when donor plasmid is added the QCR prior to dilution with DMEM/RNP, (C) when RNP is added directly to the polyplexes instead of the DMEM solution, and (D) when DMEM contains FBS or is substituted with PBS.

EMSA assays require a higher concentration of nucleic acid than what is required for a bolus transfection. The standard transfection protocol for plasmid delivery requires mixing an aqueous plasmid solution (0.02 µg/µL) with an aqueous solution of polymer at an equal volume ratio to afford a solution with a prescribed N/P ratio (quinuclidine amines/DNA phosphate groups). These polyplexes in aqueous solution, which are on the order of 60 nm in hydrodynamic diameter, need to be diluted with cell media prior to being added to cells, typically at a 2:1 v/v ratio of cell media/polyplex solution. Dynamic light scattering and fluorescence microscopy were used in *Chapter 3* to assess the kinetics of QCR polyplex aggregation upon dilution in buffered cell media (see *Section 3.3.2).* This aggregation behavior was utilized to titrate the size and number of polyplexes delivered to the cells in a bolus transfection (see *Section 3.3.3*). Since RNPs are colloidally unstable in aqueous solution, I added the annealed RNPs directly to the DMEM used for polyplex dilution in the final mixing step. Using this method, RNPs would not be exposed to unbuffered media. The mass of RNP added was at a 1.25 : 0.25 : 1 mass ratio of Cas9/sgRNA/plasmid. Dynamic light scattering was then used to observe the aggregation kinetics of the QCR/plasmid/RNP complexes upon dilution in DMEM.

Figure 4.3B (equivalent to Figure 4.4A) shows that the aggregation rate of the QCR in DMEM increased when RNP (annealed Cas9 + sgRNA) was present in the DMEM. When used by themselves, neither Cas9 or sgRNA could induce this increased aggregation rate. This increased rate was still observed when donor plasmid was pre-mixed with the QCR in water (to form polyplexes 62 nm in diameter) prior to diluting with the DMEM/RNP solution (Fig. 4.4B). This effect was not observed, however, if the RNP was added directly to aqueous polyplex solution prior to diluting with DMEM (Fig. 4.4C). These results show that 1) sgRNA and Cas9 have a synergistic effect on QCR aggregation rate and 2) the order of addition matters for full complexation of the RNP. Adding the RNP to the DMEM instead of directly to the polyplex solution is preferrable for optimal RNP binding (see Table 4.1). Lastly, Figure 4D reaffirms (see *Sections 3.3.2* and *3.3.5*) how serum albumin strongly interacts with the QCR polymer and inhibits aggregation. Prior to entering the cell, this competitive binding deleteriously effects transfection. As shown in *Chapter 3*, however, competitive binding of intracellular proteins can allow for unpackaging of the cargo.

As shown in Figure 4.3A, the QCR complexes reach nearly 1 µm in hydrodynamic diameter after approximately 10 min of incubating in the DMEM/RNP solution, and the complexes begin to precipitate out of solution and deposit onto the cells adhered to the dish surface. Upon deposition, these particles can be directly observed with widefield microscopy. Figure 4.5 shows multi-component QCR complexes formed at a range of N/Ps (where the nucleic acid/RNP mass was held constant and the polymer amount was varied) after deposition onto the dish surface in the absence of cells. Note how the morphology of the complexes becomes more compact and spherical at an N/P of 5, which coincides with optimal N/P for gene editing (see Fig. 4.11).

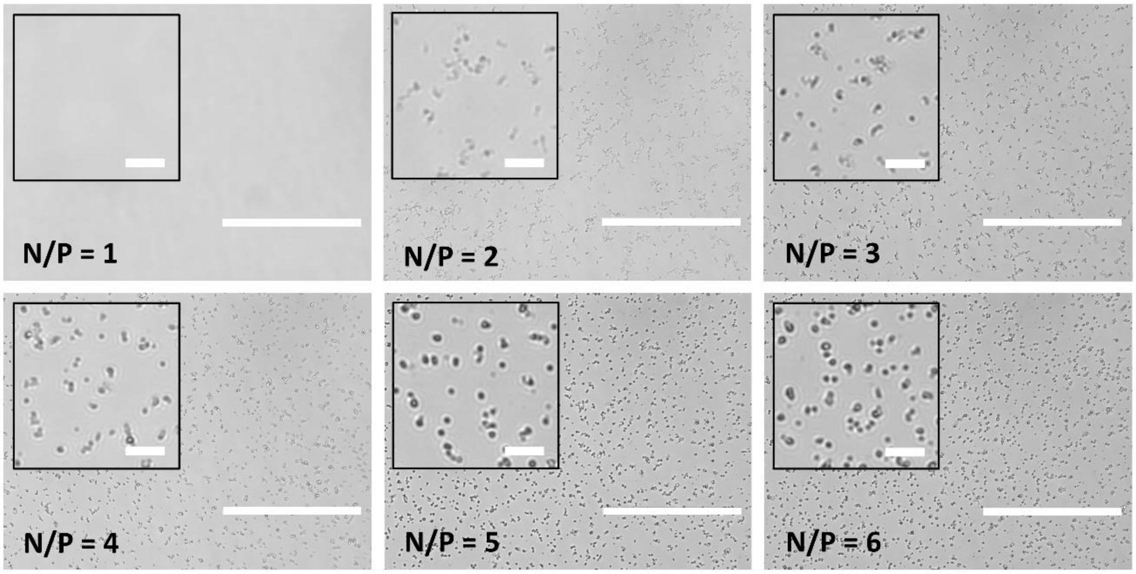

Figure 4.5. Widefield microscopy images showing multi-component (QCR/Donor/RNP) complex size and morphology is dependent on N/P ratio. Inset: scale bar = 10 µm. Large image: scale bar = 100 µm.

Although the EMSA and DLS studies suggest that the RNP in the DMEM is binding to the QCR polyplexes as they aggregate, direct visualization of the RNP is necessary to prove that binding is occurring. Cas9 was labeled with an Alexa Fluor 488 (AF488) dye and the donor plasmid was labeled with a cyanine 5 (Cy5) dye. With these dyes, along with the QCR's inherent fluorescence (see *Sections 1.5.6 and 3.3.3*), both the RNP and donor plasmid could be visualized with a fluorescence microscope. Using the deposition technique described above (Fig. 4.5), donor plasmid and RNP are visible and colocalized with the QCR particles (Fig. 4.3C). This shows that when the QCR polyplexes are diluted with the DMEM/RNP solution, the RNP complexes indeed bind to the growing aggregate. In order to determine whether the QCR particles can deliver the donor plasmid and RNP to cells, the fluorescently-labeled multi-component complexes were deposited onto HEK-293T cells in culture. Figure 4.6 shows the cells 48 hours following transfections. Due to multiple washing steps and replating of the cells, the complexes seen in the images (Fig. 4.6) are those remaining inside cells. It is clear to both donor plasmid and RNP are delivered to the cells via the QCR. Here, fluorescence microscopy provides qualitative evidence for the simultaneous binding and delivery of both RNP and donor plasmid with a single polymeric carrier.

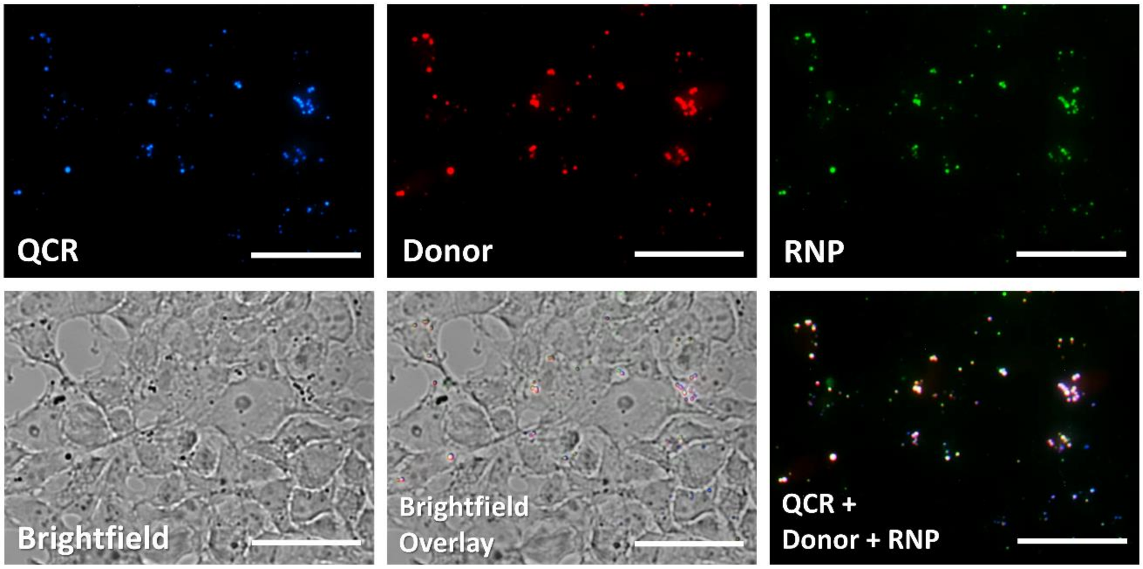

Figure 4.6. Fluorescence microscopic images of fixed HEK-293T cells 48 hrs after transfection containing multi-component (RNP/Donor/QCR) complexes. Fluorescence channels include QCR (DAPI filter), donor plasmid (Cy5), and Cas9 (AF488) with sgRNA. Scale bar = 50 µm.

Fluorescence microscopy is limited in the number of particles that can be analyzed, and for this system, requires that complexes have settled onto a surface prior to analysis. For higher-throughput assessment of multi-component complexes, we turned to flow cytometry. While flow cytometry is primarily used for the assessment of fluorescently-labeled cells, new flow cytometers are capable of analyzing small particles such as polyplexes.[300, 301] The manufacturer of the Reineke Group's flow cytometer claims that its light scattering detector is capable of detecting particles < 200 nm in diameter. Using polystyrene (PS) calibration beads, we verified that the small particle detector (spd) on the 405 laser line of our Bio-Rad ZE5 flow cytometer could distinguish PS beads ≥ 200 nm in diameter from background signal (Fig. 4.7). Below this threshold (60-150 nm), PS beads yield a scattering signal, but without a corresponding fluorescence signal, however, it is difficult to confidently differentiate PS beads from background events. Luckily, polyplexes formed in aqueous conditions with the QCR polymer can be discriminated due to the QCR's fluorescence. Figure 4.8A and Figure 4.8B shows a comparison between PS beads (d_h = 60 nm) and QCR polyplexes (d_h = 62 nm, by DLS) formed with Cy5-labeled plasmid in aqueous solution. While providing nearly identical scattering plots, the QCR particles can be discriminated by their quinine fluorescence. Of the quinine positive particles, 99.98% are Cy5+, which indicates nearly all QCR particles contain donor plasmid.

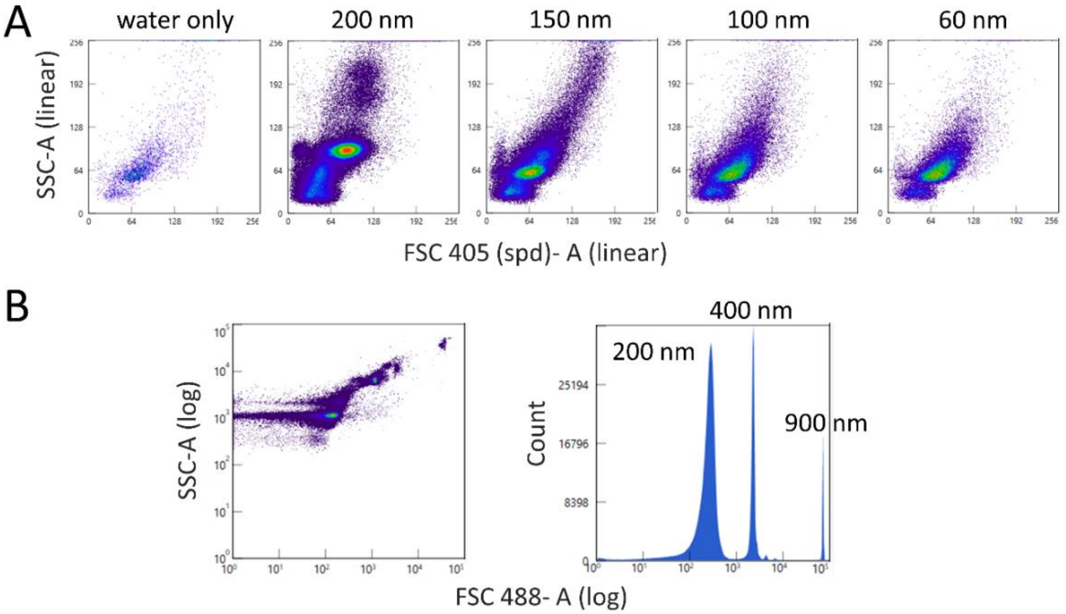

Figure 4.7. Flow cytometry of polystyrene (PS) calibration beads. (A) Scattering plots of PS beads 60-200 nm in diameter using the small particle detector (spd) with the 405 nm laser. (B) The scattering plot (left) and count histogram (right) with 200, 400, and 900 nm PS beads.

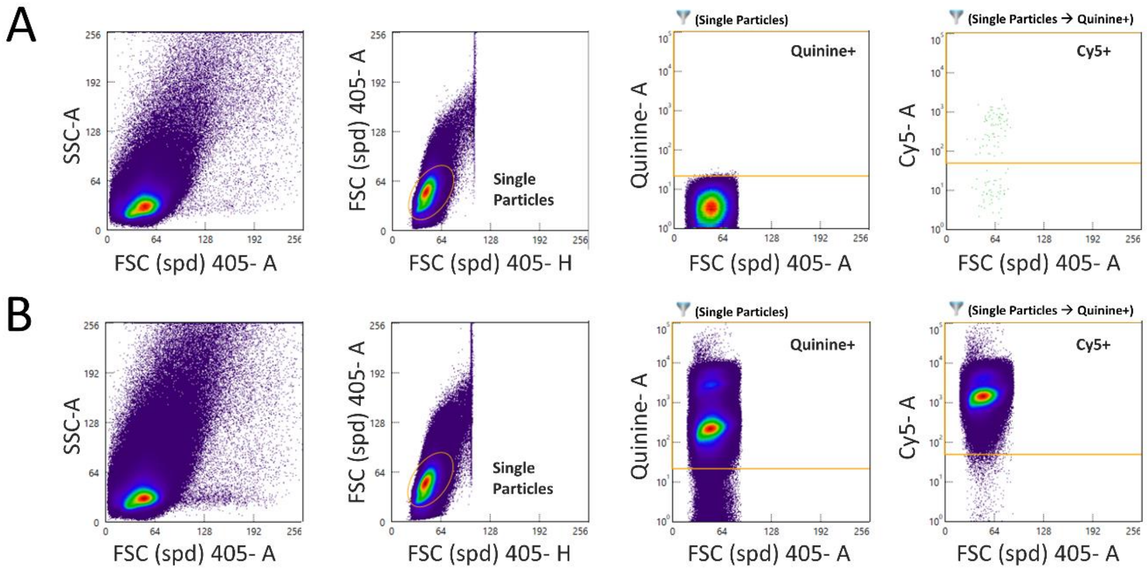

Figure 4.8. Flow cytometry of QCR polyplexes with Cy5-labeled donor plasmid. (A) PS calibration beads (60 nm). (B) QCR polyplexes after mixing QCR with Cy5-labeled donor plasmid at N/P = 5. Non-labeled plasmid was used as a negative control for Cy5 gating.

Using PS beads 200-900 nm in diameter, the detector voltage was adjusted for viewing the scattering signal of particles in this range (Fig. 4.7B), which is approximately the size range of polyplex aggregates within the first 10 minutes of aggregation in DMEM. Using labeled donor plasmid and Cas9 protein, the components within the QCR particles could monitored after dilution in DMEM (Fig. 4.3D). Combinations of the components could then be used to characterize the binding contribution of each component in multi-component QCR complex (Table 4.1). Some of the conclusions from this study are discussed here. When the DMEM/RNP solution is added to the QCR polyplex in the manner performed for the transfection experiments (line 7), nearly all the QCR+ particles retain donor plasmid and 99% of particles bind RNP to the complex. When the RNP is added directly to the polyplex solution instead of the DMEM solution, the number of QCR+ particles containing RNP decreases to 73% and suggests that the order of mixing the components is important to optimal particle formation, which supports our DLS data (Fig. 4.4C). In addition, the QCR is capable of forming complexes with RNP by itself without donor plasmid present (lines 3 and 6). The binding efficacy is diminished, but not entirely eliminated, when only Cas9 is used (lines 2 and 5). This shows that the sgRNA enhances binding of the QCR to the Cas9 protein, which is consistent with the synergistic effect of Cas9 and sgRNA on aggregation rate shown in the DLS (Fig. 4.3B). It is important to note, however, that over 60% of QCR+ particles are Cas9+ when Cas9 is presented without the sgRNA. This supports the hypothesis that QCR binding to RNP is facilitated, at least partially, through polymer/protein interaction. Polymer binding to the Cas9 is then enhanced when sgRNA is present with the Cas9 protein.

Table 4.1. Flow cytometry analysis of multi-component complex composition

#	Components with QCR (Pre-DMEM)	Components in DMEM	% QCR Particles Donor+	% QCR Particles Cas9+
1	Donor [a]		99.98	0.00
2	Cas9 only [b]		0.00	90.29
3	RNP [c]		0.00	99.85
4	Donor + RNP		99.86	72.80
5		Cas9 only	0.00	61.86
6		RNP	0.00	99.74
7	Donor	RNP	99.97	98.93

[a] Donor plasmid was labeled with Cy5 and mixed with QCR at N/P = 5.

[b] Cas9 was labeled with AF488.

[c] RNP was formed with Cas9 labeled with AF488 and unlabeled sgRNA. The components are mixed at a 1 : 1.25 : 1 donor/Cas9/sgRNA ratio with QCR and donor at N/P = 5.

4.3.2 *Improved CRISPR/Cas9 Editing with Fluorescence-Based Assay*

We showed that the QCR can simultaneously bind both donor plasmid and RNP and deliver the components into HEK 293T cells in culture. Next, we assessed the ability of the QCR to promote gene editing with the CRISPR/Cas9 system. For testing the ability of their statistical copolymer to deliver RNP and induce NHEJ editing (see *Section 1.4.4* and *1.4.5*), Kumar et al. used an HEK 293T cell line engineered with a Traffic Light Report (TLR) system.[302] This cell line was engineered by Osborn et al. to optimize conditions for Cas9/donor delivery and promote therapeutic gene editing for Fanconia anemia, a congenital blood disorder.[303] The Osborn group modified the TLR system with a portion of the *FANCC* gene identified as a target for therapeutic Cas9-based editing and then engineered a 293T cell line to contain the TLR system. Editing of these cells with RNPs (containing sgRNA with the complimentary *FANCC* sequence) allowed for a fluorescent protein-based signal for gene editing. Editing by mutational NHEJ leads to expression of the fluorescent protein mCherry while editing by HDR leads to expression of enhanced green fluorescent protein (eGFP or GFP) (Fig. 4.9A-B). This method allows for efficient quantification of genome editing with flow cytometry (see Fig. 4.10 for gating scheme), which allows us to analyze the larger number of samples required for optimization studies. In addition, it is important to note that approximately one third of mutations by NJEH in this assay lead to the particular frameshift allowing for mCherry expression, which means the percent of cells that have undergone mutational NHEJ is approximately 3× the percentage of mCherry+ cells in the assay.[302] In contrast, each cell that has undergone successful gene editing by HDR should express GFP.

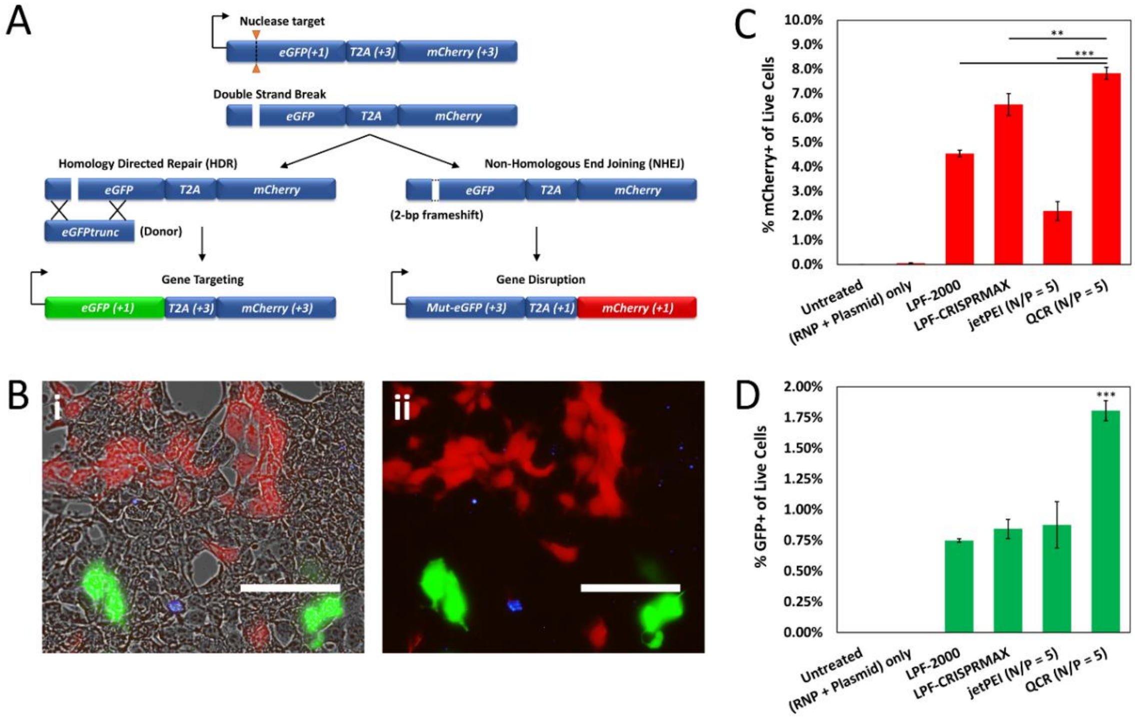

Figure 4.9. The QCR platform increased both HDR and mutational NHEJ compared to Lipofectamine CRISPRMAX. (A) We monitored relative HDR and NHEJ editing rates using a TLR fluorescence-based system. A 293T cell line was modified with a cassette containing a truncated GFP, frameshifted mCherry, and a Cas9 target adopted from the *FANCC* gene. With this assay, HDR editing leads to GFP expression while approximately 1/3 of mutational NHEJ editing events leads to mCherry expression. (B) Fluorescence microscopy can be used to visualize edited cells in culture. Panels include (i) brightfield overlay and (ii) fluorescence channels containing mCherry (red), GFP (green), and QCR (blue). Scale bar = 200 µm. (C-D) The gene editing of TLR-modified 293T cells was monitored with flow cytometry by quantifying live cells expressing (C) mCherry and (D) GFP. The analysis was performed 5 days following transfection with Lipofectamine (LPF), jetPEI, and QCR reagents bound with RNP and donor plasmid at optimized concentrations (see Fig. 4.11-13). The QCR complexes showed significant increases in both NHEJ and HDR compared to commercial controls such as LPF 2000 and LPF-CRISPRMAX (** $p<0.01$, *** $p<0.001$).

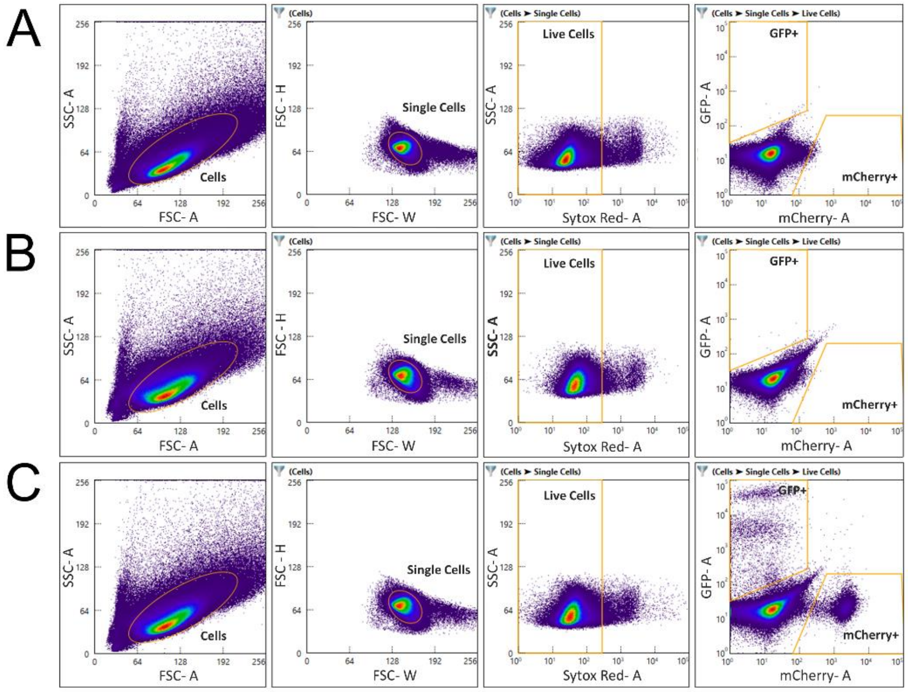

Figure 4.10. Flow cytometry gating scheme for quantifying GFP+ and mCherry+ cells in HEK-293T cells with TLR system after transfection with QCR complexes. Samples include: (A) untreated cells, (B) cells treated with QCR/donor/Cas9/neg. control sgRNA, and (C) cells treated with QCR/donor/Cas9/targeting-sgRNA. QCR particles remaining in the cells can lead to minor autofluorescence in both the GFP and mCherry channels (B and C), creating a GFP+/mCherry+ "tail" that can be gated out for accurate quantification of fluorescence only due to editing.

We performed a series of gene editing studies with TLR-modified 293T cells that aimed to optimize the conditions for both jetPEI and QCR-based delivery of RNP+donor plasmid (Fig. 4.11-12). We studied the effect of N/P ratio (1-6) on gene editing rates and cytotoxicity for both jetPEI and the QCR (Fig. 4.11). The gene editing efficacy of these systems increases with increasing N/P ratio, but the editing rates plateaus at an N/P = 5, with marginal increases in both HDR and NHEJ between N/P of 5 and 6. Further increasing the N/P beyond 5 (up to 8) for both jetPEI and QCR did not lead to gains in gene editing (Fig. 4.12). Other modifications, including increasing the quinine content of the QCR, increasing the amount of RNP relative to donor plasmid, or substituting some donor plasmid with ssDNA-oligo-donor did not lead to any further improvements in gene editing (Fig. 4.12). In addition, we tested the direct delivery of RNP versus the delivery of plasmids encoding sgRNA and Cas9 (Fig. 4.13). The data showed that comparable levels of editing could be achieved with both RNP and RNP-encoding plasmids, showing the flexibility of the QCR system to deliver CRISPR/Cas9 editing components in various forms.

Figure 4.13 shows the optimization of the delivery of RNP+donor with commercial cationic lipid-based transfection reagents. Several variations of doses and component ratios were tested with both Lipofectamine (LPF)-2000 and LPF-CRISPRMAX (see Fig. 4.13 and *Section 4.5.9.2*). In this study, these lipid-based transfections were compared head-to-head with the optimized delivery conditions of QCR and jetPEI (1 µg of plasmid per well, mass ratios of 1 : 1.25 : 0.25 plasmid/Cas9/sgRNA, N/P = 5 relative to donor plasmid). The best performing condition for each type of transfection reagent is summarized in Figure 4.9C-D. While the LPF reagents achieved relatively high mCherry expression (~ 6.0% mCherry+), their GFP expression remained low (< 1.0%). These editing levels were consistent with those achieved by Osborn et al. using LPF 2000.[303] HDR editing was not be improved by replacing the plasmid donor with an oligo donor (Fig. 4.13A). The other commercial reagent, jetPEI, had a higher GFP/mCherry ratio than LPF, but had an overall lower expression of both. In contrast, the QCR increased mCherry expression by 20% and GFP expression by more than double over LPF-CRISPRMAX, while maintaining statistically equivalent cell viability over the course of 5 days relative to untreated cells (Fig. 4.13B). This study shows that the QCR system can deliver RNP and donor to a model cell line in culture and achieve both NHEJ- and HDR-based gene editing that surpasses those achieved with commercial transfection reagents that are gold standards for non-viral chemical-based transfections.

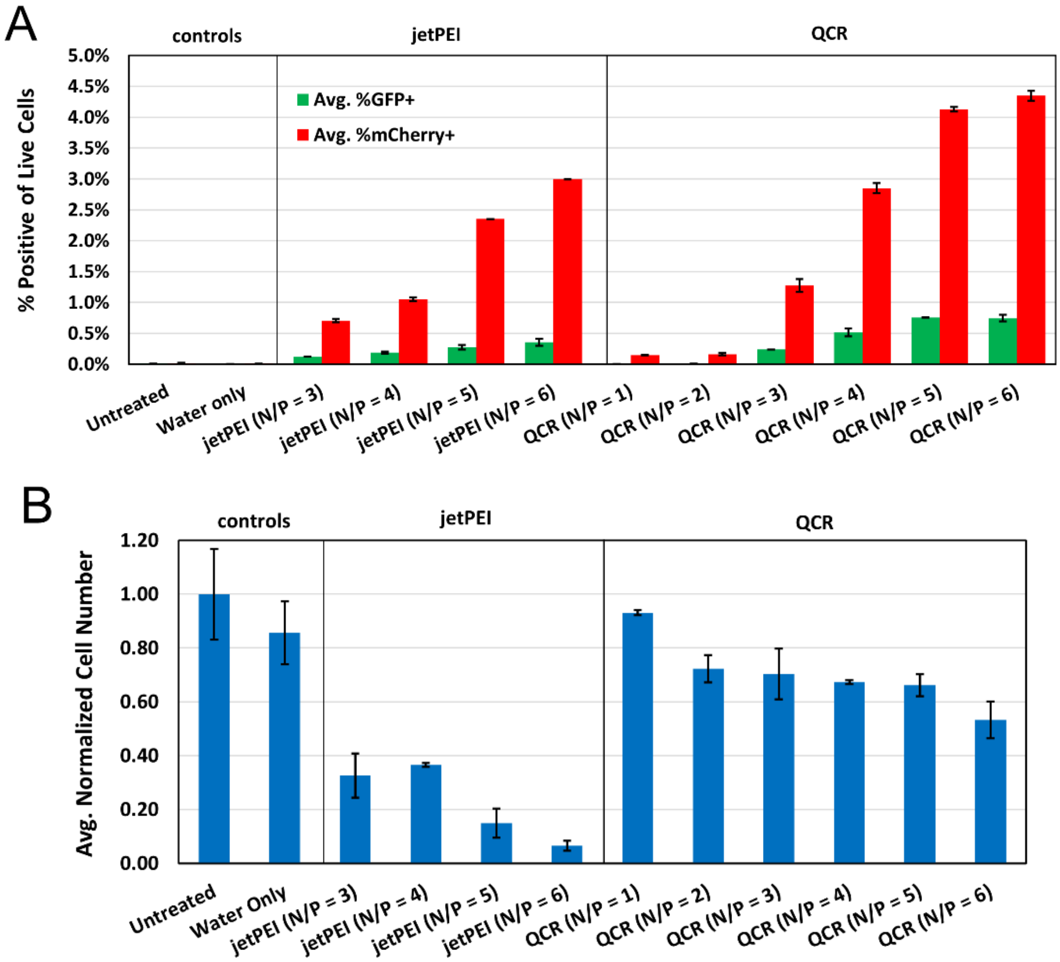

Figure 4.11. Optimization study of CRISPR-based gene editing in 293T cells with QCR and jetPEI over a range of N/P ratios. (A) Quantification of gene editing with TLR-modified 293T cells (see Fig. 4.9A) was performed with flow cytometry five days following transfection with multi-component RNP/donor complexes (1 µg of plasmid donor per well, mass ratios of 1 : 1.25 : 0.25 donor/Cas9/sgRNA, and N/P is polymer/donor). (B) Relative cell counts of transfected samples were ascertained with a Cell Counting Kit 8 (CCK-8) and spectrophotometric plate reader five days following transfection with RNP complexes to judge toxicity of treatments relative to untreated control.

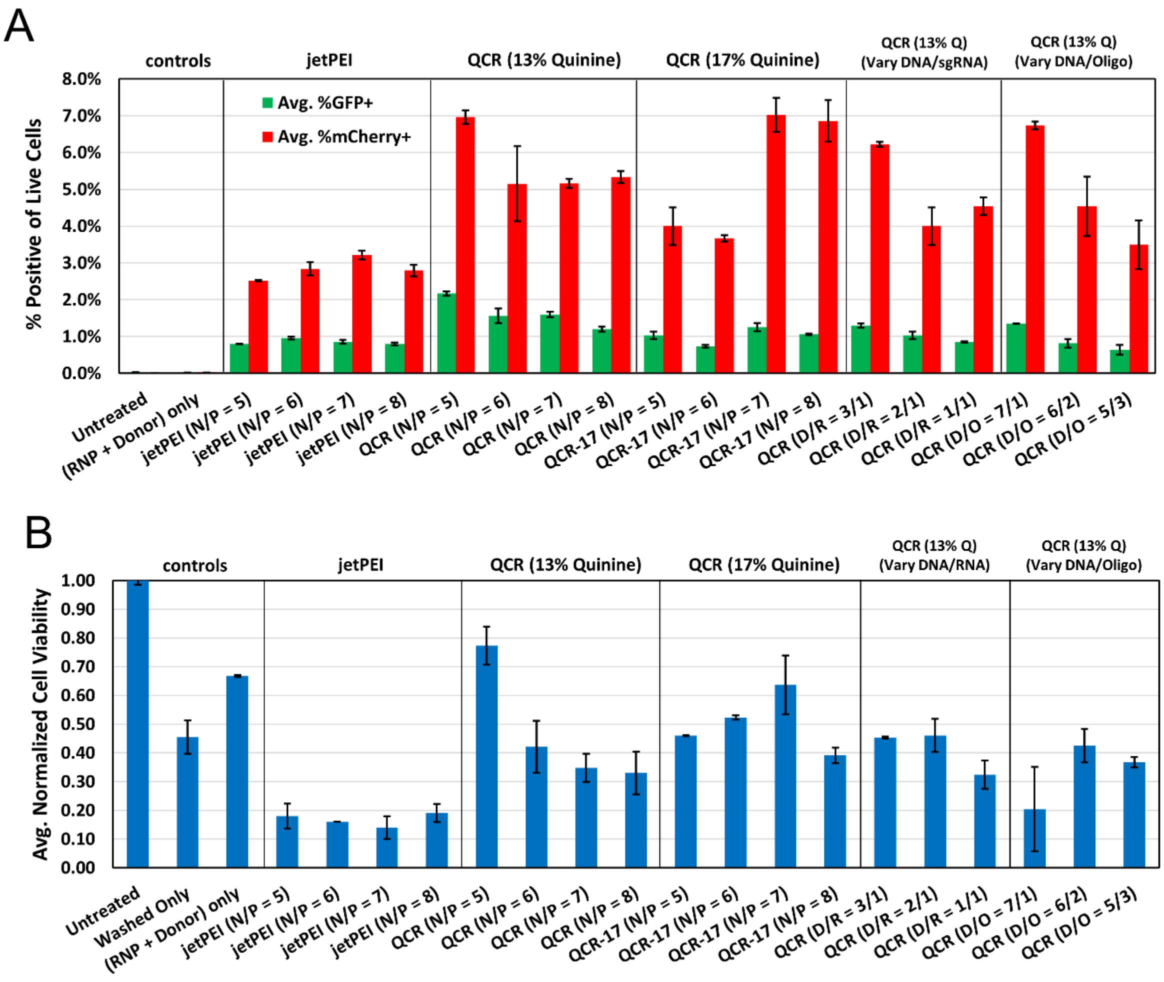

Figure 4.12. Optimization study of CRISPR-based gene editing in 293T cells with modifications to reagent N/P ratio, quinine incorporation in QCR, plasmid/RNP ratio, and plasmid/oligo ratio. (A) Quantification of gene editing with TLR-modified 293T cells (see Fig. 4.9A) was performed with flow cytometry five days following transfection with multi-component RNP/donor complexes (1 µg of plasmid donor per well, mass ratios of 1 : 1.25 : 0.25 donor/Cas9/sgRNA, and N/P is polymer/donor). QCR-17 represents a QCR variation containing 17% quinine by molarity. Another variable tested included increasing the amount of RNP relative to donor (plasmid DNA/sgRNA ratio = D/R) while maintaining 1 µg of plasmid donor per well. In addition, some plasmid DNA was substituted with ssDNA oligo donor (plasmid DNA/oligo = D/O) while maintaining a total of 1 µg per well. (B) Relative cell counts of transfected samples were ascertained with a CCK-8 kit and spectrophotometric plate reader five days following transfection with RNP complexes to judge toxicity of treatments relative to untreated control.

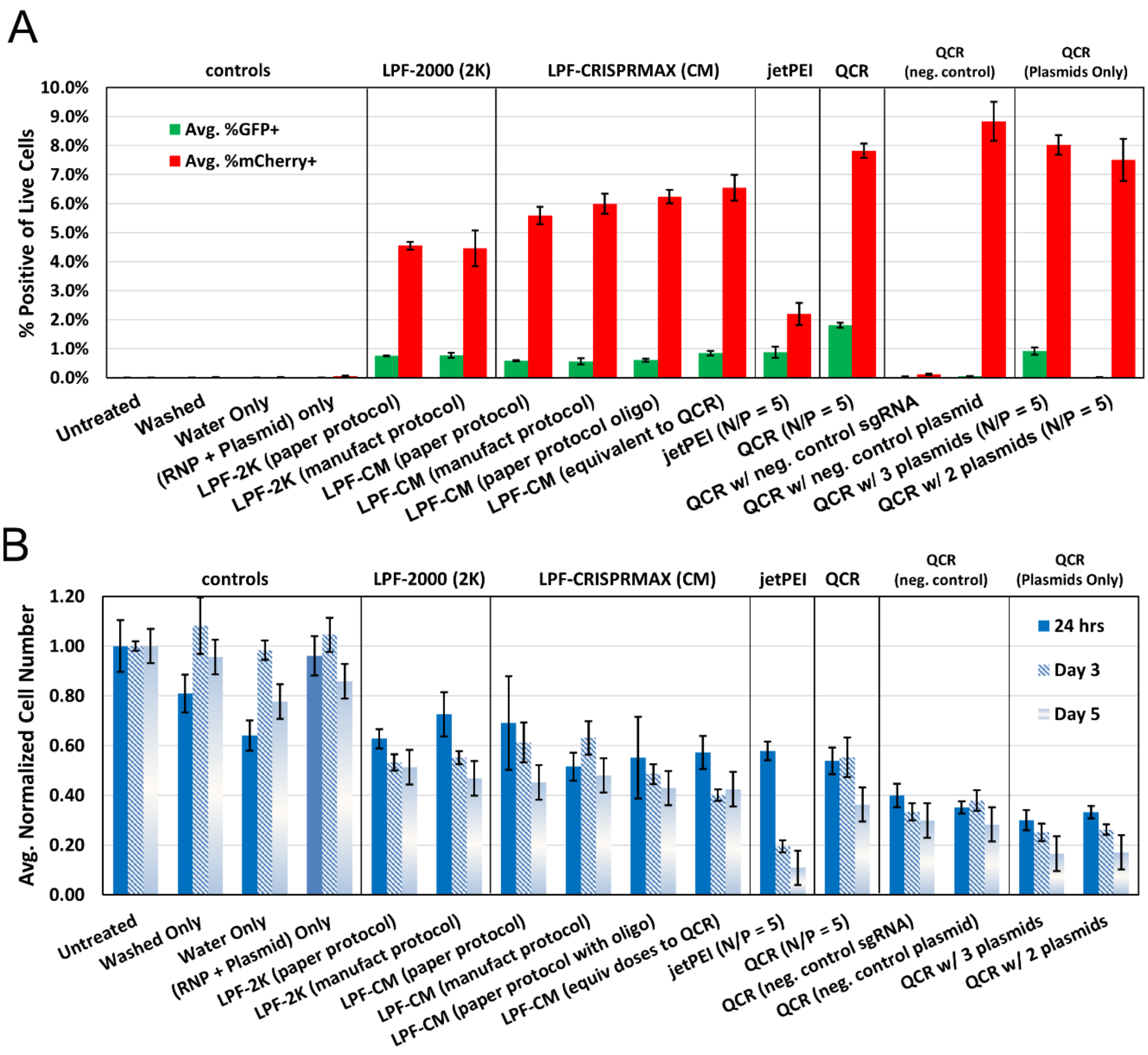

Figure 4.13. Optimization study of CRISPR-based gene editing in 293T cells with various conditions for Lipofectamine (LPF)-2000 (2K) and LPF-CRISPMAX (CM) reagents, negative controls, and Cas9- and sgRNA-encoding plasmids. (A) Quantification of gene editing with TLR-modified 293T cells (see Fig. 4.9A) was performed with flow cytometry five days following transfection with multi-component RNP/donor complexes. The optimized conditions from Fig. 4.11-12 for jetPEI and QCR were compared to LPF reagents with varying component ratios. "Paper protocol" refers to protocol by Yu et al.[304] (see *Section 4.4.9.2* for description of each protocol variation). A non-targeting sgRNA and donor plasmid (pCMV-*lac*Z) were used as negative controls. The RNP was also replaced with plasmids encoding for sgRNA and Cas9. The samples labeled "3 plasmids" includes donor plasmid while the sample "2 plasmids" is only sgRNA and Cas9 plasmids. (B) Relative cell counts of transfected samples were ascertained with a CCK-8 kit and spectrophotometric plate reader 1, 3, and 5 days following transfection with RNP complexes to judge toxicity of treatments relative to untreated control.

4.4 Concluding Remarks and Future Work

The work we performed in this chapter shows that our QCR can bind both plasmid and RNP simultaneously and deliver the components to cells in culture. Using the inherent fluorescence of the QCR, we were able to use flow cytometry to quantify the percent of QCR particles containing RNP. This methodology showed that Cas9 alone could bind the QCR to some degree, as hypothesized, but binding was improved with sgRNA annealed to the Cas9. This fluorescence-based analysis, however, leaves room for further improvement in the quantification of these multi-component complexes. For example, we aim to quantify the concentration of these components with the complexes and to better understand the binding interactions between these components. As shown in *Chapter 2-3*, the quinine within the QCR allows for analyzing these complexes with Raman microscopic imaging. Dr. Ariel Alperstein in the Frontiera Group and myself have analyzed the Raman spectrum of the RNP and adapted the Raman microscopic imaging protocol from *Chapter 3* for use with a more sensitive instrument and cell fixation protocol requiring no glycerol. With these modifications to our protocol, and with the continued research support of Dr. Alperstein, Punarbasu Roy, and Nick Kreofsky, we have begun to understand how the RNP in the complex influences the binding of QCR with its cargo, including the donor plasmid. In addition, these modification to our protocol may allow us to observe the Raman bands of the nucleic acids directly instead of indirectly through nucleic acids causing shifts to the Raman bands of quinine. Such advances would open doors to understanding the molecular binding interactions governing the packaging/unpackaging of polyplexes in the intracellular space.

In this chapter, we also showed that the simultaneous delivery of RNP and donor plasmid with the QCR can achieve higher gene editing rates than gold-standard nonviral transfection reagents such as jetPEI and Lipofectamine CRISPPRMAX in a model cell line. In developing their potential gene therapy treatment for Fanconi anemia, Osborn et al.[303] and Skvarova et al.[305] used Lipofectamine (2000 and 3000) for preliminary editing studies in 293T cells, but needed to use electroporation to achieve editing in primary fibroblasts. In *Chapter 3*, we showed that the QCR could transfect keratinocytes far more efficiently than Lipofectamine (Fig. 3.23). Using a more effective transfection agent, such as our QCR, may allow for editing of primary cells without the significant toxicity associated with electroporation. In addition, the QCR makes RNP-containing complexes amenable to both fluorescent and Raman imaging, giving us insight into intracellular trafficking and unpackaging dynamics. This diagnostic ability will help us titrate transfection conditions to achieve optimal delivery and unpackaging performance for each target cell type.

4.5 Experimental

4.5.1 *Materials*

4.5.1.1 Nucleic Acids/Proteins

The single guide RNA (sgRNA) has a sequence of GCACCUAUAGAUUACUAUCCGUUUUAGAGCUAGAAAUAGCAAGUUAAAAU AAGGCUAGUCCGUUAUCAACUUGAAAAAGUGGCACCGAGUCGGUGCUUUU and was manufactured by Synthego (Menlo Park, CA, USA).[114, 303] The ssDNA-TLR-donor oligo (55.8 kDa) was purchased from IDT (Coralville, IA, USA). The sNLS-SpCas9-sNLS nuclease (used for editing experiments), pZsGreen plasmid (4.7 kb), and donor plasmid (D14, 6.2 kb)[302] was produced by Aldevron (Fargo, ND, USA). The negative control plasmid (pCMV-*lac*Z, 7.1 kb) was purchased from PlasmidFactory GmbH & Co. KG (Bielefeld, Germany).[262] The negative control sgRNA (TrueGuide™ sgRNA Negative Control, non-targeting 1) was purchased from Thermo Fisher Scientific (Waltham, MA, USA). The donor plasmid was labeled with the *Label* IT®, Nucleic Acid Labeling Kit, Cy®5 sold by Mirus Bio (Madison, WI, USA) following manufacturer's protocol. The AlexaFluor 488-labeled Cas9 was made with lyophilized Cas9 protein purchased from Sigma-Aldrich (St. Louis, MO, USA) and labeled with the AlexaFluor 448 Protein Labeling Kit, produced by ThermoFisher Scientific following the manufacturer's protocol.

4.5.1.2 Cell Culture/Biological Assay Reagents

The cell culture reagents Dulbecco's Modified Eagle Medium (DMEM; high glucose, pyruvate, and GlutaMAX™ supplemented), Fluorobrite™ DMEM (phenol red-free media), reduced serum medium (Opti-MEM), Antibiotic-Antimycotic (AB/AM), trypsin-

EDTA (0.05%) with and without phenol red, phosphate buffered saline (PBS) pH = 7.4, UltraPure™ DNAse/RNAse-Free distilled water (diH$_2$O) was purchased from Thermo Fisher Scientific. Premium heat inactivated fetal bovine serum (HI FBS, US Sourced) was purchased from Corning (Corning, NY, USA). To perform EMSAs, low-electroendosmosis (EEO) agarose, the tris-acetate-EDTA (TAE), glycerol, and UltraPure™ ethidium bromide (10 mg/mL) were purchased from Thermo Fisher Scientific; the Quick-Load® 1 kb Extend DNA Ladder was purchased from New England Biolabs (Ipswich, MA); and the Agarose Gel Loading Dye (6×) Glycerol Based was purchased from Boston BioProducts (Ashland, MA). The transfection reagents Lipofectamine™ 2000 and Lipofectamine™ CRISPRMAX™ were purchased from ThermoFisher Scientific, and jetPEI® was purchased from Polyplus-transfection (New York, NY, USA). The flow cytometry reagents, SYTOX™ Red Dead Cell Stain and the 3000 Series Nanosphere™ Size Standards, were purchased from ThermoFisher Scientific. The cell counting kit (CCK-8) was purchased from Dojindo Molecular Technologies (Rockville, MD, USA). Collagen I coated 24-well microplates were purchased from ThermoFisher Scientific and glass-bottom dishes (35 mm, #1.5) were purchased from MatTek (Ashland, MA, US). Cells were fixed with Invitrogen™ Image-iT™ Fixative solution (formaldehyde 4% w/v, methanol-free) produced by ThermoFisher Scientific.

4.5.1.3 Cell Line

Human embryonic kidney cells (HEK 293T) were engineered to contain a traffic light reporter cassette[302] with *FANCC* gene-specific target region,[303] and were received as a gift from the laboratory of Mark Osborne at the University of Minnesota (UMN) and subcloned by the Genome Engineering Shared Resource at the UMN.

4.5.2 *Instrument Details*

4.5.2.1 Polyplex/Biological

Dynamic light scattering (DLS) measurements were made with a DynaPro® Plate Reader (Wyatt Technologies; Santa Barbara, CA, USA). EMSA gels were illuminated using a Bi-O-Vision™ ultraviolet (UV) transilluminator (Spectroline; Westbury, NY, USA) and photographed with a 16 megapixel digital camera with 28 mm lens (LG G4; Seoul, South Korea). Cell suspensions were counted with a Countess® II automated cell counter (ThermoFisher Scientific; Waltham, MA) with dead cell discrimination by dilution (1:1) with trypan blue (0.4%). Fluorescently labeled multi-component polyplexes and cell fluorescence quantification were analyzed with a ZE5™ Cell Analyzer with 355, 405, 488, 561, and 640 nm lasers (Bio-Rad; Hercules, CA). Widefield fluorescence microscopy was carried out using an EVOS FL Digital Microscope with EVOS LED light cubes including DAPI (ex: 357/44, em: 447/60), GFP (ex: 470/22, em: 525/50), Texas Red (ex: 585/29, em: 628/32), and Cy5 (ex: 628/40, em: 685/40) (AMG Life Technologies; Grand Island, NY).

4.5.3 *Polymer Synthesis and Characterization*

The Quinine Copolymer Reporter (QCR) is a copolymer of 2-hydroxyethyl acrylate (HEA) and quinine that is produced by thermally-initiated free radical copolymerization. The QCR batch used for this study was synthesized and characterized using our previously established protocol (see *Section 3.5.3.1*) and was found to contain 13% quinine by molarity.

4.5.4 *Electrophoretic Mobility Shift Assay*

For the electrophoretic mobility shift assays (EMSAs), agarose gels were formed with TAE buffer solutions containing 1.2% agarose (dissolved by heating) followed by addition of ethidium bromide (1.67 μg/mL) prior to gel formation. Cas9, sgRNA, and plasmid were dissolved in PBS at concentrations of 0.802, 0.160, and 0.160 μg/μL. These stocks were either run undiluted (see "high concentration" in Fig. 4.2A) or diluted with polymer solution (see "low concentration" in Fig. 4.2A and all samples in Fig. 4.2B) at 1:1 volume ratio. When the plasmid and sgRNA were combined together, they were diluted 3:1 plasmid/sgRNA. When combined with Cas9, the nucleic acid stock solution (7.5 μL), containing sgRNA and/or plasmid, was mixed at an equal volume ratio with the Cas9 stock (7.5 μL) and left to anneal for 10 min. Meanwhile, the QCR stock was diluted for N/P = 5 (see *Section 4.5.9.1*) relative to the molarity of phosphates (from both sgRNA and plasmid), and the resulting diluted QCR stock (15 μL) was combined at an equal volume ratio with the Cas9/sgRNA/plasmid solution (15 μL). If no polymer was present, either water (see "low concentration" in Fig. 4.2A) or 0.34% glacial acetic acid ("no polymer" samples in Fig. 4.2B) was used to dilute the Cas9/sgRNA/plasmid solution. The combined solution (30 μL) was spiked with 40% glycerol in water (6 μL), and an aliquot of the mixed solution (25 μL) was loaded onto the gel. The gel was run at 70V for 90 min, and the gel was imaged by UV transilluminator.

4.5.5 *Fluorescence Microscopy of Multi-Component Polyplexes*

Imaging of the QCR complexes was achieved by letting the multi-component complexes aggregate in cell media, settle and adhere onto glass coverslips. The presence of Cas9 and donor plasmid within these complexes could be observed by using fluorescently-labeled

Cas9 (AlexaFluor 488) and fluorescently-labeled donor plasmid (Cy5). These components were complexed with the QCR in the same manner as their delivery for transfections (see *Section 4.5.9.1*) with phenol red-free DMEM. For imaging of particles only, a droplet of the particle suspension (~200 µL) was placed on a glass coverslip, and the particles were allowed to settle onto the coverslip (~30 min). The coated coverslips were rinsed with PBS and placed in a dish containing PBS. The cells were imaged using an EVOS widefield fluorescence microscope.

4.5.6 *Dynamic Light Scattering*

The change in hydrodynamic diameter (d_h) of the QCR-based multi-component polyplexes in buffered media monitored over time using a Wyatt DynaPro Plate Reader at 25 °C. The polymer and donor DNA were mixed together in water as discussed in the transfection protocol (see *Section 4.5.9.1*). The d_h of these polyplexes in aqueous media are stable over time, and their measurement served as the value for time (t) = 0 min. The polyplexes were diluted (3×) with phenol red-free DMEM containing RNP (at the concentration described previously), and the time between the addition of media and the start of the kinetic run was noted as the first timepoint. The measurement at each timepoint consisted of 10 acquisitions (5 seconds each).

4.5.7 *Flow Cytometry of Multi-Component Polyplexes*

Upon dilution of the QCR-based multi-component polyplexes in buffered cell media, increased particle diameters (200-1000 nm within 5-10 min) allows for analysis by flow cytometry. Size standards (3000 Series Nanospheres with diameters of 200, 400, 600, and 900 nm) were used as calibration beads (diluted 10,000× in PBS) to adjust the FSC vs SSC voltages for analysis of QCR-based multi-component polyplexes within a log-based plot. The complexes were formed following the same procedure as the transfection (see above) and analyzed between 5-10 minutes following dilution in DMEM. The gating scheme for the analysis of the particles is shown in Figure 4.3D. The FSC was obtained on the 405 nm laser with a small particle detector. Quinine fluorescence was monitored with the 355 nm laser, while the AF488-labeled Cas9 and Cy5-labeled donor plasmid were monitored with the 488 and 650 nm lasers, respectively. Particle counts ranged between 1-5 × 10^6. Gates for QCR(+) particles was set with Nanosphere calibration beads serving as a negative control. Gates for QCR-complexes containing AF488(+) Cas9 or Cy5(+) donor plasmid was determined with QCR-complexes containing AF488(-) Cas9 and/or Cy5(-) plasmid serving as negative controls.

4.5.8 *Cell Culture and Plating for Transfection*

The HEK 293T cells were cultured in DMEM containing FBS (10%) and AB/AM. The cells were cultured in 75 cm^2 flasks at 37 °C under 5% CO_2 atmosphere. The cell confluency was maintained below 70%, and the cells were passaged regularly every 2-3 days without going above 20 passages. Cells were plated on 24-well microplates prior to transfection, and two alternative strategies were employed to improve adherence of HEK 293T cells to reduce cell loss with washing steps. For non-coated plates, cells were plated 2 days prior to transfection at 25,000 cells/well. Alternatively, with Collagen-I-coated plates, the cells were plated 24 hours prior transfection at 50,000 cells/well.

4.5.9 *Protocols for Complexation of Transfection Reagents with Donor DNA and Ribonucleoprotein (RNP) and their Bolus Delivery to Cells*

4.5.9.1 QCR and jetPEI

In this study, a variety of variables were modified and tested in the complexation of the polymer with the donor DNA and RNP. The optimized complexation protocol is described here in detail. The donor plasmid stock (1.00 µg/µL in water) was diluted to 0.020 µg/µL with diH_2O. In the case of the QCR reagent, a stock solution of QCR (11.0 mg/mL) was prepared by dissolving solid polymer in water (containing 2.9% glacial acetic acid, pH ~3) and filtered with a sterile filter (0.22 µm). A diluted polymer solution was formed by diluting the stock solution (either QCR or the commercial jetPEI solution) in diH_2O so that upon mixing with the diluted donor plasmid solution at equal volumes, the appropriate N/P ratio (the ratio of quinuclidine amines to negatively charged phosphates in the DNA) was achieved. For optimal gene editing, the diluted polymer stock necessary for an N/P = 5 was made and mixed with the dilute donor plasmid solution (0.020 µg/µL) at 1:1 volume to yield a polyplex solution containing 0.01 µg/µL DNA. For 24-well microplate wells in triplicate, a total of 330 µL of polyplex solution was prepared. The mixture was left to incubate at room temperature for at least 15 minutes. During this time, stocks of Cas9 in PBS (0.250 µg/µL) and sgRNA in PBS (0.050 µg/µL) were mixed together at equal volumes and left to anneal for 10 min to form an RNP solution. Enough RNP solution for a mass equivalence of 1.25 : 0.25 : 1 (Cas9/sgRNA/plasmid) was diluted in a volume of serum-free DMEM capable of diluting the polyplexes by a concentration 3×. For 24-well microplate wells in triplicate, 33 µL of RNP solution was added to 627 µL of DMEM to yield a solution with a Cas9 concentration of 6.25 ng/µL. The polyplex solution (330 µL) was then diluted in the RNP/DMEM solution (660 μL) and left to incubate at room temperature for 30 minutes. After this period, the cells were gently washed with PBS and the diluted polyplex solution was gently added to the cells (300 μL per 24-well microplate well for a total dose of 1.25 : 0.25 : 1 μg of [Cas9/sgRNA/plasmid] per well). The cells were left to incubate in the polyplex solution for 1 hour in the incubator (37 °C under 5% CO_2 atmosphere). Serum-containing DMEM (10% FBS) was then added to polyplex solution (1 mL) to quench the transfection, and the cells were placed back in the incubator.

4.5.9.2 Lipofectamine CRISPRMAX

Yu et al. Protocol: Following the protocol of Yu et al.,[304] for each well in a 24-well microplate, 0.5 μg of Cas9 and 0.125 μg sgRNA (4:1 ratio) were added to 25 μL of Opti-MEM. After mixing, 1 μL of Cas9 Plus reagent was added to the RNP solution and left to incubate at room temperature for at least 5 min. To this mixture, 0.5 μg of DNA donor (oligo or plasmid) was added. In a separate tube, 1.5 μL of Lipofectamine CRISPRMAX reagent was added to 25 μL of Opti-MEM and mixed. The RNP/donor solution was then added to the Lipofectamine CRISPRMAX solution, and the solution was mixed and left to incubate at room temperature for 10-15 minutes. The solution (50 μL) was then added directly to the cells in serum-containing media.

Manufacturer Protocol: The same protocol was followed above except with increased RNP mass and increased Cas9/sgRNA ratio (5:1) per well (1.250 μg Cas9 and 0.250 μg sgRNA). In addition, an increased dose of 2.5 μL of Cas9 Plus reagent was added to the RNP solution.

"Equivalent-to-Polymer" Protocol: To control for the difference in RNP and donor DNA masses between the Lipofectamine CRISPRMAX and polymer protocols, a variation

of the Lipofectamine CRISPRMAX protocol (above) was performed where the mass of RNP and donor plasmid (1.25 : 0.25 : 1 μg of [Cas9/sgRNA/plasmid]) per well was equivalent to the polymer protocol (see *Section 4.5.9.1*).

4.5.9.3 Lipofectamine 2000

Both the "Yu et al. protocol" and "Manufacturer Protocol" (see *Section 4.5.9.2*) were used with Lipofectamine 2000. For this variation, the Lipofectamine CRISPRMAX reagent was substituted with the Lipofectamine 2000 reagent and the Cas9 Plus reagent was not used.

4.5.10 *Cell Growth and Assessment of Cell Viability*

The fluorescent read-out (mCherry and GFP) of gene-edited cells achieved maximum fluorescence intensity approximately three days following transfection. Therefore, the cells were passaged twice prior to analysis so that the cells would not become overly confluent and skew cell viability results (relative to untreated controls). Twenty-four hours after the transfection, the cells were trypsinized, split (1/5), and plated onto new 24-well microplates. An aliquot of the remaining homogenized cell suspension (0.1 × cell total, 50 μL) was dispensed into fresh phenol red-free media containing CCK-8 solution (4:1 media/CCK-8, 50 μL total). The aliquot of cells in the CCK-8 solution were incubated 37 °C under 5% CO_2 atmosphere for 90 minutes and the absorbance of the solution was taken at 450 and 650 nm, per manufacturer's protocol, and used to determine cell number relative to untreated control. Two days following the first passage, the cells were trypsinized, split (1/2), and plated onto 6-well microplates. The same procedure (see above) was performed with the CCK-8 viability assay with the remaining homogenized cell suspension. Two days following the second passage (5 days total since transfection), the cells were trypsinized and the CCK-8 procedure (see above) was utilized again to determine cell number. The remaining cell suspension was worked up for flow cytometry analysis (see below).

4.5.11 *Flow Cytometry Analysis*

The suspension of trypsinized cells, 5 days post-transfection (see above), were pelleted by centrifugation (at 4 °C). After aspiration of the supernatant, the cells were resuspended in ice-cold PBS and pelleted once more. The pellet was resuspended in fresh cold PBS containing FBS (1%). The cell viability stain, SYTOX Red, was added directly to the cell suspension (1 µL/ well) just prior to flow cytometry analysis. Over 100,000 live cells were collected per replicate. The gating scheme is shown below (Fig. 4.10). Cells containing QCR particles show some autofluorescence in both GFP and mCherry channels. Therefore, GFP(-) or mCherry(-) live cells still containing QCR particles fell on the diagonal plane of the plot and could easily be gated out, reducing any potential false positives from QCR autofluorescence (see Fig. 4.10B-C).

4.5.12 *Fluorescence Microscopy of Transfected Cells*

Cells were plated on glass-bottom dishes, and the cells were transfected and passaged in the same manner as described above. Prior to imaging, the cells were washed with PBS and then fixed by exposure to formaldehyde (4%) for 15 min. The fixed cells were thoroughly washed (3×) in PBS and immersed in PBS during imaging.

4.6 Acknowledgements

I would like to thank Dr. Yogesh Dhande for his mentorship and trailblazing of Cas9-based editing with the Traffic Light Reporter cell line in the Reineke Group. I thank Prof. Ramya Kumar for her insightful input in adapting the EMSA assay for sgRNA binding. I thank Dr. Ariel Alperstein, Punarbasu Roy, Nick Kreofsky, Prof. Renee Frontiera, and Prof. Theresa Reineke for their continued support in ongoing Raman experiments. Funding for this work was provided by the NSF (DMR-1904853).

5. Thesis Summary and Future Outlook

5.1 Thesis Summary

Quinine sits atop a pedestal in the history of chemistry and medicine. As the first known antimalarial, acquisition of the alkaloid influenced the rise and falls of empires for hundreds of years, and the pursuit of its synthesis helped kickstart synthetic chemistry as a discipline. Throughout this last century, the compound found new starring roles in areas such asymmetric catalysis and photochemistry. With this work we hoped to repurpose quinine once again. Due to its basicity, lysomotropic properties, DNA-binding properties, chemical functional handles, natural abundance, fluorescence, and sensitive Raman spectrum, we hypothesized that the alkaloid could serve as a useful cationic moiety in a polymeric gene delivery vehicle. We envisioned a quinine-containing polymer could provide enhanced gene delivery capabilities while simultaneously serving as a diagnostic fluorescence- and Raman-based probe.

In *Chapter 2*, I worked with Dr. Dave Punihaole to help him characterize the chemical sensitivity of one particularly strong Raman band of quinine. We showed that shifting of this Raman band (1370 cm^{-1}) give insight into quinine's chemical environment and was used characterize quinine's ability to partially intercalate with DNA. In *Chapter 3,* I synthesized a series of quinine-containing statistical copolymers (QCRs) and found one variation, containing HEA, that could perform transient transfection with plasmids exceptionally well in cultured cells. Working again with Dr. Punihaole, we took advantage quinine's sensitive Raman signal and performed Raman microscopic imaging of cells transfected with QCR polyplexes. By analyzing shifts in the Raman spectrum due to QCR's unbinding with DNA and correlating it with intracellular protein concentration, we were able to provide evidence for a protein-based unpackaging mechanism. To the take advantage of the protein-binding capability of the QCR, I then used the QCR in *Chapter 4* for the simultaneous delivery of RNP and DNA donor plasmid for CRISPR/Cas9 editing. I showed in this chapter that the QCR outperforms gold-standard transfection reagents in promoting CRISPR-based genomic editing of cells in culture. Work is continuing with Dr. Ariel Alperstein to use Raman microscopic imaging to assess RNP binding in the QCR multi-component complex.

5.2 Future Outlook

With the help of colleagues Dr. Alperstein, Punarbasu Roy, and Nick Kreofsky, work will continue in the optimization of this quinine-based polymeric transfection system. While the free radical copolymerization of quinine with vinylic comonomers provided a facile route in the development the quinine-containing polymer, the route is limited in that a relatively small range of quinine incorporation is accessible through this route. In addition, free radical techniques yield little control of polymer molar mass or dispersity. To gain control of this variable space and improve the tunability of the QCR's physical properties, we have started efforts to improve the amenability of quinine to more controlled synthetic techniques. These efforts will allow the group to more easily adapt and optimize the QCR platform for a range of cargoes, cell types, transfection conditions, and therapeutic applications.

Beyond the application of the QCR platform for gene therapy, this work has also improved our fundamental understanding of the interactions of quinine with important biological macromolecules. Despite its widespread use as an antimalarial for hundreds of years, the mechanism of quinine's antimalarial activity is not entirely understood despite maintaining relatively broad effectiveness across a range of *Plasmodium* species and strains (see *Section 1.5.2*). This suggests that quinine may be acting across a range of biological macromolecules within the parasite and host. This work provides a foundation for utilizing Raman chemical imaging to better understand quinine's molecular interactions inside the cell and to help elucidate its antimalarial mode of action. In addition, chemically-sensitive Raman bands are not unique to quinine (see *Section 3.4)*, so we envision that the Raman chemical imaging performed in this work can serve as a foundation for applying this imaging technique for other chemical species in biomaterial and pharmaceutical applications. We hope that further use of Raman imaging will provide researchers with a powerful tool for assessing chemical interactions of therapeutics inside the cell.

References

(1) Lee, D. W.; Kochenderfer, J. N.; Stetler-Stevenson, M.; Cui, Y. K.; Delbrook, C.; Feldman, S. A.; Fry, T. J.; Orentas, R.; Sabatino, M.; Shah, N. N.; et al. T cells expressing CD19 chimeric antigen receptors for acute lymphoblastic leukaemia in children and young adults: a phase 1 dose-escalation trial. *The Lancet* **2015**, *385* (9967), 517-528.

(2) Russell, S.; Bennett, J.; Wellman, J. A.; Chung, D. C.; Yu, Z.-F.; Tillman, A.; Wittes, J.; Pappas, J.; Elci, O.; McCague, S.; et al. Efficacy and safety of voretigene neparvovec (AAV2-hRPE65v2) in patients with RPE65-mediated inherited retinal dystrophy: a randomised, controlled, open-label, phase 3 trial. *The Lancet* **2017**, *390* (10097), 849-860.

(3) Adams, D.; Gonzalez-Duarte, A.; O'Riordan, W. D.; Yang, C.-C.; Ueda, M.; Kristen, A. V.; Tournev, I.; Schmidt, H. H.; Coelho, T.; Berk, J. L.; et al. Patisiran, an RNAi Therapeutic, for Hereditary Transthyretin Amyloidosis. *New England Journal of Medicine* **2018**, *379* (1), 11-21.

(4) Neelapu, S. S.; Locke, F. L.; Bartlett, N. L.; Lekakis, L. J.; Miklos, D. B.; Jacobson, C. A.; Braunschweig, I.; Oluwole, O. O.; Siddiqi, T.; Lin, Y.; et al. Axicabtagene Ciloleucel CAR T-Cell Therapy in Refractory Large B-Cell Lymphoma. *New England Journal of Medicine* **2017**, *377* (26), 2531-2544.

(5) Thompson, A. A.; Walters, M. C.; Kwiatkowski, J.; Rasko, J. E. J.; Ribeil, J.-A.; Hongeng, S.; Magrin, E.; Schiller, G. J.; Payen, E.; Semeraro, M.; et al. Gene Therapy in Patients with Transfusion-Dependent β-Thalassemia. *New England Journal of Medicine* **2018**, *378* (16), 1479-1493.

(6) Asher, D. R.; Thapa, K.; Dharia, S. D.; Khan, N.; Potter, R. A.; Rodino-Klapac, L. R.; Mendell, J. R. Clinical development on the frontier: gene therapy for duchenne muscular dystrophy. *Expert Opinion on Biological Therapy* **2020**, *20* (3), 263-274.

(7) Maldonado, R.; Jalil, S.; Wartiovaara, K. Curative gene therapies for rare diseases. *Journal of Community Genetics* **2020**, 12, 267-276.

(8) Creech, C. B.; Walker, S. C.; Samuels, R. J. SARS-CoV-2 Vaccines. *JAMA* **2021**, *325* (13), 1318-1320.

(9) Tipanee, J.; Chai, Yoke C.; VandenDriessche, T.; Chuah, Marinee K. Preclinical and clinical advances in transposon-based gene therapy. *Bioscience Reports* **2017**, *37* (6).

(10) Bumcrot, D.; Manoharan, M.; Koteliansky, V.; Sah, D. W. Y. RNAi therapeutics: a potential new class of pharmaceutical drugs. *Nature Chemical Biology* **2006**, *2* (12), 711-719.

(11) Urnov, F. D.; Rebar, E. J.; Holmes, M. C.; Zhang, H. S.; Gregory, P. D. Genome editing with engineered zinc finger nucleases. *Nature Reviews Genetics* **2010**, *11* (9), 636-646.

(12) Joung, J. K.; Sander, J. D. TALENs: a widely applicable technology for targeted genome editing. *Nature Reviews Molecular Cell Biology* **2013**, *14* (1), 49-55.

(13) Jinek, M.; Chylinski, K.; Fonfara, I.; Hauer, M.; Doudna, J. A.; Charpentier, E. A Programmable Dual-RNA–Guided DNA Endonuclease in Adaptive Bacterial Immunity. *Science* **2012**, *337* (6096), 816-821.

(14) Gaudelli, N. M.; Komor, A. C.; Rees, H. A.; Packer, M. S.; Badran, A. H.; Bryson, D. I.; Liu, D. R. Programmable base editing of A•T to G•C in genomic DNA without DNA cleavage. *Nature* **2017**, *551* (7681), 464-471.

(15) Foldvari, M.; Chen, D. W.; Nafissi, N.; Calderon, D.; Narsineni, L.; Rafiee, A. Non-viral gene therapy: Gains and challenges of non-invasive administration methods. *Journal of Controlled Release* **2016**, *240*, 165-190.

(16) Xu, X.; Wan, T.; Xin, H.; Li, D.; Pan, H.; Wu, J.; Ping, Y. Delivery of CRISPR/Cas9 for therapeutic genome editing. *Journal of Gene Medicine* **2019**, *21* (7), e3107.

(17) Ke, L.; Cai, P.; Wu, Y.-L.; Chen, X. Polymeric Nonviral Gene Delivery Systems for Cancer Immunotherapy. *Advanced Therapeutics* **2020**, *3* (6), 1900213.

(18) Koijen, R.; Van Nieuwerburgh, S. Financing the War On Cancer. *National Bureau of Economic Research Working Paper Series* **2018**, *No. 24730*.

(19) Lundstrom, K. Viral Vectors in Gene Therapy. *Diseases* **2018**, *6* (2), 42.

(20) Yin, H.; Kanasty, R. L.; Eltoukhy, A. A.; Vegas, A. J.; Dorkin, J. R.; Anderson, D. G. Non-viral vectors for gene-based therapy. *Nature Reviews Genetics* **2014**, *15* (8), 541-555.

(21) Li, C.; Samulski, R. J. Engineering adeno-associated virus vectors for gene therapy. *Nature Reviews Genetics* **2020**, *21* (4), 255-272.

(22) Sadoff, J.; Gray, G.; Vandebosch, A.; Cárdenas, V.; Shukarev, G.; Grinsztejn, B.; Goepfert, P. A.; Truyers, C.; Fennema, H.; Spiessens, B.; et al. Safety and Efficacy of Single-Dose Ad26.COV2.S Vaccine against Covid-19. *New England Journal of Medicine* **2021**, *384* (23), 2187-2201.

(23) Goswami, R.; Subramanian, G.; Silayeva, L.; Newkirk, I.; Doctor, D.; Chawla, K.; Chattopadhyay, S.; Chandra, D.; Chilukuri, N.; Betapudi, V. Gene Therapy Leaves a Vicious Cycle. *Frontiers in Oncology* **2019**, *9*, 297.

(24) DiMattia, M. A.; Nam, H. J.; Van Vliet, K.; Mitchell, M.; Bennett, A.; Gurda, B. L.; McKenna, R.; Olson, N. H.; Sinkovits, R. S.; Potter, M.; et al. Structural insight into the unique properties of adeno-associated virus serotype 9. *Journal of Virology* **2012**, *86* (12), 6947-6958.

(25) Mintzer, M. A.; Simanek, E. E. Nonviral vectors for gene delivery. *Chemical Reviews* **2009**, *109* (2), 259-302.

(26) Lai, W. F.; Wong, W. T. Design of Polymeric Gene Carriers for Effective Intracellular Delivery. *Trends in Biotechnology* **2018**, *36* (7), 713-728.

(27) Alsaggar, M.; Liu, D. Chapter One - Physical Methods for Gene Transfer. In *Advances in Genetics*, Huang, L., Liu, D., Wagner, E. Eds.; Vol. 89; Academic Press, 2015; pp 1-24.

(28) Ramamoorth, M.; Narvekar, A. Non viral vectors in gene therapy- an overview. *Journal of Clinical and Diagnostic Research* **2015**, *9* (1), GE01-06.

(29) Loh, X. J.; Lee, T.-C.; Dou, Q.; Deen, G. R. Utilising inorganic nanocarriers for gene delivery. *Biomaterials Science* **2016**, *4* (1), 70-86.

(30) Kang, Z.; Meng, Q.; Liu, K. Peptide-based gene delivery vectors. *Journal of Materials Chemistry B* **2019**, *7* (11), 1824-1841.

(31) Al-Dosari, M. S.; Gao, X. Nonviral gene delivery: principle, limitations, and recent progress. *AAPS Journal* **2009**, *11* (4), 671-681.

(32) Kumar, R.; Santa Chalarca, C. F.; Bockman, M. R.; Van Bruggen, C.; Grimme, C. J.; Dalal, R. J.; Hanson, M. G.; Hexum, J. K.; Reineke, T. M. Polymeric Delivery of Therapeutic Nucleic Acids. *Chemical Reviews* **2021**, *121* (18), 11527-11652.

(33) Lara, A. R.; Ramírez, O. T.; Wunderlich, M. Plasmid DNA production for therapeutic applications. *Methods in Molecular Biology* **2012**, *824*, 271-303.

(34) Gill, D. R.; Pringle, I. A.; Hyde, S. C. Progress and Prospects: The design and production of plasmid vectors. *Gene Therapy* **2009**, *16* (2), 165-171.

(35) Hardee, C. L.; Arévalo-Soliz, L. M.; Hornstein, B. D.; Zechiedrich, L. Advances in Non-Viral DNA Vectors for Gene Therapy. *Genes (Basel)* **2017**, *8* (2), 65.

(36) Liu, C.; Zhang, L.; Liu, H.; Cheng, K. Delivery strategies of the CRISPR-Cas9 gene-editing system for therapeutic applications. *Journal of Controlled Release* **2017**, *266*, 17-26.

(37) Maeder, M. L.; Gersbach, C. A. Genome-editing Technologies for Gene and Cell Therapy. *Molecular Therapy* **2016**, *24* (3), 430-446.

(38) Yeh, C. D.; Richardson, C. D.; Corn, J. E. Advances in genome editing through control of DNA repair pathways. *Nature Cell Biology* **2019**, *21* (12), 1468-1478.

(39) Lino, C. A.; Harper, J. C.; Carney, J. P.; Timlin, J. A. Delivering CRISPR: a review of the challenges and approaches. *Drug Delivery* **2018**, *25* (1), 1234-1257.

(40) Rinkenauer, A. C.; Schubert, S.; Traeger, A.; Schubert, U. S. The influence of polymer architecture on in vitro pDNA transfection. *Journal of Materials Chemistry B* **2015**, *3* (38), 7477-7493.

(41) Wang, H.-X.; Li, M.; Lee, C. M.; Chakraborty, S.; Kim, H.-W.; Bao, G.; Leong, K. W. CRISPR/Cas9-Based Genome Editing for Disease Modeling and Therapy: Challenges and Opportunities for Nonviral Delivery. *Chemical Reviews* **2017**, *117* (15), 9874-9906.

(42) Abdelhady, H. G.; Allen, S.; Davies, M. C.; Roberts, C. J.; Tendler, S. J. B.; Williams, P. M. Direct real-time molecular scale visualisation of the degradation of condensed DNA complexes exposed to DNase I. *Nucleic Acids Research* **2003**, *31* (14), 4001-4005.

(43) Mislick, K. A.; Baldeschwieler, J. D. Evidence for the role of proteoglycans in cation-mediated gene transfer. *Proceedings of the National Academy of Sciences U S A* **1996**, *93* (22), 12349-12354.

(44) Li, Y.; Gao, J.; Zhang, C.; Cao, Z.; Cheng, D.; Liu, J.; Shuai, X. Stimuli-Responsive Polymeric Nanocarriers for Efficient Gene Delivery. In *Polymeric Gene Delivery Systems*, Cheng, Y. Ed.; Springer International Publishing, 2018; pp 167-215.

(45) Vaheri, A.; Pagano, J. S. Infectious poliovirus RNA: a sensitive method of assay. *Virology* **1965**, *27* (3), 434-436.

(46) Laemmli, U. K. Characterization of DNA condensates induced by poly(ethylene oxide) and polylysine. *Proceedings of the National Academy of Sciences U S A* **1975**, *72* (11), 4288-4292.

(47) Wu, G. Y.; Wu, C. H. Receptor-mediated gene delivery and expression in vivo. *Journal of Biological Chemistry* **1988**, *263* (29), 14621-14624.

(48) Haensler, J.; Szoka, F. C., Jr. Polyamidoamine cascade polymers mediate efficient transfection of cells in culture. *Bioconjugate Chemistry* **1993**, *4* (5), 372-379.

(49) Lächelt, U.; Wagner, E. Nucleic Acid Therapeutics Using Polyplexes: A Journey of 50 Years (and Beyond). *Chemical Reviews* **2015**, *115* (19), 11043-11078.

(50) Bus, T.; Traeger, A.; Schubert, U. S. The great escape: how cationic polyplexes overcome the endosomal barrier. *Journal of Materials Chemistry B* **2018**, *6* (43), 6904-6918.

(51) Huotari, J.; Helenius, A. Endosome maturation. *The EMBO Journal* **2011**, *30* (17), 3481-3500.

(52) Liang, W.; Lam, J. Endosomal Escape Pathways for Non-Viral Nucleic Acid Delivery Systems. *Molecular Regulation of Endocytosis* **2012**, 429-456.

(53) Degors, I. M. S.; Wang, C.; Rehman, Z. U.; Zuhorn, I. S. Carriers Break Barriers in Drug Delivery: Endocytosis and Endosomal Escape of Gene Delivery Vectors. *Accounts of Chemical Reseach* **2019**, *52* (7), 1750-1760.

(54) Boussif, O.; Lezoualc'h, F.; Zanta, M. A.; Mergny, M. D.; Scherman, D.; Demeneix, B.; Behr, J. P. A versatile vector for gene and oligonucleotide transfer into cells in culture and in vivo: polyethylenimine. *Proceedings of the National Academy of Sciences U S A* **1995**, *92* (16), 7297-7301.

(55) Behr, J.-P. The Proton Sponge: a Trick to Enter Cells the Viruses Did Not Exploit. *CHIMIA International Journal for Chemistry* **1997**, *51* (1-2), 34-36.

(56) Benjaminsen, R. V.; Mattebjerg, M. A.; Henriksen, J. R.; Moghimi, S. M.; Andresen, T. L. The Possible "Proton Sponge " Effect of Polyethylenimine (PEI) Does Not Include Change in Lysosomal pH. *Molecular Therapy* **2013**, *21* (1), 149-157.

(57) van de Wetering, P.; Cherng, J. Y.; Talsma, H.; Crommelin, D. J. A.; Hennink, W. E. 2-(dimethylamino)ethyl methacrylate based (co)polymers as gene transfer agents. *Journal of Controlled Release* **1998**, *53* (1), 145-153.

(58) Donahue, N. D.; Acar, H.; Wilhelm, S. Concepts of nanoparticle cellular uptake, intracellular trafficking, and kinetics in nanomedicine. *Advanced Drug Delivery Reviews* **2019**, *143*, 68-96.

(59) Luthman, H.; Magnusson, G. High efficiency polyoma DNA transfection of chloroquine treated cells. *Nucleic Acids Research* **1983**, *11* (5), 1295-1308.

(60) Jones, C. H.; Chen, C.-K.; Ravikrishnan, A.; Rane, S.; Pfeifer, B. A. Overcoming Nonviral Gene Delivery Barriers: Perspective and Future. *Molecular Pharmaceutics* **2013**, *10* (11), 4082-4098.

(61) Vaidyanathan, S.; Orr, B. G.; Banaszak Holl, M. M. Role of Cell Membrane–Vector Interactions in Successful Gene Delivery. *Accounts of Chemical Research* **2016**, *49* (8), 1486-1493.

(62) ur Rehman, Z.; Hoekstra, D.; Zuhorn, I. S. Mechanism of polyplex- and lipoplex-mediated delivery of nucleic acids: real-time visualization of transient membrane destabilization without endosomal lysis. *ACS Nano* **2013**, *7* (5), 3767-3777.

(63) Yue, Y.; Jin, F.; Deng, R.; Cai, J.; Dai, Z.; Lin, M. C. M.; Kung, H.-F.; Mattebjerg, M. A.; Andresen, T. L.; Wu, C. Revisit complexation between DNA and

polyethylenimine — Effect of length of free polycationic chains on gene transfection. *Journal of Controlled Release* **2011**, *152* (1), 143-151.

(64) Yue, Y.; Wu, C. Progress and perspectives in developing polymeric vectors for in vitro gene delivery. *Biomaterials Science* **2013**, *1* (2), 152-170.

(65) Reilly, M. J.; Larsen, J. D.; Sullivan, M. O. Polyplexes Traffic through Caveolae to the Golgi and Endoplasmic Reticulum en Route to the Nucleus. *Molecular Pharmaceutics* **2012**, *9* (5), 1280-1290.

(66) Fichter, K. M.; Ingle, N. P.; McLendon, P. M.; Reineke, T. M. Polymeric Nucleic Acid Vehicles Exploit Active Interorganelle Trafficking Mechanisms. *ACS Nano* **2013**, *7* (1), 347-364.

(67) Grigsby, C. L.; Leong, K. W. Balancing protection and release of DNA: tools to address a bottleneck of non-viral gene delivery. *Journal of the Royal Society, Interface* **2010**, *7 Suppl 1* (Suppl 1), S67-S82.

(68) Wattiaux, R.; Laurent, N.; Wattiaux-De Coninck, S.; Jadot, M. Endosomes, lysosomes: their implication in gene transfer. *Advanced Drug Delivery Reviews* **2000**, *41* (2), 201-208.

(69) Lechardeur, D.; Sohn, K. J.; Haardt, M.; Joshi, P. B.; Monck, M.; Graham, R. W.; Beatty, B.; Squire, J.; O'Brodovich, H.; Lukacs, G. L. Metabolic instability of plasmid DNA in the cytosol: a potential barrier to gene transfer. *Gene Therapy* **1999**, *6* (4), 482-497.

(70) Won, Y.-Y.; Sharma, R.; Konieczny, S. F. Missing pieces in understanding the intracellular trafficking of polycation/DNA complexes. *Journal of Controlled Release* **2009**, *139* (2), 88-93.

(71) Schaffer, D. V.; Fidelman, N. A.; Dan, N.; Lauffenburger, D. A. Vector unpacking as a potential barrier for receptor-mediated polyplex gene delivery. *Biotechnology and Bioengineering* **2000**, *67* (5), 598-606.

(72) Köping-Höggård, M.; Vårum, K. M.; Issa, M.; Danielsen, S.; Christensen, B. E.; Stokke, B. T.; Artursson, P. Improved chitosan-mediated gene delivery based on easily dissociated chitosan polyplexes of highly defined chitosan oligomers. *Gene Therapy* **2004**, *11* (19), 1441-1452.

(73) Piest, M.; Engbersen, J. F. J. Effects of charge density and hydrophobicity of poly(amido amine)s for non-viral gene delivery. *Journal of Controlled Release* **2010**, *148* (1), 83-90.

(74) Gabrielson, N. P.; Pack, D. W. Efficient polyethylenimine-mediated gene delivery proceeds via a caveolar pathway in HeLa cells. *Journal of Controlled Release* **2009**, *136* (1), 54-61.

(75) Kretzmann, J. A.; Ho, D.; Evans, C. W.; Plani-Lam, J. H. C.; Garcia-Bloj, B.; Mohamed, A. E.; O'Mara, M. L.; Ford, E.; Tan, D. E. K.; Lister, R.; et al. Synthetically controlling dendrimer flexibility improves delivery of large plasmid DNA. *Chemical Science* **2017**, *8* (4), 2923-2930.

(76) Pavan, G. M.; Albertazzi, L.; Danani, A. Ability to Adapt: Different Generations of PAMAM Dendrimers Show Different Behaviors in Binding siRNA. *The Journal of Physical Chemistry B* **2010**, *114* (8), 2667-2675.

(77) Mathew, A. P.; Cho, K.-H.; Uthaman, S.; Cho, C.-S.; Park, I.-K. Stimuli-Regulated Smart Polymeric Systems for Gene Therapy. *Polymers* **2017**, *9* (4), 152.

(78) Thomas, T. J.; Tajmir-Riahi, H. A.; Pillai, C. K. S. Biodegradable Polymers for Gene Delivery. *Molecules* **2019**, *24* (20), 3744.

(79) Reineke, T. M. Stimuli-Responsive Polymers for Biological Detection and Delivery. *ACS Macro Letters* **2016**, *5* (1), 14-18.

(80) Itaka, K.; Harada, A.; Yamasaki, Y.; Nakamura, K.; Kawaguchi, H.; Kataoka, K. In situ single cell observation by fluorescence resonance energy transfer reveals fast intra-cytoplasmic delivery and easy release of plasmid DNA complexed with linear polyethylenimine. *The Journal of Gene Medicine* **2004**, *6* (1), 76-84.

(81) Ketola, T.-M.; Hanzlíková, M.; Leppänen, L.; Raviña, M.; Bishop, C. J.; Green, J. J.; Urtti, A.; Lemmetyinen, H.; Yliperttula, M.; Vuorimaa-Laukkanen, E. Independent versus Cooperative Binding in Polyethylenimine–DNA and Poly(l-lysine)–DNA Polyplexes. *The Journal of Physical Chemistry B* **2013**, *117* (36), 10405-10413.

(82) Ruponen, M.; Ylä-Herttuala, S.; Urtti, A. Interactions of polymeric and liposomal gene delivery systems with extracellular glycosaminoglycans: physicochemical and transfection studies. *Biochimica et Biophysica Acta (BBA) - Biomembranes* **1999**, *1415* (2), 331-341.

(83) Ruponen, M.; Rönkkö, S.; Honkakoski, P.; Pelkonen, J.; Tammi, M.; Urtti, A. Extracellular Glycosaminoglycans Modify Cellular Trafficking of Lipoplexes and Polyplexes. *Journal of Biological Chemistry* **2001**, *276* (36), 33875-33880.

(84) Cheng, J.; Zeidan, R.; Mishra, S.; Liu, A.; Pun, S. H.; Kulkarni, R. P.; Jensen, G. S.; Bellocq, N. C.; Davis, M. E. Structure-function correlation of chloroquine and analogues as transgene expression enhancers in nonviral gene delivery. *Journal of Medicinal Chemistry* **2006**, *49* (22), 6522-6531.

(85) Forrest, M. L.; Pack, D. W. On the kinetics of polyplex endocytic trafficking: implications for gene delivery vector design. *Molecular Therapy* **2002**, *6* (1), 57-66.

(86) Erbacher, P.; Roche, A. C.; Monsigny, M.; Midoux, P. Putative role of chloroquine in gene transfer into a human hepatoma cell line by DNA/lactosylated polylysine complexes. *Experimental Cell Research* **1996**, *225* (1), 186-194.

(87) Wolfert, M. A.; Seymour, L. W. Chloroquine and amphipathic peptide helices show synergistic transfection in vitro. *Gene Therapy* **1998**, *5* (3), 409-414.

(88) Akinc, A.; Thomas, M.; Klibanov, A. M.; Langer, R. Exploring polyethylenimine-mediated DNA transfection and the proton sponge hypothesis. *The Journal of Gene Medicine* **2005**, *7* (5), 657-663.

(89) Huth, S.; Hoffmann, F.; von Gersdorff, K.; Laner, A.; Reinhardt, D.; Rosenecker, J.; Rudolph, C. Interaction of polyamine gene vectors with RNA leads to the dissociation of plasmid DNA-carrier complexes. *The Journal of Gene Medicine* **2006**, *8* (12), 1416-1424.

(90) Okuda, T.; Niidome, T.; Aoyagi, H. Cytosolic soluble proteins induce DNA release from DNA–gene carrier complexes. *Journal of Controlled Release* **2004**, *98* (2), 325-332.

(91) Chen, H. H.; Ho, Y.-P.; Jiang, X.; Mao, H.-Q.; Wang, T.-H.; Leong, K. W. Quantitative Comparison of Intracellular Unpacking Kinetics of Polyplexes by a

Model Constructed From Quantum Dot-FRET. *Molecular Therapy* **2008**, *16* (2), 324-332.

(92) Mishra, S.; Webster, P.; Davis, M. E. PEGylation significantly affects cellular uptake and intracellular trafficking of non-viral gene delivery particles. *European Journal of Cell Biology* **2004**, *83* (3), 97-111.

(93) Gabrielson, N. P.; Pack, D. W. Acetylation of Polyethylenimine Enhances Gene Delivery via Weakened Polymer/DNA Interactions. *Biomacromolecules* **2006**, *7* (8), 2427-2435.

(94) Funhoff, A. M.; van Nostrum, C. F.; Koning, G. A.; Schuurmans-Nieuwenbroek, N. M. E.; Crommelin, D. J. A.; Hennink, W. E. Endosomal Escape of Polymeric Gene Delivery Complexes Is Not Always Enhanced by Polymers Buffering at Low pH. *Biomacromolecules* **2004**, *5* (1), 32-39.

(95) Dubruel, P.; Christiaens, B.; Rosseneu, M.; Vandekerckhove, J.; Grooten, J.; Goossens, V.; Schacht, E. Buffering Properties of Cationic Polymethacrylates Are Not the Only Key to Successful Gene Delivery. *Biomacromolecules* **2004**, *5* (2), 379-388.

(96) Sprouse, D.; Reineke, T. M. Investigating the Effects of Block versus Statistical Glycopolycations Containing Primary and Tertiary Amines for Plasmid DNA Delivery. *Biomacromolecules* **2014**, *15* (7), 2616-2628.

(97) Li, H.; Cortez, M. A.; Phillips, H. R.; Wu, Y.; Reineke, T. M. Poly(2-deoxy-2-methacrylamido glucopyranose)-b-Poly(methacrylate amine)s: Optimization of Diblock Glycopolycations for Nucleic Acid Delivery. *ACS Macro Letters* **2013**, *2* (3), 230-235.

(98) Van Bruggen, C.; Hexum, J. K.; Tan, Z.; Dalal, R. J.; Reineke, T. M. Nonviral Gene Delivery with Cationic Glycopolymers. *Accounts of Chemical Research* **2019**, *52* (5), 1347-1358.

(99) Liu, Y.; Wenning, L.; Lynch, M.; Reineke, T. M. New Poly(d-glucaramidoamine)s Induce DNA Nanoparticle Formation and Efficient Gene Delivery into Mammalian Cells. *Journal of the American Chemical Society* **2004**, *126* (24), 7422-7423.

(100) Liu, Y.; Reineke, T. M. Hydroxyl Stereochemistry and Amine Number within Poly(glycoamidoamine)s Affect Intracellular DNA Delivery. *Journal of the American Chemical Society* **2005**, *127* (9), 3004-3015.

(101) Liu, Y.; Reineke, T. M. Degradation of Poly(glycoamidoamine) DNA Delivery Vehicles: Polyamide Hydrolysis at Physiological Conditions Promotes DNA Release. *Biomacromolecules* **2010**, *11* (2), 316-325.

(102) Smith, A. E.; Sizovs, A.; Grandinetti, G.; Xue, L.; Reineke, T. M. Diblock Glycopolymers Promote Colloidal Stability of Polyplexes and Effective pDNA and siRNA Delivery under Physiological Salt and Serum Conditions. *Biomacromolecules* **2011**, *12* (8), 3015-3022.

(103) Buckwalter, D. J.; Sizovs, A.; Ingle, N. P.; Reineke, T. M. MAG versus PEG: Incorporating a Poly(MAG) Layer to Promote Colloidal Stability of Nucleic Acid/“Click Cluster” Complexes. *ACS Macro Letters* **2012**, *1* (5), 609-613.

(104) Dhande, Y. K.; Wagh, B. S.; Hall, B. C.; Sprouse, D.; Hackett, P. B.; Reineke, T. M. N-Acetylgalactosamine Block-co-Polycations Form Stable Polyplexes with

Plasmids and Promote Liver-Targeted Delivery. *Biomacromolecules* **2016**, *17* (3), 830-840.

(105) Tan, Z.; Dhande, Y. K.; Reineke, T. M. Cell Penetrating Polymers Containing Guanidinium Trigger Apoptosis in Human Hepatocellular Carcinoma Cells unless Conjugated to a Targeting N-Acetyl-Galactosamine Block. *Bioconjugate Chemistry* **2017**, *28* (12), 2985-2997.

(106) Srinivasachari, S.; Liu, Y.; Prevette, L. E.; Reineke, T. M. Effects of trehalose click polymer length on pDNA complex stability and delivery efficacy. *Biomaterials* **2007**, *28* (18), 2885-2898.

(107) Sizovs, A.; Xue, L.; Tolstyka, Z. P.; Ingle, N. P.; Wu, Y.; Cortez, M.; Reineke, T. M. Poly(trehalose): Sugar-Coated Nanocomplexes Promote Stabilization and Effective Polyplex-Mediated siRNA Delivery. *Journal of the American Chemical Society* **2013**, *135* (41), 15417-15424.

(108) Tolstyka, Z. P.; Phillips, H.; Cortez, M.; Wu, Y.; Ingle, N.; Bell, J. B.; Hackett, P. B.; Reineke, T. M. Trehalose-Based Block Copolycations Promote Polyplex Stabilization for Lyophilization and in Vivo pDNA Delivery. *ACS Biomaterials Science & Engineering* **2016**, *2* (1), 43-55.

(109) Fichter, K. M.; Zhang, L.; Kiick, K. L.; Reineke, T. M. Peptide-Functionalized Poly(ethylene glycol) Star Polymers: DNA Delivery Vehicles with Multivalent Molecular Architecture. *Bioconjugate Chemistry* **2008**, *19* (1), 76-88.

(110) Srinivasachari, S.; Fichter, K. M.; Reineke, T. M. Polycationic β-Cyclodextrin "Click Clusters": Monodisperse and Versatile Scaffolds for Nucleic Acid Delivery. *Journal of the American Chemical Society* **2008**, *130* (14), 4618-4627.

(111) Jiang, Y.; Lodge, T. P.; Reineke, T. M. Packaging pDNA by Polymeric ABC Micelles Simultaneously Achieves Colloidal Stability and Structural Control. *Journal of the American Chemical Society* **2018**, *140* (35), 11101-11111.

(112) Tan, Z.; Jiang, Y.; Zhang, W.; Karls, L.; Lodge, T. P.; Reineke, T. M. Polycation Architecture and Assembly Direct Successful Gene Delivery: Micelleplexes Outperform Polyplexes via Optimal DNA Packaging. *Journal of the American Chemical Society* **2019**, *141* (40), 15804-15817.

(113) Tan, Z.; Jiang, Y.; Ganewatta, M. S.; Kumar, R.; Keith, A.; Twaroski, K.; Pengo, T.; Tolar, J.; Lodge, T. P.; Reineke, T. M. Block Polymer Micelles Enable CRISPR/Cas9 Ribonucleoprotein Delivery: Physicochemical Properties Affect Packaging Mechanisms and Gene Editing Efficiency. *Macromolecules* **2019**, *52* (21), 8197-8206.

(114) Kumar, R.; Le, N.; Tan, Z.; Brown, M. E.; Jiang, S.; Reineke, T. M. Efficient Polymer-Mediated Delivery of Gene-Editing Ribonucleoprotein Payloads through Combinatorial Design, Parallelized Experimentation, and Machine Learning. *ACS Nano* **2020**, *14* (12), 17626-17639.

(115) Wang, C.; Du, L.; Zhou, J.; Meng, L.; Cheng, Q.; Wang, C.; Wang, X.; Zhao, D.; Huang, Y.; Zheng, S.; et al. Elaboration on the Distribution of Hydrophobic Segments in the Chains of Amphiphilic Cationic Polymers for Small Interfering RNA Delivery. *ACS Applied Materials & Interfaces* **2017**, *9* (38), 32463-32474.

(116) Canning, S. L.; Neal, T. J.; Armes, S. P. pH-Responsive Schizophrenic Diblock Copolymers Prepared by Polymerization-Induced Self-Assembly. *Macromolecules* **2017**, *50* (16), 6108-6116.

(117) Thomas, M.; Klibanov, A. M. Enhancing polyethylenimine's delivery of plasmid DNA into mammalian cells. *Proceedings of the National Academy of Sciences U S A* **2002**, *99* (23), 14640-14645.

(118) Incani, V.; Lavasanifar, A.; Uludağ, H. Lipid and hydrophobic modification of cationic carriers on route to superior gene vectors. *Soft Matter* **2010**, *6* (10), 2124-2138.

(119) Kaufman, T. S.; Rúveda, E. A. The Quest for Quinine: Those Who Won the Battles and Those Who Won the War. *Angewandte Chemie International Edition* **2005**, *44* (6), 854-885.

(120) Song, C. E. An Overview of Cinchona Alkaloids in Chemistry. In *Cinchona Alkaloids in Synthesis and Catalysis*, Song, C. E. Ed; Wiley, 2009; pp 1-10.

(121) Casteel, D. A. Antimalarial Agents. In *Burger's Medicinal Chemistry and Drug Discovery Sixth Edition*, Vol. 5, Abraham, D. J. Ed.; Wiley, 2003; pp. 933.

(122) Ding, H.-H.; Zhao, M.-H.; Zhai, L.; Zhen, J.-B.; Sun, L.-Y.; Chigan, J.-Z.; Chen, C.; Li, J.-Q.; Gao, H.; Yang, K.-W. A quinine-based quaternized polymer: a potent scaffold with bactericidal properties without resistance. *Polymer Chemistry* **2021**, *12* (16), 2397-2403.

(123) Latorre-Sánchez, A.; Johansson, M.; Zhang, Y.; Malkoch, M.; Pomposo, J. A. Active quinine-based films able to release antimicrobial compounds via melt quaternization at low temperature. *Journal of Materials Chemistry B* **2018**, *6* (1), 98-104.

(124) Marshall, E. A Renewed Assault on an Old and Deadly Foe. *Science* **2000**, *290* (5491), 428-430.

(125) Esu, E. B.; Effa, E. E.; Opie, O. N.; Meremikwu, M. M. Artemether for severe malaria. *Cochrane Database of Systematic Reviews* **2019**, *6* (6), CD010678.

(126) Foley, M.; Tilley, L. Quinoline antimalarials: mechanisms of action and resistance and prospects for new agents. *Pharmacology & Therapeutics* **1998**, *79* (1), 55-87.

(127) Sanchez, C. P.; Stein, W. D.; Lanzer, M. Dissecting the components of quinine accumulation in plasmodium falciparum. *Molecular Microbiology* **2008**, *67* (5), 1081-1093.

(128) Wink, M. Molecular modes of action of cytotoxic alkaloids: from DNA intercalation, spindle poisoning, topoisomerase inhibition to apoptosis and multiple drug resistance. *Alkaloids: Chemistry and Biology* **2007**, *64*, 1-47.

(129) Khozoie, C.; Pleass, R. J.; Avery, S. V. The antimalarial drug quinine disrupts Tat2p-mediated tryptophan transport and causes tryptophan starvation. *Journal of Biological Chemistry* **2009**, *284* (27), 17968-17974.

(130) Islahudin, F.; Tindall, S. M.; Mellor, I. R.; Swift, K.; Christensen, H. E. M.; Fone, K. C. F.; Pleass, R. J.; Ting, K.-N.; Avery, S. V. The antimalarial drug quinine interferes with serotonin biosynthesis and action. *Scientific Reports* **2014**, *4* (1), 3618.

(131) Chen, G. L.; Sutrina, S. L.; Frayer, K. L.; Chen, W. W. Effects of lysosomotropic agents on lipogenesis. *Archives of Biochemistry and Biophysics* **1986**, *245* (1), 66-75.

(132) Egan, T. J.; Mavuso, W. W.; Ross, D. C.; Marques, H. M. Thermodynamic factors controlling the interaction of quinoline antimalarial drugs with ferriprotoporphyrin IX. *Journal of Inorganic Biochemistry* **1997**, *68* (2), 137-145.

(133) Pagola, S.; Stephens, P. W.; Bohle, D. S.; Kosar, A. D.; Madsen, S. K. The structure of malaria pigment β-haematin. *Nature* **2000**, *404* (6775), 307-310.

(134) O'Brien, R. L.; Olenick, J. G.; Hahn, F. E. Reactions of quinine, chloroquine, and quinacrine with DNA and their effects on the DNA and RNA polymerase reactions. *Proceedings of the National Academy of Sciences U S A* **1966**, *55* (6), 1511-1517.

(135) Perkin, W. H. LXXIV.—On mauveine and allied colouring matters. *Journal of the Chemical Society, Transactions* **1879**, *35* (0), 717-732.

(136) Woodward, R. B.; Doering, W. E. The Total Synthesis of Quinine^1. *Journal of the American Chemical Society* **1944**, *66* (5), 849-849.

(137) Gutzwiller, J.; Uskokovic, M. Total synthesis of quinine and quinidine. II. *Journal of the American Chemical Society* **1970**, *92* (1), 204-205. DOI: 10.1021/ja00704a037.

(138) Taylor, E. C.; Martin, S. F. Facile synthesis of quinine and related cinchona alkaloids. *Journal of the American Chemical Society* **1972**, *94* (17), 6218-6220.

(139) Stork, G.; Niu, D.; Fujimoto, R. A.; Koft, E. R.; Balkovec, J. M.; Tata, J. R.; Dake, G. R. The first stereoselective total synthesis of quinine. *Journal of the American Chemical Society* **2001**, *123* (14), 3239-3242.

(140) Raheem, I. T.; Goodman, S. N.; Jacobsen, E. N. Catalytic Asymmetric Total Syntheses of Quinine and Quinidine. *Journal of the American Chemical Society* **2004**, *126* (3), 706-707.

(141) Igarashi, J.; Katsukawa, M.; Wang, Y.-G.; Acharya, H. P.; Kobayashi, Y. Stereocontrolled synthesis of quinine and quinidine. *Tetrahedron Letters* **2004**, *45* (19), 3783-3786.

(142) Marcelli, T.; Hiemstra, H. Cinchona Alkaloids in Asymmetric Organocatalysis. *Synthesis* **2010**, *2010* (08), 1229-1279.

(143) Yoon, T. P.; Jacobsen, E. N. Privileged Chiral Catalysts. *Science* **2003**, *299* (5613), 1691.

(144) Kobayashi, N.; Iwai, K. Functional polymers. 1. Poly(cinchona alkaloid-co-acrylonitrile)s. New polymer catalysts for asymmetric synthesis. *Journal of the American Chemical Society* **1978**, *100* (22), 7071-7072.

(145) Hermann, K.; Wynberg, H. Polymergebundene Cinchonaalkaloide als Katalysatoren in der Michael Reaktion. *Helvetica Chimica Acta* **1977**, *60* (7), 2208-2212.

(146) Hodge, P.; Khoshdel, E.; Waterhouse, J. Michael reactions catalysed by polymer-supported quaternary ammonium salts derived from cinchona and ephedra alkaloids. *Journal of the Chemical Society, Perkin Transactions 1* **1983**, *1* (399), 2205-2209.

(147) Moon Kim, B.; Sharpless, K. B. Heterogeneous catalytic asymmetric dihydroxylation: Use of a polymer-bound alkaloid *Tetrahedron Letters* **1990** *31* (21), 3003-3006.

(148) Alvarez, R.; Hourdin, M. A.; Cavé, C.; D'Angelo, J.; Chaminade, P. New polymer-supported catalysts derived from Cinchona alkaloids: Their use in the asymmetric Michael reaction. *Tetrahedron Letters* **1999**, *40* (39), 7091-7094.

(149) Lee, J.-H.; Yoo, M.-S.; Jew, S.-s.; Park, H.-g.; Jeong, B.-S. Polymeric chiral phase-transfer catalysts derived from cinchona alkaloids for enantioselective synthesis of alpha-amino acids. *Tetrahedron* **2007**, *63* (33), 7906-7915.

(150) Jacobsen, E. N.; Marko, I.; Mungall, W. S.; Schroeder, G.; Sharpless, K. B. Asymmetric dihydroxylation via ligand-accelerated catalysis. *Journal of the American Chemical Society* **1988**, *110* (6), 1968-1970.

(151) Edward, J. A.; Kiesewetter, M. K.; Kim, H.; Flanagan, J. C.; Hedrick, J. L.; Waymouth, R. M. Organocatalytic synthesis of quinine-functionalized poly(carbonate)s. *Biomacromolecules* **2012**, *13* (8), 2483-2489.

(152) Chinchilla, R.; Mazón, P.; Nájera, C. Polymer-supported Cinchona alkaloid-derived ammonium salts as recoverable phase-transfer catalysts for the asymmetric synthesis of alpha-amino acids. *Tetrahedron: Asymmetry* **2000**, *11* (16), 3277-3281.

(153) Minoru, I.; Jun, H.; Yukio, Y.; Jun’ichi, O. Asymmetric Induction in the Base-Catalyzed Reactions Using Polymer-Supported Quinines with Spacer Groups. *Bulletin of the Chemical Society of Japan* **1987**, *60* (11), 4121-4126.

(154) Borchan, S. M.-A.; Zadneprovskaya, I. V.; Babayev, T. M.; Musayev, U. N. Copolymerization of N-vinylpyrrolidone with quinine. *Polymer Science U.S.S.R.* **1987**, *29* (1), 43-49.

(155) Hiemenz, P. C.; Lodge, T. Chain Growth Polymerization. In *Polymer chemistry*; CRC Press, 2007; pp. 77.

(156) Mortimer, G. A.; Arnold, L. C. Free-radical polymerization of olefins. *Journal of Polymer Science Part A: General Papers* **1964**, *2* (9), 4247-4253.

(157) Odian, G. Radical Chain Polymerization. In *Principles of Polymerization*, Odian, G. Ed.; Wiley, 2004; pp. 198-349.

(158) Lakowicz, J. R. Introduction to Fluorescence. In *Principles of Fluorescence Spectroscopy*, Lakowicz, J. R. Ed.; Springer US, 2006; pp 1-26.

(159) Herschel, J. F. W. IV. ’Αμόρφωϒa, no. I.— on a case of superficial colour presented by a homogeneous liquid internally colourless. *Philosophical Transactions of the Royal Society of London* **1845**, *135*, 143-145.

(160) Stokes, G. G. XXX. On the change of refrangibility of light. *Philosophical Transactions of the Royal Society of London* **1852**, *142*, 463-562.

(161) O'Reilly, J. E. Fluorescence experiments with quinine. *Journal of Chemical Education* **1975**, *52* (9), 610.

(162) Nawara, K.; Waluk, J. Goodbye to Quinine in Sulfuric Acid Solutions as a Fluorescence Quantum Yield Standard. *Analytical Chemistry* **2019**, *91* (8), 5389-5394.

(163) Melhuish, W. H. A Standard Fluorescence Spectrum for Calibrating Spectro-Fluorophotometers. *The Journal of Physical Chemistry* **1960**, *64* (6), 762-764.

(164) Udenfriend, S. Development of the spectrophotofluorometer and its commercialization. *Protein science : a publication of the Protein Society* **1995**, *4* (3), 542-551.

(165) Bohórquez, E. B.; Chua, M.; Meshnick, S. R. Quinine localizes to a non-acidic compartment within the food vacuole of the malaria parasite Plasmodium falciparum. *Malaria Journal* **2012**, *11* (1), 350.

(166) Kelkar, S. S.; Reineke, T. M. Theranostics: Combining Imaging and Therapy. *Bioconjugate Chemistry* **2011**, *22* (10), 1879-1903.

(167) Kajimoto, S.; Takeuchi, M.; Nakabayashi, T. Raman Imaging Microscopy for Quantitative Analysis of Biological Samples. In *Multi-Parametric Live Cell Microscopy of 3D Tissue Models*, Dmitriev, R. I. Ed.; Springer International Publishing, 2017; pp 163-172.

(168) Bantz, K. C.; Meyer, A. F.; Wittenberg, N. J.; Im, H.; Kurtuluş, Ö.; Lee, S. H.; Lindquist, N. C.; Oh, S.-H.; Haynes, C. L. Recent progress in SERS biosensing. *Physical Chemistry Chemical Physics* **2011**, *13* (24), 11551-11567.

(169) Tong, L.; Lu, Y.; Lee, R. J.; Cheng, J.-X. Imaging Receptor-Mediated Endocytosis with a Polymeric Nanoparticle-Based Coherent Anti-Stokes Raman Scattering Probe. *The Journal of Physical Chemistry B* **2007**, *111* (33), 9980-9985.

(170) Lane, L. A.; Qian, X.; Nie, S. SERS Nanoparticles in Medicine: From Label-Free Detection to Spectroscopic Tagging. *Chemical Reviews* **2015**, *115* (19), 10489-10529.

(171) Chen, Y.; Dai, J.; Zhou, X.; Liu, Y.; Zhang, W.; Peng, G. Raman Spectroscopy Analysis of the Biochemical Characteristics of Molecules Associated with the Malignant Transformation of Gastric Mucosa. *PLOS ONE* **2014**, *9* (4), e93906.

(172) Samuel, A. Z.; Miyaoka, R.; Ando, M.; Gaebler, A.; Thiele, C.; Takeyama, H. Molecular profiling of lipid droplets inside HuH7 cells with Raman micro-spectroscopy. *Communications Biology* **2020**, *3* (1), 372.

(173) Keren, S.; Zavaleta, C.; Cheng, Z.; de la Zerda, A.; Gheysens, O.; Gambhir, S. S. Noninvasive molecular imaging of small living subjects using Raman spectroscopy. *Proceedings of the National Academy of Sciences U S A* **2008**, *105* (15), 5844.

(174) Bartelmess, J.; Quinn, S. J.; Giordani, S. Carbon nanomaterials: multi-functional agents for biomedical fluorescence and Raman imaging. *Chemical Society Reviews* **2015**, *44* (14), 4672-4698.

(175) Chernenko, T.; Sawant, R. R.; Miljkovic, M.; Quintero, L.; Diem, M.; Torchilin, V. Raman Microscopy for Noninvasive Imaging of Pharmaceutical Nanocarriers: Intracellular Distribution of Cationic Liposomes of Different Composition. *Molecular Pharmaceutics* **2012**, *9* (4), 930-936.

(176) Christian, M.; Tatyana, C.; Luis, Q.; Lara, M.; Amit, K.; Mansoor, A.; Vladimir, T.; Max, D. Raman microscopic imaging of cells and applications monitoring the uptake of drug delivery systems. In *Proceedings SPIE*, 2008; Vol. 6991. DOI: 10.1117/12.800385.

(177) Hu, F.; Brucks, S. D.; Lambert, T. H.; Campos, L. M.; Min, W. Stimulated Raman scattering of polymer nanoparticles for multiplexed live-cell imaging. *Chemical Communications* **2017**, *53* (46), 6187-6190.

(178) Garrett, N. L.; Lalatsa, A.; Begley, D.; Mihoreanu, L.; Uchegbu, I. F.; Schätzlein, A. G.; Moger, J. Label-free imaging of polymeric nanomedicines using coherent anti-stokes Raman scattering microscopy. *Journal of Raman Spectroscopy* **2012**, *43* (5), 681-688.

(179) Chernenko, T.; Matthäus, C.; Milane, L.; Quintero, L.; Amiji, M.; Diem, M. Label-Free Raman Spectral Imaging of Intracellular Delivery and Degradation of Polymeric Nanoparticle Systems. *ACS Nano* **2009**, *3* (11), 3552-3559.

(180) Zhao, Z.; Chen, C.; Wei, S.; Xiong, H.; Hu, F.; Miao, Y.; Jin, T.; Min, W. Ultra-bright Raman dots for multiplexed optical imaging. *Nature Communications* **2021**, *12* (1), 1305.

(181) Tian, S.; Li, H.; Li, Z.; Tang, H.; Yin, M.; Chen, Y.; Wang, S.; Gao, Y.; Yang, X.; Meng, F.; et al. Polydiacetylene-based ultrastrong bioorthogonal Raman probes for targeted live-cell Raman imaging. *Nature Communications* **2020**, *11* (1), 81.

(182) Schie, I. W.; Huser, T. Methods and Applications of Raman Microspectroscopy to Single-Cell Analysis. *Applied Spectroscopy* **2013**, *67* (8), 813-828.

(183) Luan, C. R.; Liu, Y. H.; Zhang, J.; Yu, Q. Y.; Huang, Z.; Wang, B.; Yu, X. Q. Low Molecular Weight Oligomers with Aromatic Backbone as Efficient Nonviral Gene Vectors. *ACS Applied Materials & Interfaces* **2016**, *8* (17), 10743-10751.

(184) Yi, W. J.; Yu, X. C.; Wang, B.; Zhang, J.; Yu, Q. Y.; Zhou, X. D.; Yu, X. Q. TACN-based oligomers with aromatic backbones for efficient nucleic acid delivery. *Chemical Communications* **2014**, *50* (49), 6454-6457.

(185) Ehsanian, R.; Van Waes, C.; Feller, S. M. Beyond DNA binding - a review of the potential mechanisms mediating quinacrine's therapeutic activities in parasitic infections, inflammation, and cancers. *Cell Communication and Signaling* **2011**, *9* (1), 13.

(186) Irvin, J. L.; Irvin, E. M.; Parker, F. S. The Interaction of Antimalarials with Nucleic Acids. *Science* **1949**, *110* (2860), 426-428.

(187) Parker, F. S.; Irvin, J. L. The interaction of chloroquine with nucleic acids and nucleoproteins. *Journal Biological Chemistry* **1952**, *199* (2), 897-909.

(188) Cohen, S. N.; Yielding, K. L. Spectrophotometric Studies of the Interaction of Chloroquine with Deoxyribonucleic Acid. *Journal Biological Chemistry* **1965**, *240*, 3123-3131.

(189) Davidson, M. W.; Griggs, B. G.; Boykin, D. W.; Wilson, W. D. Mefloquine, a clinically useful quinolinemethanol antimalarial which does not significantly bind to DNA. *Nature* **1975**, *254* (5501), 632-634.

(190) Davidson, M. W.; Griggs, B. G.; Boykin, D. W.; Wilson, W. D. Molecular structural effects involved in the interaction of quinolinemethanolamines with DNA. Implications for antimalarial action. *Journal of Medicinal Chemistry* **1977**, *20* (9), 1117-1122.

(191) Jones, R. L.; Davidson, M. W.; Wilson, W. D. Comparative viscometric analysis of the interaction of chloroquine and quinacrine with superhelical and sonicated DNA. *Biochimica et Biophysica Acta* **1979**, *561* (1), 77-84.

(192) Wilson, W. D.; Jones, R. L. Intercalating drugs: DNA binding and molecular pharmacology. *Advances in Pharmacology and Chemotherapy* **1981**, *18*, 177-222.

(193) Lai, X.; Lin, Y.; Zhang, C.; Zhou, X. Study on the interaction between quinine sulfate and DNA by multiple spectral methods and their analytical applications. *Analytical Sciences* **2013**, *29* (4), 435-440.

(194) Wesełucha-Birczyńska, A.; Nakamoto, K. UV resonance raman studies on cinchonine - polynucleotide interactions. *Journal of Molecular Structure* **1993**, *294* (1-2), 127-129.

(195) Wesełucha-Birczyńska, A.; Nakamoto, K. Study of the Interaction of the Antimalarial Drug Cinchonine with Nucleic Acids by Raman Spectroscopy. *Journal of Raman Spectroscopy* **1996**, *27* (12), 915-919.

(196) Schneider, S. H.; Kratochvil, H. T.; Zanni, M. T.; Boxer, S. G. Solvent-Independent Anharmonicity for Carbonyl Oscillators. *The Journal of Physical Chemistry B* **2017**, *121* (10), 2331-2338.

(197) Andrews, S. S.; Boxer, S. G. Vibrational Stark Effects of Nitriles I. Methods and Experimental Results. *The Journal of Physical Chemistry A* **2000**, *104* (51), 11853-11863.

(198) Andrews, S. S.; Boxer, S. G. Vibrational Stark Effects of Nitriles II. Physical Origins of Stark Effects from Experiment and Perturbation Models. *The Journal of Physical Chemistry A* **2002**, *106* (3), 469-477.

(199) Levinson, N. M.; Fried, S. D.; Boxer, S. G. Solvent-Induced Infrared Frequency Shifts in Aromatic Nitriles Are Quantitatively Described by the Vibrational Stark Effect. *The Journal of Physical Chemistry B* **2012**, *116* (35), 10470-10476.

(200) Fried, S. D.; Bagchi, S.; Boxer, S. G. Measuring Electrostatic Fields in Both Hydrogen-Bonding and Non-Hydrogen-Bonding Environments Using Carbonyl Vibrational Probes. *Journal of the American Chemical Society* **2013**, *135* (30), 11181-11192.

(201) Fried, S. D.; Boxer, S. G. Measuring Electric Fields and Noncovalent Interactions Using the Vibrational Stark Effect. *Accounts of Chemical Research* **2015**, *48* (4), 998-1006.

(202) Elenewski, J. E.; Hackett, J. C. Solvatochromism and the solvation structure of benzophenone. *The Journal of Chemical Physics* **2013**, *138* (22), 224308.

(203) Ritchie, A. W.; Webb, L. J. Understanding and Manipulating Electrostatic Fields at the Protein–Protein Interface Using Vibrational Spectroscopy and Continuum Electrostatics Calculations. *The Journal of Physical Chemistry B* **2015**, *119* (44), 13945-13957.

(204) Błasiak, B.; Londergan, C. H.; Webb, L. J.; Cho, M. Vibrational Probes: From Small Molecule Solvatochromism Theory and Experiments to Applications in Complex Systems. *Accounts of Chemical Research* **2017**, *50* (4), 968-976.

(205) Oh, K. I.; Fiorin, G.; Gai, F. How Sensitive is the Amide I Vibration of the Polypeptide Backbone to Electric Fields? *Chemphyschem* **2015**, *16* (17), 3595-3598.

(206) Chalyavi, F.; Hogle, D. G.; Tucker, M. J. Tyrosine as a Non-perturbing Site-Specific Vibrational Reporter for Protein Dynamics. *The Journal of Physical Chemistry B* **2017**, *121* (26), 6380-6389.

(207) Frosch, T.; Schmitt, M.; Popp, J. In situ UV resonance Raman micro-spectroscopic localization of the antimalarial quinine in cinchona bark. *The Journal of Physical Chemistry B* **2007**, *111* (16), 4171-4177.

(208) Roman, M.; Chruszcz-Lipska, K.; Baranska, M. Vibrational analysis of cinchona alkaloids in the solid state and aqueous solutions. *Journal of Raman Spectroscopy* **2015**, *46* (11), 1041-1052.

(209) Domes, R.; Domes, C.; Albert, C. R.; Bringmann, G.; Popp, J.; Frosch, T. Vibrational spectroscopic characterization of arylisoquinolines by means of Raman spectroscopy and density functional theory calculations. *Physical Chemistry Chemical Physics* **2017**, *19* (44), 29918-29926.

(210) Punihaole, D.; Workman, R. J.; Upadhyay, S.; Van Bruggen, C.; Schmitz, A. J.; Reineke, T. M.; Frontiera, R. R. New Insights into Quinine-DNA Binding Using Raman Spectroscopy and Molecular Dynamics Simulations. *The Journal of Physical Chemistry B* **2018**, *122* (43), 9840-9851.

(211) Zhao, Y.; Truhlar, D. G. The M06 suite of density functionals for main group thermochemistry, thermochemical kinetics, noncovalent interactions, excited states, and transition elements: two new functionals and systematic testing of four M06-class functionals and 12 other functionals. *Theoretical Chemistry Accounts* **2008**, *120* (1), 215-241.

(212) Dunning, T. H. Gaussian basis sets for use in correlated molecular calculations. I. The atoms boron through neon and hydrogen. *The Journal of Chemical Physics* **1989**, *90* (2), 1007-1023.

(213) Hush, N. S.; Reimers, J. R. Vibrational Stark Spectroscopy. 1. Basic Theory and Application to the CO Stretch. *The Journal of Physical Chemistry* **1995**, *99* (43), 15798-15805.

(214) Onsager, L. Electric Moments of Molecules in Liquids. *Journal of the American Chemical Society* **1936**, *58* (8), 1486-1493.

(215) *CRC Handbook of Chemistry and Physics, 89th Edition*, Lide, D. R. Ed.; CRC Press, 2008; Ch. 3, pp. 454.

(216) Sen, A.; Bouchet, A.; Lepère, V.; Le Barbu-Debus, K.; Scuderi, D.; Piuzzi, F.; Zehnacker-Rentien, A. Conformational Analysis of Quinine and Its Pseudo Enantiomer Quinidine: A Combined Jet-Cooled Spectroscopy and Vibrational Circular Dichroism Study. *The Journal of Physical Chemistry A* **2012**, *116* (32), 8334-8344.

(217) Dudik, J. M.; Johnson, C. R.; Asher, S. A. Wavelength dependence of the preresonance Raman cross sections of CH_3CN, SO_4^{2-}, ClO_4^{-}, and NO_3^{-}. *The Journal of Chemical Physics* **1985**, *82* (4), 1732-1740.

(218) Estensen, R. D.; Krey, A. K.; Hahn, F. E. Studies on a deoxyribonucleic acid-quinine complex. *Molecular Pharmacology* **1969**, *5* (5), 532-541.

(219) Deng, H.; Bloomfield, V. A.; Benevides, J. M.; Thomas, G. J., Jr. Dependence of the Raman signature of genomic B-DNA on nucleotide base sequence. *Biopolymers* **1999**, *50* (6), 656-666.

(220) Savitzky, A.; Golay, M. J. E. Smoothing and Differentiation of Data by Simplified Least Squares Procedures. *Analytical Chemistry* **1964**, *36* (8), 1627-1639.

(221) Krimer, N. I.; Mirenda, M. Re-evaluation of the steady-state self-quenching constant of quinine bisulphate from fluorescence measurements in transmission geometry. *Methods and Applications in Fluorescence* **2017**, *5* (3), 034001.

(222) Phillips, J. C.; Braun, R.; Wang, W.; Gumbart, J.; Tajkhorshid, E.; Villa, E.; Chipot, C.; Skeel, R. D.; Kalé, L.; Schulten, K. Scalable molecular dynamics with NAMD. *Journal of Computational Chemistry* **2005**, *26* (16), 1781-1802.

(223) Huang, J.; MacKerell, A. D., Jr. CHARMM36 all-atom additive protein force field: validation based on comparison to NMR data. *Journal of Computational Chemistry* **2013**, *34* (25), 2135-2145.

(224) Vanommeslaeghe, K.; Hatcher, E.; Acharya, C.; Kundu, S.; Zhong, S.; Shim, J.; Darian, E.; Guvench, O.; Lopes, P.; Vorobyov, I.; et al. CHARMM general force field: A force field for drug-like molecules compatible with the CHARMM all-atom additive biological force fields. *Journal of Computational Chemistry* **2010**, *31* (4), 671-690.

(225) Hornak, V.; Abel, R.; Okur, A.; Strockbine, B.; Roitberg, A.; Simmerling, C. Comparison of multiple Amber force fields and development of improved protein backbone parameters. *Proteins: Structure, Function, and Bioinformatics* **2006**, *65* (3), 712-725.

(226) Wang, J.; Wolf, R. M.; Caldwell, J. W.; Kollman, P. A.; Case, D. A. Development and testing of a general amber force field. *Journal of Computational Chemistry* **2004**, *25* (9), 1157-1174.

(227) Jorgensen, W. L.; Chandrasekhar, J.; Madura, J. D.; Impey, R. W.; Klein, M. L. Comparison of simple potential functions for simulating liquid water. *The Journal of Chemical Physics* **1983**, *79* (2), 926-935.

(228) Humphrey, W.; Dalke, A.; Schulten, K. VMD: visual molecular dynamics. *Journal of Molecular Graphics* **1996**, *14* (1), 33-38, 27-38.

(229) Rutledge, L. R.; Durst, H. F.; Wetmore, S. D. Evidence for Stabilization of DNA/RNA−Protein Complexes Arising from Nucleobase−Amino Acid Stacking and T-Shaped Interactions. *Journal of Chemical Theory and Computation* **2009**, *5* (5), 1400-1410.

(230) van der Loo, J. C.; Wright, J. F. Progress and challenges in viral vector manufacturing. *Human Molecular Genetics* **2016**, *25* (R1), R42-52.

(231) Elverum, K.; Whitman, M. Delivering cellular and gene therapies to patients: solutions for realizing the potential of the next generation of medicine. *Gene Therapy* **2020**, *27* (12), 537-544.

(232) Ma, C.-C.; Wang, Z.-L.; Xu, T.; He, Z.-Y.; Wei, Y.-Q. The approved gene therapy drugs worldwide: from 1998 to 2019. *Biotechnology Advances* **2020**, *40*, 107502.

(233) Wu, P.; Chen, H.; Jin, R.; Weng, T.; Ho, J. K.; You, C.; Zhang, L.; Wang, X.; Han, C. Non-viral gene delivery systems for tissue repair and regeneration. *Journal of Translational Medicine* **2018**, *16* (1), 29.

(234) Iida, T.; Mori, T.; Katayama, Y.; Niidome, T. Overall interaction of cytosolic proteins with the PEI/DNA complex. *Journal of Controlled Release* **2007**, *118* (3), 364-369.

(235) Zhang, J. H.; Yang, H. Z.; Zhang, J.; Liu, Y. H.; He, X.; Xiao, Y. P.; Yu, X. Q. Biodegradable Gene Carriers Containing Rigid Aromatic Linkage with Enhanced DNA Binding and Cell Uptake. *Polymers (Basel)* **2018**, *10* (10), 1080.

(236) McKinlay, C. J.; Vargas, J. R.; Blake, T. R.; Hardy, J. W.; Kanada, M.; Contag, C. H.; Wender, P. A.; Waymouth, R. M. Charge-altering releasable transporters (CARTs) for the delivery and release of mRNA in living animals. *Proceedings of the National Academy of Sciences U S A* **2017**, *114* (4), E448-E456.

(237) Xie, Y.; Yu, F.; Tang, W.; Alade, B. O.; Peng, Z. H.; Wang, Y.; Li, J.; Oupický, D. Synthesis and Evaluation of Chloroquine-Containing DMAEMA Copolymers as Efficient Anti-miRNA Delivery Vectors with Improved Endosomal Escape and Antimigratory Activity in Cancer Cells. *Macromolecular Biosciences* **2018**, *18* (1), DOI: 10.1002/mabi.201700194.

(238) Yu, F.; Xie, Y.; Wang, Y.; Peng, Z. H.; Li, J.; Oupický, D. Chloroquine-Containing HPMA Copolymers as Polymeric Inhibitors of Cancer Cell Migration Mediated by the CXCR4/SDF-1 Chemokine Axis. *ACS Macro Letters* **2016**, *5* (3), 342-345.

(239) Zhang, B.; Zhang, Y.; Mallapragada, S. K.; Clapp, A. R. Sensing Polymer/DNA Polyplex Dissociation Using Quantum Dot Fluorophores. *ACS Nano* **2011**, *5* (1), 129-138.

(240) Godbey, W. T.; Wu, K. K.; Mikos, A. G. Tracking the intracellular path of poly(ethylenimine)/DNA complexes for gene delivery. *Proceedings of the National Academey of Sciences U S A* **1999**, *96* (9), 5177-5181.

(241) Kiang, T.; Bright, C.; Cheung, C. Y.; Stayton, P. S.; Hoffman, A. S.; Leong, K. W. Formulation of chitosan-DNA nanoparticles with poly(propyl acrylic acid) enhances gene expression. *Journal of Biomaterials Science, Polymer Edition* **2004**, *15* (11), 1405-1421.

(242) Saar, B. G.; Contreras-Rojas, L. R.; Xie, X. S.; Guy, R. H. Imaging drug delivery to skin with stimulated Raman scattering microscopy. *Molecular Pharmaceutics* **2011**, *8* (3), 969-975.

(243) Hosokawa, M.; Ando, M.; Mukai, S.; Osada, K.; Yoshino, T.; Hamaguchi, H. O.; Tanaka, T. In vivo live cell imaging for the quantitative monitoring of lipids by using Raman microspectroscopy. *Analytical Chemistry* **2014**, *86* (16), 8224-8230.

(244) Lu, F. K.; Basu, S.; Igras, V.; Hoang, M. P.; Ji, M.; Fu, D.; Holtom, G. R.; Neel, V. A.; Freudiger, C. W.; Fisher, D. E.; et al. Label-free DNA imaging in vivo with stimulated Raman scattering microscopy. *Proceedings of the National Academy of Sciences U S A* **2015**, *112* (37), 11624-11629.

(245) Hu, F.; Wei, L.; Zheng, C.; Shen, Y.; Min, W. Live-cell vibrational imaging of choline metabolites by stimulated Raman scattering coupled with isotope-based metabolic labeling. *Analyst* **2014**, *139* (10), 2312-2317.

(246) Punihaole, D.; Hong, Z.; Jakubek, R. S.; Dahlburg, E. M.; Geib, S.; Asher, S. A. Glutamine and Asparagine Side Chain Hyperconjugation-Induced Structurally Sensitive Vibrations. *The Journal of Physical Chemistry B* **2015**, *119* (41), 13039-13051.

(247) Punihaole, D.; Jakubek, R. S.; Workman, R. J.; Asher, S. A. Interaction Enthalpy of Side Chain and Backbone Amides in Polyglutamine Solution Monomers and Fibrils. *The Journal of Physical Chemistry Letters* **2018**, *9* (8), 1944-1950.

(248) Mikhonin, A. V.; Bykov, S. V.; Myshakina, N. S.; Asher, S. A. Peptide Secondary Structure Folding Reaction Coordinate: Correlation Between UV Raman Amide III Frequency, Ψ Ramachandran Angle, and Hydrogen Bonding. *The Journal of Physical Chemistry B* **2006**, *110* (4), 1928-1943.

(249) Wang, Y.; Purrello, R.; Georgiou, S.; Spiro, T. G. UVRR Spectroscopy of the Peptide Bond. 2. Carbonyl H-Bond Effects on the Ground- and Excited-State Structures of N-Methylacetamide. *Journal of the American Chemical Society* **1991**, *113* (17), 6368-6377.

(250) Punihaole, D.; Jakubek, R. S.; Dahlburg, E. M.; Hong, Z.; Myshakina, N. S.; Geib, S.; Asher, S. A. UV resonance Raman investigation of the aqueous solvation dependence of primary amide vibrations. *The Journal of Physical Chemistry B* **2015**, *119* (10), 3931-3939.

(251) Erfurth, S. C.; Kiser, E. J.; Peticolas, W. L. Determination of the backbone structure of nucleic acids and nucleic acid oligomers by laser Raman scattering. *Proceedings of the National Academy of Sciences U S A* **1972**, *69* (4), 938-941.

(252) Zhou, S.; Fan, S.; Au-yeung, S. C. F.; Wu, C. Light-scattering studies of poly(N-isopropylacrylamide) in tetrahydrofuran and aqueous solution. *Polymer* **1995**, *36* (7), 1341-1346.

(253) McCool, M. B.; Senogles, E. The self-catalysed hydrolysis of poly(N,N-dimethylaminoethyl acrylate). *European Polymer Journal* **1989**, *25* (7-8), 857-860.

(254) Liu, Y.; Reineke, T. M. Poly(glycoamidoamine)s for Gene Delivery. Structural Effects on Cellular Internalization, Buffering Capacity, and Gene Expression. *Bioconjugate Chemistry* **2007**, *18* (1), 19-30. DOI: 10.1021/bc060029d.

(255) Liu, Y.; Reineke, T. M. Poly(glycoamidoamine)s for Gene Delivery: Stability of Polyplexes and Efficacy with Cardiomyoblast Cells. *Bioconjugate Chemistry* **2006**, *17* (1), 101-108.

(256) Goula, D.; Remy, J. S.; Erbacher, P.; Wasowicz, M.; Levi, G.; Abdallah, B.; Demeneix, B. A. Size, diffusibility and transfection performance of linear PEI/DNA complexes in the mouse central nervous system. *Gene Therapy* **1998**, *5* (5), 712-717.

(257) Burke, R. S.; Pun, S. H. Extracellular Barriers to in Vivo PEI and PEGylated PEI Polyplex-Mediated Gene Delivery to the Liver. *Bioconjugate Chemistry* **2008**, *19* (3), 693-704.

(258) Strauch, S.; Dressman, J. B.; Shah, V. P.; Kopp, S.; Polli, J. E.; Barends, D. M. 2012. Biowaiver monographs for immediate-release s.olid oral dosage forms: Quinine sulfate. *Journal Pharmecutical Sciences* **2012**, *101* (2), 499-508.

(259) Avdeef, A.; Box, K. J.; Comer, J. E. A.; Gilges, M.; Hadley, M.; Hibbert, C.; Patterson, W.; Tam, K. Y. PH-metric logP 11. pKa determination of water-insoluble drugs in organic solvent–water mixtures. *Journal of Pharmaceutical and Biomedical Analysis* **1999**, *20* (4), 631-641.

(260) Behr, J.-P. Synthetic Gene Transfer Vectors II: Back to the Future. *Accounts of Chemical Research* **2012**, *45* (7), 980-984.

(261) Pezzoli, D.; Giupponi, E.; Mantovani, D.; Candiani, G. Size matters for in vitro gene delivery: investigating the relationships among complexation protocol, transfection medium, size and sedimentation. *Scientific Reports* **2017**, *7* (1), 44134.

(262) Luo, D.; Saltzman, W. M. Enhancement of transfection by physical concentration of DNA at the cell surface. *Nature Biotechnology* **2000**, *18* (8), 893-895.

(263) Agrawal, P.; Ingle, N. P.; Boyle, W. S.; Ward, E.; Tolar, J.; Dorfman, K. D.; Reineke, T. M. Fast, Efficient, and Gentle Transfection of Human Adherent Cells in Suspension. *ACS Applied Materials & Interfaces* **2016**, *8* (14), 8870-8874.

(264) von Gersdorff, K.; Sanders, N. N.; Vandenbroucke, R.; De Smedt, S. C.; Wagner, E.; Ogris, M. The Internalization Route Resulting in Successful Gene Expression Depends on both Cell Line and Polyethylenimine Polyplex Type. *Molecular Therapy* **2006**, *14* (5), 745-753.

(265) Rejman, J.; Oberle, V.; Zuhorn, I. S.; Hoekstra, D. Size-dependent internalization of particles via the pathways of clathrin- and caveolae-mediated endocytosis. *Biochemical Journal* **2004**, *377* (1), 159-169.

(266) Mavilio, F.; Pellegrini, G.; Ferrari, S.; Di Nunzio, F.; Di Iorio, E.; Recchia, A.; Maruggi, G.; Ferrari, G.; Provasi, E.; Bonini, C.; et al. Correction of junctional epidermolysis bullosa by transplantation of genetically modified epidermal stem cells. *Nature Medicine* **2006**, *12* (12), 1397-1402.

(267) Bauer, J. W.; Koller, J.; Murauer, E. M.; De Rosa, L.; Enzo, E.; Carulli, S.; Bondanza, S.; Recchia, A.; Muss, W.; Diem, A.; et al. Closure of a Large Chronic Wound through Transplantation of Gene-Corrected Epidermal Stem Cells. *Journal of Investigative Dermatology* **2017**, *137* (3), 778-781.

(268) Hirsch, T.; Rothoeft, T.; Teig, N.; Bauer, J. W.; Pellegrini, G.; De Rosa, L.; Scaglione, D.; Reichelt, J.; Klausegger, A.; Kneisz, D.; et al. Regeneration of the entire human epidermis using transgenic stem cells. *Nature* **2017**, *551* (7680), 327-332.

(269) Deyrieux, A. F.; Wilson, V. G. In vitro culture conditions to study keratinocyte differentiation using the HaCaT cell line. *Cytotechnology* **2007**, *54* (2), 77-83.

(270) Dickens, S.; Van den Berge, S.; Hendrickx, B.; Verdonck, K.; Luttun, A.; Vranckx, J. J. Nonviral Transfection Strategies for Keratinocytes, Fibroblasts, and Endothelial Progenitor Cells for Ex Vivo Gene Transfer to Skin Wounds. *Tissue Engineering Part C: Methods* **2010**, *16* (6), 1601-1608.

(271) Liang, X.; Potter, J.; Kumar, S.; Zou, Y.; Quintanilla, R.; Sridharan, M.; Carte, J.; Chen, W.; Roark, N.; Ranganathan, S.; et al. Rapid and highly efficient mammalian cell engineering via Cas9 protein transfection. *Journal of Biotechnology* **2015**, *208*, 44-53.

(272) Zhao, C.; Zhao, J.; Li, X.; Wu, J.; Chen, S.; Chen, Q.; Wang, Q.; Gong, X.; Li, L.; Zheng, J. Probing structure-antifouling activity relationships of polyacrylamides and polyacrylates. *Biomaterials* **2013**, *34* (20), 4714-4724.

(273) Zolk, M.; Eisert, F.; Pipper, J.; Herrwerth, S.; Eck, W.; Buck, M.; Grunze, M. Solvation of Oligo(ethylene glycol)-Terminated Self-Assembled Monolayers Studied by Vibrational Sum Frequency Spectroscopy. *Langmuir* **2000**, *16* (14), 5849-5852.

(274) Zheng, J.; Li, L.; Chen, S.; Jiang, S. Molecular Simulation Study of Water Interactions with Oligo (Ethylene Glycol)-Terminated Alkanethiol Self-Assembled Monolayers. *Langmuir* **2004**, *20* (20), 8931-8938.

(275) Tuzar, Z.; Kratochvíl, P. Determination of the composition of copolymers by differential refractometry in mixed solvents. *Journal of Polymer Science Part B: Polymer Letters* **1969**, *7* (12), 825-828.

(276) McLendon, P. M.; Buckwalter, D. J.; Davis, E. M.; Reineke, T. M. Interaction of Poly(glycoamidoamine) DNA Delivery Vehicles with Cell-Surface Glycosaminoglycans Leads to Polyplex Internalization in a Manner Not Solely Dependent on Charge. *Molecular Pharmaceutics* **2010**, *7* (5), 1757-1768.

(277) Lee, J. S.; Wee, T. L.; Brown, C. M. Calibration of wide-field deconvolution microscopy for quantitative fluorescence imaging. *Journal of Biomolecular Techniques* **2014**, *25* (1), 31-40.

(278) Richardson, W. H. Bayesian-Based Iterative Method of Image Restoration. *Journal of the Optical Society of America* **1972**, *62* (1), 55-59.

(279) Lucy, L. B. An iterative technique for the rectification of observed distributions. *Astronomical Journal* **1974**, *79*, 745-754.

(280) Bolte, S.; Cordelières, F. P. A guided tour into subcellular colocalization analysis in light microscopy. *Journal of Microscopy* **2006**, *224* (3), 213-232.

(281) Manders, E. M. M.; Verbeek, F. J.; Aten, J. A. Measurement of co-localization of objects in dual-colour confocal images. *Journal of Microscopy* **1993**, *169* (3), 375-382.

(282) Gary, D. J.; Lee, H.; Sharma, R.; Lee, J.-S.; Kim, Y.; Cui, Z. Y.; Jia, D.; Bowman, V. D.; Chipman, P. R.; Wan, L.; et al. Influence of Nano-Carrier Architecture on in Vitro siRNA Delivery Performance and in Vivo Biodistribution: Polyplexes vs Micelleplexes. *ACS Nano* **2011**, *5* (5), 3493-3505.

(283) McLendon, P. M.; Fichter, K. M.; Reineke, T. M. Poly(glycoamidoamine) Vehicles Promote pDNA Uptake through Multiple Routes and Efficient Gene Expression via Caveolae-Mediated Endocytosis. *Molecular Pharmaceutics* **2010**, *7* (3), 738-750.

(284) Boyle, W. S.; Senger, K.; Tolar, J.; Reineke, T. M. Heparin Enhances Transfection in Concert with a Trehalose-Based Polycation with Challenging Cell Types. *Biomacromolecules* **2017**, *18* (1), 56-67.

(285) Miao, L.; Li, J.; Liu, Q.; Feng, R.; Das, M.; Lin, C. M.; Goodwin, T. J.; Dorosheva, O.; Liu, R.; Huang, L. Transient and Local Expression of Chemokine and Immune Checkpoint Traps To Treat Pancreatic Cancer. *ACS Nano* **2017**, *11* (9), 8690-8706.

(286) Bharti, R.; Srivastava, A.; Roy, T.; Verma, K.; Reddy, D. V. S.; Shafi, H.; Verma, S.; Raman, S. K.; Singh, A. K.; Singh, J.; et al. Transient Transfection of the Respiratory Epithelium with Gamma Interferon for Host-Directed Therapy in Pulmonary Tuberculosis. *Molecular therapy- Nucleic acids* **2020**, *22*, 1121-1128.

(287) Adli, M. The CRISPR tool kit for genome editing and beyond. *Nature Communications* **2018**, *9* (1), 1911.

(288) Lu, Y.; Xue, J.; Deng, T.; Zhou, X.; Yu, K.; Deng, L.; Huang, M.; Yi, X.; Liang, M.; Wang, Y.; et al. Safety and feasibility of CRISPR-edited T cells in patients with refractory non-small-cell lung cancer. *Nature Medicine* **2020**, *26* (5), 732-740.

(289) Frangoul, H.; Altshuler, D.; Cappellini, M. D.; Chen, Y.-S.; Domm, J.; Eustace, B. K.; Foell, J.; de la Fuente, J.; Grupp, S.; Handgretinger, R.; et al. CRISPR-Cas9 Gene Editing for Sickle Cell Disease and β-Thalassemia. *New England Journal of Medicine* **2020**, *384* (3), 252-260.

(290) Maeder, M. L.; Stefanidakis, M.; Wilson, C. J.; Baral, R.; Barrera, L. A.; Bounoutas, G. S.; Bumcrot, D.; Chao, H.; Ciulla, D. M.; DaSilva, J. A.; et al. Development of a gene-editing approach to restore vision loss in Leber congenital amaurosis type 10. *Nature Medicine* **2019**, *25* (2), 229-233.

(291) Uddin, F.; Rudin, C. M.; Sen, T. CRISPR Gene Therapy: Applications, Limitations, and Implications for the Future. *Frontiers in Oncology* **2020**, *10*, 1387.

(292) Kim, S.; Kim, D.; Cho, S. W.; Kim, J.; Kim, J.-S. Highly efficient RNA-guided genome editing in human cells via delivery of purified Cas9 ribonucleoproteins. *Genome Research* **2014**, *24* (6), 1012-1019.

(293) Sun, W.; Ji, W.; Hall, J. M.; Hu, Q.; Wang, C.; Beisel, C. L.; Gu, Z. Self-Assembled DNA Nanoclews for the Efficient Delivery of CRISPR–Cas9 for Genome Editing. *Angewandte Chemie International Edition* **2015**, *54* (41), 12029-12033.

(294) Cheng, H.; Zhang, F.; Ding, Y. CRISPR/Cas9 Delivery System Engineering for Genome Editing in Therapeutic Applications. *Pharmaceutics* **2021**, *13* (10), 1649.

(295) Mout, R.; Ray, M.; Yesilbag Tonga, G.; Lee, Y.-W.; Tay, T.; Sasaki, K.; Rotello, V. M. Direct Cytosolic Delivery of CRISPR/Cas9-Ribonucleoprotein for Efficient Gene Editing. *ACS Nano* **2017**, *11* (3), 2452-2458.

(296) Liu, C.; Wan, T.; Wang, H.; Zhang, S.; Ping, Y.; Cheng, Y. A boronic acid–rich dendrimer with robust and unprecedented efficiency for cytosolic protein delivery and CRISPR-Cas9 gene editing. *Science Advances* **2019**, *5* (6), eaaw8922.

(297) Jacinto, F. V.; Link, W.; Ferreira, B. I. CRISPR/Cas9-mediated genome editing: From basic research to translational medicine. *Journal of Cellular and Molecular Medicine* **2020**, *24* (7), 3766-3778.

(298) Lee, B.; Lee, K.; Panda, S.; Gonzales-Rojas, R.; Chong, A.; Bugay, V.; Park, H. M.; Brenner, R.; Murthy, N.; Lee, H. Y. Nanoparticle delivery of CRISPR into the brain rescues a mouse model of fragile X syndrome from exaggerated repetitive behaviours. *Nature Biomedical Engineering* **2018**, *2* (7), 497-507.

(299) Wang, Y.; Ma, B.; Abdeen, A. A.; Chen, G.; Xie, R.; Saha, K.; Gong, S. Versatile Redox-Responsive Polyplexes for the Delivery of Plasmid DNA, Messenger RNA, and CRISPR-Cas9 Genome-Editing Machinery. *ACS Applied Materials & Interfaces* **2018**, *10* (38), 31915-31927.

(300) van Gaal, E. V.; Spierenburg, G.; Hennink, W. E.; Crommelin, D. J.; Mastrobattista, E. Flow cytometry for rapid size determination and sorting of nucleic acid containing nanoparticles in biological fluids. *Journal of Controlled Release* **2010**, *141* (3), 328-338.

(301) Welsh, J. A.; Jones, J. C. Small Particle Fluorescence and Light Scatter Calibration Using FCMPASS Software. *Current Protocols in Cytometry* **2020**, *94* (1), e79.

(302) Certo, M. T.; Ryu, B. Y.; Annis, J. E.; Garibov, M.; Jarjour, J.; Rawlings, D. J.; Scharenberg, A. M. Tracking genome engineering outcome at individual DNA breakpoints. *Nature Methods* **2011**, *8* (8), 671-676.

(303) Osborn, M. J.; Gabriel, R.; Webber, B. R.; DeFeo, A. P.; McElroy, A. N.; Jarjour, J.; Starker, C. G.; Wagner, J. E.; Joung, J. K.; Voytas, D. F.; et al. Fanconi anemia gene editing by the CRISPR/Cas9 system. *Human Gene Therapy* **2015**, *26* (2), 114-126.

(304) Yu, X.; Liang, X.; Xie, H.; Kumar, S.; Ravinder, N.; Potter, J.; de Mollerat du Jeu, X.; Chesnut, J. D. Improved delivery of Cas9 protein/gRNA complexes using lipofectamine CRISPRMAX. *Biotechnology Letters* **2016**, *38* (6), 919-929.

(305) Skvarova Kramarzova, K.; Osborn, M. J.; Webber, B. R.; DeFeo, A. P.; McElroy, A. N.; Kim, C. J.; Tolar, J. CRISPR/Cas9-Mediated Correction of the FANCD1 Gene in Primary Patient Cells. *International Journal of Molecular Sciences* **2017**, *18* (6), 1269.